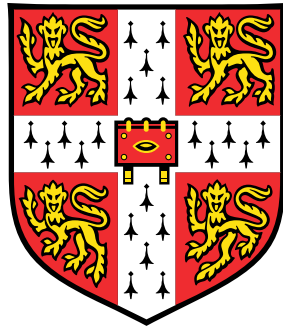


The mechanics of the soundpost in the violin



Myles Cameron Nadarajah

Department of Engineering
University of Cambridge

This dissertation is submitted for the degree of
Doctor of Philosophy

Declaration

This dissertation is the result of my own work and includes nothing which is the outcome of work done in collaboration except as declared in the Preface and specified in the text. It is not substantially the same as any that I have submitted, or, is being concurrently submitted for a degree or diploma or other qualification at the University of Cambridge or any other University or similar institution except as declared in the Preface and specified in the text. I further state that no substantial part of my dissertation has already been submitted, or, is being concurrently submitted for any such degree, diploma or other qualification at the University of Cambridge or any other University or similar institution except as declared in the Preface and specified in the text. It does not exceed the prescribed word limit for the relevant Degree Committee.

Myles Nadarajah

September 2018

Abstract

Title: The mechanics of the soundpost in the violin

Name: Myles Cameron Nadarajah

The violin soundpost, a small cylindrical rod of wood wedged between the front and back plates of the violin body, serves a crucial — if incompletely understood — role in violin acoustics. Although violin makers take great care to ensure its set-up optimises the instrument's sound, our understanding of its mechanics and precise acoustical function is still evolving.

This thesis closely examines all aspects of soundpost set-up — specifically, tightness, fit, and position — and draws on the foundations of existing research to develop a new simplified theoretical model of the soundpost that substantially improves its modelling capability.

The model, in which the tightness and fit of the soundpost are modelled by axial and bending springs that couple the soundpost to the plates, has been used to carry out extensive and systematic parameter studies of the effect of soundpost coupling strength on the dynamics of the plates and on the soundpost itself.

Representing a significant addition to previous modelling, a simplified model of the violin bridge is also developed and used in conjunction with our model of the violin body and soundpost. Providing for the ability to locate the driving force at each of the four strings, it illuminates questions pertaining to the 'balance of the strings'. We examine results which demonstrate that driving at the different strings influences the magnitude of the body resonances.

The radiated sound pressure generated by the model is estimated and used to assess 'loudness' for a given configuration of the soundpost. We conduct extensive parameter studies involving variations to the stiffness of the axial and bending springs, and to the location of the soundpost, to demonstrate the 'optimal' location for the soundpost at which radiated sound pressure is maximised. It is concluded that an asymmetrically placed soundpost is favourable in terms of boosting sound radiation at low frequencies, demonstrating agreement with the positioning of the soundpost in a real violin.

Finally, a physical model of a simplified violin body is developed and compared to our theoretical model. The bending vibration of the soundpost is directly measured by an accelerometer, and a specially designed adjustable soundpost is used to investigate the effect of 'tightness' on the dynamics of the body.

Acknowledgements

My warmest acknowledgement goes to my supervisor Professor Jim Woodhouse, whose unstinting generosity and unrivalled knowledge in the field has had an immeasurable impact on this thesis and on my academic development.

My thanks also go to my advisor Dr James Talbot, for his valuable discussions and advice, and to all my friends and colleagues in the Dynamics and Vibration Research Group at the University of Cambridge and beyond, for their support over my years of research.

I gratefully acknowledge the funding of my research by the UK Engineering and Physical Sciences Research Council and the financial support I have received from the Peterhouse Gunn Fund.

Contents

Declaration	iii
Abstract	v
Acknowledgements	vii
Contents	ix
List of Figures	xv
List of Tables	xxix
Introduction	1
1 Literature review	3
1.1 An introduction to the violin	3
1.1.1 The history of the violin	3
1.1.2 The parts of a violin	4
1.1.3 The basic mechanics of the violin	5
1.2 Areas of violin acoustics research	6
1.2.1 The vibration of the body	7
1.2.2 The bowed string	8
1.2.3 Perceptual studies	8
1.2.4 Playability	9
1.3 The soundpost	9
1.3.1 The history of the soundpost	10
1.3.2 The role of the soundpost	10
1.4 How violin makers approach soundpost set-up	12

1.4.1	The position of the soundpost	12
1.4.2	The ‘tightness’ of the soundpost	13
1.4.3	The ‘fit’ of the soundpost	15
1.4.4	The wood used to make the soundpost	16
1.5	Previous research on the soundpost	16
1.5.1	Nineteenth century research	17
1.5.2	Modern research	17
1.5.3	Experimental work	18
1.5.4	Finite-element calculations	19
1.6	Thesis outline	22
2	A simplified model of the violin body and soundpost	25
2.1	The design and mathematical implementation of the theoretical model	25
2.1.1	Simplifying the design of the violin body	25
2.1.2	Implementing a theoretical model	26
2.2	The elements of the model	28
2.2.1	The vibration of a simply-supported orthotropic rectangular plate	28
2.2.2	The axial vibration of a free–free rod	30
2.2.3	The combined system of plates, axial rod and axial springs	31
	Kinetic energy	33
	Potential energy	34
2.2.4	Solving the equation of motion	35
2.2.5	Orthogonality of eigenvectors	36
2.2.6	Calculating the displacement for a given mode	36
2.2.7	Calculating the admittance	37
2.2.8	Adding soundpost bending to the model	37
	Bending vibration of an Euler beam	38
	Potential energy of the torsional springs	39
	Kinetic energy of the beam	40
	Potential energy of the beam	40
2.3	Choosing the model parameters	41
2.3.1	The properties of the plate	41
2.3.2	The properties of the soundpost	42
2.4	Testing the model	43

2.4.1	No coupling between the plates and soundpost	43
2.4.2	The plates and soundpost coupled	44
2.4.3	Comparison to Schelleng's model	44
2.5	Convergence checks	46
2.5.1	How to compare modes	47
2.6	Comparison to a real violin	49
3	The vibrational behaviour of the soundpost and springs	51
3.1	The effect of axial spring stiffness on axial soundpost motion	51
3.1.1	Verifying the axial vibrational behaviour of the soundpost	53
3.2	The effect of axial spring stiffness on the plate dynamics	57
3.2.1	Comparing the admittance calculated on the front and back plates	59
3.3	The effect of bending spring stiffness on bending soundpost motion	62
3.3.1	The difference between the two orientations of the soundpost bending beams	63
3.4	The effect of bending spring stiffness on the plate dynamics	64
3.5	Comparing our soundpost model to a rigid massless link	66
3.5.1	The effect of added mass	67
3.5.2	Varying the axial spring stiffness	68
3.6	Varying soundpost size and material properties	69
3.6.1	Effect on the axial resonances of the soundpost	69
3.6.2	Effect on the bending resonances of the soundpost	71
3.6.3	Effect on the plate resonances	72
3.7	A comparison to the results of Gough	74
3.7.1	Varying the axial spring stiffness	74
3.7.2	Varying the position of the soundpost	75
4	Developing an enhanced bridge model	77
4.1	The design of the violin bridge	78
4.1.1	Previous bridge models	79
4.1.2	The 'balance of the strings'	79
4.1.3	Introducing our new proposed bridge model	80
4.2	Calculating input admittance including the bridge model	81
4.2.1	The horizontal and vertical components of the driving force	82
4.2.2	The velocity at the string notch	83

4.2.3	The displacement of the bridge feet	84
4.2.4	Balancing moments and forces	85
	The bridge base	85
	The upper half of the bridge	86
4.2.5	Solving the simultaneous equations	88
4.2.6	How the angles are calculated	89
4.2.7	Calculating the stiffness of the torsional spring	90
4.2.8	Verifying the model	91
4.3	Exploring the influence of the bridge base height	92
4.3.1	The effect of including a bridge base height	93
4.3.2	Calculating the response ‘skeleton’	95
4.3.3	Varying the bridge base height	95
4.3.4	Varying the bridge base height and bridge mass together	96
5	Exploring the behaviour of the enhanced bridge model	101
5.1	Calculating the bridge input admittance without a soundpost	101
5.1.1	The regular bridge model set-up	101
5.1.2	A vertical driving force	104
5.1.3	A horizontal driving force	108
5.2	Calculating the bridge input admittance with a soundpost	110
5.2.1	The regular model set-up	110
5.2.2	Placing the soundpost directly underneath the left bridge foot	114
5.3	The influence of soundpost position on the bridge input admittance	115
5.3.1	East–West variation in soundpost position	116
5.3.2	North–South variation in soundpost position	117
5.4	The influence of the soundpost coupling strength on the bridge input admittance	120
6	The influence of the soundpost on radiated sound pressure	123
6.1	Estimating radiated sound pressure from the model	124
6.1.1	Calculating the net volume change of the body	125
6.1.2	The radiated sound pressure from a pulsating sphere	126
6.2	Understanding how the model vibrates with and without a soundpost	127
6.2.1	No soundpost	128
6.2.2	With soundpost	130
6.2.3	A metric for ‘total radiated sound pressure’	133

6.3	A parameter study using a point excitation force	133
6.3.1	Varying the position	133
6.3.2	Varying the axial and bending spring stiffness	134
6.3.3	Testing multiple soundpost locations while keeping the spring stiffness fixed	134
6.3.4	Varying the bending and axial spring stiffness	136
6.3.5	The ‘ideal’ soundpost position for different stiffnesses	138
6.4	Excitation of the plate using the bridge model	140
6.4.1	Varying the stiffness and the position of the soundpost	140
6.4.2	The differences between the four strings	147
6.4.3	Small changes to the position	148
	Moving the soundpost E–W	148
	Moving the soundpost N–S	149
6.4.4	The optimal soundpost location for the four different strings	150
7	Experimental work	153
7.1	An overview of the equipment and experimental techniques used	153
7.2	A simplified physical model of a violin body	154
7.2.1	The separate plates	155
7.2.2	The complete physical model	155
7.2.3	Without a soundpost	157
7.2.4	With a soundpost	158
7.3	Examining the vibration of the soundpost	162
7.4	Experiments using an adjustable soundpost	165
7.5	Experiments on a real violin	170
8	Conclusion	173
8.1	An overview of our findings	173
8.2	Directions for future work	176
	Bibliography	179

List of Figures

1.1	The 1721 ‘Lady Blunt’ by Antonio Stradivari (from tarisio.com, 2018).	3
1.2	An exploded view of the violin with all the main components labelled (from Beament, 1997).	4
1.3	A diagram illustrating the Helmholtz motion of a bowed string. The blue line highlights the characteristic shape of the string: it is formed of two straight lines and a sharp kink known as the ‘Helmholtz corner’. For an up-bow near the bridge, the ‘Helmholtz corner’ travels anti-clockwise along a path indicated by the dashed line. The black solid lines show the string at different stages of this cycle.	5
1.4	An illustration showing how Chladni patterns can be formed by drawing a bow across the edge of a square plate. Sand scattered on the surface collects at the nodal lines (from Stone, 1879).	7
1.5	A standard violin soundpost made from spruce. It is around 60 mm in length.	9
1.6	An overhead view of violin body focusing on the region around the <i>f</i> -holes. The location of the two bridge feet is marked by the rectangular boxes. The bass bar is shown under the left-hand foot with dashed lines. The location of the soundpost is marked by the black circle. This is typically where the soundpost is positioned; slightly behind the treble foot of the bridge (from McLennan, 2005).	11
1.7	A CT scan of a violin by Giuseppe Guarneri ‘del Gesù’. The arching of the plates can be seen to be distorted at the soundpost position (from Bissinger and Oliver, 2010).	13
1.8	An example of soundpost-induced damage: (a) a circular ‘dent’ is seen on the underside of the front plate, due to soundpost pressing into the wood; (b) the damage is repaired by attaching a thin veneer of wood (from Curtin, 2018).	14

1.9	A diagram illustrating the difference between ‘poor fit’ and ‘good fit’. A soundpost with good fit has full wood-to-wood contact with the plates. A soundpost with poor fit might have incomplete contact with the plates, for example being pinned on an edge, as shown in the diagram.	15
1.10	A figure from Schelleng (1971) illustrating the “effect of the soundpost in enhancing radiation of sound from a rectangular plate”. (a) The shape of the modes (1,1) and (1,2) are plotted using a dashed line on top of the outline of a rectangular plate. (b) A ‘side-on’ view of the mode shapes. (c) Inserting an immovable soundpost at B causes the two previously independent modes to combine.	18
1.11	These diagrams show experimental data obtained using laser vibrometry. The measurements show a cross-sectional view of the body at the position of the soundpost, with each diagram showing the operating deflection shape at a particular frequency. From left to right, these measurements correspond to resonances at 777, 851, 951, 1109, 1185 and 1347 Hz (by permission of George Bissinger).	19
1.12	A reproduction of Figure 10 from Gough (2015a). The lowest three body modes are shown. From left to right, we see the effect of having no soundpost, having a centrally placed soundpost, and having a soundpost offset from the centre by 2cm to the right.	20
1.13	These graphs show the impact of offsetting an initially centrally positioned soundpost (0 cm) longitudinally and transversely. (a) positive offset indicates moving towards the lower bouts. (b) offset is towards the treble side bridge foot (from Gough, 2015b).	21
1.14	The soundpost coupling strength is increased from very small to a typical normal strength. The soundpost is placed centrally and the mode shape diagrams show a scaled soundpost coupling strength of 0.2 (from Gough, 2015b).	22
2.1	A diagram depicting two rough surfaces in contact with each other.	27
2.2	A diagram of a single rectangular plate showing the coordinate system and variables used to describe it. The length, a_i , is defined in the x -axis. The width, b_i , is defined in the y -axis. The thickness is given by h_i	28
2.3	A diagram of the soundpost modelled as a rod. The length, L , is defined in the z -axis. The rod has radius, r , which is used to calculate the cross-sectional area, A	30

- 2.4 A diagram showing how the soundpost is positioned in between the two plates. On the left, we have a three dimensional view. On the right, a side-on view of the rod and the springs, with stiffnesses k_1 and k_2 , which join the plates at the coordinates (x_1, y_1) and (x_2, y_2) 32
- 2.5 Two diagrams showing how the soundpost, modelled as a bending beam with torsional springs at either end, is positioned within the plates. 38
- 2.6 A diagram showing the side-on view of two rectangular plates with a beam and two torsional springs connecting the two plates. This particular diagram shows the beam associated with vibration in the x direction. 39
- 2.7 A plot of the modes obtained when there is no coupling between the soundpost and the plates. Each subplot shows both plate mode shapes and the three soundpost modes: axial (A), bending in the x direction (B x) and bending in the y direction (B y). The red and blue colours on the plate plots indicate areas of opposite phase. As there is no coupling between the soundpost and plates, diagrams f_2 – f_9 show displacement in the plates only, while the soundpost remains static. f_{10} and f_{11} show the first soundpost bending modes in the x and y directions, which occur at the same frequency. The first axial mode is seen in f_{14} , where the longitudinal displacement is plotted using a transverse representation. Note that f_1 shows the rigid body motion of the soundpost at 0 Hz. 43
- 2.8 A plot of the modes obtained when there is coupling between the soundpost and the plates. Each subplot shows both plate mode shapes and the three soundpost modes: axial (A), bending in the x direction (B x) and bending in the y direction (B y). The red and blue colours on the plate plots indicate areas of opposite phase. For axial modes (A), the mode shape is visualised in the x – y plane. For the three soundpost mode shape plots, the blue line shows the displacement scaled to the maximum value obtained in the calculation. The orange line shows the displacement individually scaled to the size of the displayed axes. The green circle shows the location of the soundpost. 45
- 2.9 A comparison to Figure 1.10. In this simulation, the back plate has been made infinitely stiff. *Top*: the two lowest modes of the uncoupled front plate. *Bottom*: with the addition of a rigid soundpost, the two uncoupled modes are combined to make one new mode. This shows very good agreement with Schelleng (1971). 46

- 2.10 A reproduction of Figure 2.9 without an infinitely stiff back plate. The solid lines show a cross-section through the front and back plates. The horizontal dashed lines show the position of the plates at rest, while the vertical dashed line highlights the position where the soundpost would like. The thick solid black bar represents the soundpost and shows that it is present in the calculation that generates the two lower diagrams. Without an infinitely stiff back plate, a new back plate mode, $f = 127$ Hz, causes a different set of coupled modes to be obtained when a rigid soundpost is added. 47
- 2.11 *Left*: A graph showing how the mode shape convergence ratio changes as the value of N_i is increased. Once the ratio is sufficiently close to 1, then small markers are plotted. *Right*: A similar plot, but this time mode frequency convergence is plotted. Note that the scale is different because frequencies that are being compared can either be higher or lower than the benchmark. Once again, if the ratio is sufficiently close to 1, then small markers are plotted. 48
- 2.12 *Top*: an admittance measurement from a real violin. An accelerometer was placed on the surface of the front plate directly above the position of the soundpost. An instrumented hammer was used to deliver a driving point excitation force. *Bottom*: an equivalent simulation from the model, using the parameters determined in this chapter. 50
- 3.1 A diagram of the axial rod used to model the axial vibration of the soundpost. The excitation point used when computing the axial frequency response is shown by the red cross. This is at a length $\frac{L}{\pi}$ along the rod, to ensure that a nodal point is not probed. The red arrow illustrates that we are simulating a force being applied axially. 52
- 3.2 Two plots showing ‘slices’ taken from Figure 3.3. (a) The axial frequency response of the soundpost when $k_1 = k_2 = 10^6$ N/m. (b) The axial frequency response of the soundpost when $k_1 = k_2 = 10^5$ N/m. 53
- 3.3 The axial frequency response of the soundpost plotted as a function of axial spring stiffness. The two red dashed lines mark the location of ‘slices’ of this plot which are shown in Figure 3.2. 54
- 3.4 A diagram of an axial rod with a free end at $z = L$. At $z = 0$, it is coupled to a spring with stiffness k_2 . This spring is in turn coupled to a rigid surface. 55

3.5	(a) The axial frequency response of the soundpost when $k_1 = 0$ and the back plate is made infinitely stiff. (b) In black, Equation 3.12 is plotted. Equation 3.13 is plotted using a dashed red line.	56
3.6	A diagram of the soundpost positioned between the two plates. The location of the excitation point (x_B, y_B) on the front plate is shown by the red cross.	58
3.7	The frequency response, calculated at (x_B, y_B) on the front plate, plotted as a function of axial spring stiffness.	59
3.8	A plot of Equation 3.21 for an axial stiffness of $k = 10^9$ N/m.	60
3.9	A graph showing $H_2 - H_1$, a transfer function representing the displacement across the points on the plates where the soundpost is positioned. Increasing axial spring stiffness is plotted on the y -axis.	60
3.10	A diagram of one of the bending beams used to model the bending vibration of the soundpost. The excitation point used when computing the bending frequency responses is shown by the red cross. This is at a length $\frac{L}{\pi}$ along the beam, to ensure that a nodal point is not probed. The red arrow illustrates that we are simulating a force being applied perpendicular to the length of the soundpost.	62
3.11	The bending frequency response of the soundpost plotted as a function of bending spring stiffness. This particular plot shows bending modes in the x direction. The number of plate modes used in the calculation is low.	63
3.12	The bending frequency response of soundpost plotted as a function of bending spring stiffness. Bending in the x -direction is shown in (a), while bending in the y -direction is shown in (b). The number of plate modes used in these calculations is high.	64
3.13	This plot shows the difference between the bending frequency response in the x -direction compared to the y -direction.	64
3.14	The frequency response, calculated at (x_B, y_B) on the front plate, plotted as a function of bending spring stiffness.	65
3.15	Zoomed-in sections of Figure 3.14.	66
3.16	(a) A plot showing H_1 in red and H_{coup} in black. (b) A plot showing $H_1 - H_{\text{coup}}$	67
3.17	(a) A plot showing H_{coup} in black and $H_{\text{coup}+m_s}$ in blue. (b) A plot showing $H_{\text{coup}} - H_{\text{coup}+m_s}$	69
3.18	A plot of $H_{\text{coup}} - H_1$, where the axial spring stiffness used when calculating H_1 is varied. The highest value of axial spring stiffness, 10^8 N/m, represents the data shown in Figure 3.16(b)	70

3.19	The axial frequency response of the soundpost plotted as a function of soundpost density, radius and Young's modulus.	71
3.20	The bending frequency response of the soundpost plotted as a function of soundpost density, radius and Young's modulus.	72
3.21	The frequency response, calculated at (x_S, y_S) on the front plate, plotted as a function of the soundpost density, radius and Young's modulus.	73
3.22	Plots comparable to those produced by Gough (2015b): see Figure 1.14. The mode frequencies obtained from our model as the axial spring stiffness is varied: (a) for a centrally placed soundpost, (b) for a soundpost placed at (x_S, y_S)	74
3.23	Plots comparable to those produced by Gough (2015b): see Figure 1.13. The mode frequencies obtained from our model as a result of varying the position of the soundpost: (a) positive longitudinal offset indicates moving towards the upper bouts; (b) transverse offset is towards the treble side bridge foot.	76
4.1	(a) A labelled diagram of a violin bridge highlighting features important to our research, including the bridge feet, waist and string notch. (b) An illustration of the lowest in-plane bridge resonance as shown in Cremer (1984) and Woodhouse (2005). The solid line shows the position at rest; the dashed line indicates the displaced position. The filled circle located in the waist area indicates the axis of rotation.	78
4.2	A simplified model of the bridge proposed by Woodhouse (2005). A mass, m_b , is connected to a rigid base by a bending spring with stiffness κ_b . There is a horizontal driving force, F , acting on the mass. Both ends of the bridge base, which has length d_b , make contact with the body.	79
4.3	A diagram of the proposed bridge model with important system variables labelled. The model is shown overlaid on an outline of a real violin bridge.	81
4.4	A diagram showing how the driving force, F_i , is defined in terms of the angles θ_1 , θ_2 , α_i and β_i . The horizontal and vertical components of the driving force, F_i^x and F_i^y , are also illustrated here. The coordinates of the string notch, shown by the red circle, are given by (x_i, y_i) . The angles $(\theta_1 + \theta_2 + \alpha_i)$ define the direction of the unit vector \hat{r}_i , which connects the string notch to the axis of rotation.	82
4.5	A diagram showing the forces present at the location of the spring and at the two bridge feet.	86
4.6	(a) A diagram showing the forces acting on the upper half of the bridge. (b) The string driving force, F_i , defined in terms of its horizontal and vertical components.	86

-
- 4.7 A diagram showing how the parameters \mathcal{H}_i , \mathcal{W}_i and ϕ_i are assigned. From these parameters, the values of α_i , β_i and r_i can be calculated. The E string, which is labelled as the fourth string, is shown here as an example. 90
- 4.8 The magnitude and phase of the input admittance calculated directly at the mass, Y_b . This plot is based on the model presented here, and shows perfect agreement with Figure 7 by Woodhouse (2005). 92
- 4.9 A diagram of the front plate showing the location of the left (L) and right (R) bridge feet. The location of the soundpost is shown by a red circle below the right bridge foot. 93
- 4.10 The magnitude and phase of the input admittance at the G string for three different base heights: 0, 5 and 10 mm. Three diagrams beneath illustrate these different models. Note that the height of the mass, H_m , remains fixed as h_b is varied. The length of the mass arm, a_b , is adjusted accordingly. 94
- 4.11 A reproduction of Figure 13 from Woodhouse (2005) showing skeleton curves for the bridge input admittance Y_b . In these plots, the bridge frequency, Ω_b , is kept fixed while the mass, m_b , and stiffness, κ_b , are varied. The plots show a mass of $m_b = 0.2, 0.3, 0.5, 1.0$ and 2.0 g, the first value being indicated by a red line and the others following in an obvious sequence. 96
- 4.12 ‘Skeleton’ curves of the input admittance Y_b , showing how the ‘bridge hill’ varies. In each subplot, h_b is varied from 0 mm (plotted in red) to 2.5, 5.0, 7.5 and 10 mm: the order of the plots following in an obvious sequence. In (a), κ_b , the stiffness of the waist area, is varied while keeping m_b and Ω_b fixed. In (b), m_b , the bridge mass, is varied while keeping κ_b and Ω_b fixed. In (c), Ω_b , the bridge frequency, is varied while keeping κ_b and m_b fixed. 97
- 4.13 ‘Skeleton’ curves of the input admittance Y_b , showing how the ‘bridge hill’ varies. In each subplot, h_b and m_b are varied in conjunction with each other: h_b from 0 mm (plotted in red) to 2.5, 5.0, 7.5 and 10 mm and m_b from 0.75 g to 0.6, 0.5, 0.4 and 0.25 g. The order of the plots follows in an obvious sequence. In (a), κ_b , the stiffness of the waist area, is varied while keeping Ω_b fixed. In (b), Ω_b , the bridge frequency, is varied while keeping κ_b fixed. 98
- 5.1 The input admittance, Y_i , calculated at the four string notches. This calculation is for the model without a soundpost. The angles of the driving force follow those presented in Table 4.1. 102

-
- 5.2 Calculating the plate ODS when an input driving force is applied at the G string. Each subplot shows a particular frequency which was chosen as a result of a peak finding algorithm applied to Y_1 , the input admittance of the G string. This model does not include a soundpost. The two filled green circles indicate the position of the bridge feet on the front plate. The filled black circle acts as a guide showing the position of the soundpost were it to be included. 103
- 5.3 Plots showing a cross-section through the box at the position of the bridge. Each subplot corresponds to driving at one of the four strings, the active string is highlighted by a green circle. The outline of the bridge is plotted in blue. The direction of the driving force is shown by an arrow. These particular ODS are associated with the resonance at 103.2 Hz from Figure 5.1. Although the phase of the ODS is dependent on whether the component of vertical force is positive or negative, this is not important to the interpretation of the results. 105
- 5.4 Plots showing a cross-section through the box at the position of the bridge. Each subplot corresponds to driving at one of the four strings, the active string is highlighted by a green circle. The outline of the bridge is plotted in blue. The direction of the driving force is shown by an arrow. The red crosses highlight the points where the plate ODS passes through zero. These particular ODS are associated with the resonance at 238.2 Hz from Figure 5.1. Although the phase of each diagram is similar in this instance, the phase is not important to the interpretation of the results. 106
- 5.5 The input admittance, Y_i , calculated at the four string notches. This calculation is for the model without a soundpost and with a vertical driving force at the string notch. 107
- 5.6 Plots showing a cross-section through the box at the position of the bridge. Each subplot corresponds to driving at one of the four strings, the active string is highlighted by a green circle. The outline of the bridge is plotted in blue. The direction of the driving force is shown by an arrow. These particular ODS are associated with the resonance at 103.2 Hz from Figure 5.5. 107

- 5.7 Plots showing a cross-section through the box at the position of the bridge. Each subplot corresponds to driving at one of the four strings, the active string is highlighted by a green circle. The outline of the bridge is plotted in blue. The direction of the driving force is shown by an arrow. The red crosses highlight the points where the plate ODS passes through zero. These particular ODS are associated with the resonance at 238.2 Hz from Figure 5.5. 108
- 5.8 The input admittance, Y_i , calculated at the four string notches. This calculation is for the model without a soundpost and with a horizontal driving force at the string notch. 109
- 5.9 Plots showing a cross-section through the box at the position of the bridge. Each subplot corresponds to driving at one of the four strings, the active string is highlighted by a green circle. The outline of the bridge is plotted in blue. The direction of the driving force is shown by an arrow. These particular ODS are associated with the resonance at 238.2 Hz from Figure 5.8. 109
- 5.10 The input admittance, Y_i , measured at the four string notches. This calculation is for the model with a soundpost. 110
- 5.11 Calculating the plate ODS when an input driving force is applied at the G string. Each subplot shows a particular frequency which was chosen as a result of a peak finding algorithm applied to Y_1 , the input admittance of the G string. This model does include a soundpost, which is marked by a filled black circle. The two filled green circles indicate the position of the bridge feet on the front plate. 111
- 5.12 Plots showing a cross-section through the box at the position of the bridge. Each subplot corresponds to driving at one of the four strings, the active string is highlighted by a green circle. The outline of the bridge is plotted in blue. The direction of the driving force is shown by an arrow. These particular ODS are associated with the resonance at 119.2 Hz from Figure 5.10. 112
- 5.13 Plots showing a cross-section through the box at the position of the bridge. Each subplot corresponds to driving at one of the four strings, the active string is highlighted by a green circle. The outline of the bridge is plotted in blue. The direction of the driving force is shown by an arrow. These particular ODS are associated with the resonance at 217.2 Hz from Figure 5.10. 113
- 5.14 The input admittance, Y_i , measured at the four string notches. This calculation is for the model with a soundpost placed directly below the left bridge foot. 113

- 5.15 Plots showing a cross-section through the box at the position of the bridge. Each subplot corresponds to driving at one of the four strings, the active string is highlighted by a green circle. The outline of the bridge is plotted in blue. The direction of the driving force is shown by an arrow. These particular ODS are associated with the resonance at 225.2 Hz from Figure 5.14. 114
- 5.16 A face down view of the front plate of our model. The two bridge feet are shown by the black circles. The red cross shows the ‘base’ location of the soundpost. The black line extending out from this shows ± 15 mm. 115
- 5.17 *Top*: The input admittance calculated at string number 1, the G string, plotted as the position of the soundpost is varied along the y -axis of the front plate. The position is adjusted ± 15 mm from the base position. See Figure 5.16(a) for a diagram of how the position is adjusted. *Below*: Three graphs showing the input admittance measured at the three remaining strings 2–4, where in each case the input admittance has been divided by the input admittance of string number 1. . . 116
- 5.18 The same data as shown in Figure 5.17, but for the frequency range of 300–5000 Hz. 118
- 5.19 *Top*: The input admittance calculated at string number 1, the G string, plotted as the position of the soundpost is varied along the x -axis of the front plate. The position is adjusted ± 15 mm from the base position. See Figure 5.16(b) for a diagram of how the position is adjusted. *Below*: Three graphs showing the input admittance measured at the three remaining strings 2–4, where in each case the input admittance has been divided by the input admittance of string number 1. . . 119
- 5.20 (a) The input admittance at the G string plotted as a function of axial spring stiffness. The black vertical line labelled ‘G’ marks the frequency of the open violin G string. (b)–(d) Three graphs showing the input admittance calculated at the three remaining strings (D, A and E) but in each case the input admittance has been divided by the input admittance of the G string. These are also plotted as a function of axial spring stiffness. Similarly labelled vertical black lines indicate the open string frequencies. 121

- 5.21 (a) The input admittance at the G string plotted as a function of bending spring stiffness. The black vertical line labelled ‘G’ marks the frequency of the open violin G string. (b)–(d) Three graphs showing the input admittance calculated at the three remaining strings (D, A and E) but in each case the input admittance has been divided by the input admittance of the G string. These are also plotted as a function of bending spring stiffness. Similarly labelled vertical black lines indicate the open string frequencies. 122
- 6.1 A diagram of our simplified violin body and soundpost model with solid sides joining the edges of the front and back plates. This creates a closed box which is analogous to the closed cavity of a violin body. 124
- 6.2 A diagram of a pulsating spherical source. The arrows indicate how the sphere is expanding and contracting. The alternating solid and dashed circles surrounding the sphere represent areas of high and low pressure respectively. 126
- 6.3 The mode shape patterns seen on the plates of the simplified violin body model. The soundpost is completely decoupled from the plates in this instance. Therefore, we observe the standard mode shape patterns for rectangular simply-supported plates. The left hand plate in each pair of plates represents the front plate. The first 25 modes are shown here. 128
- 6.4 The lower graph shows the amplitude of the radiated sound pressure plotted as a function of frequency, using a decibel scale. The upper graph shows a cumulative sum of the amplitude as the frequency increases, shown using a linear scale. The model in question does not have a soundpost. The grey area relates to the ‘total sound pressure radiation’, a metric which will be defined in Section 6.2.3. . . . 129
- 6.5 The mode shape patterns seen on the plates of the simplified violin body model with a soundpost. The left hand plate in each pair of plates represents the front plate. Only the first 25 modes are shown here. The black cross indicates the location of the soundpost. 131
- 6.6 The lower graph shows the amplitude of the radiated sound pressure plotted as a function of frequency, on a decibel scale. The upper graph shows a cumulative sum of the amplitude as the frequency increases, shown on a linear scale. The model in question has a soundpost, which is placed at the position shown in Figure 6.5. The grey area relates to the ‘total sound pressure radiation’, a metric which will be defined in Section 6.2.3. 132

- 6.7 A surface plot showing the total radiated sound pressure from the model for different locations of the soundpost. The filled red marker shows the location of the fixed excitation point and the black cross marks the soundpost location which generates the largest total radiated sound pressure. The hollow red circle acts as a guide, showing where the right bridge foot would approximately lie. 135
- 6.8 In the top plot, multiple soundpost locations were tested for different combinations of the bending spring stiffness and the axial spring stiffness. For each combination, the largest total radiated sound pressure was recorded and this value plotted in the surface plot above. Beneath this, two smaller plots display the x and y coordinates which correspond to the largest value of total radiated sound pressure that was recorded. The red crosses mark the position of plots shown in Figure 6.9. 137
- 6.9 Four plots showing the total radiated sound pressure measured at locations across the plate. Each plot represents a fixed value of k and κ and these are indicated on Figure 6.8 by the four red crosses. The order of the plots follows the order of the crosses. The total radiated sound pressure is plotted on a linear scale. 139
- 6.10 In the top plot, multiple soundpost locations were tested for different combinations of the bending spring stiffness and the axial spring stiffness. For each combination, the largest total radiated sound pressure was recorded and this value plotted in the surface plot above. Beneath this, two smaller plots display the x and y coordinates which correspond to the largest value of total radiated sound pressure that was recorded. This figure corresponds with a driving force being applied at the G string notch. 141
- 6.11 A ‘slice’ taken from Figure 6.10 for bending spring stiffness equal to 10^4 Nm/rad. 142
- 6.12 Four plots showing the total radiated sound pressure measured at locations across the plate. Each plot represents a fixed value of k and κ , indicated on Figure 6.10 by the four red crosses. The order of the plots follows the order of the crosses. 143
- 6.13 A plot showing all the soundpost positions that recorded the largest value of total radiated sound pressure, for combinations of k and κ as used in Figure 6.10. However, in this calculation a smaller area of points were examined, as illustrated by the inner rectangle. The colour of each of the circles indicates how many times that location was chosen. The two red circles represent the location of the two bridge feet. 144

- 6.14 A plot showing all the soundpost positions that recorded the largest value of total radiated sound pressure, for combinations of k and κ as used in Figure 6.10. However, in this calculation a smaller area of points were examined, as illustrated by the inner rectangle. The colour of the data points represent the sum of the total radiated sound pressure added up for every instance where it was a ‘maximum’ location. 145
- 6.15 A plot showing all the soundpost positions that recorded the largest value of total radiated sound pressure, for combinations of k and κ as used in Figure 6.10. However, in this calculation a smaller area of points were examined, as illustrated by the inner rectangle. The sum of the total radiated sound pressure as shown in Figure 6.14 has been divided by the number of times the location was chosen. This gives an average total radiated sound pressure measured at each of these locations. 146
- 6.16 The total radiated sound pressure when driving at each of the four strings as a function of East–West soundpost position. A diagram illustrating the position of the soundpost in this plot can be seen in Figure 5.16. The G string is shown in red, the D string in orange, the A string in light blue and the E string in dark blue. 148
- 6.17 The total radiated sound pressure when driving at each of the four strings as a function of North–South soundpost position. A diagram illustrating the position of the soundpost in this plot can be seen in Figure 5.16. The G string is shown in red, the D string in orange, the A string in light blue and the E string in dark blue. 149
- 6.18 Four plots showing the total radiated sound pressure at different soundpost positions when applying the input driving force at the four different strings. The colours represent the total radiated sound pressure using a linear scale. The number above the plot corresponds to string in question. Note that the soundpost positions that were tested lie in a concentrated area around the bridge feet (shown by filled red circles). Hence, the outline of the plate lies beyond the coloured area. 150
- 7.1 A schematic diagram of the experimental set-up used to measure the admittance of the separate plates. The plate is raised off the ground using pieces of foam placed at the edges. 155
- 7.2 The driving point admittance measured on the front and back plates when separated. Figure 7.1 shows a schematic diagram of the experimental set-up. . . 156

7.3	A schematic diagram of the experimental set-up used in Sections 7.2.3 and 7.2.4. Our simplified physical model of the violin body is shown hanging from a retort stand. The side-on view illustrates how a soundpost may be positioned between the two plates.	157
7.4	The admittance measured on the front plate (black line) and the back plate (red line) for the physical model without a soundpost. A diagram of the experimental set-up is shown in Figure 7.3.	157
7.5	<i>Top</i> : The admittance measured on the front plate (black line) and the back plate (red line) for the physical model with a soundpost. <i>Below</i> : The difference between the two responses, i.e. the response for plate 1 minus the response for plate 2. A diagram of the experimental set-up is shown in Figure 7.3.	159
7.6	A equivalent plot to Figure 7.5 calculated using our theoretical model. <i>Top</i> : The admittance calculated on the front plate (black line) and the back plate (red line) for the theoretical model with a soundpost. <i>Below</i> : The difference between the two responses, i.e. the response for plate 1 minus the response for plate 2. . . .	160
7.7	The admittance measured on the side of soundpost when an impulse is applied to the side of the soundpost.	162
7.8	The driving point admittance of the soundpost calculated using our theoretical model using a bending spring stiffness of 4 Nm/rad. This value of bending spring stiffness was chosen so that frequency of the first bending resonance matches the experimental result.	163
7.9	The admittance measured on the side of soundpost when an impulse is applied to the front plate. The location of the impulse is the same as that in Section 7.2.2. .	163
7.10	An equivalent theoretical calculation of the experimental result presented in Figure 7.9. As in Figure 7.8, a bending spring stiffness of 4 Nm/rad was chosen so that first bending resonance of the soundpost matches the experimental result. The axial springs have been set to 10^6 N/m.	164
7.11	The adjustable soundpost design that we developed. It is made from PVC and consists of two parts: a 1BA screw head and a tapped body (seen in black) of length 3.2 cm. The radius of the screw head, measured at the top is 3.5 mm, while the radius of the body is 4.0 mm.	166
7.12	A diagram showing the lengths of the adjustable soundpost used in our experiment	166

-
- 7.13 The admittance measured on the front plate on top of the position of the soundpost. Each plot shows a soundpost of different length, where green is the shortest and red is the longest: see Figure 7.12. 167
- 7.14 A zoomed-in view of a selection of resonances from Figure 7.13. 168
- 7.15 *Top*: The admittance measured on the front and back plates at the position of the soundpost, for a hammer impulse applied at the top left hand side of the bridge. *Below*: The difference between the two responses: i.e. the response for the front plate minus the response for the back plate. 170

List of Tables

2.1	Properties of the plates used in our theoretical model.	41
2.2	Properties of the soundpost used in our theoretical model.	42
4.1	The parameters which define the fixed location of each string notch, as illustrated in Figure 4.7.	90
7.1	Properties of the plywood plates from our experimental model.	156
7.2	Properties of the soundpost used in our experimental model.	158

Introduction

Music is an art form widely practised across all world cultures. Western classical music, in particular, is deeply embedded in our shared global culture of music, and provides the foundation for much of our modern music-making. Forming one of the pillars of the classical music tradition is the violin family of instruments. Musicologists often credit the pre-eminence of the violin to the remarkable similarity of its timbre to that of the human singing voice, as suggested by its early history of use in doubling vocal parts (Hutchins, 1983). What is undoubted is that since its Italian origins in the early sixteenth century, the violin has grown to become an instrument of immense global popularity and continuing influence (Kolneder and Pauly, 1998; Schoenbaum, 2013).

The field of violin acoustics occupies a unique space within the scientific community. Driven by a desire to create better sounding instruments, scientists and musicians alike have been fascinated by the physical mechanisms of violin sound. The modern violin has evolved out of a long history of experimentation, accumulating developments by luthiers, and, from the nineteenth-century onwards, scientific investigation, making it the product of “nearly 200 years of empirical research and development” (Hutchins, 1983).

Notwithstanding this long history of interest and research, which has generated a substantial bibliography of violin scholarship (see Katz, 2006), scientific research into violin acoustics has always been challenged by its close proximity to questions of art. In 1819, physicist Felix Savart observed that:

It is to be presumed that we have arrived at a time when the efforts of scientists and those of artists are going to unite to bring to perfection an art which for so long has been limited to blind routine. (Savart, 1819; quoted in Bissinger, 1998)

Almost precisely 200 years later, and despite the many insights of modern acoustical research, and advances in the fields of perception and psychoacoustics, we remain far from having achieved a ‘perfect’ scientific account of the violin. There are many questions still to be explored, and

we are still far away from filling in all the pieces of the puzzle. As one modern researcher has observed, “[i]t is commonly thought that the violin is the most perfect acoustically of all musical instruments. It is quite uncommon to find someone who can explain exactly why” (Marchese, 2007).

Forming the basis of a research question is an interesting process for a violin acoustician, as there are a number of different groups of people from whom inspiration can be drawn. First, there are the musicians: interested primarily in playability, they ask how an instrument feels under their fingers and responds to their input. Then, there are the discerning listeners, invested most in how the violin sounds to their ears. Finally, there are the violin makers, who inquire into how they might change the design and set-up of their instruments to achieve a desired sound.

We have decided to focus our investigation on the mechanics of the violin body. In particular, we will explore the role of the soundpost, a small rod of wood which is wedged between the plates of the instrument. This small yet essential component of the violin has a significant influence over the vibration of the instrument and therefore, ultimately, its sound. We will make our contribution to acoustical research by using various simplified theoretical models to investigate the underlying physical mechanisms which govern the vibration of the soundpost and the violin body. This will advance the field of violin acoustics by adding clarity and detail to an area of research that possesses a significant level of complexity and many unanswered questions. Finally, providing the field with a new body of research data will point the way for further future productive areas of research.

1

Literature review

1.1 An introduction to the violin

The modern day violin family consists of four instruments: the violin, viola, cello and double bass. The fundamental design and mechanical properties of all four instruments are identical: the main difference being one of scale. Therefore, the ‘acoustics of the violin’ can be extended to describe the acoustics of the other members of the violin family in most circumstances. In this thesis, we have chosen to reflect the existing body of acoustics research into string instruments by taking the violin as our exemplary instrument to study in close detail.

1.1.1 The history of the violin

Bowed string instruments in various forms have been used for over a thousand years, with the origins of the modern violin family most evident in medieval bowed string instruments such as the *rebec*, *vielle* and *lira da braccio*. The early violin first appeared in sixteenth century Italy and, although aspects of the design have changed slightly over the centuries, the fundamental violin design remains remarkably unchanged from the preminent form established by makers in the early eighteenth-century. Notable exponents include Giuseppe Guarneri ‘del Gesù’ and Antonio Stradivari; whose violin is pictured in Figure 1.1.



Figure 1.1: The 1721 ‘Lady Blunt’ by Antonio Stradivari (from tarisio.com, 2018).

1.1.2 The parts of a violin

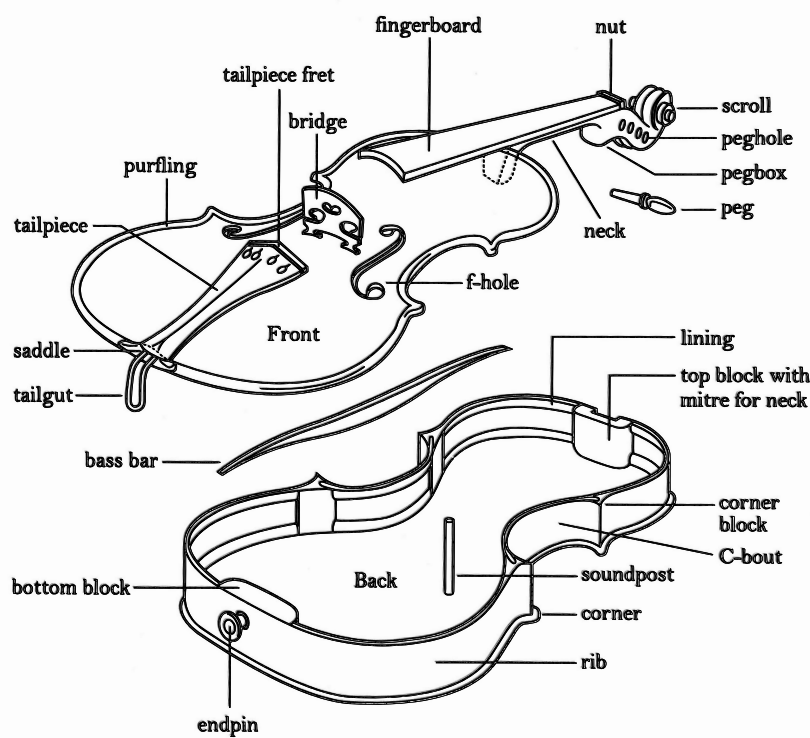


Figure 1.2: An exploded view of the violin with all the main components labelled (from Beament, 1997).

Figure 1.2 depicts an exploded view of the main parts of a violin. Here, there are three parts of the violin which demand our particular attention. The first is the two pieces of wood, or plates, which are the main components of the ‘body’ of the violin. These are labelled as the ‘Front’ and ‘Back’ plates in the diagram above.¹ The majority of the sound produced by the instrument comes from the vibration of the body. The wooden plates are therefore of fundamental importance to the acoustics of the instrument. Second is the cylindrical rod of wood identified as the ‘soundpost’. The soundpost plays a important role in governing the vibration of the instrument body and is at the centre of this thesis: its properties, function, and place within previous acoustical research will be explored in detail later in this chapter. Third is the ‘bridge’, which couples the strings to the body of the instrument, and which is another component that will be explored in detail later in this thesis.

¹Although most parts of the violin have well-defined names, the ‘plates’ of the violin are referred to inconsistently in the literature. Most often, they are referred to as the front and back plates of the instrument. However the front plate is often called the ‘belly’ by violin makers, and they are occasionally also identified as the ‘top’ and ‘bottom’ plates. To avoid any confusion, in this thesis the plates will be referred to as the front and back plates, exactly as they are described in Figure 1.2.

1.1.3 The basic mechanics of the violin

Before proceeding to a review of violin acoustics research, an overview of the basic mechanics of the violin will be presented. On its own, a vibrating string is a poor emitter of sound energy: the string cross-section is small in comparison to the wavelength of sound being produced. This means that the air flows around the vibrating string and the amplitude of sound energy being radiated is low. However, when coupled with the wooden body of the violin, with its larger surface area, the energy is able to radiate as sound much more effectively. At the most basic level, the violin can be described as a wooden box which acts as a mechanical transformer, turning energy from a vibrating string into sound (Woodhouse, 2014).

The string of a violin is usually set into motion in one of two ways: a finger can be used to pluck it, or a bow strung with horsehair can be pulled across it. Bowing the string results in a sustained note while a plucked string has a fairly short decay. A plucked string is, to a good approximation, a linear system. A bowed string, on the other hand, is strongly non-linear. The oscillation of the string when bowed is governed by a stick-slip cycle. Depending on the amount of bow force being applied and the position of the bow on the string, among other variables, a range of different oscillations can occur. The most common is the periodic oscillation known as ‘Helmholtz motion’, illustrated in Figure 1.3 (see Guettler, 2002).

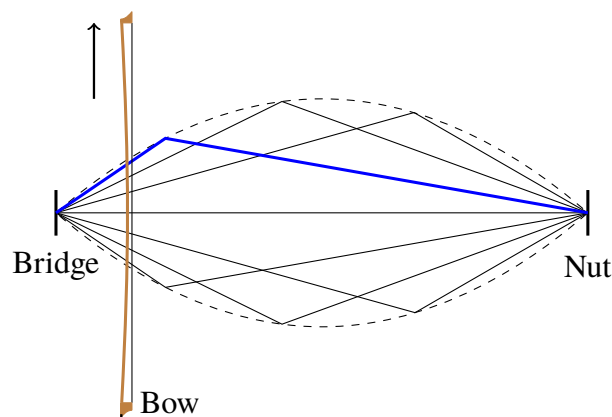


Figure 1.3: A diagram illustrating the Helmholtz motion of a bowed string. The blue line highlights the characteristic shape of the string: it is formed of two straight lines and a sharp kink known as the ‘Helmholtz corner’. For an up-bow near the bridge, the ‘Helmholtz corner’ travels anti-clockwise along a path indicated by the dashed line. The black solid lines show the string at different stages of this cycle.

The strings are coupled to the body of the instrument via the bridge, which is held in place under compression from the strings. The motion of the string causes a force to be applied at the bridge; this in turn sets the bridge into motion. The combination of the horizontal and

vertical components of the string's oscillation causes the bridge to exhibit side-to-side rocking and 'bounce' up and down. The motion of the bridge causes forces to be applied to the front plate of the instrument through the bridge feet, and various 'body modes' are excited. The 'box', made up of the plates and ribs, vibrates at a set of modal frequencies. This causes sound waves to radiate from the surface of the wood. Additionally, air inside the cavity of the instrument acts like a Helmholtz resonator. The air cavity is a crucial component in the design of the violin as below 400 Hz there are no strongly radiating structural resonances. Therefore, the Helmholtz air resonance is important in boosting the lower frequency range of the violin (which extends down to 190 Hz).

The acoustical properties of the plates are determined from a number of factors, but foremost among them is the density of the wood, its elastic properties, and its geometric shape (which includes variations in thickness and the degree of arching). The front plate of the body is typically made of spruce and the back is typically made from maple. Wood is, of course, a natural material, and this presents a challenge to a violin maker. No two pieces of wood are identical, therefore variations in the grain and density must be taken into account, and the plates carved accordingly, in order to achieve the desired vibration mode shapes and frequencies. Two important components are added to the carved wooden body: the bass bar and the soundpost. As will be discussed later in this chapter, the soundpost plays an important role introducing asymmetry into the design. This asymmetry is crucial in determining the shape of the modes and their radiating efficiency. For more information on the physics of the violin see Cremer (1984).

1.2 Areas of violin acoustics research

Formal scientific investigation into the physics of the violin family has been ongoing since the mid-nineteenth century. Today, the field of violin acoustics, while still fairly specialised, has a large interest from the public sphere and a sizeable group of dedicated researchers probing some of the many questions about the instrument which remain unanswered. Currently, research on the violin can broadly be divided into four main areas. These are:

- the vibration of the body;
- the bowed string;
- perceptual studies; and
- playability.

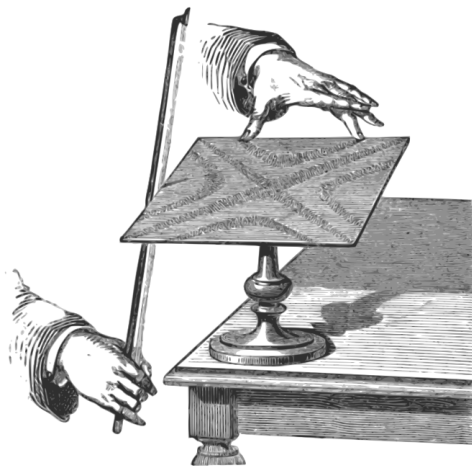


Figure 1.4: An illustration showing how Chladni patterns can be formed by drawing a bow across the edge of a square plate. Sand scattered on the surface collects at the nodal lines (from Stone, 1879).

These areas will now be briefly introduced with particular attention paid to the ‘vibration of the body’, as the research presented in this thesis will fall under this category. For a complete review of all areas of violin acoustics research see Woodhouse (2014).

1.2.1 The vibration of the body

A basic understanding of the vibration of the body would have been known to makers ever since violins first started to be produced. By simply tapping the free plates² with a finger, one is able to hear the lowest vibration modes of the free plates (at around 100–300 Hz). Makers, even today, regularly use this technique to guide their design process.

One of first steps towards a deeper understanding of the vibration of the violin body was undertaken by Chladni. Regarded by many historians as the ‘father of acoustics’, he developed a technique by which the modes of vibration could be visualised on a vibrating surface. Chladni patterns, as they are called today, can be formed by sprinkling sand, or another suitable powder, onto a rigid surface and exciting a vibration mode: see Figure 1.4. The movement of the surface will cause the sand to gather at the nodal lines, where the motion is at a minimum (see Gough, 2007). Savart was the first to utilise this method on the free plates of a violin (see Savart, 1819).

To measure the vibration modes of a complete violin body, there are various techniques which can be employed. At low frequencies, using a forced vibration input, such as a shaker, it is possible to visualise the movement of the plates using holographic interferometry (see Jansson et al., 1970). However, methods involving forced vibration input do not strictly measure

²The term ‘free plates’ refers to the front and back plate when they are not glued to ribs.

resonance modes. With the advent of digital measuring techniques, the bridge input admittance has become one of the most common measurements used to define the vibrational behaviour of the instrument body (see Zhang and Woodhouse, 2013). This method involves using an impact hammer to provide an impulse excitation force at the bridge and recording the resulting vibration using an accelerometer or laser vibrometer. Alternatively, the sound radiation resulting from the hammer impact can be measured using a microphone (see Curtin, 2009; Gough, 2013). It is the combination of mode frequencies of the body that give the violin its characteristic sound. Therefore, measurements of the instrument's frequency response capture an 'acoustic fingerprint' which is unique for each instrument.

More recently, theoretical physical modelling of the violin body has seen considerable progress. This has included analytical models of simplified violin designs (see Woodhouse, 2005) and more detailed finite-element based models (see Gough, 2015a,b).

Research on the vibration of the body largely focuses on answering questions that concern violin makers. Players, on the other hand, are typically less concerned with the mechanics of the wooden box than they are in the behaviour of the bowed string.

1.2.2 The bowed string

The physics of the bowed string is a topic rich in complexity and one that spans many scientific disciplines. Although the vibration of the body and the bowed string are commonly studied as separate fields, the two are fundamentally interconnected. It is the motion of the string that drives the vibration of the body. The vibration of the body, conversely, influences the motion of the string. While the focus of this thesis will be on how the body vibrates, in studying the bridge, we do recognise that the force applied to the bridge comes from the strings. We will, however, approach this in a simplified fashion, without replicating the exact dynamics of a bowed string. For more information on the bowed string see Woodhouse and Galluzzo (2004).

1.2.3 Perceptual studies

The violin is, ultimately, an instrument designed for the purpose of music-making. Therefore, how an instrument sounds to a player and to an audience is perhaps its most important quality: mechanical measurements of the violin can only reveal so much, and, eventually, the opinion of a listener must be consulted. Questions such as "what is the secret of Stradivari?" still continue to fascinate scientists and the wider public. Comparing mechanical measurements is one way of trying to approach these type of questions. More recently, though, acousticians have decided to address questions like this from the perspective of psychoacoustics. Is it possible to hear the

differences between an original Stradivari violin and a modern copy? These studies involve procedures including blind-testing of instruments and ranking instruments in order of preference. For the purposes of our research, perception of violin sound will not be considered. For more information on perceptual studies see Fritz et al. (2007, 2012, 2014).

1.2.4 Playability

In contrast to judgements made by independent listeners, playability involves making an assessment of a violin based on player feedback. The sound of a violin is dependant on many factors. The physical instrument is of course central, but the contribution made by the player obviously also has a huge influence on the final sound. Both the player and the instrument are connected in a feedback loop; the player not only provides the input, but also reacts to the output of the instrument, both in terms of the sound they hear and the vibration felt via the bow.

There is some crossover with playability when discussing the vibration of the body. Players often talk about an instrument being ‘easier to play’ when changes are made to the body, such as an adjustment to the soundpost. There is no doubt that physical changes to the body will influence the way an instrument ‘feels’ to a player. However, this is an incredibly complex interaction. For the purposes of our research, the player will be removed from the equation. For more information on playability see Woodhouse (1993a,b) and Zhang (2015).

1.3 The soundpost

The soundpost, pictured in Figure 1.5, is a small cylindrical rod of wood which is placed under the treble foot of the bridge³, wedged between the front and back plates of the instrument. It is held under compression; no glue or adhesive is used to hold it in place. Violin makers place great importance on this small but crucial component of the instrument, with Italian instrument-makers calling it *l’anima*: ‘the soul’ of the violin (Pace, 1988).

What purpose does the soundpost serve? The name ‘soundpost’ itself gestures to its role in the instrument: clearly it must have some notable influence on the sound of the instrument. In this section, we will overview the history of the soundpost and discuss its role in the instrument in further detail.



Figure 1.5: A standard violin soundpost made from spruce. It is around 60 mm in length.

³The two feet of the bridge can be distinguished as either being on the treble side (under the E string) or on the bass side (under the G string) of the bridge.

1.3.1 The history of the soundpost

While the use of a wooden box to more efficiently radiate sound energy from a vibrating string has a very long history, early string instruments would not have incorporated soundposts. Their introduction into the modern instrument is likely to have been driven by the need to increase the structural integrity of ever-louder instruments.

We can hypothesise that as instrument makers pursued designs capable of producing louder sounds, they refined the wooden body to be as light and flexible as possible, with countervailingly ‘heavy’ strings. This is because in order to make an acoustic string instrument louder, one aims to maximise the amount of energy transferred from the string to the body. The limiting factor in this process is the difference in impedance between the string and the body, with the strings having a relatively lower impedance in comparison to the body.

As instrument makers experimented with reducing the difference in impedances of the strings and body, they were likely to have encountered boxes which collapsed under the force exerted down upon them by the strings. Placing a supporting strut inside the box would have increased the stiffness of the plates, and potentially solved structural concerns. It is at this point that makers would have discovered a noticeable acoustic effect as a result of adding a supporting strut. Through trial and error, they would have adjusted the position until an ‘optimum’ location was settled upon.

It is difficult to pinpoint exactly when the soundpost was first developed. It is, however, perhaps surprising to discover that the first printed reference to the word ‘soundpost’ in the English language comes in Shakespeare’s *Romeo and Juliet*.⁴ Written between 1591 and 1596, the play’s reference gives us an indication that by this time, the soundpost was already established in string instrument design. Note that soundposts are also found in other string instruments such as the viol family.

1.3.2 The role of the soundpost

While early precursors to the soundpost may have been added to provide a structural support inside the instrument, the soundpost is now recognised as serving an important acoustical role. Still, it is often purported that without the soundpost the front plate would collapse. The strings

⁴An on-stage musician is given the name “James Soundpost” and this is referred to out loud by another character. Knowledge of the existence of the soundpost remains, even today, restricted to only those involved closely with the violin world. One assumes that the soundpost would have been equally unknown to broader Elizabethan audiences. John Dilworth remarks that the name “James Soundpost” was likely a joke intended for the musicians rather than the audience: “Was the actor who played James Soundpost in real life continually adjusting his viol, neurotically shifting the post around while the author pleaded with him to get on the stage and play the thing?” (Dilworth, 2014).

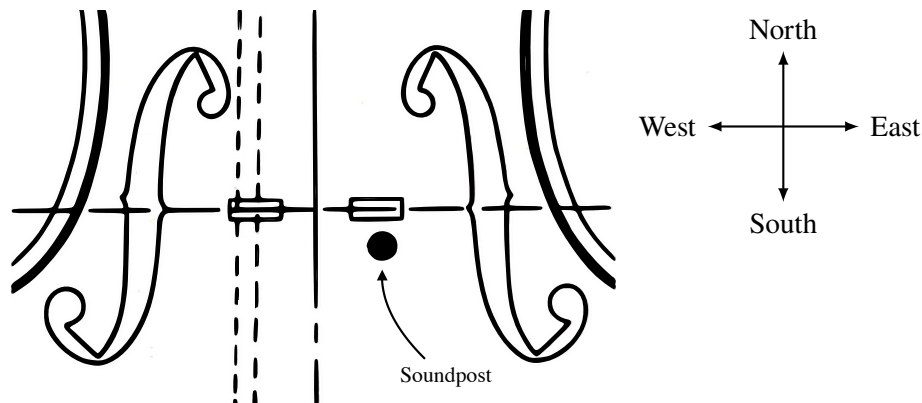


Figure 1.6: An overhead view of violin body focusing on the region around the *f*-holes. The location of the two bridge feet is marked by the rectangular boxes. The bass bar is shown under the left-hand foot with dashed lines. The location of the soundpost is marked by the black circle. This is typically where the soundpost is positioned; slightly behind the treble foot of the bridge (from McLennan, 2005).

do exert a large downward force on the front plate, in the region of 10 kg. But at the same time, the curved design of the front plate is, in a well-made instrument, stiff enough that it will not collapse if the soundpost were to be removed.

The main role of the soundpost is in fact to introduce asymmetry to the design of the instrument body. Figure 1.6 shows the position of the soundpost and bass bar relative to the centre of the instrument. If we consider the body of the violin without the soundpost and bass bar, then it is perfectly symmetrical bilaterally. If we imagine that the bridge undergoes a rocking motion with equal and opposite forces at the two feet, this will excite modes which are also bilaterally symmetric (Schelleng, 1971). As a result, these modes produce no net volume change of the box, barring second-order effects.

In order to radiate efficiently at low frequencies, where the wavelength of sound is large compared with the size of the body, the instrument must behave like a ‘simple source’ (Schelleng, 1971). A cyclical change in the total volume of air displaced helps boost sound radiation. For this to occur, the violin must “swell more in one area than it shrinks in another” (Schelleng, 1971). The addition of the soundpost, placed off-centre, enables this to happen: the symmetry of the modes is disturbed.

The addition of the bass bar also contributes to the asymmetry of the body. However, its main role is to keep the upper and lower bouts of the front plate in step with the bass foot of the bridge (Schelleng, 1971). From the perspective of violin makers, the soundpost also serves as a resource for sound adjustment in the finished instrument. Small changes to the set-up of the

soundpost have an influence on the vibration of the body and are said to have a large influence of the sound of the instrument.

1.4 How violin makers approach soundpost set-up

Violin makers place great importance on fitting the soundpost ‘perfectly’ to ensure their instruments produce what they believe to be ‘optimal sound’. Over the centuries, makers have, largely through trial and error, settled on a basic set of rules regarding the various parameters that govern soundpost set-up. Through private discussion with violin makers over the course of this thesis (Woodhouse et al.) and from reviewing literature on violin making, we have identified three factors which makers place most importance on when setting up a soundpost. These are, in order of importance to the acoustics of the instrument: ‘tightness’, ‘position’ and ‘fit’. These parameters do not necessarily dictate the order in which a violin maker might set-up a soundpost. For example, first the position might be decided, then the fit and tightness established as the ends of the soundpost are shaped.

In this section, we will explore these parameters in more detail to try to understand how soundpost set-up influences the acoustics of the instrument. We will also introduce the idea that the soundpost behaves as an axial rod and as a bending beam. This is relevant because parameters such as tightness and fit will directly influence the axial and bending modes of the soundpost by altering its boundary conditions. The views of violin makers will be considered as they usefully draw attention to some of the key issues relating to soundpost set-up.

1.4.1 The position of the soundpost

In practice, the position of the soundpost does not vary greatly from its ‘base’ position. However, violin makers strongly advocate that very small adjustments to this base position, in the order of fractions of millimetres, can have a considerable impact on the sound of the instrument. In addition to this, they advocate that by moving the position of the soundpost in certain directions, it is possible to change the sound of the instrument in a controlled fashion. Heron-Allen (1885) includes the following guidelines on soundpost position:

When, though even, the tone is rough and harsh, the [sound]post must be moved back a little; if the high strings are weak and the lower ones harsh, the [sound]post must be moved a little outwards towards the *f*-hole; if the low notes are weak and the high ones shrill, it must be moved very slightly towards the centre.

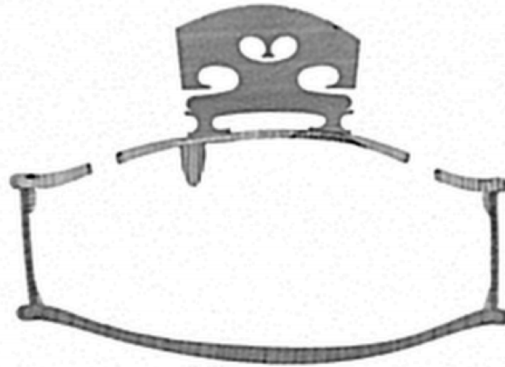


Figure 1.7: A CT scan of a violin by Giuseppe Guarneri ‘del Gesù’. The arching of the plates can be seen to be distorted at the soundpost position (from Bissinger and Oliver, 2010).

These guidelines are by no means the only set of rules concerning soundpost position. Our research has revealed many differing opinions on how soundpost position influences the sound of the instrument. Dealing with qualitative and subjective descriptions of sound — words such as harsh, shrill, mellow, bright and nasal — makes this topic particularly challenging. However, we will attempt to summarise some of the recurring statements made by makers.

Taking the base position of the soundpost as slightly behind the treble foot of the bridge (see Figure 1.6), we can describe small adjustments around this point using the terms north, south, east and west. Moving the soundpost north is said to increase the loudness of the instrument, while moving it south is said to decrease the loudness. Moving the soundpost east is said to boost the top register, while moving it west is said to boost the low register.

From a physical perspective, if we consider the soundpost as a rigid link wedged between the front and back plates, it is clear that moving the position of the soundpost will have a direct influence on the mode shapes of the plates. The mode frequencies will also be affected. How these changes to the modes influences the sound of the instrument must then be addressed. In addition, is it possible to relate these changes to the verbal descriptions used by makers and players?

1.4.2 The ‘tightness’ of the soundpost

‘Tightness’ is a word used by violin makers to describe how ‘tightly fitting’ a soundpost is. A soundpost is considered tightly-fitting when it presses firmly against the plates. A loosely-fitting soundpost is one that doesn’t press strongly against the plates; the limit of a loose soundpost is the point at which it is no longer held under compression and collapses. A question that often arises



Figure 1.8: An example of soundpost-induced damage: (a) a circular ‘dent’ is seen on the underside of the front plate, due to soundpost pressing into the wood; (b) the damage is repaired by attaching a thin veneer of wood (from Curtin, 2018).

is whether there exists a preference towards fitting a soundpost tightly or loosely. Discussion with violin makers has revealed many opinions on the matter. None claim that a loosely fitting soundpost is desirable. Some claim that there is a sweet spot: an optimum level of tightness. Others say they prefer to fit the soundpost as tightly as possible.

An interesting observation that can be made of many violins, both old and modern, is that there is often significant damage to the plates caused by the soundpost. Looking at CT scans of high-quality violins dating from the eighteenth century, the shape of the violin can be measured very accurately and internal structures can be seen clearly. A cross-section through the body of a violin, near the location of the soundpost, is shown in Figure 1.7. Here, we can observe that the arching of the plates has been distorted: there is a noticeable bulge at the position where the soundpost sits. This is likely due to a tightly fitting soundpost exerting pressure on the plates and gradually bending them out the shape.⁵ On close inspection, repair work at the point at which the soundpost makes contact with the plates can be seen.

This raises another aspect of soundpost-induced damage: the potential for the soundpost to ‘dig into’ the wood of the plates. Figure 1.8 shows this phenomenon clearly, along with an example of how this damage is repaired. The relatively soft wood of the violin front plate is, of course, naturally prone to such damage. However, it demonstrates that the soundpost has been, in this example instrument, pressing very firmly against the plates.

The question we as acousticians must now ask is, what are the underlying physical consequences of variations to the tightness of the soundpost? In effect, changing the tightness changes the coupling strength between the soundpost and the plates. This has both an effect

⁵Many old violins exhibit this deformation due to the soundpost bending the plates. This begs the question whether this semi-accidental change in the shape of the body has a considerable effect on the body modes. Perhaps this is what is meant when players say an instrument takes years to season?

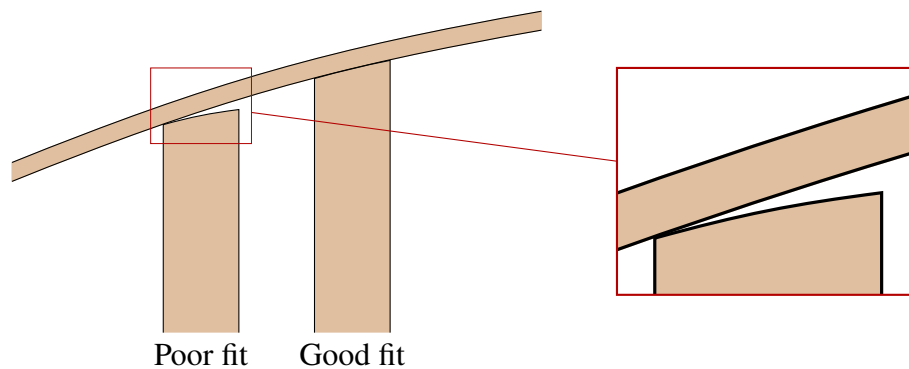


Figure 1.9: A diagram illustrating the difference between ‘poor fit’ and ‘good fit’. A soundpost with good fit has full wood-to-wood contact with the plates. A soundpost with poor fit might have incomplete contact with the plates, for example being pinned on an edge, as shown in the diagram.

on the plates of the instrument and an effect on the soundpost itself. A tight soundpost can be described as having a clamping effect at the point where the soundpost makes contact with the plates. Changes to the tightness will change this clamping effect. This will undoubtedly have an influence on the modes of the plate. In addition, the ends of a tight soundpost could be said to have clamped–clamped boundary conditions. This will influence the axial vibration modes of the soundpost. A loose soundpost will be less coupled to the plates and may have free–free end boundary conditions.

We can hypothesise that a tight soundpost may increase the overall stiffness of the plates, raising the modal frequencies. However, whether there is coupling between the soundpost and plates, and how changes to the coupling strength change the dynamics of the body, is harder to predict. Theoretical modelling is required to explore this further.

1.4.3 The ‘fit’ of the soundpost

The ‘fit’ of the soundpost describes the wood-to-wood contact between the ends of the soundpost and the plates. The curved surface of the plates mean that, in order to achieve full wood-to-wood contact, the ends of the soundpost must be carefully shaped to match the contour of the plates. Makers place importance on achieving an accurate fit between the soundpost and plates: full wood-to-wood contact is desirable. Achieving accurate fit requires skill on the part of the maker, and it is not uncommon to find poorly-fitted soundposts. A poorly-fitted soundpost might have ends which are able to move independently from the plates. A well-fitted soundpost, on the other hand, is more or less clamped to the plates. See Figure 1.9 for an illustration of the difference between poor and good fit.

If we imagine the soundpost as a bending beam, then changes to the fit can be described in terms of changes to the end boundary conditions. A soundpost that has full wood-to-wood contact with the plates may be described as having clamped–clamped boundary conditions; a soundpost that doesn't have full wood-to-wood contact may be described as having pinned–pinned boundary conditions. These different boundary conditions will influence the frequencies of the bending modes of the soundpost. Further to this, the different boundary conditions will influence the coupling between the soundpost and the plates. What effect this has on the plate modes, and whether there are audible consequences, is a promising topic for investigation (Woodhouse, 2002).

1.4.4 The wood used to make the soundpost

In addition to tightness, position and fit, the type of wood used to make the soundpost is another variable to consider. The soundpost is most commonly fabricated out of spruce, although other woods are sometimes used. Some makers advocate that the type of wood, and in particular the quality of the wood, is important to soundpost set-up.

Most makers will insist that suitably well-seasoned wood should always be used. The reasoning behind this is straightforward: the better-seasoned the wood the more stable it is. Heron-Allen (1885) writes that “when a soundpost has been made of unseasoned wood, it contracts after being set in a [violin]”. It is obvious that this sort of issue is to be avoided. Choice of wood is therefore important from the perspective of stability. But, beyond this, do the material properties of the soundpost have an influence on the vibration of the body? If we imagine the soundpost as a rigid body, then the density of the wood will influence the mass of the soundpost. If the soundpost behaves as if it is more than just a rigid body, with axial and bending modes of its own which have an influence on the vibration of the box, then the Young's modulus of the wood will also be important.

On a practical level, makers will often advocate that the soundpost be orientated so that its grain runs perpendicular to that of the violin body. Heron-Allen (1885) writes that “[the soundpost] fibres must be set *across* the fibres of the [front plate]”. This is so the winter grain lines of the soundpost do not interlock with the grain lines of the front plate and potentially cause wear or damage. We will address the possible vibrational consequences of soundpost orientation later in this thesis.

1.5 Previous research on the soundpost

A comprehensive search of all previous literature on soundpost research has been undertaken. In the following section, we will highlight some of the most significant results.

1.5.1 Nineteenth century research

Huggins (1883) explores how the tightness of the soundpost affects the back plate by placing rubber at the ends of a soundpost which is then inserted into an instrument. With very primitive experimental methods (sensing using fingers), he concludes that the back plate does not vibrate as much with the rubber in place, leading him to conclude that the soundpost is important in transferring energy to the back plate. This view of the role of the soundpost is held by some makers. However, it has been argued more recently by others that the back plate in fact has very little impact on the sound radiation of instrument (Schelleng, 1971).

1.5.2 Modern research

Schelleng (1971) undertakes a theoretical approach and considers a simplified violin body and soundpost system. The violin body is modelled as a “closed cigar box” and the soundpost modelled as a rigid link between the two plates. Using simple modal analysis, he is able to demonstrate that the addition of an off-centre soundpost forces two bilaterally symmetric modes to be coupled, forming a single asymmetric mode shape. Schelleng’s own diagram illustrating this is shown in Figure 1.10.

This theoretical work offers a simple explanation to the function of the soundpost, at least at low frequency. However, it models the soundpost as a rigid link only. It considers the axial stiffness of the soundpost to be infinite, and bending of the soundpost is also not considered.

Woodhouse (2002) recognises that the soundpost, as a thin rod, “will have resonances of its own”. The lowest bending resonance frequency is estimated to fall in the region of 3 kHz. This is well within the frequency range at which a violin operates. Woodhouse (2002) concludes that further theoretical modelling would be required to determine if the bending modes of the soundpost do have a significant influence on the vibration of the box.

The relationship between the soundpost and the bridge is raised by Schelleng (1971). In violin-making, it is standard practice to position the bridge in relation to the *f*-hole notches. This means that location of the bridge feet is fairly fixed. Moving the soundpost therefore always changes the distance from the bridge to the soundpost. Schelleng concedes that “in the present state of knowledge it would be hazardous to guess the relative importance of these two factors”.

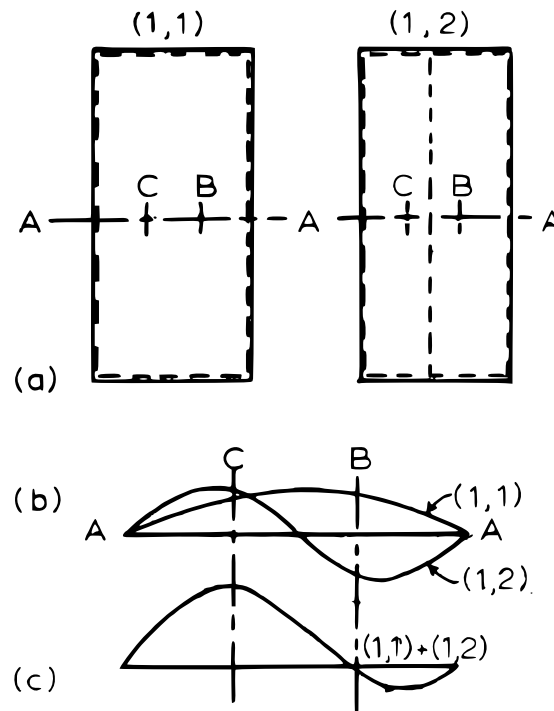


Figure 1.10: A figure from Schelleng (1971) illustrating the “effect of the soundpost in enhancing radiation of sound from a rectangular plate”. (a) The shape of the modes (1,1) and (1,2) are plotted using a dashed line on top of the outline of a rectangular plate. (b) A ‘side-on’ view of the mode shapes. (c) Inserting an immovable soundpost at B causes the two previously independent modes to combine.

Hutchins (1974) writes in response to Schelleng (1971) that there is perhaps another role of the soundpost. This is the effect of the soundpost on the air resonances of the instrument. The presence of the soundpost has the effect of making the front and back plates stiffer. This raises the frequency of the Helmholtz air resonance.

1.5.3 Experimental work

Fang and Rodgers (1992), Saldner et al. (1996) and Rodgers (1997) and Bissinger (1995, 1998) take an experimental approach in their investigations of the action of the soundpost.

Fang and Rodgers (1992) investigate elastic vibration of the soundpost by attempting to measure axial modes of the soundpost. They estimate that the first axial mode of the soundpost, when coupled to the plates, occurs at 10 kHz. To measure the axial motion of the soundpost, two accelerometers are placed on the front and back of a violin at the positions where the soundpost makes contact with plates. From their results, they claim to observe a resonance at 8 kHz which they attribute to the axial motion of the soundpost.

Saldner et al. (1996) use holographic techniques to visualise the vibration of the violin body, taking measurements with and without the soundpost inside the instrument. At low frequency, they find nodal points at the position of the soundpost, which they claim supports the theory that the main role of the soundpost is to make the violin asymmetric.

Rodgers (1997) tests three different positions of the soundpost inside the instrument. However, these experiments reveal very little about the effects of soundpost position on the vibration of the instrument.

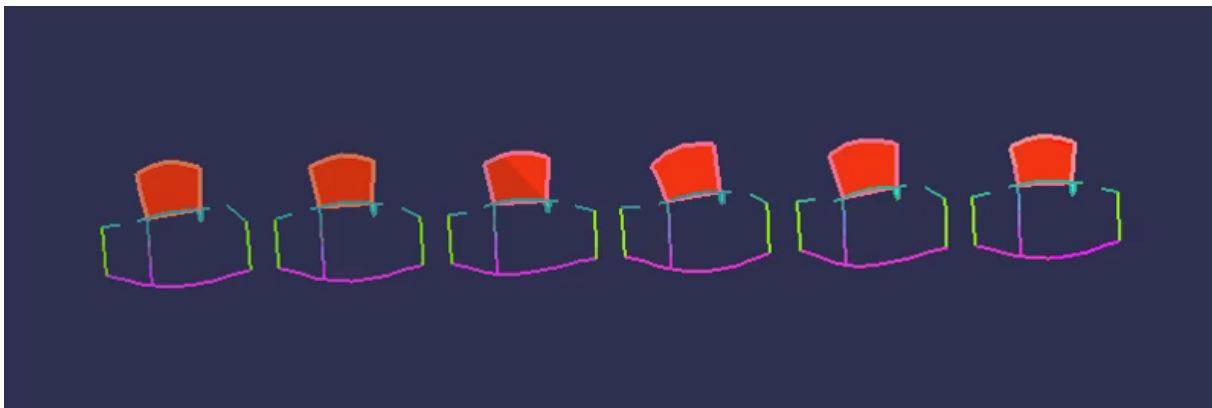


Figure 1.11: These diagrams show experimental data obtained using laser vibrometry. The measurements show a cross-sectional view of the body at the position of the soundpost, with each diagram showing the operating deflection shape at a particular frequency. From left to right, these measurements correspond to resonances at 777, 851, 951, 1109, 1185 and 1347 Hz (by permission of George Bissinger).

Bissinger has conducted a range of experiments which probe the vibration of the violin body. He writes that “the acoustic consequences of manipulating the soundpost dimensions, tightness of fit and position between the front and back plates are proof that it has a substantial effect on the mechanical vibrational response of the violin” (Bissinger, 1995). However, the paper does not fully explore the acoustic consequences of manipulating the soundpost in terms of its dimensions, tightness and fit. Instead, Bissinger (1995) focuses primarily on the difference between a violin with and without a soundpost. A measurement of the ‘acoustic output’ of the instrument is made using a microphone. His results show that there is increased output when the soundpost is present.

In more recent research, Bissinger has used 3D laser vibrometry to visualise the body modes of the instrument. With regard to the soundpost, Bissinger has isolated a cross-section around the soundpost position and plotted the displacement of the plates for different modes. An example of these results is shown in Figure 1.11. These plots raise the question of whether the soundpost might create ‘hill-like’ features (see Woodhouse, 2005).

1.5.4 Finite-element calculations

A recent and very interesting development in violin acoustics research is the application of finite element analysis to the body of the instrument. Gough (2015a,b, 2018) uses these methods to model the violin body, including the soundpost. Some of his results relating to the soundpost are shown in Figures 1.12–1.14.

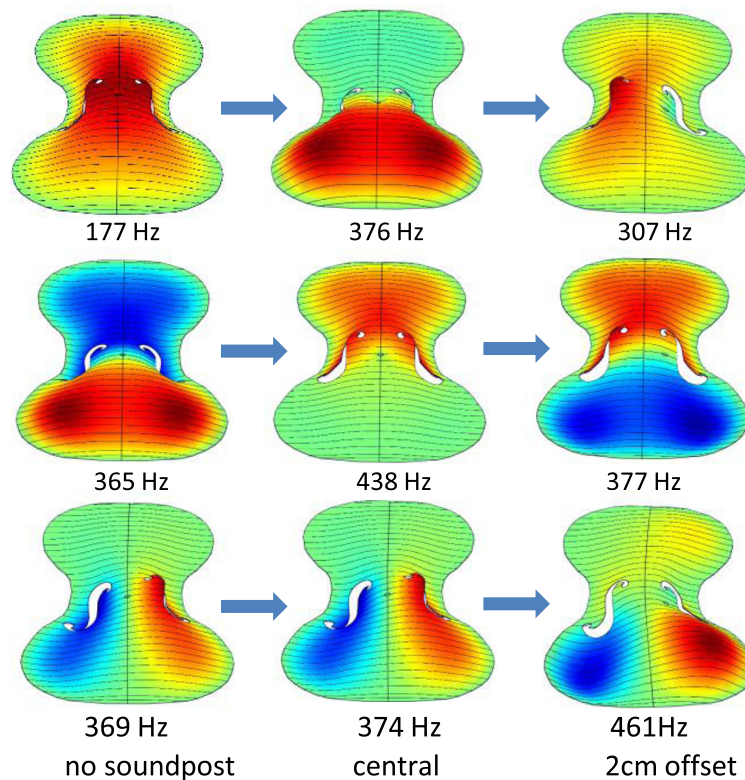


Figure 1.12: A reproduction of Figure 10 from Gough (2015a). The lowest three body modes are shown. From left to right, we see the effect of having no soundpost, having a centrally placed soundpost, and having a soundpost offset from the centre by 2cm to the right.

In Figure 1.12, the influence of the soundpost and its position on the mode shapes and modal frequencies of the three lowest corpus modes is shown. As can be seen from the diagram, inserting a soundpost raises the modal frequency of all the modes. In the top right hand diagram (307 Hz) we can clearly see that an off-centre soundpost produces an asymmetrically shaped resonance mode of the front plate (Gough, 2015a).

Gough (2015b) further explores the effect of soundpost position on the resonance modes of the body as shown in Figure 1.13. These graphs show the impact on the body resonances when the soundpost is moved longitudinally and transversely. In another test, Gough (2015b) varies the coupling strength between the soundpost and plates. The effect this has on the body resonances

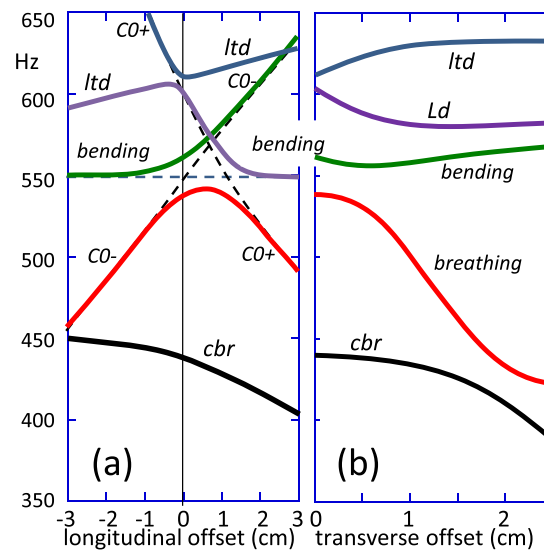


Figure 1.13: These graphs show the impact of offsetting an initially centrally positioned soundpost (0 cm) longitudinally and transversely. (a) positive offset indicates moving towards the lower bouts. (b) offset is towards the treble side bridge foot (from Gough, 2015b).

is shown in Figure 1.14. This research highlights two of the most important questions relating to the soundpost: its position and its ‘tightness’. By conducting systematic parameter studies using a simplified model of the violin, Gough is able to explore the physical mechanisms which underlie the interaction between the soundpost and the body. Gough’s approach has provided significant motivation for the research methodology we have adopted in our study.

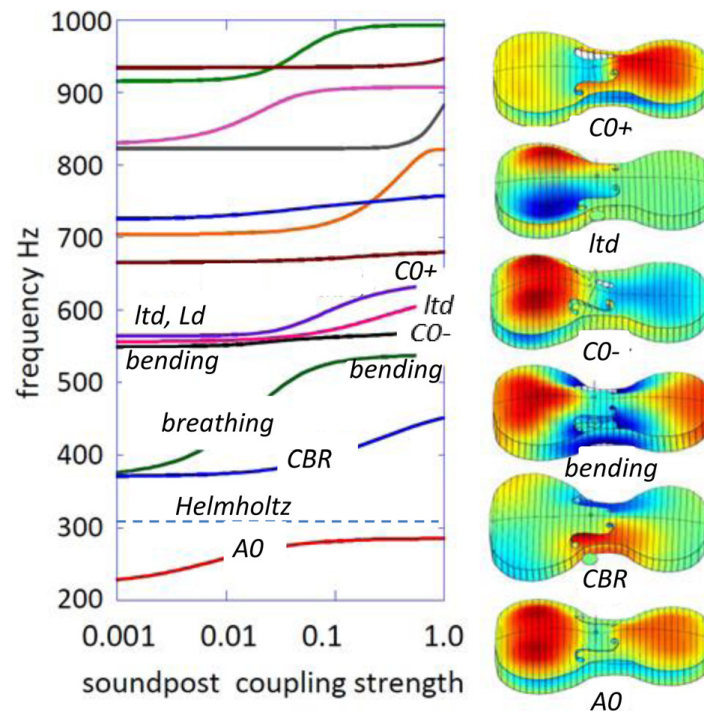


Figure 1.14: The soundpost coupling strength is increased from very small to a typical normal strength. The soundpost is placed centrally and the mode shape diagrams show a scaled soundpost coupling strength of 0.2 (from Gough, 2015b).

1.6 Thesis outline

The structure of the thesis which follows will be briefly outlined:

- **Chapter 2** – We introduce and develop a simplified theoretical model of the violin body and soundpost, building upon research by Woodhouse (2015). The theory underpinning the model is presented and preliminary tests are performed to assess its validity.
- **Chapter 3** – Extensive parameter studies are conducted, investigating all aspects of the vibrational behavior of the soundpost. Specifically we look at varying the coupling strength between the plates and soundpost to investigate questions pertaining to the tightness and fit of the soundpost.
- **Chapter 4** – We introduce an enhanced bridge model which provides the ability to locate the driving point at each of the four string notches. This allows us to address questions pertaining to the ‘balance of the strings’. A validation of the new bridge model is subsequently performed.

-
- **Chapter 5** – The bridge model introduced in Chapter 4 is utilised to investigate the influence of the soundpost on the vibration of the model. Specifically we investigate how driving at the four different strings influences the body resonances.
 - **Chapter 6**– To assess the ‘loudness’ of the model, we develop a method for estimating radiated sound pressure. Extensive parameter studies are performed to investigate how the soundpost influences the radiated sound pressure.
 - **Chapter 7** – We depart from our theoretical work to perform some experimental investigation into the soundpost. Using a physical simplified model of the violin body, we probe the vibration of the soundpost and design an adjustable soundpost.

2

A simplified model of the violin body and soundpost

As the findings laid out in the literature review demonstrate, the soundpost serves an important acoustical role in many types of bowed string instrument. Although existing acoustics research, together with anecdotal evidence from instrument makers, gives us some idea as to its acoustical role, the physical processes lying behind the effects described are poorly understood. In this chapter, we will introduce a simplified theoretical model of the violin body and soundpost, which will be used extensively throughout this thesis. This will be used to help gain a better understanding of the vibrational behaviour of the soundpost and its interactions with the body.

First, we will consider how the design of the violin can be simplified to produce an achievable theoretical model. Then, we will implement the model mathematically using a Lagrangian approach to calculate the mode frequencies and mode shapes of the system. We will then go on to discuss the material and design characteristics of a real violin to establish our model's parameters. Finally, we will carry out some preliminary tests to establish the validity of the model.

2.1 The design and mathematical implementation of the theoretical model

2.1.1 Simplifying the design of the violin body

At the most basic level, the violin body can be thought of as two similar plates joined together at the sides to form a closed box. However, in its original form, this box is still a fairly complex structure. The front and back plates are curved and the thickness of the wood varies throughout the entire structure. In addition to this, the wood, being an organic material, is inhomogeneous

and highly variable. The grain structure within a single piece of wood is rarely perfectly uniform. Therefore, for a minimal model of the violin body, we will simplify both its design and its material properties in order to make a model that can be expressed analytically.

In terms of the material properties, it makes sense to treat the wood as being homogenous. While the stiffness and density properties can be chosen to match those of typical violin wood, we will disregard the small differences in grain structure which would be hard to model and add significant complexity.

The shape of the violin body — or more specifically the outline and profile of the front and back plates — could in theory be reproduced in a very detailed fashion and modelled using a finite element package. Research by Gough (2015a,b) has shown this to be possible using software available today. However, at this stage it is worth pausing to carefully consider what our model aims to achieve, which is to observe how the soundpost behaves when wedged between the front and back plates of a violin.

We can model the soundpost fairly straightforwardly, as a rod or a beam with a circular cross-section. As our goal is to study the soundpost in close detail, is it important that the soundpost resembles its true form. However, including all the design features of a violin's front and back plates does not provide significant added benefit. To the contrary, it would add unnecessary complication to the model. Stripping away as much complicating detail from the violin body enables us to form a clearer picture of the role of the soundpost. It is therefore advantageous to use a simple approximation of a violin's front and back plates.

One of the simplest approximations is to represent the plates of the violin as flat orthotropic rectangular plates, as used by Woodhouse (2005). Simplifying the design of the plates in such a way makes them straightforward to model, as their vibrational behaviour is well understood. This is optimal for the purposes of our investigation as it enables the effects of the soundpost to be clearly identified in contrast to the behaviour of plates.

2.1.2 Implementing a theoretical model

Now that we have a basic design for our model in mind, we need to implement this mathematically. In the section to follow, the mechanics of plates, rods and beams will be introduced: these objects form the basis of our simplified model. The front and back plates will be modelled as rectangular orthotropic plates and the soundpost will be modelled as both an axial rod and as a bending beam.

One of the key findings to draw from the literature review is that violin makers consider the 'tightness' and 'fit' of the soundpost to be very important. This relates to how tightly the soundpost is wedged between the front and back plates and the amount of wood-to-wood contact

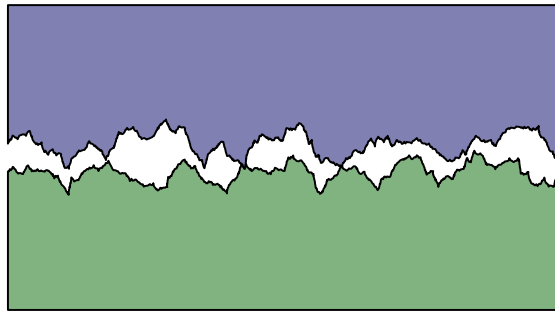


Figure 2.1: A diagram depicting two rough surfaces in contact with each other.

between the ends of the soundpost and the plates. The main physical quantity that makers are changing when they make changes to the length and end shape of a soundpost is likely to be the contact stiffness between the soundpost and the plates. At the microscopic level, the surface of the plates and soundpost ends are rough: see Figure 2.1. Therefore, the real contact area between the two surfaces is actually smaller than the apparent contact area (see Bowden and Tabor, 1950, and Johnson, 1985). Subsequently, how tightly these surfaces are pushed together will change the contact stiffness of the interface. To model the interaction between the soundpost and plates in our model, we will therefore use a combination of axial springs and torsional springs. By adjusting the stiffness of these springs we can, for example, simulate the effect of a having a tightly fitting soundpost versus a loosely fitting soundpost. The effects of independently varying the axial springs and the torsional springs can also be explored, in order to determine whether a particular type of stiffness dominates any of the vibrational behaviour.

In order to calculate the modal response of this multi-component coupled system, we will use the ‘assumed modes method’. This is a method widely used in mechanical engineering to determine the resonance frequencies and mode shapes of multi-degree-of-freedom systems (see Tongue, 2002, ch. 6, and Rao, 2007, ch. 17). The displacement of the system can be written as a linear combination of a set of trial shape functions and generalised coordinates. We can then formulate expressions for the potential and kinetic energy of the system in terms of our assumed displacement functions. Lagrange’s equations can then be used to derive the equations of motion of the system. By solving these equations, we obtain eigenvalues which relate to the mode frequencies and eigenvectors which relate to the mode shapes of the system.

2.2 The elements of the model

In this section, we will introduce the theory of rectangular plates, which are used to model the violin plates, and the theory of axial rods and bending beams, which are used to model the soundpost. We will also demonstrate how the mode shapes and mode frequencies of the combined system can be calculated using a Lagrangian approach. Finally, we will outline the steps required to calculate a vibration transfer function.

2.2.1 The vibration of a simply-supported orthotropic rectangular plate

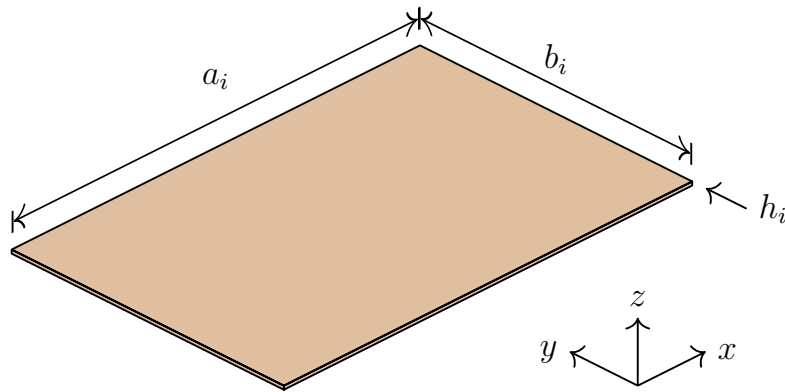


Figure 2.2: A diagram of a single rectangular plate showing the coordinate system and variables used to describe it. The length, a_i , is defined in the x -axis. The width, b_i , is defined in the y -axis. The thickness is given by h_i .

To model the plates of the violin, flat orthotropic rectangular plates with simply-supported boundary conditions along all edges will be used: see Figure 2.2. Simply-supported edges have been chosen to approximate the boundary conditions found on real front and back plates, which are glued at the edges to the ribs. Although in a real violin there is likely to be some movement at the edges, this is not significant to the main question we are addressing. Having an orthotropic plate allows us to model the elastic properties of spruce more closely. Elastic constants can be chosen to reflect the different stiffnesses along the grain and across the grain of the wood.

Using classical plate theory, the potential energy, V , and the kinetic energy, T , of an orthotropic rectangular plate can be defined. The potential energy for a single plate, V_i , is expressed as

$$V_i = \frac{h_i^3}{2} \int_0^{a_i} \int_0^{b_i} \left[D_1^i \left(\frac{\partial^2 u_i}{\partial x^2} \right)^2 + D_2^i \left(\frac{\partial^2 u_i}{\partial x^2} \right) \left(\frac{\partial^2 u_i}{\partial y^2} \right) + D_3^i \left(\frac{\partial^2 u_i}{\partial y^2} \right)^2 + D_4^i \left(\frac{\partial^2 u_i}{\partial x \partial y} \right)^2 \right] dx dy, \quad (2.1)$$

where u_i is the transverse displacement, h_i is the plate thickness and a_i and b_i are the length and width of the plate respectively.¹ The four independent elastic constants — D_1^i , D_2^i , D_3^i and D_4^i — are proposed by McIntyre and Woodhouse (1988). These are related to: the Young's moduli along the two principal directions (E_x and E_y), the two Poisson's ratios between the x and y directions (ν_{xy} and ν_{yx}), and the in-plane shear modulus (G_{xy}). The notation for the Poisson's ratios refers to the following: ν_{xy} refers to the amount of contraction in the y direction when a stretch is applied in the x direction; ν_{yx} represents the opposite case. These four elastic constants are defined as follows:

$$D_1 = \frac{E_x}{12\mu}, \quad (2.2)$$

$$D_2 = \frac{\nu_{xy}E_y}{6\mu} = \frac{\nu_{yx}E_x}{6\mu}, \quad (2.3)$$

$$D_3 = \frac{E_y}{12\mu} \quad (2.4)$$

and
$$D_4 = \frac{G_{xy}}{3}, \quad (2.5)$$

where $\mu = 1 - \nu_{xy}\nu_{yx}$. The kinetic energy of a single plate, T_i , is expressed as

$$T_i = \frac{1}{2}h_i\rho_i \int_0^{a_i} \int_0^{b_i} \left(\frac{\partial u_i}{\partial t} \right)^2 dx dy, \quad (2.6)$$

where ρ_i is the volume density (mass per unit volume) of the plate.

We will use the assumed modes method: generically, a displacement $u(x, y, t)$ can be written as a linear combination of a finite set of assumed shape functions,

$$u(x, y, t) \approx \sum_{p=1}^N \alpha_p(t)\psi_p(x, y), \quad (2.7)$$

where $\psi_p(x, y)$ are the prescribed shape functions, $\alpha_p(t)$ are the generalised coordinates, which are time dependent, and N represents the finite number of shape functions being calculated. Note that each generalised coordinate corresponds with one degree of freedom of the system. The shape functions are chosen specifically to satisfy the boundary conditions of the problem. Therefore, for the case of a simply-supported rectangular plate we will use shape functions

¹The suffix i , later in the chapter, will be used to identify the two plates. The front plate will be referred to as plate 1 and the back plate as plate 2.

consisting of sine functions. The free motion of a single rectangular plate takes the form

$$u_i(x, y, t) \approx \sum_{p=1}^{N_i} \sum_{q=1}^{N_i} \alpha_i^{pq} \sin\left(\frac{p\pi x}{a_i}\right) \sin\left(\frac{q\pi y}{b_i}\right), \quad (2.8)$$

where N_i is a constant and α_i^{pq} is a matrix of generalised coordinates. For the sake of simplicity, we have used N_i as the upper limit for both summation terms. These can be altered, if so desired, but for the purposes of our model we have kept both equal. This means that the total number of shape functions used to calculate the displacement for a given plate mode is simply N_i^2 .

We have now defined expressions for the kinetic energy, potential energy and displacement for simply-supported orthotropic rectangular plates. These will model the two plates of our simplified violin body. Next, we will consider how to model the soundpost.

2.2.2 The axial vibration of a free–free rod

To begin with, we will consider the soundpost as a rod with axial vibration modes. Bending motion of the soundpost — which can be achieved by modelling it as a beam — will be introduced later. But for now, to gain a clear understanding of the theory behind our modelling approach, we will examine only axial motion. A diagram of the rod we are modelling is shown in Figure 2.3.

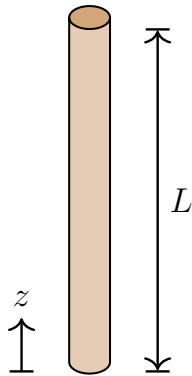


Figure 2.3: A diagram of the soundpost modelled as a rod. The length, L , is defined in the z -axis. The rod has radius, r , which is used to calculate the cross-sectional area, A .

The soundpost is not glued or fixed to the plates of the violin. Instead, it is held in place by compressional forces from the front and back plates. The isolated soundpost resembles a rod with free boundary conditions at both ends. To model the interaction between the soundpost and plates, we will use springs.

The soundpost is positioned upright between the two plates, which lie in the x - y plane; see Figure 2.4. Hence, the contraction and expansion of the soundpost as it vibrates axially occurs

along the z -axis. The kinetic energy of a rod, T_r , is given by

$$T_r = \frac{1}{2} \rho A \int_0^L \left(\frac{\partial u_r}{\partial t} \right)^2 dz, \quad (2.9)$$

where ρ is the volume density, A is the cross-sectional area and L is the length of the rod.² The cross-sectional area for a cylindrical rod can be calculated using $A = \pi r^2$, where r is the radius of the rod. Similarly, the potential energy, V_r , of a rod is expressed as

$$V_r = \frac{1}{2} EA \int_0^L \left(\frac{\partial u_r}{\partial z} \right)^2 dz, \quad (2.10)$$

where E is the Young's modulus.

As before, we will define the displacement of the rod in terms of our choice of assumed shape functions. For a rod with free–free boundary conditions, the analytic modes consist of cosine functions. The displacement function, u_r , for free motion can be written as

$$u_r(z, t) \approx \sum_{p=0}^{N_r-1} \alpha_r^p \cos\left(\frac{p\pi z}{L}\right), \quad (2.11)$$

where N_r is the number of rod shape functions and α_r^p is a matrix of generalised coordinates. Note that the summation starts at $p = 0$, because we must include the rigid-body motion of the soundpost.

2.2.3 The combined system of plates, axial rod and axial springs

We will now show how the two rectangular plates can be coupled to the rod using axial springs. This arrangement is illustrated in Figure 2.4. The springs are used to model the contact stiffness between the plates and the soundpost. The total kinetic energy, T_T , of the combined system is simply given by the sum of the kinetic energy for each plate and the rod:

$$T_T = T_1 + T_r + T_2. \quad (2.12)$$

For the total potential energy, we must take into account the contribution from the axial springs. Therefore, V_T is expressed as

$$V_T = V_1 + V_{s_1} + V_r + V_{s_2} + V_2, \quad (2.13)$$

²The subscript r will be used to differentiate variables relating to rod vibration from similarly named variables which relate to plate or, later, beam vibration.

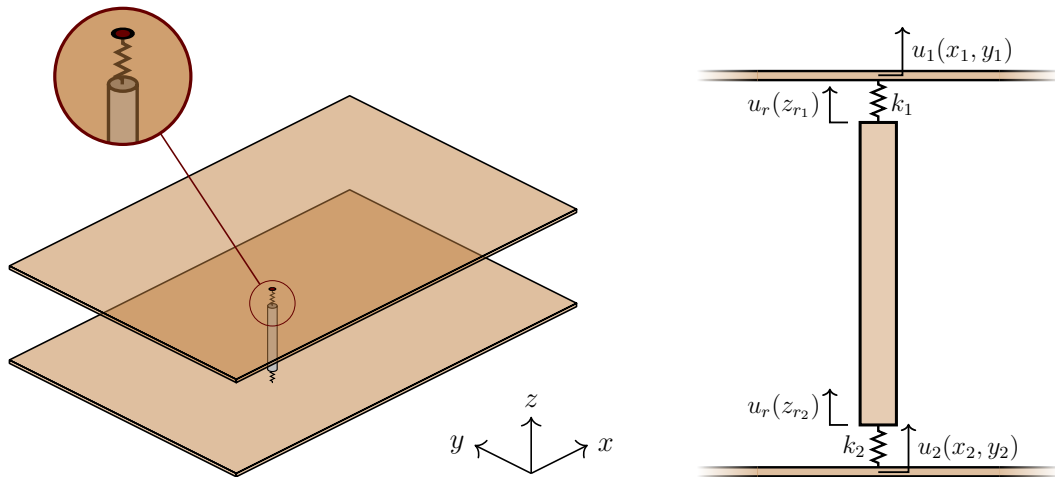


Figure 2.4: A diagram showing how the soundpost is positioned in between the two plates. On the left, we have a three dimensional view. On the right, a side-on view of the rod and the springs, with stiffnesses k_1 and k_2 , which join the plates at the coordinates (x_1, y_1) and (x_2, y_2) .

where V_{s_1} and V_{s_2} refer to the potential energy associated with the springs connected to the front and back plate respectively. We can define the potential energy for a spring as

$$V_s = \frac{1}{2}k\chi^2, \quad (2.14)$$

where k is the spring constant and χ is the extension from its equilibrium length. Using this formula, the potential energy for each spring is defined as

$$V_{s_1} = \frac{1}{2}k_1 \left[u_1(x_1, y_1) - u_r(z_{r_1}) \right]^2 \quad (2.15)$$

and

$$V_{s_2} = \frac{1}{2}k_2 \left[u_r(z_{r_2}) - u_2(x_2, y_2) \right]^2. \quad (2.16)$$

In the case of our model, the values of z_{r_1} and z_{r_2} are fixed: these are the top of the rod ($z_{r_1} = L$) and the bottom of the rod ($z_{r_2} = 0$). However, the location on the plates where the axial springs are connected can of course vary. This models the location at which the soundpost is fixed between the plates. For the front plate, this is given by (x_1, y_1) and for the back plate this is given by (x_2, y_2) .

We need to explicitly define the kinetic and potential energy in terms of the generalised coordinates before we can apply Lagrange's equations. The steps required to do this will now be briefly laid out.

Kinetic energy

To calculate T_1 and T_2 , we substitute the plate displacement function, Equation 2.8, into the expression for the kinetic energy of a plate, Equation 2.6, and evaluate the integrals. Notice that our displacement function involves two summations, which are then squared when substituted into the kinetic energy expression. As a simple example of how this is handled, we will consider the case of $N_i = 2$. Working through this example we will see that many terms go to zero. First, consider that

$$\gamma = \left(\frac{\partial u(x, y, t)}{\partial t} \right)^2 \quad (2.17)$$

and

$$u(x, y, t) = \sum_{p=1}^2 \sum_{q=1}^2 \alpha^{pq}(t) \psi_p(x) \phi_q(y), \quad (2.18)$$

where

$$\psi_p(x) = \sin\left(\frac{p\pi x}{a}\right) \quad \text{and} \quad \phi_q(y) = \sin\left(\frac{q\pi y}{b}\right). \quad (2.19)$$

Therefore:

$$\gamma = \left(\sum_{p=1}^2 \sum_{q=1}^2 \dot{\alpha}^{pq} \psi_p \phi_q \right)^2, \quad (2.20)$$

$$\gamma = \left(\dot{\alpha}^{(1,1)} \psi_1 \phi_1 + \dot{\alpha}^{(1,2)} \psi_1 \phi_2 + \dot{\alpha}^{(2,1)} \psi_2 \phi_1 + \dot{\alpha}^{(2,2)} \psi_2 \phi_2 \right)^2. \quad (2.21)$$

Expanding this, we obtain four ‘squared’ terms: $(\dot{\alpha}^{(1,1)} \psi_1 \phi_1)^2$, $(\dot{\alpha}^{(1,2)} \psi_1 \phi_2)^2$, $(\dot{\alpha}^{(2,1)} \psi_2 \phi_1)^2$ and $(\dot{\alpha}^{(2,2)} \psi_2 \phi_2)^2$. In addition, we obtain 12 ‘cross-terms’. When we evaluate the integral

$$I = \int_0^a \int_0^b \gamma \, dx \, dy, \quad (2.22)$$

due to the orthogonality of sine functions, these ‘cross-terms’ will equal zero. Formally, we can write

$$\int_0^a \psi_n(x) \psi_m(x) \, dx = \begin{cases} 0, & n \neq m \\ \frac{a}{2}, & n = m \end{cases} \quad (2.23)$$

and

$$\int_0^b \phi_n(y) \phi_m(y) \, dy = \begin{cases} 0, & n \neq m \\ \frac{b}{2}, & n = m. \end{cases} \quad (2.24)$$

Therefore, the kinetic energy for each plate is given by

$$T_1 = \frac{1}{2} h_1 \rho_1 \left(\frac{a_1}{2} \right) \left(\frac{b_1}{2} \right) \sum_{p=1}^{N_1} \sum_{q=1}^{N_1} (\dot{\alpha}_1^{pq})^2 \quad (2.25)$$

and

$$T_2 = \frac{1}{2} h_2 \rho_2 \left(\frac{a_2}{2} \right) \left(\frac{b_2}{2} \right) \sum_{p=1}^{N_2} \sum_{q=1}^{N_2} (\dot{\alpha}_2^{pq})^2. \quad (2.26)$$

For T_r , we substitute Equation 2.11 into the expression of kinetic energy for the rod, Equation 2.9.

We need to take particular care of when $p = 0$. When integrating the cosine term we obtain

$$\int_0^L \cos\left(\frac{p\pi z}{L}\right) dz = \begin{cases} L, & p = 0 \\ \frac{L}{2}, & p \geq 1. \end{cases} \quad (2.27)$$

Therefore, the kinetic energy of the rod is given by

$$T_r = \frac{1}{2} \rho A L (\dot{\alpha}_r^0)^2 + \frac{1}{2} \rho A \left(\frac{L}{2} \right) \sum_{p=1}^{N_r-1} (\dot{\alpha}_r^p)^2. \quad (2.28)$$

Potential energy

To calculate V_1 and V_2 , we substitute the plate displacement function, Equation 2.8, into the expression of potential energy for the plate, Equation 2.1. For V_1 we have

$$V_1 = \frac{h_1^3}{2} \left(\frac{a_1}{2} \right) \left(\frac{b_1}{2} \right) \sum_{p=1}^{N_1} \sum_{q=1}^{N_1} (\alpha_1^{pq})^2 \left[D_1^{(1)} \left(\frac{p\pi}{a_1} \right)^4 + D_3^{(1)} \left(\frac{q\pi}{b_1} \right)^4 + \left(D_2^{(1)} + D_4^{(1)} \right) \left(\frac{p\pi}{a_1} \right)^2 \left(\frac{q\pi}{b_1} \right)^2 \right] \quad (2.29)$$

and for V_2 we have

$$V_2 = \frac{h_2^3}{2} \left(\frac{a_2}{2} \right) \left(\frac{b_2}{2} \right) \sum_{p=1}^{N_2} \sum_{q=1}^{N_2} (\alpha_2^{pq})^2 \left[D_1^{(2)} \left(\frac{p\pi}{a_2} \right)^4 + D_3^{(2)} \left(\frac{q\pi}{b_2} \right)^4 + \left(D_2^{(2)} + D_4^{(2)} \right) \left(\frac{p\pi}{a_2} \right)^2 \left(\frac{q\pi}{b_2} \right)^2 \right]. \quad (2.30)$$

To calculate V_r , we substitute the rod displacement function, Equation 2.11, into the expression of potential energy for the rod, Equation 2.10, which gives

$$V_r = \frac{1}{2}EA \left(\frac{L}{2}\right) \sum_{p=0}^{N_r-1} (\alpha_r^p)^2 \left(\frac{p\pi}{L}\right)^2. \quad (2.31)$$

To calculate the potential energy for the springs we simply substitute equations 2.8 and 2.11 into equations 2.15–2.16. The next step is to use Lagrange's equations to express the equations of motion of the system, written in terms of mass and stiffness matrices.

2.2.4 Solving the equation of motion

At this stage, it is convenient to write the generalised coordinates in vector form such that

$$\boldsymbol{\alpha} = \left[\begin{array}{c} \alpha_1^{(1,1)} \\ \vdots \\ \alpha_1^{(N_1, N_1)} \\ \alpha_r^{(0)} \\ \vdots \\ \alpha_r^{N_r-1} \\ \alpha_2^{(1,1)} \\ \vdots \\ \alpha_2^{(N_2, N_2)} \end{array} \right] \left. \begin{array}{l} \left. \begin{array}{l} \text{Plate 1} \end{array} \right\} \\ \left. \begin{array}{l} \text{Rod} \end{array} \right\} \\ \left. \begin{array}{l} \text{Plate 2} \end{array} \right\} \end{array} \right\} N_1^2 + N_r + N_2^2 \quad (2.32)$$

In terms of this vector, and assuming small motions in all generalised coordinates, we can express the kinetic energy and potential energy in terms of a mass matrix, \mathbf{M} , and a stiffness matrix, \mathbf{K} . The equation of motion

$$\mathbf{M}\ddot{\boldsymbol{\alpha}} + \mathbf{K}\boldsymbol{\alpha} = 0 \quad (2.33)$$

is obtained for free motion of our system. Note that the vector $\boldsymbol{\alpha}$ is equal in length to the number of degrees of freedom of the system. A modal solution is sought, so we assume that

$$\boldsymbol{\alpha} = \mathbf{A}e^{i\omega t}. \quad (2.34)$$

Substituting equation 2.34 into 2.33 gives

$$[\mathbf{K} - \omega^2\mathbf{M}]\mathbf{A} = 0. \quad (2.35)$$

This is a classic eigenvalue problem. The solution $\mathbf{A} = 0$ can be ignored, as this implies there is no motion at all. Therefore, a solution for finite \mathbf{A} needs to be obtained. This occurs when $[\mathbf{K} - \omega^2\mathbf{M}]$ is not invertible. If we could calculate an inverse, then premultiplying Equation 2.35 by this inverse would result in the trivial solution $\mathbf{A} = 0$. The requirement for a matrix not to be invertible is that its determinant must be equal to zero. Therefore, we must solve

$$\det[\mathbf{K} - \omega^2\mathbf{M}] = 0. \quad (2.36)$$

The roots of this equation (the eigenvalues of Equation 2.35) give us $\omega_1^2, \omega_2^2, \dots, \omega_{N_T}^2$, the squared natural frequencies of the system. Using these eigenvalues, we can calculate the eigenvectors \mathbf{A} . For large multiple-degree-of-freedom systems like ours, this problem can be easily solved using the MATLAB function `eig`.

2.2.5 Orthogonality of eigenvectors

Since \mathbf{K} and \mathbf{M} are symmetric, the eigenvectors \mathbf{A} are orthogonal with respect to both the mass and stiffness matrices. Any scalar multiple of the eigenvectors \mathbf{A} are also valid eigenvectors. We choose to normalise the eigenvectors with respect to the mass matrix, known as ‘mass-normalisation’. The normalised eigenvectors, written $\tilde{\mathbf{A}}$, thus satisfy:

$$\tilde{\mathbf{A}}^{(n)\top}\mathbf{M}\tilde{\mathbf{A}}^{(m)} = \begin{cases} 0, & n \neq m, \\ 1, & n = m, \end{cases} \quad (2.37)$$

and

$$\tilde{\mathbf{A}}^{(n)\top}\mathbf{K}\tilde{\mathbf{A}}^{(m)} = \begin{cases} 0, & n \neq m, \\ \omega_n^2, & n = m. \end{cases} \quad (2.38)$$

2.2.6 Calculating the displacement for a given mode

The steps required to calculate the displacement for a given mode, n , will now be briefly laid out. For a given modal frequency of the system, ω_n , there is an associated eigenvector $\tilde{\mathbf{A}}^{(n)}$. As an example, to calculate the mass-normalised displacement of plate 1 for a given mode, n , recall that

$$\tilde{\mathbf{u}}_1^{(n)}(x, y) = \sum_{p=1}^{N_1} \sum_{q=1}^{N_1} \alpha_1^{pq} \sin\left(\frac{p\pi x}{a_1}\right) \sin\left(\frac{q\pi y}{b_1}\right). \quad (2.39)$$

We can substitute in values for α_1^{pq} , from the eigenvector associated with mode n . These take the form

$$\alpha_1^{pq} = \begin{bmatrix} \tilde{\mathbf{A}}^{(n)(1,1)} \\ \tilde{\mathbf{A}}^{(n)(2,1)} \\ \vdots \\ \tilde{\mathbf{A}}^{(n)(N_1,N_1)} \end{bmatrix} e^{i\omega_n t}. \quad (2.40)$$

2.2.7 Calculating the admittance

A classic vibration calculation, which will be used extensively throughout this thesis, is to probe the velocity at a given point on a structure in response to a harmonic force of unit amplitude and frequency ω , a quantity called the admittance, H , (also known as the mobility) which is defined as the velocity per unit force:

$$H(\omega) = \frac{V(\omega)}{F(\omega)}. \quad (2.41)$$

We can calculate the admittance of a vibrating structure by summing the contributions of all the modes, using the standard formula (see Skudrzyk, 1968, ch. 11, and Hodges and Woodhouse, 1986)

$$H(\mathbf{r}_j, \mathbf{r}_k, \omega) = i\omega \sum_{n=1}^N \frac{\tilde{\mathbf{u}}^{(n)}(\mathbf{r}_j) \tilde{\mathbf{u}}^{(n)}(\mathbf{r}_k)}{\omega_n^2 + 2i\omega\omega_n\zeta_n - \omega^2}. \quad (2.42)$$

The coordinates of the ‘measurement point’ are written here as \mathbf{r}_j and the ‘driving point’ as \mathbf{r}_k . Note that if $\mathbf{r}_j = \mathbf{r}_k$, the result is referred to as the driving point admittance. An important property of Equation 2.42 is that it is symmetric in j and k . The response obtained at j when driving at k is identical if these points are reversed. This is known as the reciprocal theorem (see Woodhouse, 1995). The modal damping factor ζ_n is related to the modal Q -factor by $Q = 1/2\zeta_n$. Following Woodhouse (2005), we will use a value of $Q = 50$, for all modes.

2.2.8 Adding soundpost bending to the model

So far we have considered the soundpost’s axial motion only. We now introduce bending motion. To account for bending in both the x and y directions, we will model two beams, one for each direction. Figure 2.5 shows an illustration of this set-up. Figure 2.6 shows a diagram defining the model for a bending beam moving in the x direction.

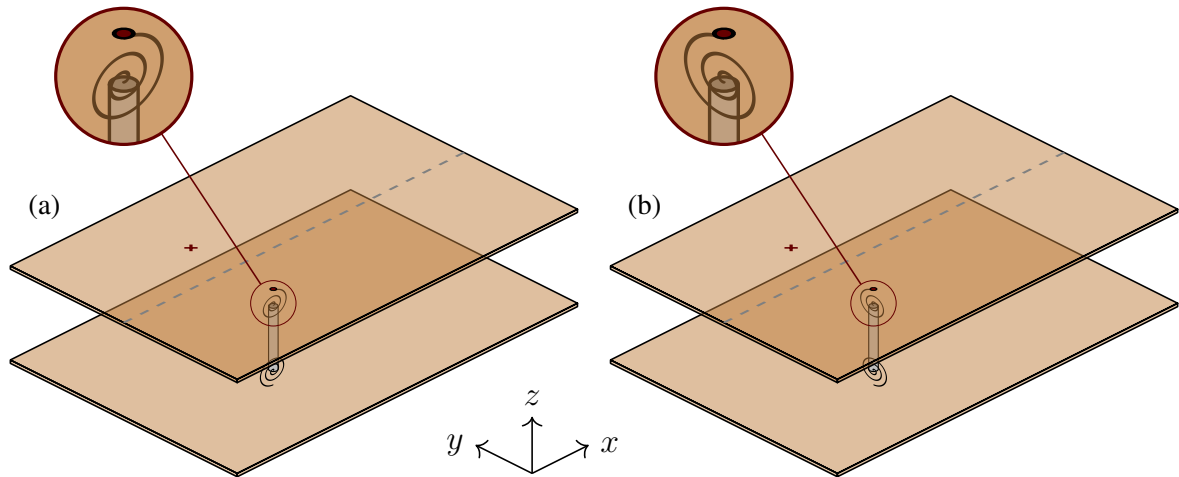


Figure 2.5: Two diagrams showing how the soundpost, modelled as a bending beam with torsional springs at either end, is positioned within the plates.

Bending vibration of an Euler beam

Consider the soundpost as a pinned–pinned beam. The kinetic energy of a beam in the x and y directions, T_b^x and T_b^y , is given by

$$T_b^x = \frac{1}{2} \rho A \int_0^L \left(\frac{\partial u_b^x}{\partial t} \right)^2 dx \quad (2.43)$$

and

$$T_b^y = \frac{1}{2} \rho A \int_0^L \left(\frac{\partial u_b^y}{\partial t} \right)^2 dy, \quad (2.44)$$

where ρ is the density, A is the cross-sectional area and L is the length of the beam. Similarly, the potential energy, V , of a beam is expressed as

$$V_b^x = \frac{1}{2} EI \int_0^L \left(\frac{\partial^2 u_b^x}{\partial x^2} \right)^2 dx \quad (2.45)$$

and

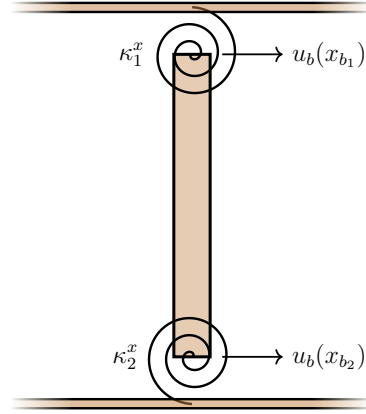
$$V_b^y = \frac{1}{2} EI \int_0^L \left(\frac{\partial^2 u_b^y}{\partial y^2} \right)^2 dy, \quad (2.46)$$

where E is the elastic modulus and I is the second moment of area. For a beam with a circular cross-section with radius r , $I = \pi r^4/4$.

The motion of the beam for displacement in the x and y directions can be written as

$$u_b^x(x, t) = \sum_{p=1}^{N_b} \alpha_{b_x}^p \sin\left(\frac{p\pi x}{L}\right) \quad (2.47)$$

Figure 2.6: A diagram showing the side-on view of two rectangular plates with a beam and two torsional springs connecting the two plates. This particular diagram shows the beam associated with vibration in the x direction.



and

$$u_b^y(y, t) = \sum_{p=1}^{N_b} \alpha_{b_y}^p \sin\left(\frac{p\pi y}{L}\right). \quad (2.48)$$

Potential energy of the torsional springs

The potential energy of a torsional spring with stiffness κ is given by

$$V = \frac{1}{2} \kappa \theta^2, \quad (2.49)$$

where θ is the angle of twist from the equilibrium position. In the case of our model, we are interested in the potential energy stored in the spring which is held between the plate and rod. We have springs in the x and y directions at both ends of the beam giving a total of four potential energy expressions. These are given by

$$V_{\kappa_1}^x = \frac{1}{2} \kappa_1^x \left[\theta_1^x(x_1, y_1) - \theta_b^x(x_{b_1}) \right]^2 = \frac{1}{2} \kappa_1^x \left[\frac{\partial u_1(x_1, y_1)}{\partial x} - \frac{\partial u_b^x(x_{b_1})}{\partial x} \right]^2, \quad (2.50)$$

$$V_{\kappa_1}^y = \frac{1}{2} \kappa_1^y \left[\theta_1^y(x_1, y_1) - \theta_b^y(y_{b_1}) \right]^2 = \frac{1}{2} \kappa_1^y \left[\frac{\partial u_1(x_1, y_1)}{\partial y} - \frac{\partial u_b^y(y_{b_1})}{\partial y} \right]^2, \quad (2.51)$$

$$V_{\kappa_2}^x = \frac{1}{2} \kappa_2^x \left[\theta_b^x(x_{b_2}) - \theta_2^x(x_2, y_2) \right]^2 = \frac{1}{2} \kappa_2^x \left[\frac{\partial u_b^x(x_{b_2})}{\partial x} - \frac{\partial u_2(x_2, y_2)}{\partial x} \right]^2 \quad (2.52)$$

and

$$V_{\kappa_2}^y = \frac{1}{2} \kappa_2^y \left[\theta_b^y(y_{b_2}) - \theta_2^y(x_2, y_2) \right]^2 = \frac{1}{2} \kappa_2^y \left[\frac{\partial u_b^y(y_{b_2})}{\partial y} - \frac{\partial u_2(x_2, y_2)}{\partial y} \right]^2. \quad (2.53)$$

Kinetic energy of the beam

The kinetic energy of the beam is calculated by substituting Equations 2.47–2.48 into Equations 2.43–2.44. For the case of x direction bending

$$T_b^x = \frac{1}{2} \rho A \sum_{p=1}^{N_b} (\dot{\alpha}_{b_x}^p)^2 \left(\frac{L}{2} \right). \quad (2.54)$$

Potential energy of the beam

The potential energy of the beam can be calculated in a similar manner by substituting the beam displacement functions into Equations 2.45–2.46. The final result, shown here for the x displacement beam, is given by

$$V_b^x = \frac{1}{2} EI \sum_{p=1}^{N_b} (\alpha_{b_x}^p)^2 \left(\frac{p\pi}{L} \right)^4 \left(\frac{L}{2} \right). \quad (2.55)$$

We can combine these terms for bending motion into our mass and stiffness matrices from the previous section. The vector of generalised coordinates now reads

$$\alpha = \left[\begin{array}{c} \alpha_1^{(1,1)} \\ \vdots \\ \alpha_1^{(N_1, N_1)} \\ \alpha_{b_x}^{(1)} \\ \vdots \\ \alpha_{b_x}^{N_b} \\ \alpha_{b_y}^{(1)} \\ \vdots \\ \alpha_{b_y}^{N_b} \\ \alpha_r^{(0)} \\ \vdots \\ \alpha_r^{N_r-1} \\ \alpha_2^{(1,1)} \\ \vdots \\ \alpha_2^{(N_2, N_2)} \end{array} \right] \left. \begin{array}{l} \left. \begin{array}{l} \text{Plate 1} \\ \text{Beam } x \end{array} \right\} \\ \left. \begin{array}{l} \text{Beam } y \\ \text{Rod} \end{array} \right\} \\ \left. \begin{array}{l} \text{Plate 2} \end{array} \right\} \end{array} \right\} N_1^2 + 2N_b + N_r + N_2^2 \quad (2.56)$$

2.3 Choosing the model parameters

The final step to complete our model is to determine what values to use for the various model parameters. We need to choose values for the size of the plates and the soundpost, as well as values for the material properties of these parts.

2.3.1 The properties of the plate

In determining the properties of the plates used in our model — their dimensions, density, and elastic constants — we have followed Woodhouse (2005). Our model uses rectangular plates, the dimensions of which will be guided by the dimensions of real violin plates. The length, a_i , can be straightforwardly assigned as the distance from the saddle to the point at which the neck joins the body. The width, b_i , is less obvious because of the curved outline of the violin, but we have chosen the point of maximum width. Unlike real violin plates, the rectangular plates in our model have a fixed thickness, arrived at by averaging the thickness of real front and back violin plates. The two woods typically used to make the body of the instrument are maple (for the back plate) and spruce (for the front plate), and the model takes suitable values for these wood densities from published data. The plates that have been used in the model are orthotropic. We have defined the stiffness of the plates in terms of four elastic constants: D_1^i , D_2^i , D_3^i and D_4^i . As with the density, we can obtain values for these constants from published data. A table of the plate properties is given in Table 2.1.

Table 2.1: Properties of the plates used in our theoretical model.

Property	Plate 1			Plate 2		
	Symbol	Value	Unit	Symbol	Value	Unit
Length	a_1	321	mm	a_2	321	mm
Width	b_1	204	mm	b_2	204	mm
Thickness	h_1	2.9	mm	h_2	4.0	mm
Density	ρ_1	420	kg m ⁻³	ρ_2	650	kg m ⁻³
Elastic Constants	$D_1^{(1)}$	1100	MPa	$D_1^{(2)}$	860	MPa
	$D_2^{(1)}$	67	MPa	$D_2^{(2)}$	140	MPa
	$D_3^{(1)}$	84	MPa	$D_3^{(2)}$	170	MPa
	$D_4^{(1)}$	230	MPa	$D_4^{(2)}$	230	MPa

2.3.2 The properties of the soundpost

The soundpost, in a geometrical sense, closely resembles a cylindrical rod of wood. The exact length and radius of the soundpost varies slightly from instrument to instrument. The length is dependent on the distance between the front and back plates and also on how tightly the maker fits the soundpost between the plates. In our model, making an adjustment to the length does not affect the coupling between the soundpost and the plates, as the stiffnesses of the axial and bending springs used to couple the soundpost and plates are set independently from the soundpost's length. Additionally, we choose to neglect tension in the plates and damping at the contact between the soundpost and plates. For the purposes of our model, it is therefore sufficient to choose a length which represents an average soundpost length. In a real violin, it is the radius of the soundpost that primarily determines how much wood-to-wood contact there is between it and the plates. Although wood-to-wood contact is not included in our simplified model, the radius of the soundpost is relevant in determining the cross-sectional area of the soundpost and therefore the second moment of area, which influences the bending modes. The values used for the density and Young's modulus of the soundpost were informed based on experimental findings in Chapter 7. A table of the soundpost properties is given in Table 2.2.

Table 2.2: Properties of the soundpost used in our theoretical model.

Property	Soundpost		
	Symbol	Value	Unit
Length	L	60	mm
Radius	r	2.75	mm
Density	ρ	500	kg m ⁻³
Young's Modulus	E	4	GPa

2.4 Testing the model

We will now undertake some preliminary tests of the model to verify its validity. As a simple first test, all coupling between the plates and soundpost will be removed. The uncoupled behaviour of the plates and soundpost is then straightforward to verify. Following this, we will make the axial and bending springs stiff and verify the coupled behaviour.

2.4.1 No coupling between the plates and soundpost

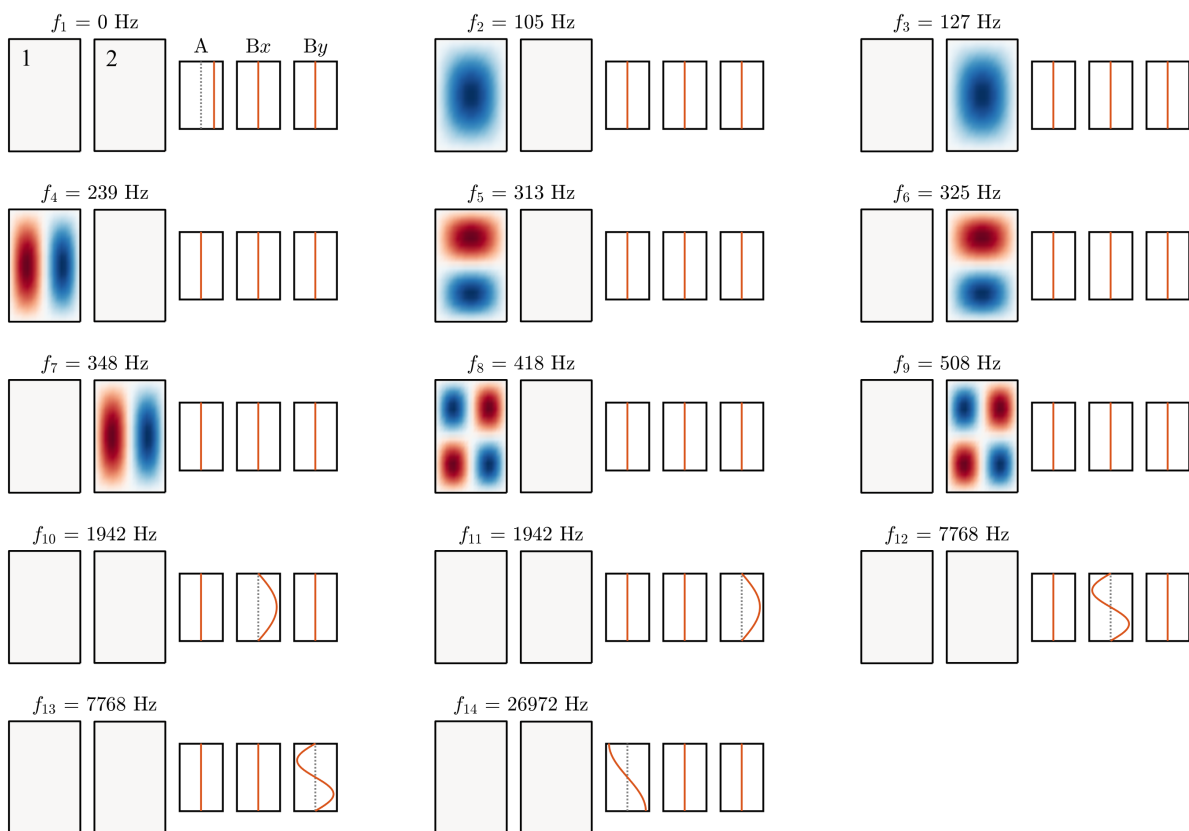


Figure 2.7: A plot of the modes obtained when there is no coupling between the soundpost and the plates. Each subplot shows both plate mode shapes and the three soundpost modes: axial (A), bending in the x direction (Bx) and bending in the y direction (By). The red and blue colours on the plate plots indicate areas of opposite phase. As there is no coupling between the soundpost and plates, diagrams f_2 – f_9 show displacement in the plates only, while the soundpost remains static. f_{10} and f_{11} show the first soundpost bending modes in the x and y directions, which occur at the same frequency. The first axial mode is seen in f_{14} , where the longitudinal displacement is plotted using a transverse representation. Note that f_1 shows the rigid body motion of the soundpost at 0 Hz.

To uncouple the plates and soundpost, the stiffnesses of the axial and bending springs joining them have been set to zero. The results of this simulation are shown in Figure 2.7. For simplicity, only a few modes for each subsystem³ have been calculated. At each mode frequency obtained from the calculation, the mode shapes of all the subsystems are plotted. But, because the subsystems are all uncoupled in this simulation, the result is that each mode frequency corresponds to motion in only one subsystem. This can be verified in Figure 2.7. At $f_1 = 0$ Hz, the rigid-body mode of the soundpost is observed. Mode frequencies f_2 – f_9 show the lowest four plate modes for each plate. The front plate (modelled on spruce) has lower mode frequencies than the equivalent modes for the back plate (modelled on maple). These results compare well with real violin plates, as the uncoupled back plate has higher mode frequencies than the uncoupled front plate. At f_{10} and above, we can observe the uncoupled soundpost bending and axial modes.

2.4.2 The plates and soundpost coupled

To couple the plates and soundpost, the stiffnesses of the axial and bending springs have been set to a finite value. The results of this simulation are shown in Figure 2.8. The values of axial and bending spring stiffness have been chosen based on further results in Chapter 3, and represent what can be described as ‘stiff’ coupling between the plates and soundpost. As can be seen in Figure 2.8, the coupled behaviour is clearly visible. The location of the soundpost, (x_S, y_S) , was chosen so that it aligns with no significant nodal point on the plate. Therefore, $x_S = a_1/\pi$ and $y_S = b_1/\pi$ was chosen. Additionally, in order to achieve sufficient mode convergence, a large number of plate modes have been included in the calculation: see Section 2.5 for details.

Looking at the plate mode shapes, we can observe two main types of behaviour. In the first, the motion of the front and back plates is coupled together, such as $f_1 = 122$ Hz; in the second, the soundpost acts like a constraint and causes the plates to vibrate around a point, for example $f_2 = 169$ Hz. The orange line in the three soundpost plots show that there is now displacement observed in the soundpost modes. However, the blue line, which is the displacement scaled to the maximum value obtained in the calculation, shows that at low frequencies this displacement is small.

2.4.3 Comparison to Schelleng’s model

In Section 1.5.2, research on the soundpost by Schelleng (1971) was introduced. The violin body model used by Schelleng is similar to our model in that it considers the plates as flat rectangular

³‘Subsystem’ here refers to the physical parts which make up the model. These are: the two plates, the soundpost as an axial rod, and the soundpost as a bending beam (in 2 directions). This makes a total of five subsystems.

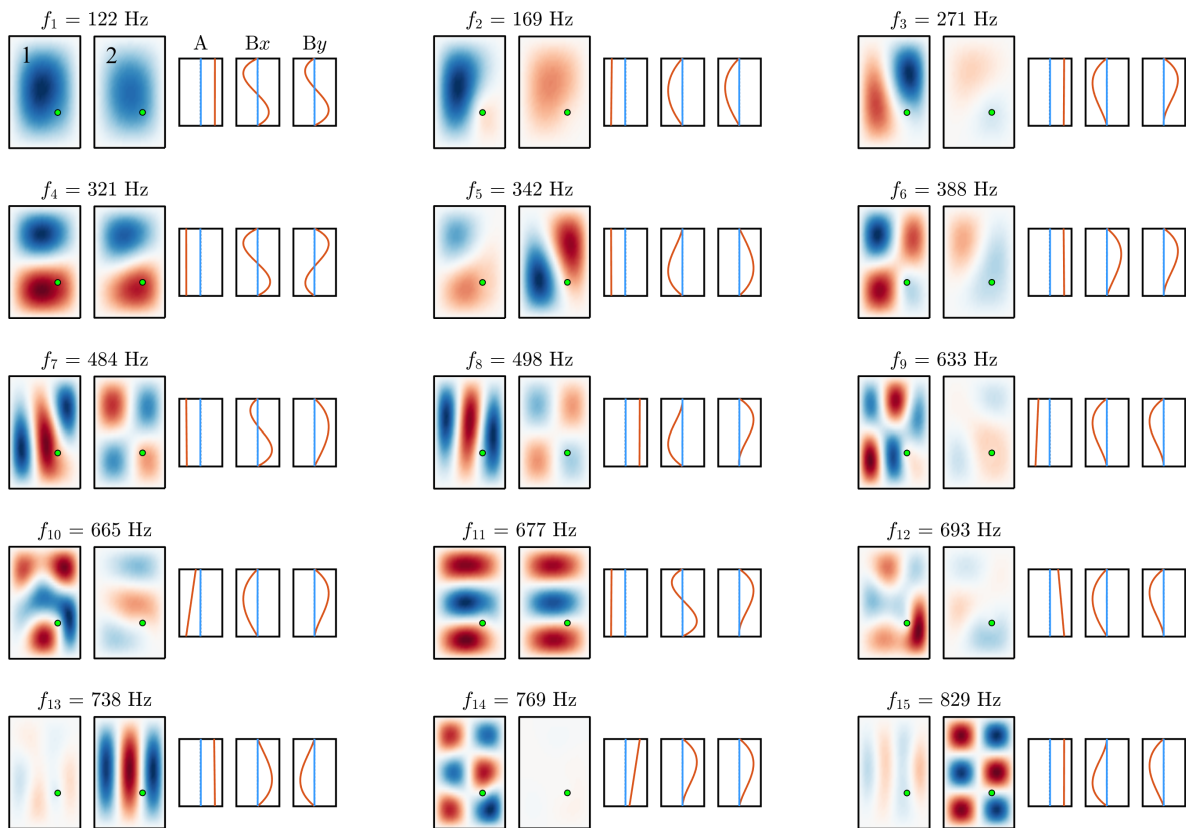


Figure 2.8: A plot of the modes obtained when there is coupling between the soundpost and the plates. Each subplot shows both plate mode shapes and the three soundpost modes: axial (A), bending in the x direction (Bx) and bending in the y direction (By). The red and blue colours on the plate plots indicate areas of opposite phase. For axial modes (A), the mode shape is visualised in the x - y plane. For the three soundpost mode shape plots, the blue line shows the displacement scaled to the maximum value obtained in the calculation. The orange line shows the displacement individually scaled to the size of the displayed axes. The green circle shows the location of the soundpost.

plates. However, Schelleng considered the back plate to be infinitely stiff. Using this model, Schelleng was able to demonstrate that the addition of an off-set rigid link between the two plates results in the combination of two previously uncoupled modes in the front plate. His result is shown in Figure 1.10. We will now attempt to reproduce Schelleng's result. To replicate the rigid link soundpost used by Schelleng, the coupling spring stiffnesses are set to a large value. The axial and bending modes of the soundpost fall outside of the frequency range we are interested in. As in Schelleng's model, the back plate has been made infinitely stiff. Figure 2.9 shows our result. This shows agreement with Schelleng (1971): the addition of the soundpost causes the two lowest modes in the front plate to combine and form a new mode.

Schelleng (1971) describes the back plate as having a small contribution to the overall acoustics of the instrument. He therefore concluded that it was reasonable to neglect any

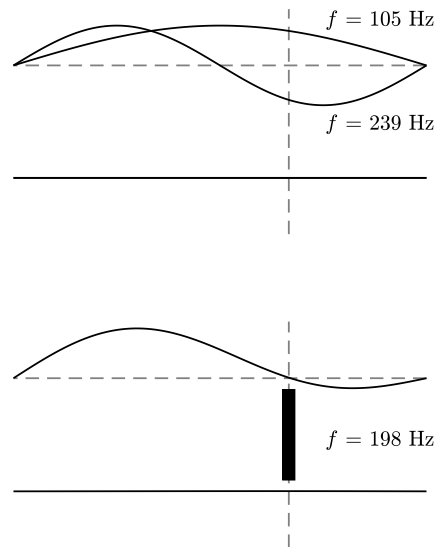


Figure 2.9: A comparison to Figure 1.10. In this simulation, the back plate has been made infinitely stiff. *Top:* the two lowest modes of the uncoupled front plate. *Bottom:* with the addition of a rigid soundpost, the two uncoupled modes are combined to make one new mode. This shows very good agreement with Schelleng (1971).

contribution from the back plate, which he achieved by making it infinitely stiff. However, in our model, using the back plate parameters we have determined, the back plate has mode frequencies which lie close to the mode frequencies of the front plate. As shown in Figure 2.7, the lowest mode of the back plate, $f_3 = 127$ Hz, occurs at a frequency between the two lowest modes of the front plate. This challenges Schelleng's view that the back plate can be treated as being infinitely stiff. If we re-run our simulation, without an infinitely stiff back plate, then we see a different set of results. These results are shown in Figure 2.10. There is now an extra back plate mode in between the two lowest front plate modes. Therefore, we obtain a different set of coupled modes. The first has the front and back plates coupling in phase with each other, and the second has the lowest mode of the back plate coupled to the second lowest mode of the front plate.

2.5 Convergence checks

We will briefly consider the subject of convergence: how many shape functions are required when running the calculations to ensure that the mode frequencies are sufficiently converged? In practice, this refers to the value given to the variables N_i , N_b and N_r . First and foremost, the values of N_i , N_b and N_r need to be large enough so that we can calculate all the modes within the frequency range we are interested in. Once that is established, then we must make sure that those modes are sufficiently converged. Ultimately, increasing the number of plate and soundpost modes is always beneficial to the accuracy of the calculated values. However, increasing the

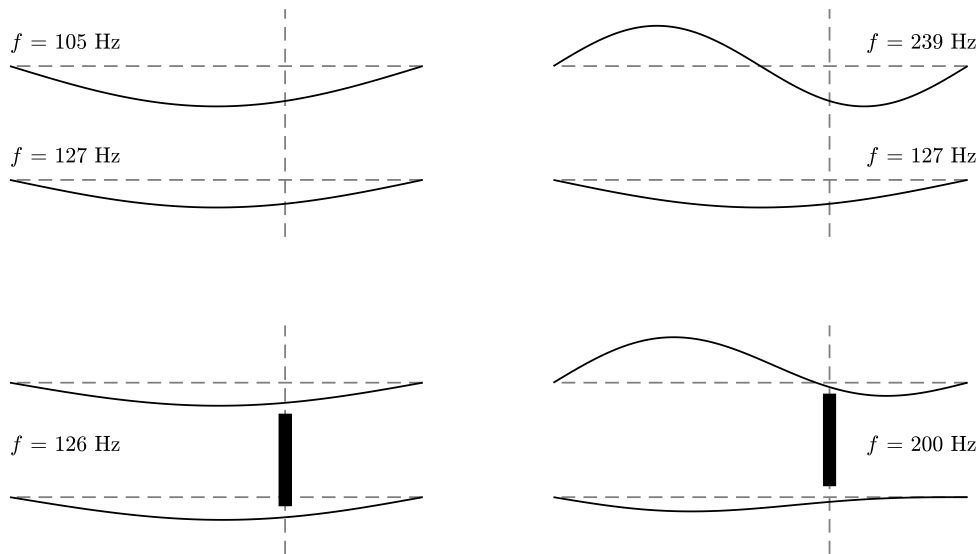


Figure 2.10: A reproduction of Figure 2.9 without an infinitely stiff back plate. The solid lines show a cross-section through the front and back plates. The horizontal dashed lines show the position of the plates at rest, while the vertical dashed line highlights the position where the soundpost would like. The thick solid black bar represents the soundpost and shows that it is present in the calculation that generates the two lower diagrams. Without an infinitely stiff back plate, a new back plate mode, $f = 127$ Hz, causes a different set of coupled modes to be obtained when a rigid soundpost is added.

number of modes increases the amount of computation required. It is therefore desirable to find a sufficient compromise between accuracy of the values and computation time. At a certain point, the values of N_i , N_b and N_r become large enough that the change in modal frequency caused by additional modes is negligible.

As the soundpost mode frequencies generally fall in a much higher frequency range than the plate modes, it is easy to calculate enough soundpost modes to obtain suitable mode convergence. Setting N_r and N_b to 10 was shown to be sufficient. Therefore, our focus in this section will be with choosing a suitable value for N_i , which will determine the number of assumed shape functions in the plates.

2.5.1 How to compare modes

Using different values of N_i , N_b and N_r in our simulation naturally returns eigenvector matrices of different sizes. Therefore, it is not trivial to directly compare modes obtained from different calculations, as there is no immediate way of knowing which modes are related to each other. A method to address this problem is therefore needed. Our solution was to first calculate a benchmark set of eigenvectors using a suitably high value of N_i . Then, smaller values of N_i were processed and the results from these calculations compared to the benchmark case.

The similarity of two modes can be calculated by determining their cosine similarity, $\cos(\theta)$. For two generic vectors, \mathbf{A} and \mathbf{B} , with length M , the cosine similarity is calculated by

$$\cos(\theta) = \frac{\mathbf{A} \cdot \mathbf{B}}{\|\mathbf{A}\| \|\mathbf{B}\|} = \frac{\sum_{i=1}^M A_i B_i}{\sqrt{\sum_{i=1}^M A_i^2} \sqrt{\sum_{i=1}^M B_i^2}}. \quad (2.57)$$

If the two vectors \mathbf{A} and \mathbf{B} are exactly equal, then $\cos(\theta) = 1$. If the two vectors are orthogonal to each other, then $\cos(\theta) = 0$. If we take one eigenvector from a given calculation, and calculate its cosine similarity with every eigenvector from the benchmark case, then we can find the mode it is most similar to and then compare the two. We can compare both the mode shapes, from the eigenvectors, and also the mode frequencies, by comparing the corresponding eigenvalues.

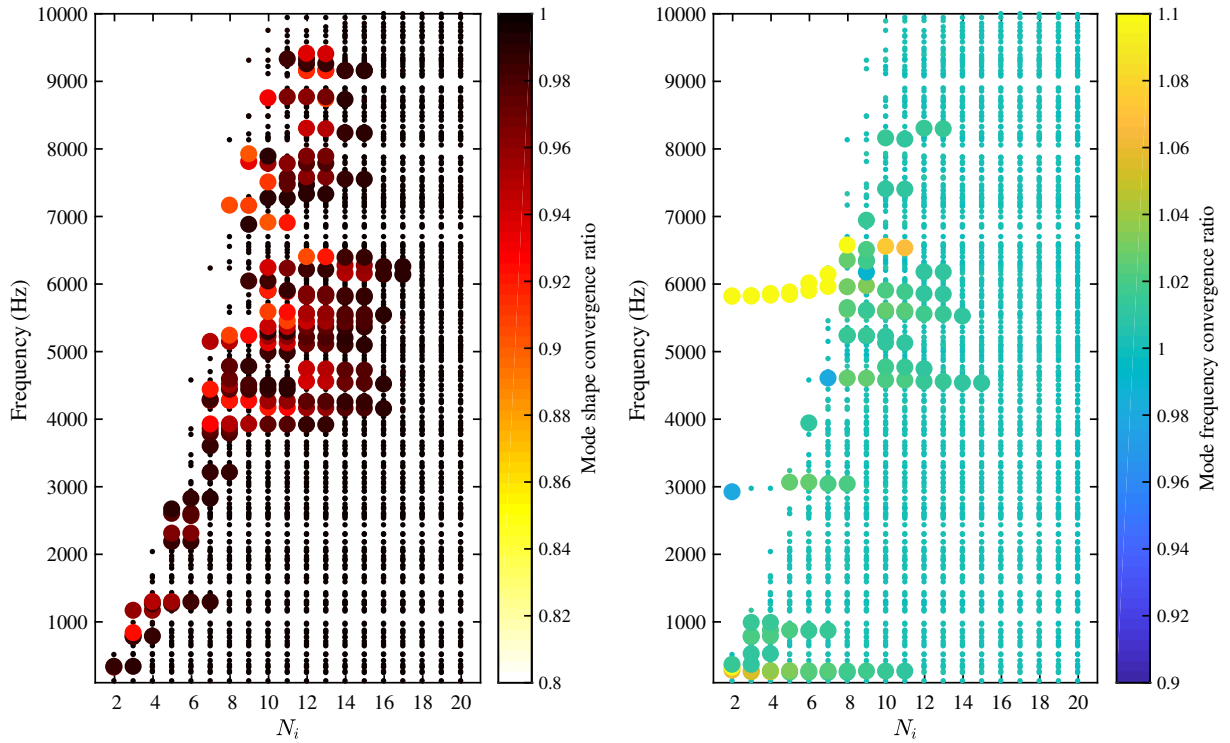


Figure 2.11: *Left:* A graph showing how the mode shape convergence ratio changes as the value of N_i is increased. Once the ratio is sufficiently close to 1, then small markers are plotted. *Right:* A similar plot, but this time mode frequency convergence is plotted. Note that the scale is different because frequencies that are being compared can either be higher or lower than the benchmark. Once again, if the ratio is sufficiently close to 1, then small markers are plotted.

Figure 2.11 shows our results. The main conclusion to be drawn from these results is that above approximately $N_i = 15$ we can be confident of achieving sufficient mode convergence. We have also found that mode convergence is partly also dependant on the position of the soundpost

within the plates. The results in Figure 2.11 were calculated using a soundpost placed at the length and width divided by π . However, if the soundpost is placed at a ‘rational position’ on the plate — for example, $(\frac{a}{2}, \frac{b}{2})$ — then mode convergence occurs very quickly using low values of N_i .

2.6 Comparison to a real violin

At this stage, it is helpful to compare the results from our model to a measurement taken on a real violin. Figure 2.12 shows two sets of data: one from a real violin and the other from our model. Both sets of data represent an admittance. In the case of the real violin, an accelerometer is placed on the surface of the front plate directly above the position of the soundpost, and an instrumented hammer used to deliver a driving point excitation force. An equivalent theoretical result is calculated using Equation 2.42.

The key feature to take note of is the difference in modal density at low frequencies, below 1000 Hz. As identified by Woodhouse (2005), the reason the ‘flat-plate violin’ model has a higher density of resonances at low frequencies, when compared to a real violin, is likely to be largely a result of its lack of arched plates. Curved shells have low modal density below the “ring frequency”, but at higher frequencies the modal densities of flat plates and curved shells become comparable (see Szechenyi, 1971). This can be verified by comparing the modal densities at frequencies above 1000 Hz, which are similar.

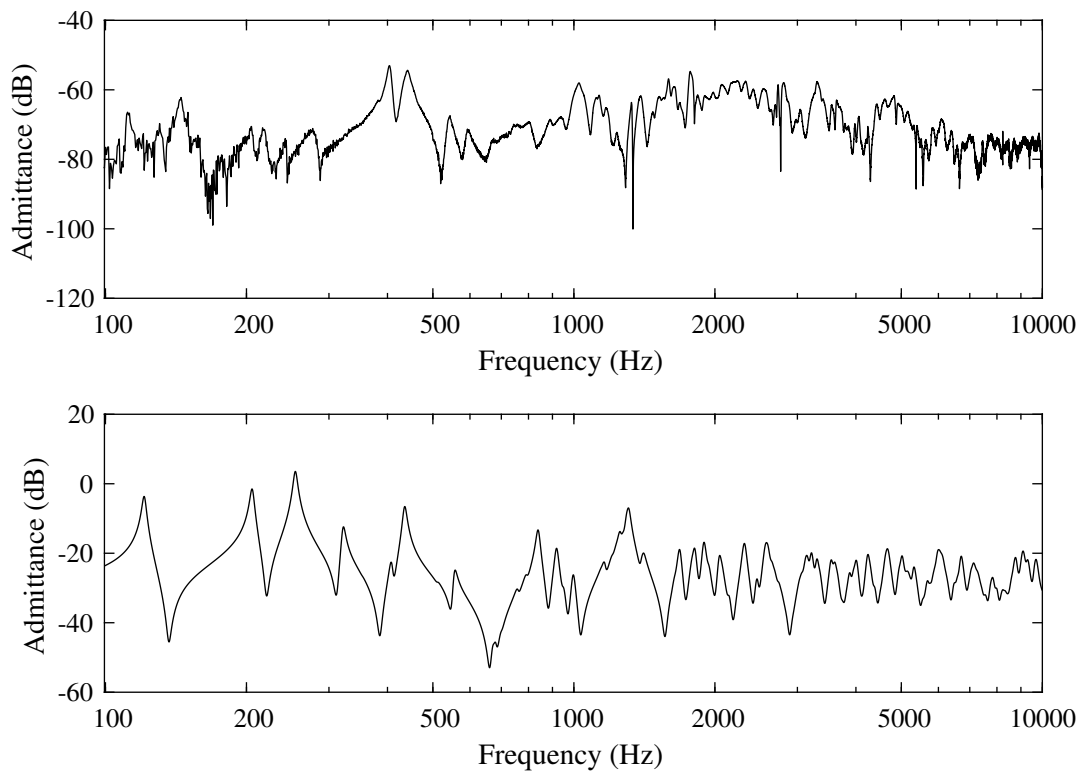


Figure 2.12: *Top:* an admittance measurement from a real violin. An accelerometer was placed on the surface of the front plate directly above the position of the soundpost. An instrumented hammer was used to deliver a driving point excitation force. *Bottom:* an equivalent simulation from the model, using the parameters determined in this chapter.

3

The vibrational behaviour of the soundpost and springs

In the following chapter, we will investigate the influence of axial and bending spring stiffness on the vibration modes of the soundpost and the plates. Our approach will be to calculate the frequency response at various points on the model while the stiffness of the springs in our model is varied. Investigating the axial and bending springs separately, we will be able to determine the range of values of spring stiffness which are relevant to our model, and, in doing so, to better understand the vibrational behaviour of the model. For many violin makers, the coupling stiffness between the soundpost and violin body is one of the most important considerations in their instrument design. The axial and bending springs have been included to model this behaviour, and it is our aim is to provide an insight into the effects of both ‘tightness’ and ‘fit’ of a soundpost.

3.1 The effect of axial spring stiffness on axial soundpost motion

We will now investigate the effect of axial spring stiffness on the axial vibration modes of the soundpost. In all subsequent calculations, the bending spring stiffness, κ , will be set to zero. This effectively de-couples the two ‘bending beam’ soundposts from the plates, leaving only the ‘axial rod’ soundpost. This can be envisaged as a model of an ill-fitted soundpost, contacting the plates only at a single point at each end. As before, we will locate the soundpost at a position between the plates determined by their length and width divided by π . This ensures that we avoid any significant nodal lines, as well as roughly corresponding to the location at which a maker would typically place a soundpost in a real violin. We will study the motion of the soundpost

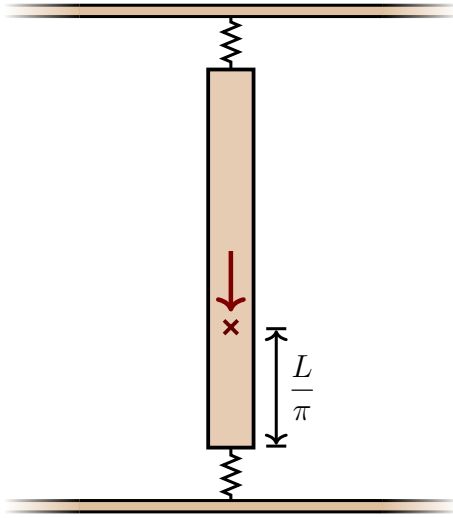


Figure 3.1: A diagram of the axial rod used to model the axial vibration of the soundpost. The excitation point used when computing the axial frequency response is shown by the red cross. This is at a length $\frac{L}{\pi}$ along the rod, to ensure that a nodal point is not probed. The red arrow illustrates that we are simulating a force being applied axially.

by calculating the frequency response at a particular point on the rod. Figure 3.1 illustrates our set-up, which corresponds, in real experimental terms, to applying an axial excitation force at a single point on the rod and measuring the velocity at that same point. For our theoretical model, the admittance can be obtained directly from the mass-normalised displacement using

$$H_r\left(\frac{L}{\pi}, \omega\right) = i\omega \sum_{n=1}^N \frac{\left(\tilde{\mathbf{u}}_r^{(n)}\left(\frac{L}{\pi}\right)\right)^2}{\omega_n^2 + 2i\omega\omega_n\zeta_n - \omega^2}. \quad (3.1)$$

Figure 3.2 shows two examples of this admittance calculation, for two different values of k . We will extend these plots to cover an entire range of spring stiffnesses by plotting these frequency responses as a surface plot. Figure 3.3 shows the admittance plotted as a function of the axial spring stiffness. This graph has many interesting features. We will start by looking at the frequency response at low axial spring stiffness, 10^1 – 10^4 N/m. At low frequency, 50–1000 Hz, we can see a clear mode resonance that increases as the axial spring stiffness increases. As will be conclusively verified later, this is the rigid-body mode of the soundpost. At high frequencies, above 10 kHz, we see resonances which appear unaffected by the changes to axial spring stiffness within the range of 10^1 – 10^4 N/m. These are the axial modes of the soundpost. At low axial spring stiffness, the soundpost is behaving as if it is a free–free rod with unconstrained ends. This free–free behaviour continues until the axial spring stiffness reaches a value of around 10^6 N/m. At this point, the springs start to have a clamping effect on the ends of the soundpost and the resonance frequencies increase. Beyond 10^8 N/m, the soundpost behaves as a rod with fixed ends and the axial mode frequencies settle to a maximum value.

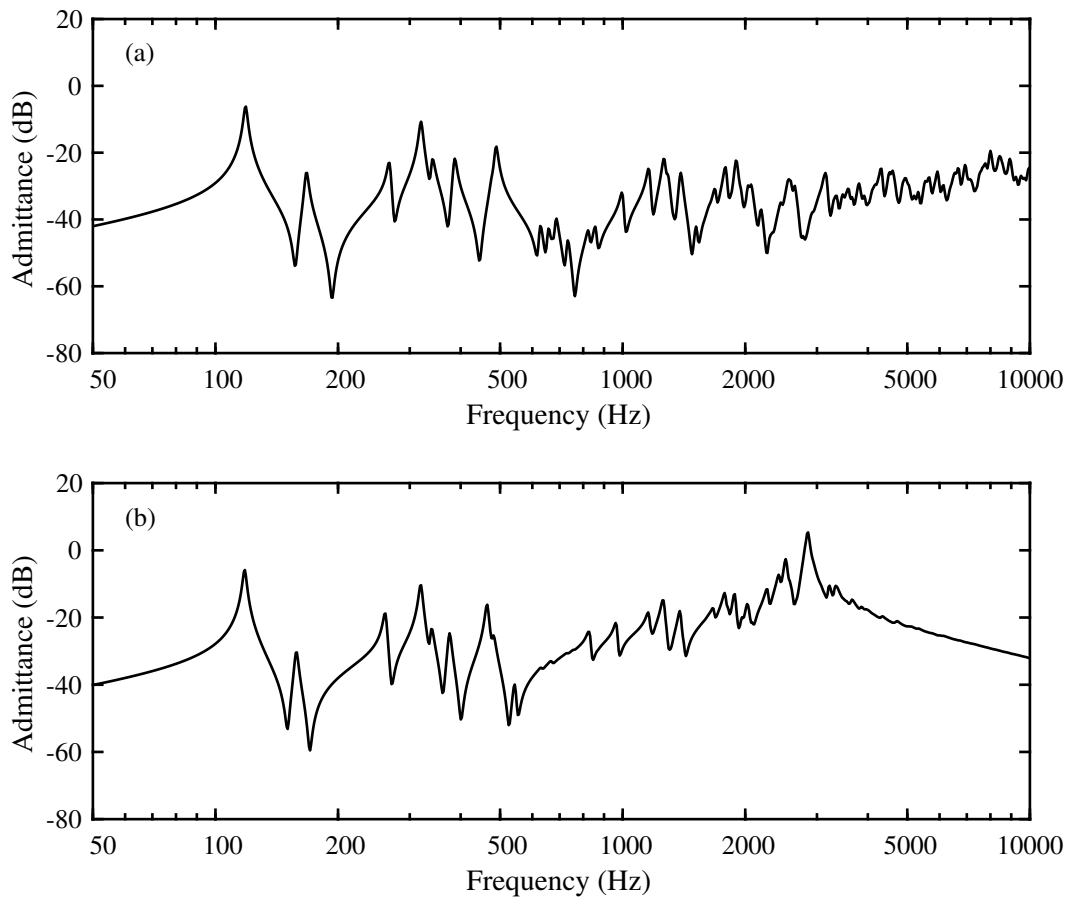


Figure 3.2: Two plots showing ‘slices’ taken from Figure 3.3. (a) The axial frequency response of the soundpost when $k_1 = k_2 = 10^6$ N/m. (b) The axial frequency response of the soundpost when $k_1 = k_2 = 10^5$ N/m.

Focusing our attention back on the rigid-body mode, we notice that as this mode increases in frequency, there are resonances associated with the plates which become coupled to the soundpost. This is represented by the high density of mode resonances seen ‘above’ the rigid body mode. To examine this in more detail, we return to Figure 3.2, which shows two ‘slices’ taken from Figure 3.3. Here, we can see that below 10 kHz, the axial frequency response of the soundpost is dominated by the plate modes. Figure 3.2(b) shows the response when 10^5 N/m, and at this stiffness we observe the rigid-body mode occurring at around 3 kHz.

3.1.1 Verifying the axial vibrational behaviour of the soundpost

One way to verify our results is to consider a simple soundpost and spring model. Figure 3.4 illustrates our chosen set-up: an axial rod coupled at one end to a rigid surface via a spring. This

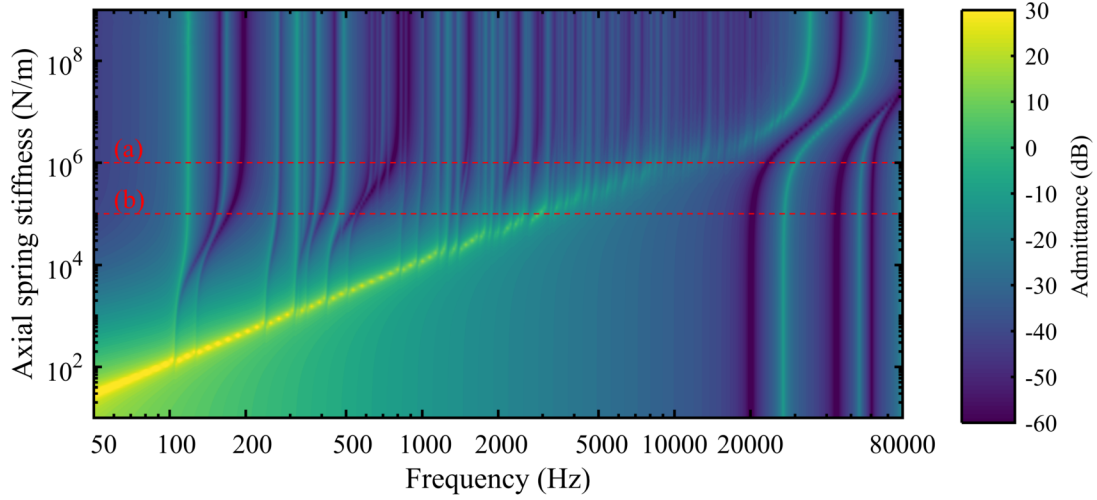


Figure 3.3: The axial frequency response of the soundpost plotted as a function of axial spring stiffness. The two red dashed lines mark the location of ‘slices’ of this plot which are shown in Figure 3.2.

simplified model still incorporates all the important features of the soundpost: it has rigid body motion as well as axial motion. However, a key advantage of this simplified model is that we can derive a closed form solution, before comparing the result to a calculation obtained from our main model. An equivalent set-up in our main model can be achieved by setting $k_1 = 0$ and making the back plate ‘infinitely stiff’.

The axial vibration of a uniform rod is governed by the familiar wave equation

$$\frac{\partial^2 u_r(z, t)}{\partial z^2} = \frac{1}{c^2} \frac{\partial^2 u_r(z, t)}{\partial t^2}, \quad (3.2)$$

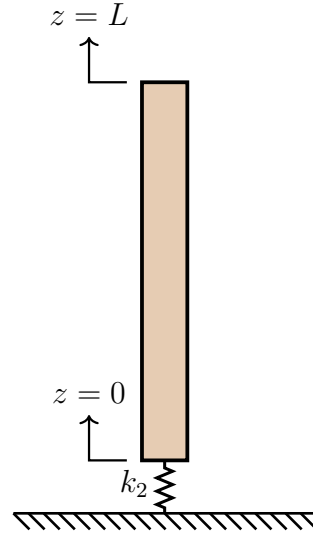
where the Young’s modulus, E , and density, ρ , determine $c = \sqrt{E/\rho}$. Using the method of separation of variables, the general solution to Equation 3.2 is given by

$$u_r(z, t) = \left(\mathcal{A} \cos \frac{\omega z}{c} + \mathcal{B} \sin \frac{\omega z}{c} \right) (\mathcal{C} \cos \omega t + \mathcal{D} \sin \omega t), \quad (3.3)$$

where ω is the frequency of vibration and \mathcal{A} – \mathcal{D} are constants determined by the boundary conditions and initial conditions of the rod. The tensile force, F_{ten} , acting at a given portion on the rod is given by

$$F_{\text{ten}} = \sigma A, \quad (3.4)$$

Figure 3.4: A diagram of an axial rod with a free end at $z = L$. At $z = 0$, it is coupled to a spring with stiffness k_2 . This spring is in turn coupled to a rigid surface.



where σ is the axial stress and A is the cross-sectional area of the soundpost. This can be written as

$$F_{\text{ten}} = EA \frac{\partial u_r}{\partial z}, \quad (3.5)$$

where $\partial u_r / \partial z$ is the axial strain. At $z = L$, the end of the rod is free. Therefore, there is no tensile force acting at this point:

$$EA \frac{\partial u_r(L, t)}{\partial z} = 0. \quad (3.6)$$

Substituting Equation 3.3 into Equation 3.6 gives

$$-A \sin \frac{\omega L}{c} + B \cos \frac{\omega L}{c} = 0. \quad (3.7)$$

At $z = 0$, balancing forces across this junction using Hooke's law gives

$$EA \frac{\partial u_r(0, t)}{\partial z} = k_2 u_r(0, t). \quad (3.8)$$

Substituting Equation 3.3 into Equation 3.8 gives

$$EA \frac{B\omega}{c} (C \cos \omega t + D \sin \omega t) = k_2 A (C \cos \omega t + D \sin \omega t) \quad (3.9)$$

$$\frac{BEA\omega}{k_2 c} = A. \quad (3.10)$$

Finally, by substituting Equation 3.10 into Equation 3.7 we obtain

$$-\frac{\mathcal{B}EA\omega}{k_2c} \sin \frac{\omega L}{c} + \mathcal{B} \cos \frac{\omega L}{c} = 0 \quad (3.11)$$

$$\cot \frac{\omega L}{c} - \frac{EA\omega}{k_2c} = 0. \quad (3.12)$$

Equation 3.12 is the closed form expression whose roots are the natural frequencies of the simple soundpost model, as pictured in Figure 3.4. The roots of this equation, of which there are an infinite number, can be found using the Newton–Raphson method. MATLAB was used to perform this calculation and the results are plotted in Figure 3.5(b). As an equivalent comparison, in Figure 3.5(a) we have plotted the soundpost axial frequency response directly obtained from our model when $k_1 = 0$ and the back plate is infinitely stiff. There is perfect agreement between these two plots.

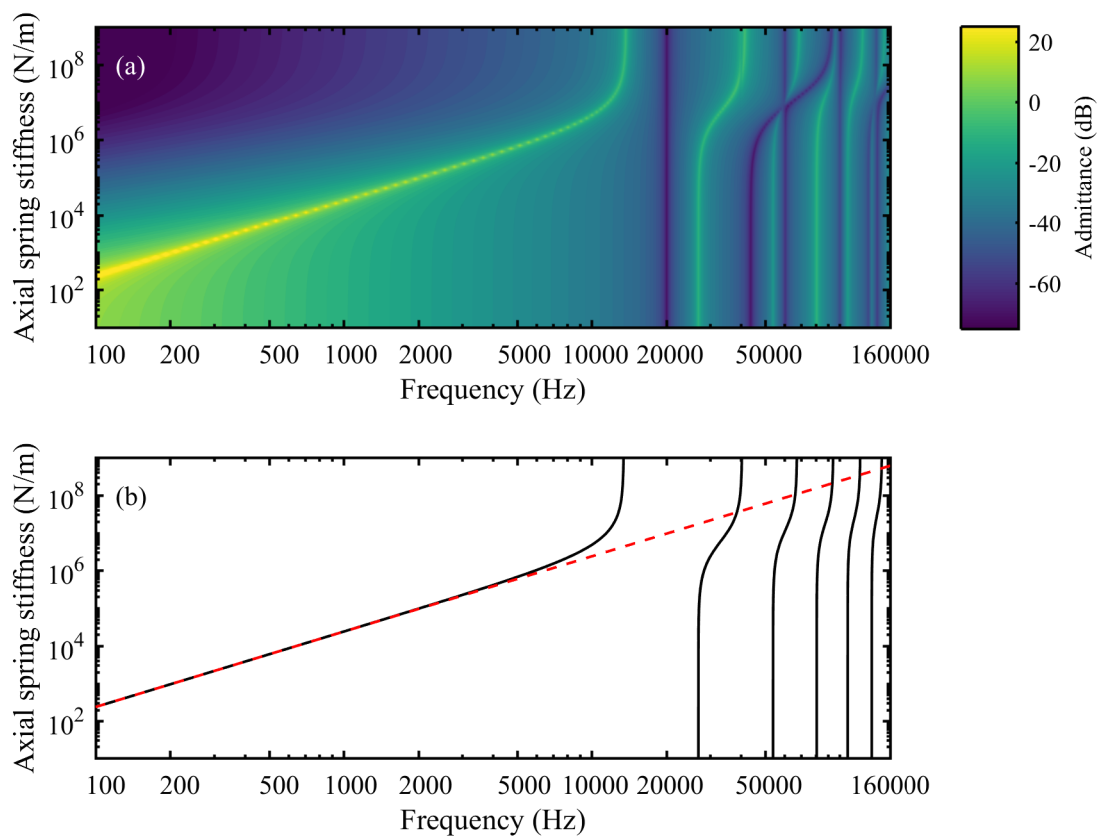


Figure 3.5: (a) The axial frequency response of the soundpost when $k_1 = 0$ and the back plate is made infinitely stiff. (b) In black, Equation 3.12 is plotted. Equation 3.13 is plotted using a dashed red line.

If we consider just the rigid-body motion of the simple soundpost and spring model, as pictured in Figure 3.4, then, for a given spring stiffness, k_2 , the natural frequency of the rigid body motion is given by the familiar

$$f_{\text{RB}} = \frac{1}{2\pi} \sqrt{\frac{k_2}{m_s}} = \frac{1}{2\pi} \sqrt{\frac{k_2}{\rho AL}}, \quad (3.13)$$

where m_s is the mass of the soundpost, which can be written in terms of the density, cross-sectional area and length as $m_s = \rho AL$. This function is plotted in Figure 3.5(b) using a dashed red line. Below 5000 Hz, this dashed red line matches perfectly with Equation 3.12. The agreement between Equation 3.12 and Equation 3.13 at low frequency can be further verified by calculating the Taylor-series expansion of the cotangent term:

$$\cot x = \frac{1}{x} - \frac{x}{3} + O(x^2). \quad (3.14)$$

Applying only the first term of this expansion to Equation 3.12 gives

$$\frac{c}{\omega L} - \frac{EA\omega}{k_2 c} = 0, \quad (3.15)$$

which can be rearranged in terms of ω to give

$$\omega = \sqrt{\frac{k_2}{\rho AL}}, \quad (3.16)$$

showing agreement with Equation 3.13. This concludes our investigation into the axial vibrational behaviour of the soundpost. Our next focus will be on how the plate dynamics are affected by axial spring stiffness.

3.2 The effect of axial spring stiffness on the plate dynamics

Our results in the previous section reveal the range in which the axial spring stiffnesses are relevant to the model. This will guide our next investigation, into the effect of the coupling between the soundpost and the plates on the modes of the complete coupled model. We know that the soundpost resonates axially at frequencies much higher than are relevant to the sound of a violin. The rigid body mode, however, operates at much lower frequencies, and so could have an influencing behaviour on the plates.

To probe the vibration of the plates, we will calculate the frequency response at a point on the front plate. Probing directly at the soundpost location is not ideal as we may encounter nodal

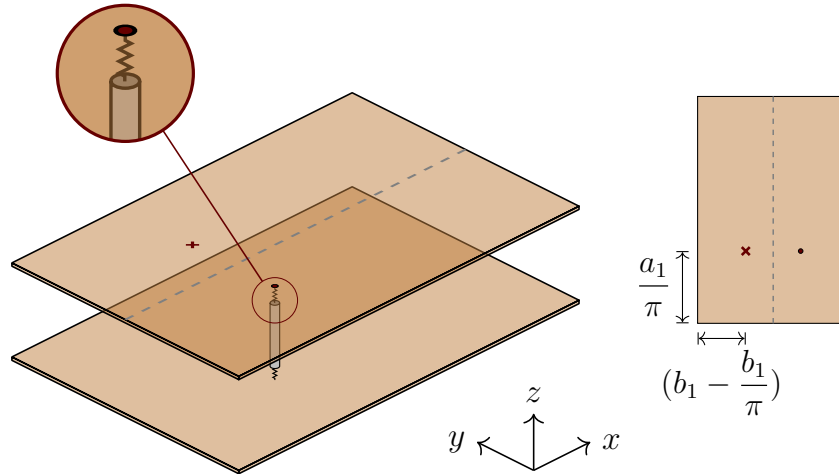


Figure 3.6: A diagram of the soundpost positioned between the two plates. The location of the excitation point (x_B, y_B) on the front plate is shown by the red cross.

points at this position. Instead, the location that has been chosen is shown in Figure 3.6: this corresponds to the position at which the left-hand bridge foot would normally lie, and usefully demonstrates how the contact points of the bridge feet significantly influence the vibration of the body. The left-hand bridge foot has been specifically chosen in preference to the right-hand foot, which lies close to the position of the soundpost. We will define the coordinates of the calculation point shown in Figure 3.6 as \mathbf{r}_B .

Our goal is to understand how changes to the coupling between the soundpost and the plates influences the modal frequencies. Therefore, the axial spring stiffness will be varied, and for each spring stiffness, the frequency response will be calculated. This is explicitly defined as

$$H_1(\mathbf{r}_B, \omega) = i\omega \sum_{n=1}^N \frac{\left(\tilde{\mathbf{u}}_1^{(n)}(x_B, y_B)\right)^2}{\omega_n^2 + 2i\omega\omega_n\zeta_n - \omega^2}. \quad (3.17)$$

The result of this calculation is shown in Figure 3.7. The y -axis shows the axial spring stiffness increasing and the colour of the surface represents the amplitude of the frequencies. At low axial spring stiffness, the plates vibrate independently as if they are uncoupled. As the spring stiffness increases, the mode frequencies of the plate also increase. This is consistent with the expectation that raising the stiffness in a vibrational system will always cause mode frequencies to increase. The range of 10^4 – 10^6 N/m appears to be region at which the vibration of the plates is most sensitive to changes in axial spring stiffness. In particular, we notice that new resonances become visible. This is consistent with the interlacing theorem (see Rayleigh, 1894), which states that the modal frequencies of a constrained system (f') interlace with the modal frequencies of

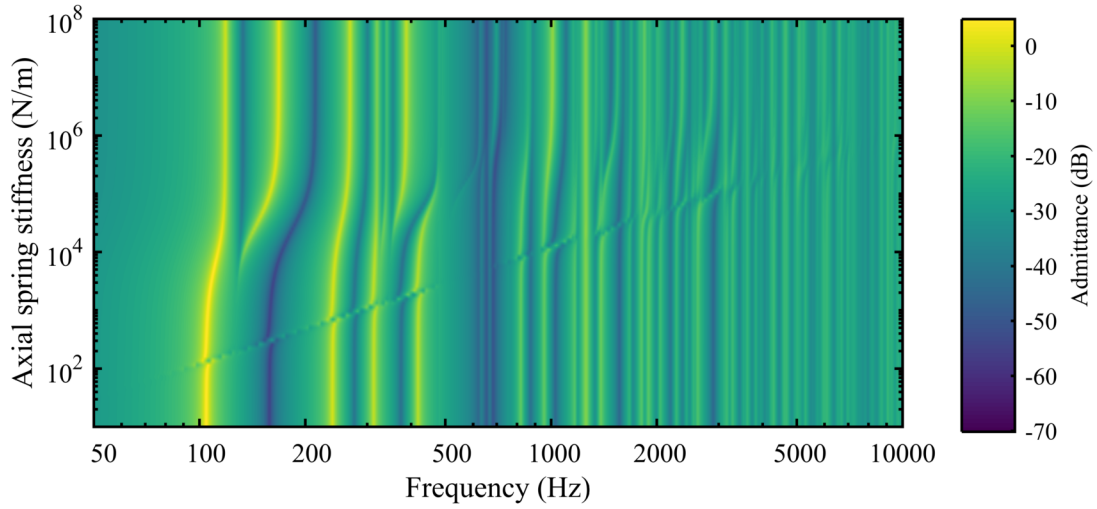


Figure 3.7: The frequency response, calculated at (x_B, y_B) on the front plate, plotted as a function of axial spring stiffness.

the system when it is unconstrained (f), such that

$$f_n \leq f'_n \leq f_{n+1}. \quad (3.18)$$

Above 10^7 N/m, the plates are effectively locked together and the mode frequencies remain constant from this point onwards. Another interesting feature is that the rigid body mode can be faintly seen in the plate admittance. This reflects the fact that the rigid body couples to each body mode in turn as the frequencies coincide.

3.2.1 Comparing the admittance calculated on the front and back plates

So far, we have only considered the admittance calculated on the front plate, H_1 . In this section, we will investigate the admittance calculated on the back plate, H_2 , and in particular the difference $H_2 - H_1$. Consider the points on the front and back plate where the soundpost is coupled: $\mathbf{r}_S = (x_S, y_S)$, where

$$x_S = \frac{a_1}{\pi} \quad (3.19)$$

and

$$y_S = \frac{b_1}{\pi}. \quad (3.20)$$

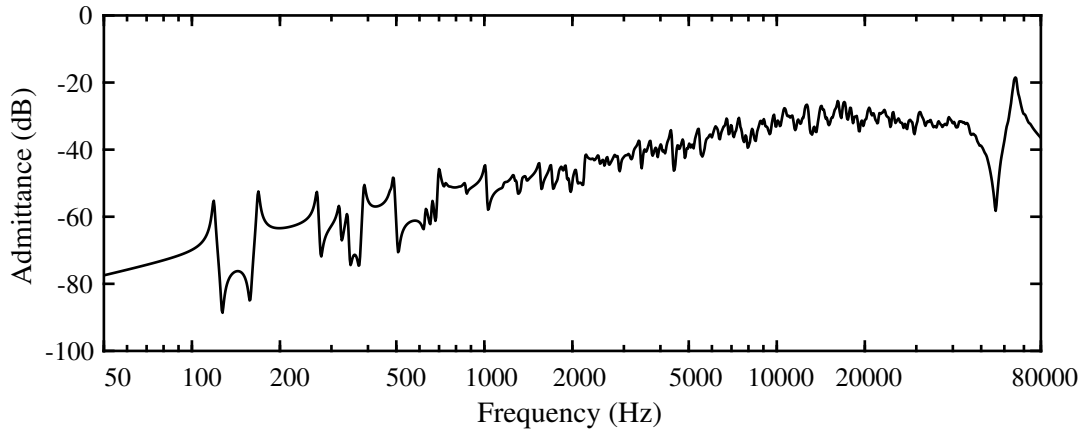


Figure 3.8: A plot of Equation 3.21 for an axial stiffness of $k = 10^9$ N/m.

Explicitly, we are calculating the following transfer function:

$$H_2(\mathbf{r}_S, \omega) - H_1(\mathbf{r}_S, \omega) = i\omega \sum_{n=1}^N \frac{\tilde{\mathbf{u}}_1^{(n)}(x_S, y_S) \tilde{\mathbf{u}}_2^{(n)}(x_S, y_S)}{\omega_n^2 + 2i\omega\omega_n\zeta_n - \omega^2} - i\omega \sum_{n=1}^N \frac{\left(\tilde{\mathbf{u}}_1^{(n)}(x_S, y_S)\right)^2}{\omega_n^2 + 2i\omega\omega_n\zeta_n - \omega^2}. \quad (3.21)$$

Figure 3.8 shows a calculation of Equation 3.21 for an axial stiffness of $k = 10^9$ N/m. If the plates were coupled by a rigid link, then we would expect the result of Equation 3.21 to be zero across all frequencies. However, these results show that there is a difference between the admittance as calculated on the back plate compared to the front plate. Above 50,000 Hz, we observe a soundpost axial resonance.

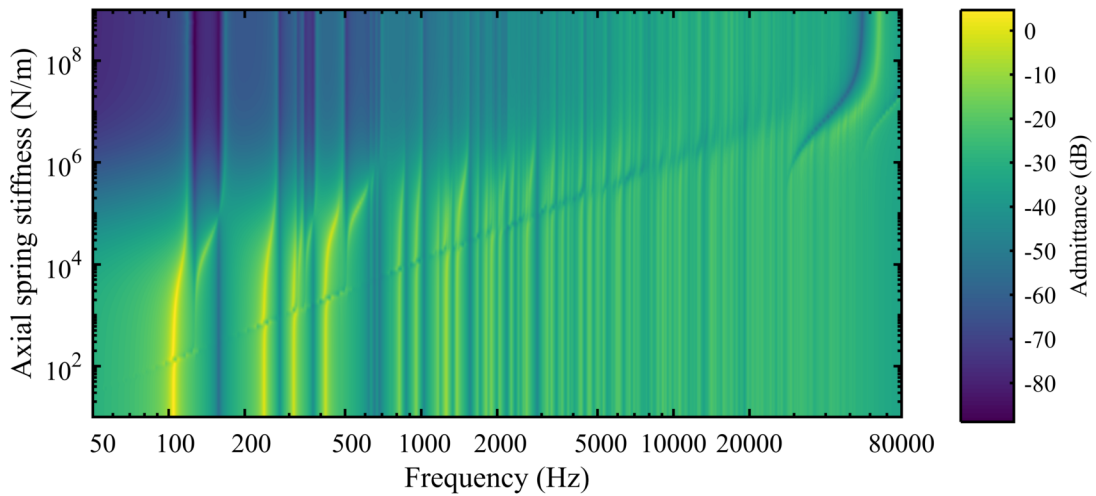


Figure 3.9: A graph showing $H_2 - H_1$, a transfer function representing the displacement across the points on the plates where the soundpost is positioned. Increasing axial spring stiffness is plotted on the y -axis.

Taking this analysis one step further, we have plotted Equation 3.21 as a function of axial spring stiffness in Figure 3.9. This graph has a number of interesting features. At low axial spring stiffness we see that the plates are effectively uncoupled from each other. Therefore, we see only the modes of plate 1. However, as the axial spring stiffness increases, the plates become coupled and the difference between H_2 and H_1 becomes smaller. This is shown by the level of the admittance, which reduces as the axial spring stiffness increases.

Above 20,000 Hz, we see the first axial mode of the soundpost appearing clearly in the plot. There is a clearly noticeable anti-resonance and peak, seen in Figure 3.8 as well.

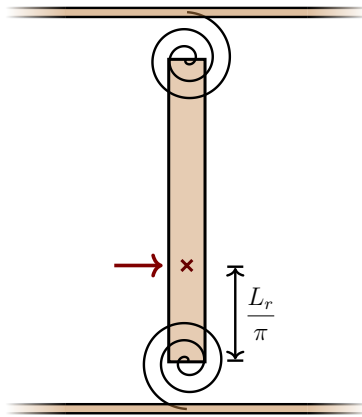


Figure 3.10: A diagram of one of the bending beams used to model the bending vibration of the soundpost. The excitation point used when computing the bending frequency responses is shown by the red cross. This is at a length $\frac{L_r}{\pi}$ along the beam, to ensure that a nodal point is not probed. The red arrow illustrates that we are simulating a force being applied perpendicular to the length of the soundpost.

3.3 The effect of bending spring stiffness on bending soundpost motion

As with our previous treatment of the axial springs, the value of the bending spring stiffness will be varied from a very low value (in the order 10^{-4} Nm/rad) to a very high value (10^6 Nm/rad). These values were chosen after some initial testing to gauge a suitable range. By testing low and high values of bending spring stiffness until we are able to observe very little change in the frequencies of the vibration modes, it is possible to gauge where the limits of low and high values lie.

In the following calculations, the axial spring stiffness has been set to zero. Additionally, because we have two orientations of the soundpost, we will be looking at the x -direction bending modes and y -direction bending modes separately. Explicitly, we are calculating the following transfer function:

$$H_b\left(\frac{L}{\pi}, \omega\right) = i\omega \sum_{n=1}^N \frac{\left(\mathbf{u}_b^{(n)}\left(\frac{L}{\pi}\right)\right)^2}{\omega_n^2 + 2i\omega\omega_n\zeta_n - \omega^2}. \quad (3.22)$$

A diagram showing this set-up is shown in Figure 3.10.

Figure 3.11 shows how the bending behaviour of the soundpost changes as the bending spring stiffness is varied from low to high. In this calculation, a low number of plate shape functions, $N_i = 3$, have deliberately been used. There are therefore no plate modes above 1000 Hz and we observe purely the bending soundpost modes without any coupling. Because of this, and because the bending beams in the x and y direction are identical to each other, the bending frequency response for both orientations is identical. We are therefore showing the result only for bending in the x -direction.

Figure 3.11 shows two very clear resonance peaks which correspond to the first two bending modes of the soundpost. These, interestingly, lie within a frequency range relevant to the sound

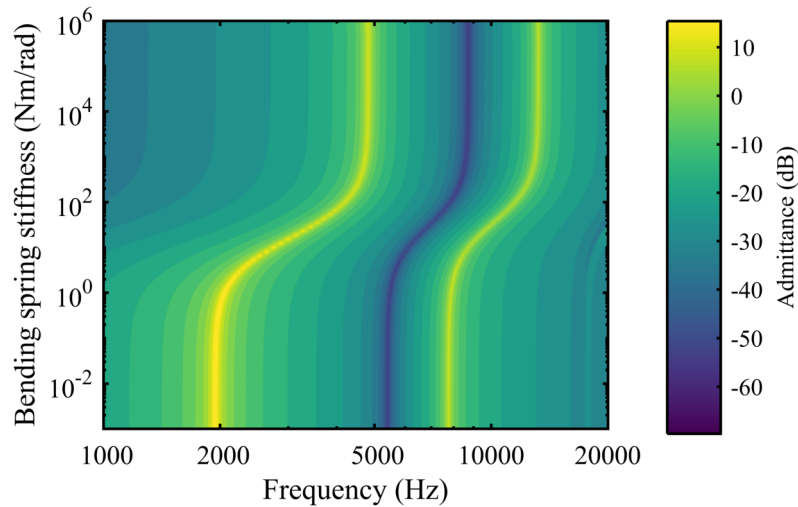


Figure 3.11: The bending frequency response of the soundpost plotted as a function of bending spring stiffness. This particular plot shows bending modes in the x direction. The number of plate modes used in the calculation is low.

of the violin. When the bending spring stiffness is weak, the first bending mode is seen just below 2000 Hz. When the bending spring stiffness reaches a value of $\kappa = 10^0$ Nm/rad the influence of the springs becomes noticeable and the first bending frequency increases until it reaches a threshold. Beyond 10^4 Nm/rad, the spring stiffness effectively clamps the soundpost so the frequency remains fixed. What effect this first bending frequency — which is well within the range of important violin modes — has on the vibration of the plates is worth investigating next. First, though, we will explore the differences between the bending frequency response in the two orientations when the number of plate modes is increased.

3.3.1 The difference between the two orientations of the soundpost bending beams

Increasing the number of plate modes used in the calculation, so that there are plate modes across the entire frequency range we are interested in, changes the coupling between the plates and the soundpost. Figure 3.12 shows these results. Compared to Figure 3.11, we see that above 10^2 Nm/rad, the plate modes are coupled to the soundpost and the influence of the plate modes appears in the frequency response. Furthermore, there are now differences between the x and y orientations of the soundpost. This is because it is the gradient of the plate displacement at the coupling point which is being used in the calculation of \mathbf{u}_b .

To better visualise the differences between Figure 3.12(a) and Figure 3.12(b), Figure 3.13 shows $H_{b_x} - H_{b_y}$. Below 10^0 Nm/rad, the soundpost is effectively uncoupled from the plates,

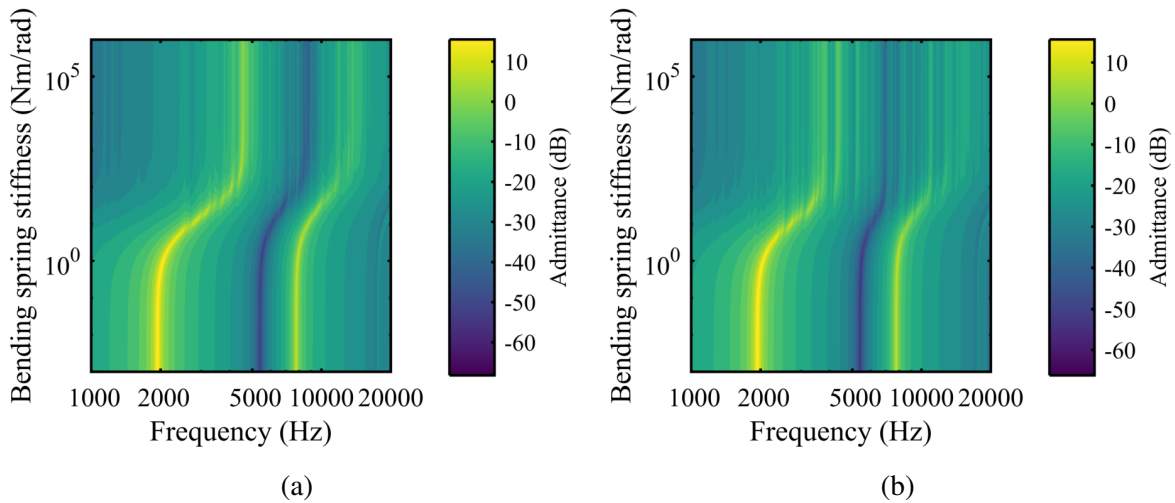


Figure 3.12: The bending frequency response of soundpost plotted as a function of bending spring stiffness. Bending in the x -direction is shown in (a), while bending in the y -direction is shown in (b). The number of plate modes used in these calculations is high.

and so we see no difference between the orientations. However, once the soundpost is coupled to the plates, the differences become clear.

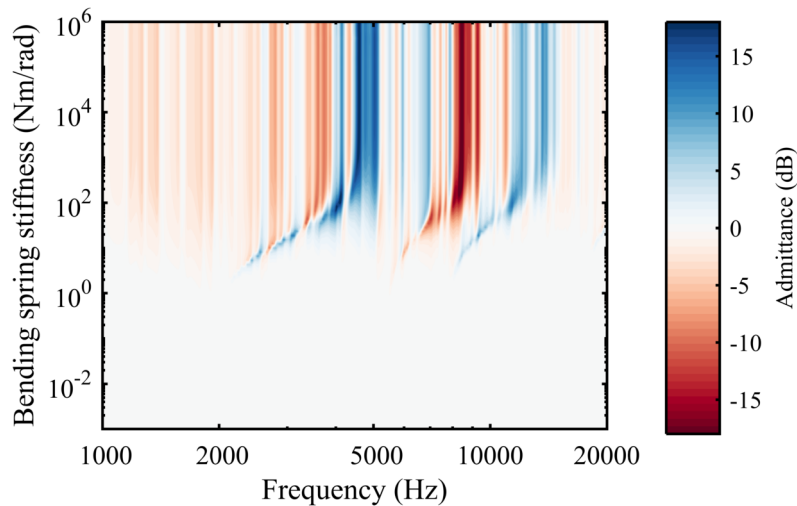


Figure 3.13: This plot shows the difference between the bending frequency response in the x -direction compared to the y -direction.

3.4 The effect of bending spring stiffness on the plate dynamics

In this section we focus on the behaviour of the plates rather than the soundpost itself. The axial spring stiffness will remain zero and we again focus only on varying the bending spring stiffness.

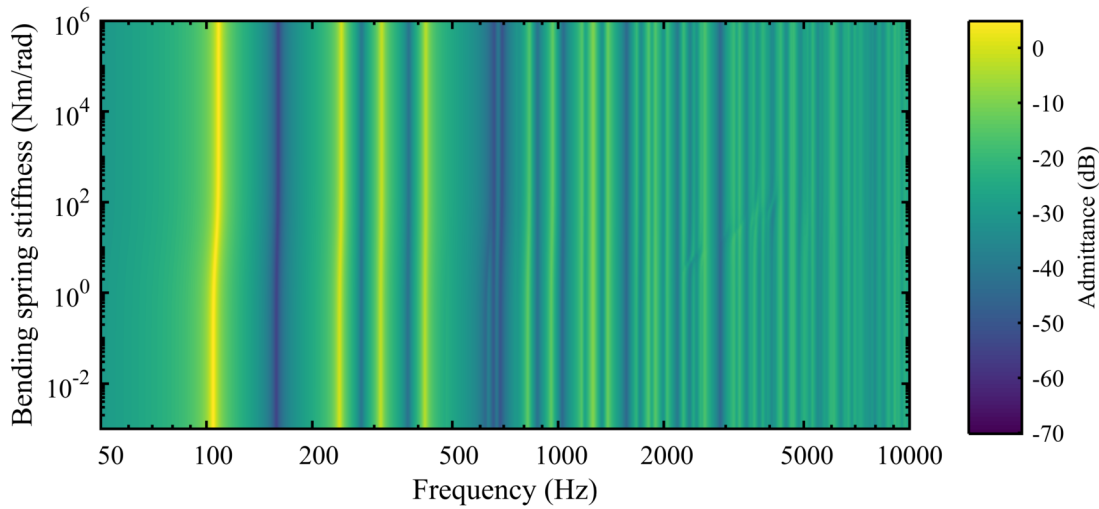


Figure 3.14: The frequency response, calculated at (x_B, y_B) on the front plate, plotted as a function of bending spring stiffness.

Figure 3.14 shows the results. It shows that the bending spring stiffness has rather little effect on the plate resonances: without the presence of the axial springs the plates behave almost as though they are uncoupled.

However, although the bending spring stiffness has much less of an effect on the plate resonances than varying the axial spring stiffness, there are still some features which can be seen in Figure 3.14 upon close inspection. Figure 3.15(a) shows a magnified view of the first main resonance, which occurs at just above 100 Hz. Magnifying the frequency scale for this resonance reveals that there is indeed a direct relationship between the mode frequency and the bending spring stiffness. Comparing Figure 3.15(a) to Figure 3.11 confirms this direct link: the first resonance of the plate is changing in a similar manner to the bending resonances of the soundpost, in response to the bending spring stiffness. Compared to the way in which the first plate resonance changes in response to the axial spring stiffness, though, the effect is very small, only changing by roughly 4 Hz.

Another observation that can be made upon close inspection is shown in Figure 3.15(b). Here the frequency range of 2000–5000 Hz is magnified and mode veering effects can be seen. This is due to coupling between the first bending mode of the soundpost and the plates.

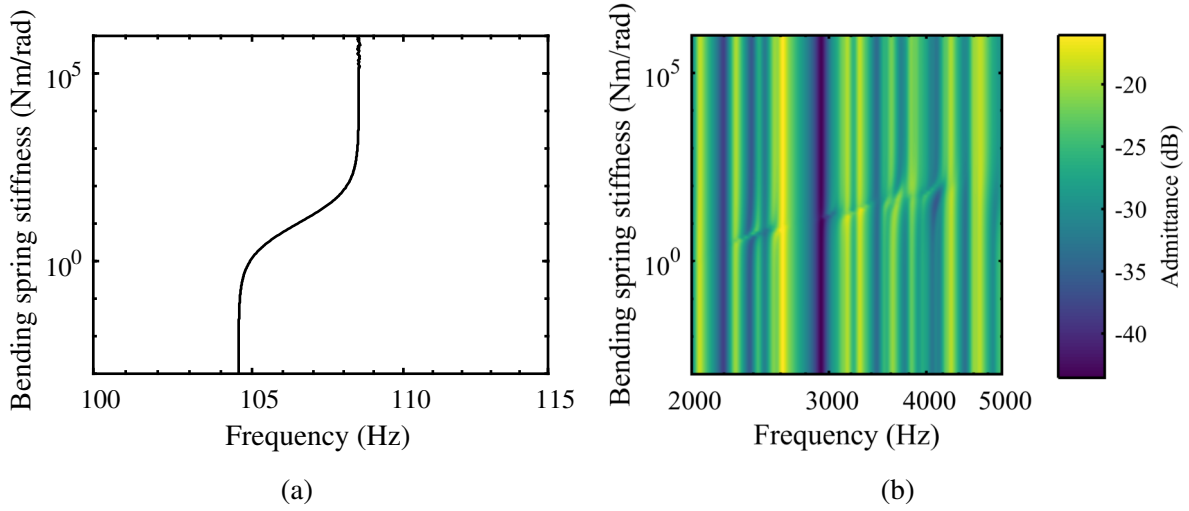


Figure 3.15: Zoomed-in sections of Figure 3.14.

3.5 Comparing our soundpost model to a rigid massless link

One interesting question to ask is, how does our soundpost model compare to a rigid massless link? The ‘rigid massless link’ model of the soundpost has previously been investigated by Woodhouse (2005). Consider the coordinates on the front and back plate, (x_1, y_1) and (x_2, y_2) , where the soundpost joins the plates. If these two points were connected by a massless rigid link, then the admittance calculated at these two points would be identical. It is straightforward to calculate the admittance at this coupling point, H_{coup} , using the appropriate combination of admittances:

$$\frac{1}{H_{\text{coup}}} = \frac{1}{H_1^{\text{uncoup}}} + \frac{1}{H_2^{\text{uncoup}}}, \quad (3.23)$$

where H_1^{uncoup} and H_2^{uncoup} represent the admittance calculated on the front and back plates at the coordinates (x_1, y_1) and (x_2, y_2) respectively, when the plates are uncoupled. We can compare this rigid massless link model to our soundpost model when it is similarly ‘rigid’. Therefore, the stiffness of the coupling springs (both axial and bending) were set to nominally high values, based on the previous findings. The results are shown in Figure 3.16. In Figure 3.16(a), we see a direct comparison between the rigid massless link model and our soundpost model. The most noticeable differences occur at around 5000 Hz and above. Here we see that admittance calculated using our soundpost model is larger than the admittance of the rigid massless link model.

To help visualise the differences, Figure 3.16(b) shows a plot of $H_{\text{coup}} - H_1$. Below 5000 Hz, the peaks seen in this plot appear to be largely due to small frequency differences between the

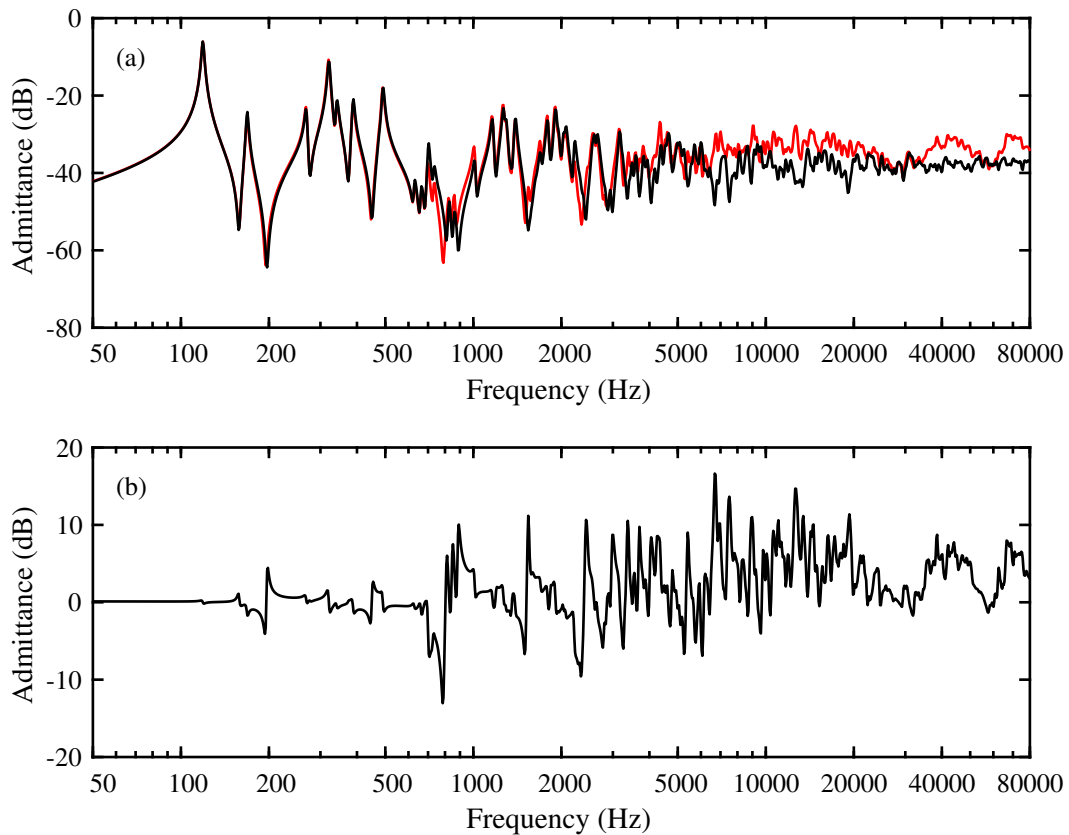


Figure 3.16: (a) A plot showing H_1 in red and H_{coup} in black. (b) A plot showing $H_1 - H_{\text{coup}}$.

two calculations. This may be caused by the presence of added mass in our soundpost model. This will be investigated in Section 3.5.1.

Above 20 kHz, we observe two broad peaks in the admittance of H_1 , whereas H_{coup} remains fairly constant in this region. These peaks may well be due to the axial modes of the soundpost: see Figure 3.3. Similarly, we will investigate this in Section 3.5.2.

3.5.1 The effect of added mass

How does the lack of mass in the rigid massless link model influence the results? One can envisage that the small frequency shifts we are seeing are due to the effect of added mass. One simple test for this is to include the mass of the soundpost in the rigid massless link model: making it in effect a ‘rigid link with mass’. We can calculate the admittance of a mass m using Newton’s second law,

$$F = ma, \quad (3.24)$$

which tells us that the force, F , needed to set a mass into vibration is proportional to the acceleration, a . For sinusoidal motion at a frequency ω , the acceleration is related to the velocity, ν , by

$$a = i\omega\nu. \quad (3.25)$$

Therefore, the admittance of the soundpost mass, m_s , is given by

$$H_{m_s} = \frac{\nu}{F} = \frac{1}{i\omega m_s}. \quad (3.26)$$

Adding the mass of soundpost to our coupling point means we must now calculate the following combination of admittances:

$$\frac{1}{H_{\text{coup}+m_s}} = \frac{1}{H_1^{\text{uncoup}}} + \frac{1}{H_2^{\text{uncoup}}} + \frac{1}{H_{m_s}}. \quad (3.27)$$

A comparison of $H_{\text{coup}+m_s}$ to H_{coup} is shown in Figure 3.17. Interestingly, the effect of adding mass to the rigid link model seems to make a small difference at frequencies below 5000 Hz. In comparison to Figure 3.16, we might have expected to see differences in the admittance in the order of ± 10 dB. The most striking feature of Figure 3.17 is that at frequencies above 20,000 Hz, the added mass strongly influences the admittance. There is a sharp drop-off in the admittance in this range.

3.5.2 Varying the axial spring stiffness

To further investigate the peaks in Figure 3.16 seen at frequencies above 20,000 Hz, we will vary the axial spring stiffness while calculating $H_{\text{coup}} - H_1$. The result of this calculation is plotted in Figure 3.18. The most striking feature of this plot is that both the rigid-body mode of the soundpost and the axial vibration modes can be seen. The rigid-body mode can be seen at all values of axial spring stiffness, and where it occurs the admittance is 0 dB. It is only at high axial stiffness, above 10^6 N/m, that the axial modes also produce an admittance of 0 dB. A value of 0 dB admittance means that at this point there is no difference between H_{coup} and H_1 . Comparing Figure 3.18 to Figure 3.3, it appears that the areas of 0 dB admittance in Figure 3.18 correspond to areas where the soundpost axial modes experience an anti-resonance. This makes physical sense: where there is an anti-resonance, the model behaves exactly as if it was joined by a rigid link.

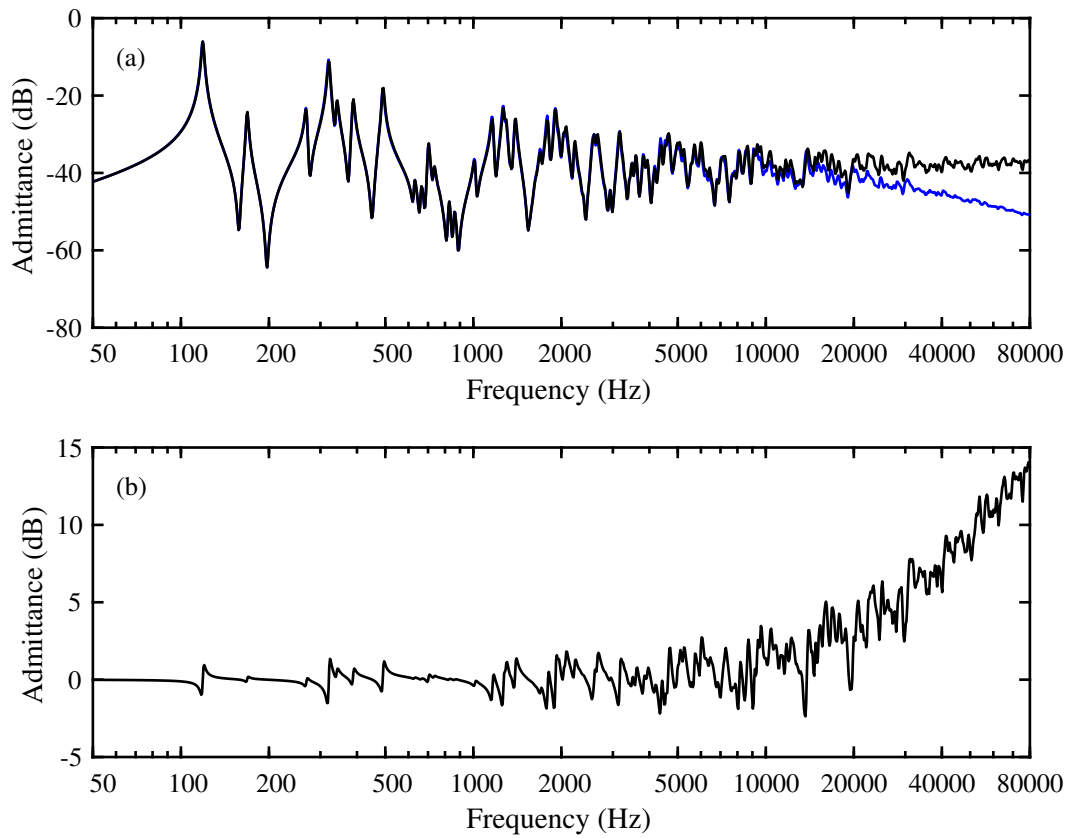


Figure 3.17: (a) A plot showing H_{coup} in black and $H_{\text{coup}+m_s}$ in blue. (b) A plot showing $H_{\text{coup}} - H_{\text{coup}+m_s}$.

3.6 Varying soundpost size and material properties

There are three main variables involved in the design of the soundpost:

- the density;
- the Young’s modulus; and
- the radius.

In the following study, we will adjust each of these variables individually to observe the effect they have on resonances of the model.

3.6.1 Effect on the axial resonances of the soundpost

As in Section 3.1, we will probe the axial resonances of the soundpost by calculating the driving point axial response directly on the soundpost using Equation 3.1. As before, this is calculated at

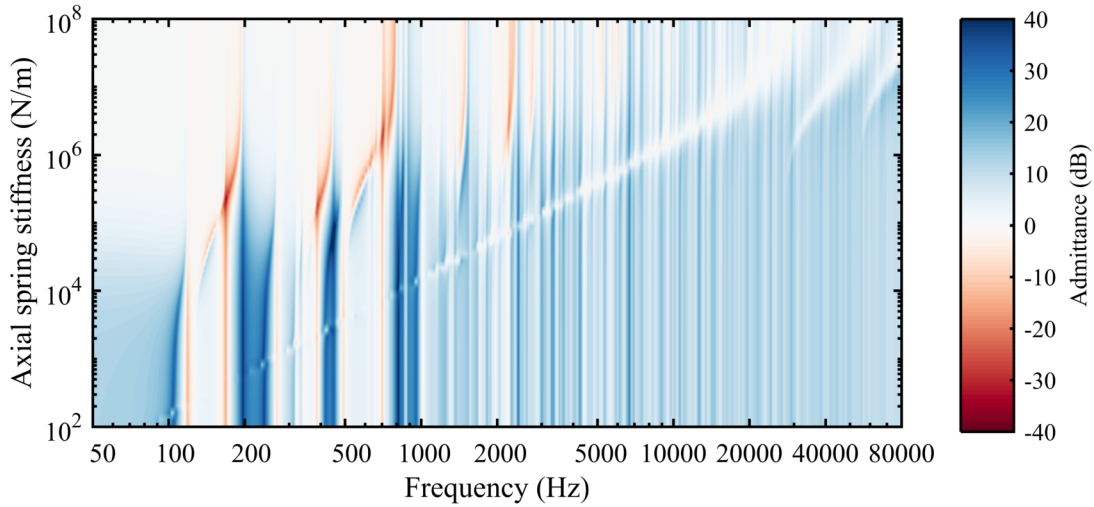


Figure 3.18: A plot of $H_{\text{coup}} - H_1$, where the axial spring stiffness used when calculating H_1 is varied. The highest value of axial spring stiffness, 10^8 N/m, represents the data shown in Figure 3.16(b)

a distance $\frac{l}{\pi}$ along the soundpost. The axial and bending spring stiffnesses will be kept constant throughout all these simulations. Values of $k = 10^6$ N/m and $\kappa = 10^4$ Nm/rad have been chosen as they both fall within ranges that exhibit coupled behaviour between the soundpost and the plates.

Figure 3.19 shows the results of varying the density, radius and Young's modulus of the soundpost. In each simulation the number of plate shape functions used in the calculation has been set deliberately low, $N_i = 3$. Therefore, above 5 kHz we see well-defined resonance peaks which correspond to axial motion of the soundpost. The first of these main resonances, at around 10 kHz, is the rigid body motion of the soundpost. Resonances at higher frequencies correspond to axial vibration of the soundpost.

The density and Young's modulus of the soundpost are determined by the choice of wood used to make it, typically spruce. In Figure 3.19, we have varied both parameters over plausible ranges for the variations of spruce. The plots show behaviour in line with expectations. Increasing density increases the mass of the post, hence resonance frequencies fall. Increasing the Young's modulus, conversely, makes the resonance frequencies rise. For the rigid body mode, however, one would expect the Young's modulus to have no effect on the resonance frequency. The reason the rigid body mode frequency appears to vary is due to mode veering effects. As the Young's modulus decreases a transition point is reached at which the first axial resonance is lower than the rigid body mode.

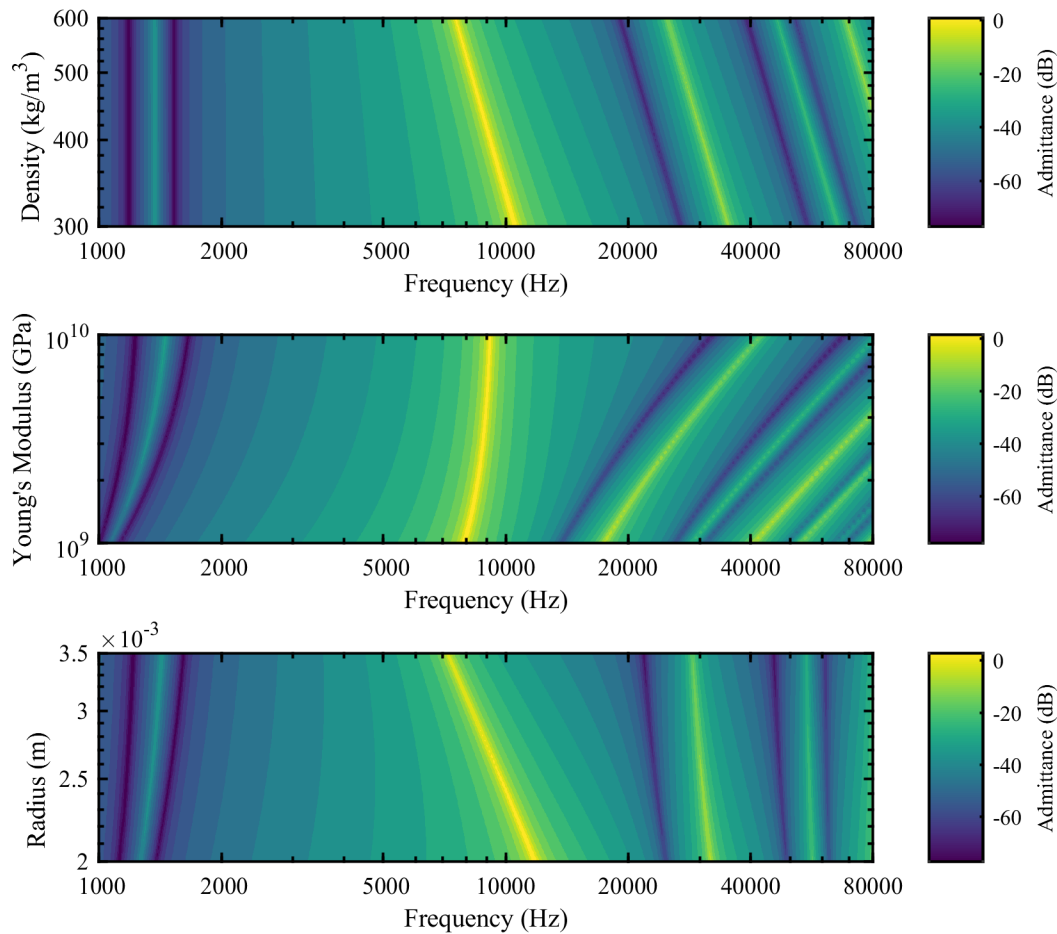


Figure 3.19: The axial frequency response of the soundpost plotted as a function of soundpost density, radius and Young's modulus.

The effect of changing the radius is more complicated. For the rigid-body mode, due to the increase in mass, the frequency falls. But for higher axial modes, the wave speed is independent of radius and so the frequencies change very little.

3.6.2 Effect on the bending resonances of the soundpost

We will now investigate the effect of varying the soundpost density, radius and Young's modulus on the bending resonances of the soundpost. As in Section 3.3, we will probe the bending resonances of the soundpost using a calculation of the admittance as defined in Equation 3.22. The stiffness of the axial and bending springs follow the same values as used in Section 3.6.1. In addition, a low number of plate shape functions have been used in the calculation. The results, shown in Figure 3.20, are straightforward to interpret. Increasing the density increases the

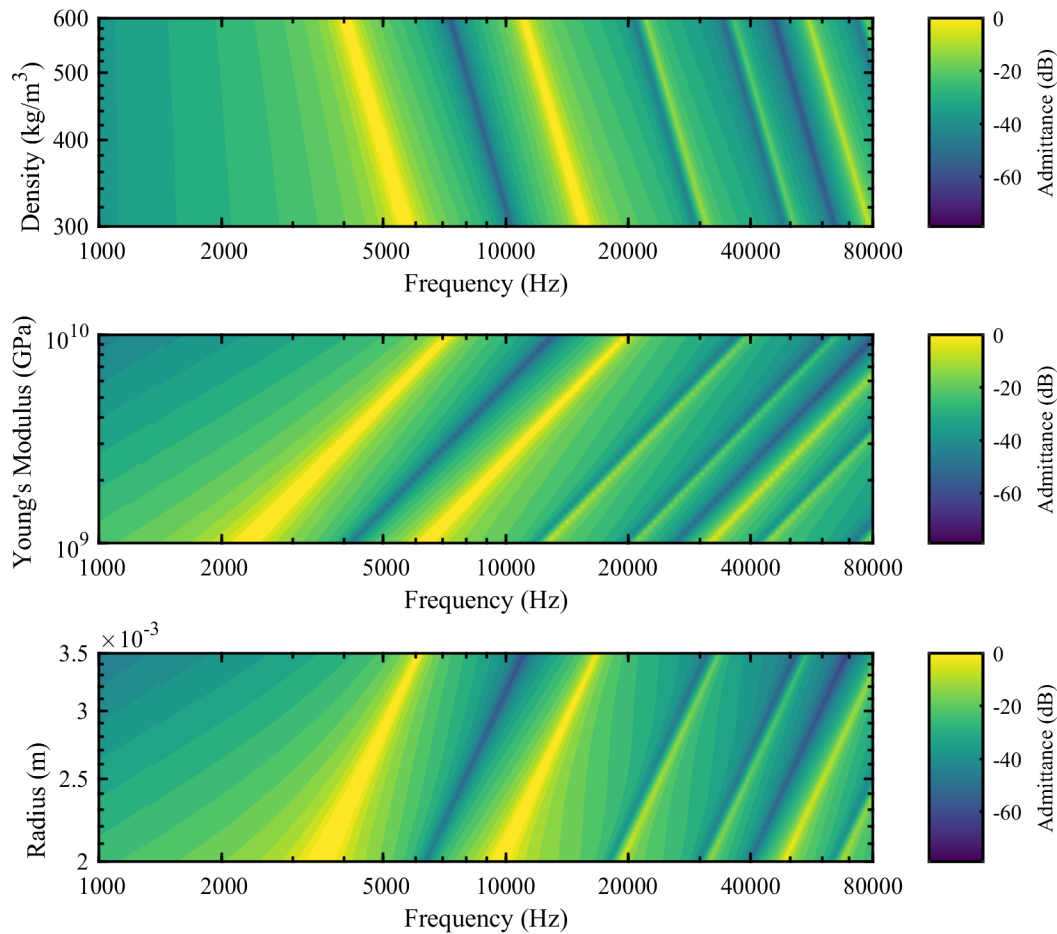


Figure 3.20: The bending frequency response of the soundpost plotted as a function of soundpost density, radius and Young's modulus.

mass of the soundpost, causing the resonance frequencies to be lowered. Conversely, increasing the Young's modulus causes resonance frequencies to increase. Increasing the radius of the soundpost increases the second moment of area which in turn causes the resonance frequencies to increase.

3.6.3 Effect on the plate resonances

To complement the previous two studies, where the admittance of the soundpost was probed, we will also present results for the admittance calculated on the front plate. Figure 3.21 shows the admittance calculated on the front plate directly at the coupling point with the soundpost, (x_S, y_S) . As in Figures 3.19 and 3.20, the density, radius and Young's modulus of the soundpost have been varied. In these calculations, many more plate shape functions have been included.

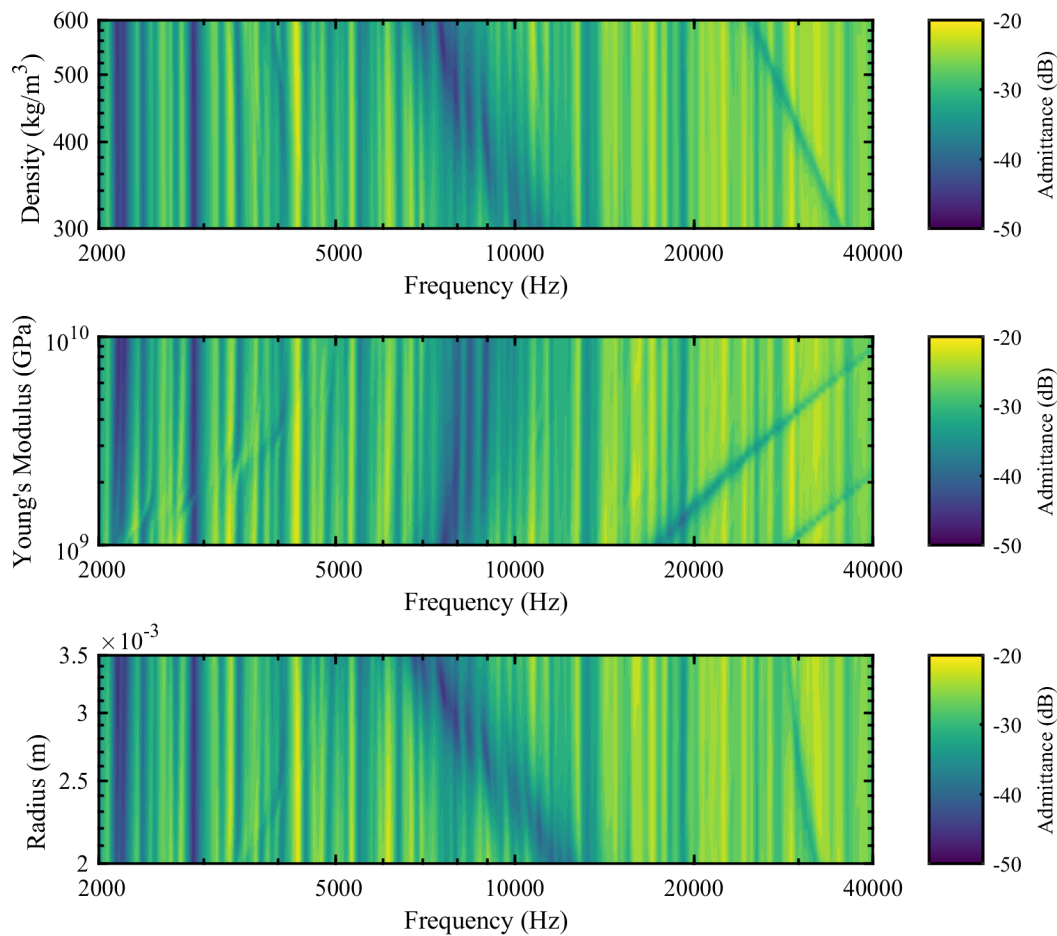


Figure 3.21: The frequency response, calculated at (x_S, y_S) on the front plate, plotted as a function of the soundpost density, radius and Young's modulus.

As a result, we observe many resonance peaks, which appear as tightly packed vertical lines in the plots. The most prominent feature which stands out in each of the three plots is a band of low admittance in the region of 10 kHz. We can understand this feature via a comparison with Figure 3.19. This band of low admittance is associated with the rigid body mode of the soundpost. The rigid body resonance in each of the three plots in Figure 3.19 perfectly matches with the bands of low admittance in the three plots in Figure 3.21. This feature can be attributed to the soundpost behaving as a tuned absorber. Similar bands of low admittance can be seen in Figure 3.21 at higher frequencies, which again match with the higher axial resonances seen in Figure 3.19. Although the effect is subtle, careful inspection of the resonances in the frequency range of 2000–5000 Hz reveals the presence of the first soundpost bending resonance.

3.7 A comparison to the results of Gough

In Section 1.5.4, two results from Gough (2015b) relating to the soundpost were presented. In this section, we will use our simplified violin body and soundpost model to perform similar calculations.

3.7.1 Varying the axial spring stiffness

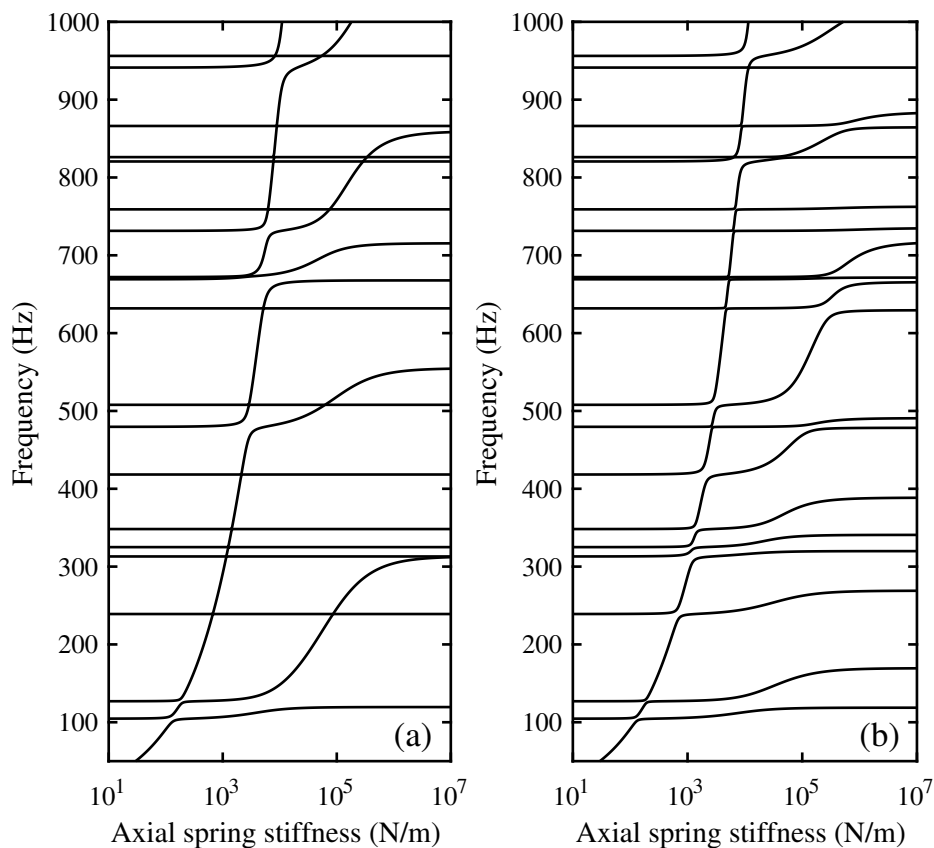


Figure 3.22: Plots comparable to those produced by Gough (2015b): see Figure 1.14. The mode frequencies obtained from our model as the axial spring stiffness is varied: (a) for a centrally placed soundpost, (b) for a soundpost placed at (x_S, y_S) .

First, we must refer back to Figure 1.14, which shows a result produced by Gough (2015b). In this test, Gough (2015b) varies the ‘soundpost coupling strength’ over four orders of magnitude, for the case of a centrally placed soundpost. To replicate this using our model, we vary the axial stiffness of the springs connecting the soundpost to the plates. The bending spring stiffness is set to zero. The results are shown in Figure 3.22(a). We have plotted the complete set of mode frequencies obtained directly from the calculated eigenvalues, in the frequency range 50–1000 Hz,

while the axial spring stiffness is varied over six orders of magnitude. The prominent near-vertical lines which trace out a path from 10^1 – 10^4 N/m are associated with the rigid body mode of the soundpost. As the axial spring stiffness increases, the rigid body mode rises in frequency. Note that this does not appear as a single line on the graph because of mode veering effects.

Figure 3.22(b) shows the results obtained for the case of an off-centre soundpost, placed at (x_S, y_S) , as defined in Equation 3.19. At low axial stiffness, $k = 10^1$ N/m, the mode frequencies match those for a centrally placed soundpost. This shows that in this range, the soundpost is effectively de-coupled from the plates. As the axial stiffness rises, we see the same line mapping the rigid body mode of the soundpost, which rapidly increases in frequency. At high axial stiffness, $k = 10^5$ – 10^7 N/m, we see that many modes are increasing in frequency. Compared to Figure 3.22(a), a greater number of modes undergo a change in frequency. This because the off-centre soundpost is situated in a position that, for many modes, corresponds with plate movement, while the centre of the plate is often a nodal point for many vibration modes.

Comparing these results to Figure 1.14, we observe general agreement with the results of Gough. While the exact mode frequencies calculated using our model are of course different, we see the same increase in the mode frequencies as the coupling strength is increased. Additionally, disregarding the rigid body mode of the soundpost, if we look at the resonances associated with the vibration of the plates, we see that the resonance frequencies are influenced by the soundpost coupling strength over a range of four orders of magnitude in both sets of results.

3.7.2 Varying the position of the soundpost

First, we must refer back to Figure 1.13, which shows a result produced by Gough (2015b). This test involves varying the position of the soundpost. The stiffness of the axial and bending springs was set to the same values as used in Section 3.6.1. Figure 3.23(a) shows the resonance frequencies from our model for an initially central soundpost that is shifted ± 30 mm along the length of the plate (positive offset indicating towards the upper bouts). However, due to the symmetry of our model, moving the soundpost towards the upper bouts returns the same resonances as moving it towards the lower bouts, as can be seen in Figure 3.23(a). Although Gough's model does not share this same symmetry and the frequencies involved are not directly comparable, we see similar mode veering features in both plots.

Figure 3.23(b) shows the resonance frequencies as a function of transverse offset of an initially centrally placed soundpost. Moving the soundpost in such a way causes some resonance frequencies to fall, while some rise. Similarly to Figure 3.23(a), there are resonances which are

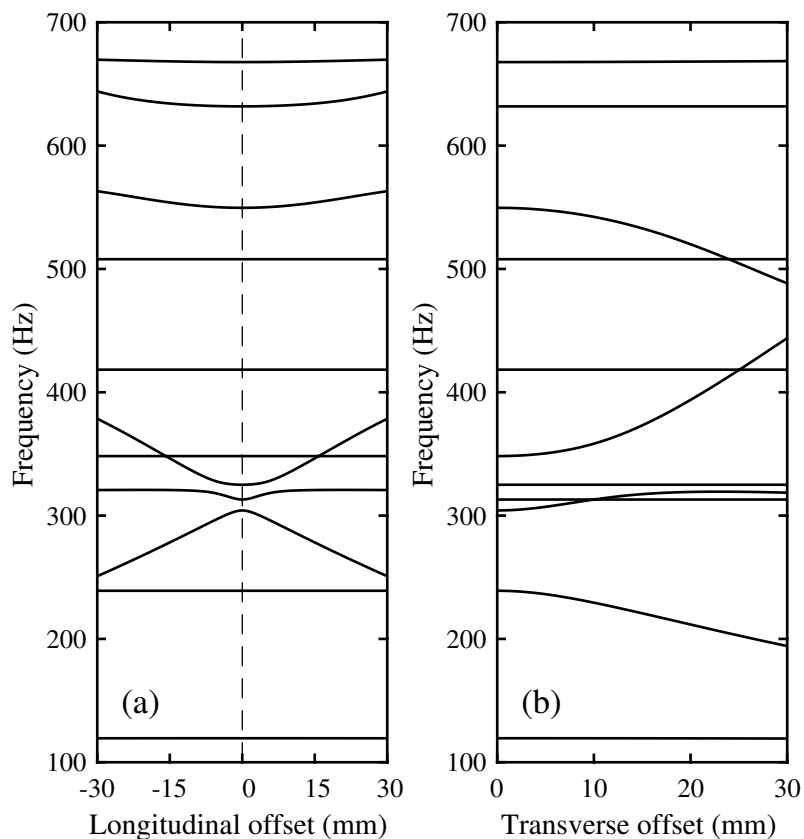


Figure 3.23: Plots comparable to those produced by Gough (2015b): see Figure 1.13. The mode frequencies obtained from our model as a result of varying the position of the soundpost: (a) positive longitudinal offset indicates moving towards the upper bouts; (b) transverse offset is towards the treble side bridge foot.

unaffected by the change in soundpost position. This is because either the soundpost is positioned on a nodal point of that particular mode shape, or the two plates exhibit coupled behaviour.

4

Developing an enhanced bridge model

In this chapter, we will develop a simplified model of the violin bridge, drawing on and enhancing previous theoretical modelling. The bridge, an important component in stringed instruments, is a device used to couple the strings to the instrument body. Because it serves a key role in the transfer of vibrational energy from the strings to the body, the dynamics of the violin bridge and its coupling to the body of the instrument is of significant interest to us.

In a violin, the bridge couples to the body via two ‘bridge feet’: see Figure 4.1(a). Up until now, we have been considering the excitation of the body by a single point harmonic force only. That approach does not, however, capture the fact that a real violin body has two points of contact which provide excitation forces to the body. Therefore, it has been our aim to develop a simplified model of the bridge and to couple this with our model of the violin body and soundpost.

Further, we wish to investigate how the dynamics of the bridge change according to which of the four strings is providing the input driving force. Therefore, we will develop a model that includes the ability to vary the location of the driving force, to replicate the effect of driving at the different strings. This will enable us to investigate questions pertaining to the ‘balance of the strings’, a concept that will be explained in more detail in Section 4.1.2.

We will begin by analysing the design of the violin bridge and the mechanical role it plays in transferring vibrational energy from the strings to the body. We will then consider existing bridge models, before outlining improvements and additions and proceeding to derive our own simplified bridge model. Finally, we will conduct a study of bridge parameters, focusing on how variations to these parameters influence the input admittance of a single string.

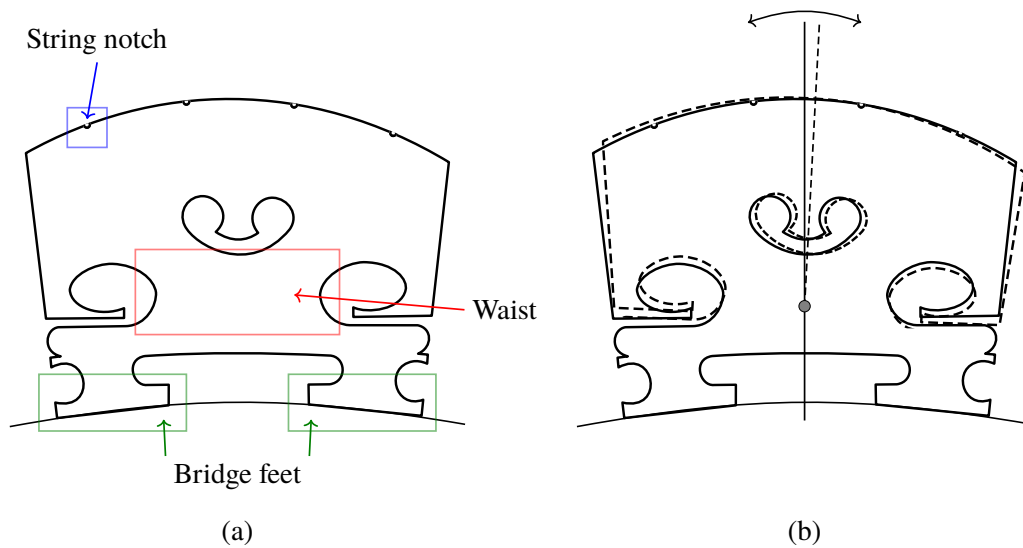


Figure 4.1: (a) A labelled diagram of a violin bridge highlighting features important to our research, including the bridge feet, waist and string notch. (b) An illustration of the lowest in-plane bridge resonance as shown in Cremer (1984) and Woodhouse (2005). The solid line shows the position at rest; the dashed line indicates the displaced position. The filled circle located in the waist area indicates the axis of rotation.

4.1 The design of the violin bridge

In the guitar family of plucked stringed instruments, the bridge is very low and the strings almost flush with the front surface of the body. In the violin family, however, the positioning of the bridge has evolved to allow the strings to be raised from the surface of the front plate, making it possible to bow each string individually without making contact with other strings or with the body.

When a string is bowed, there is a significant component of horizontal force acting on the bridge. The principal role of the bridge is to convert this horizontal force into a vertical force which is applied to the front plate in order to excite the body of the instrument. As a rigid body, the bridge is able to fulfil this requirement by rocking from side-to-side. However, the bridge has also evolved to be able to rotate around a central axis. This area is known as the ‘waist’: see Figure 4.1(a). The area below the waist is known as the bridge base and is largely a rigid construction consisting of the two bridge feet.

Having a flexible waist is particularly important in transmitting high frequency vibration to the body. Reinicke (1973) was the first to experimentally observe that the lowest in-plane resonance of a violin bridge occurs around 3 kHz. This resonance occurs when the bridge feet are rigidly clamped and the top half of the bridge undergoes side-to-side rocking about an axis of

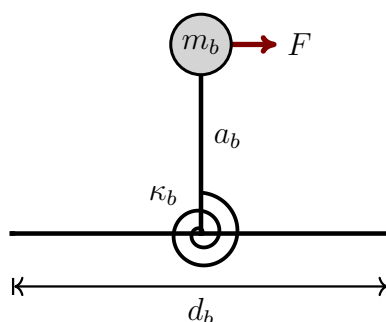


Figure 4.2: A simplified model of the bridge proposed by Woodhouse (2005). A mass, m_b , is connected to a rigid base by a bending spring with stiffness κ_b . There is a horizontal driving force, F , acting on the mass. Both ends of the bridge base, which has length d_b , make contact with the body.

rotation located in the waist area: see Figure 4.1(b). Experimental studies by Dännwald (1991) and Jansson (1997) have shown that violins in fact exhibit a peak of response around 2–3 kHz, which can be attributed to a filtering effect associated with this bridge resonance (Woodhouse, 2005). This feature has become known as the ‘bridge hill’. Further experimental studies by Jansson and Niewczyk (1997, 1999) and Jansson (2004) have shown that the appearance and frequency of the bridge hill is influenced by a number of factors including the spacing of the bridge feet and the stiffness/mass of the front plate in the vicinity of the bridge.

4.1.1 Previous bridge models

In addition to the extensive body of experimental work conducted on the bridge, investigation into simplified theoretical models of the bridge has also been undertaken. Figure 4.2 shows a simplified bridge model proposed by Woodhouse (2005). It consists of a mass, m_b , on a rigid link with length a_b , connected to a torsional spring with stiffness κ_b . This torsional spring is in turn joined to a flat base of length d_b . Both the top half of the bridge (i.e. the mass) and the bottom half (i.e. the base) are free to rotate independently around the axis of the torsional spring. The torsional spring in this context models the waist area of a real bridge. The mass-loaded rigid link models the rotational inertia of the top half of the bridge. The bridge base is modelled as a rigid body, the mass of which can be assumed to be negligible. A harmonic driving force, F , is applied horizontally at the location of the mass, and both ends of the bridge base make contact with the violin body. Woodhouse (2005) demonstrates how this model, in conjunction with a simplified violin body model that is similar to our own, can reproduce bridge hill features observed experimentally.

4.1.2 The ‘balance of the strings’

Violin makers and players often talk about the ‘balance of the strings’. Broadly speaking, this phrase is used to describe the relative strengths of the four strings. For example, when an instrument is played a player might describe one of the strings as being ‘louder’ than another. Often this is viewed as a negative characteristic and a player might seek the advice of a maker to adjust the balance of the strings. When makers approach this problem, they often consider soundpost set-up to be a major factor affecting the balance of the strings.

Dilworth (2017) remarks that

If the sound is unbalanced across the strings, adjust the top and bottom end of the post separately: the bottom of the post seems to affect the bass strings and vice versa.

This observation is particularly interesting as it concerns the boundary conditions at either end of the soundpost and implies that differences between the front and back plate coupling can affect the balance of different strings. On soundpost position, Filmer (2009) remarks that

Moving the post towards the lower strings or to the upper strings adds more focus to those strings.

While it is difficult to define precisely what ‘focus’ means in this context, one can assume that it relates in part to the loudness of the string.

From an acoustics perspective, there is no doubt that adjustments to the soundpost, in terms of position and coupling strength, do influence the resonances of the body. But the question here is whether we can attempt to understand how the dynamics at each of the different string notches is influenced by the soundpost. The ‘string notches’ are small grooves cut into the top of the bridge at the position of each string: see Figure 4.1(a). The profile of the top of a violin bridge is both curved and asymmetric between the left and right sides. Additionally, with the soundpost typically placed off-centre, near the right bridge foot, it is clear that the dynamics of the instrument will differ depending on which string is providing the input force to the bridge and subsequently the body.

4.1.3 Introducing our new proposed bridge model

We will now present a new simplified bridge model. Building upon the model proposed by Woodhouse (2005), our bridge model introduces some additional features. These additional features concern the rigid bridge base and the location of the input driving force.

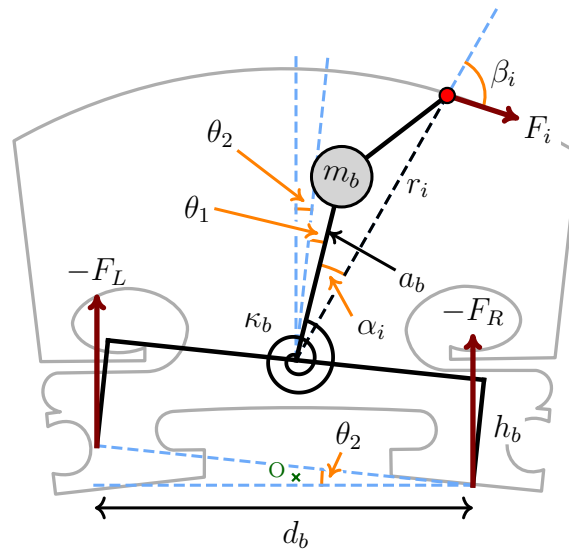


Figure 4.3: A diagram of the proposed bridge model with important system variables labelled. The model is shown overlaid on an outline of a real violin bridge.

In the bridge model proposed by Woodhouse (2005), the waist area of the bridge, modelled by the torsional spring, is positioned in line with the bridge base, which itself is a flat construction. We propose a new rigid bridge base design which has a height h_b . An illustration of this feature can be seen in Figure 4.3.

We wish to investigate questions surrounding aspects of string balance. To tackle such problems, we need to model the way in which the string comes into contact with the bridge. The bridge model proposed by Woodhouse (2005) considers a horizontal driving force applied at the location of the bridge mass only. Our aim has been to build upon this by changing the location of the driving force so that it can be positioned at the four string notch locations. In addition, we have developed the model so that it allows us to change the angle associated with the plane of motion of the bowed string. We are therefore able to model both horizontal and vertical components of the driving force: see Figure 4.3.

4.2 Calculating input admittance including the bridge model

In this section, we will derive an expression for the input admittance at a given string notch using our new bridge model, shown in Figure 4.3 overlaid on a real violin bridge outline. The two new defining features of our bridge model are: a) that the rigid bridge base now has a height h_b and b) that the input driving force, F_i , can be applied at each of the four string notches.¹

¹The subscript i is used here to indicate the four strings which will be labelled from 1–4. Going from left to right, the G string is labelled 1, D is 2, A is 3 and the E string is 4.

The coordinates of the string notch position will be defined as (x_i, y_i) , relative to the origin of coordinates O, mid-way between the bridge feet. The driving force F_i is applied at an angle β_i relative to r_i , which defines the distance from the string notch to the axis of rotation, i.e. the location of the torsional spring. The angle between the mass arm, which has length a_b , and r_i , is given by α_i . The rotation of the bridge base is defined by the angle θ_2 , while the rotation of the top half of the bridge is defined by the angle θ_1 . Dashed blue lines in Figure 4.3 illustrate how these angles rotate the bridge from its equilibrium position.

4.2.1 The horizontal and vertical components of the driving force

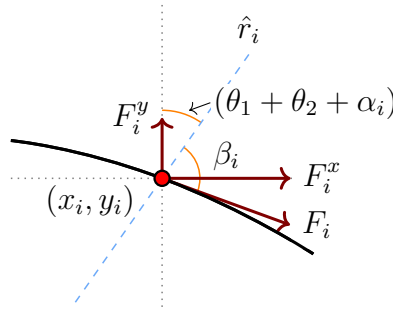


Figure 4.4: A diagram showing how the driving force, F_i , is defined in terms of the angles θ_1 , θ_2 , α_i and β_i . The horizontal and vertical components of the driving force, F_i^x and F_i^y , are also illustrated here. The coordinates of the string notch, shown by the red circle, are given by (x_i, y_i) . The angles $(\theta_1 + \theta_2 + \alpha_i)$ define the direction of the unit vector \hat{r}_i , which connects the string notch to the axis of rotation.

To calculate the input admittance, we need to calculate the velocity at the string notch, (\dot{x}_i, \dot{y}_i) , in the direction in which it is being forced. This will therefore be determined by the orientation of the force vector. Figure 4.4 shows a magnified view of the string notch and demonstrates how the angle of the driving force, F_i , relates to the various system variables. From this, the horizontal and vertical components of the driving force can be defined as

$$F_i^x = F_i \sin(\theta_1 + \theta_2 + \alpha_i + \beta_i) \quad (4.1)$$

and
$$F_i^y = F_i \cos(\theta_1 + \theta_2 + \alpha_i + \beta_i). \quad (4.2)$$

Therefore, the orientation of the force vector is governed by the unit vector

$$\mathbf{n}_i = \left[\sin(\theta_1 + \theta_2 + \alpha_i + \beta_i), \cos(\theta_1 + \theta_2 + \alpha_i + \beta_i) \right]. \quad (4.3)$$

Expanding the cosine and sine terms, using compound angle formulae, and writing the x and y components separately for clarity, we have

$$n_i^x \approx \cos(\theta_1 + \theta_2) \sin(\alpha_i + \beta_i) + \sin(\theta_1 + \theta_2) \cos(\alpha_i + \beta_i) \quad (4.4)$$

and
$$n_i^y \approx \cos(\theta_1 + \theta_2) \cos(\alpha_i + \beta_i) - \sin(\theta_1 + \theta_2) \sin(\alpha_i + \beta_i). \quad (4.5)$$

Small angle approximations for θ_1 and θ_2 will be made throughout this derivation. These are

$$\sin \theta \approx \theta, \quad (4.6)$$

$$\cos \theta \approx 1 - \frac{\theta^2}{2} \approx 1 \quad (4.7)$$

and
$$\tan \theta \approx \theta. \quad (4.8)$$

Therefore, Equations 4.4 and 4.5 can be written as

$$n_i^x \approx \sin(\alpha_i + \beta_i) + (\theta_1 + \theta_2) \cos(\alpha_i + \beta_i) \quad (4.9)$$

and
$$n_i^y \approx \cos(\alpha_i + \beta_i) - (\theta_1 + \theta_2) \sin(\alpha_i + \beta_i). \quad (4.10)$$

We can now formally define Y_i as

$$Y_i = \frac{(\dot{x}_i, \dot{y}_i) \cdot \mathbf{n}_i}{F_i}. \quad (4.11)$$

4.2.2 The velocity at the string notch

The coordinates of the string notch can be determined from Figure 4.3. Measured from the origin, O, these are

$$x_i \approx h_b \theta_2 + r_i \sin(\alpha_i + \theta_1 + \theta_2) \quad (4.12)$$

and
$$y_i \approx \frac{y_L + y_R}{2} + h_b + r_i \cos(\alpha_i + \theta_1 + \theta_2). \quad (4.13)$$

Using compound angle formulae and the appropriate small angle approximations we can write

$$x_i \approx h_b \theta_2 + r_i (\sin \alpha_i + (\theta_1 + \theta_2) \cos \alpha_i) \quad (4.14)$$

and
$$y_i \approx \frac{y_L + y_R}{2} + h_b + r_i (\cos \alpha_i - (\theta_1 + \theta_2) \sin \alpha_i). \quad (4.15)$$

Taking the derivative of (x_i, y_i) with respect to time gives

$$\dot{x}_i \approx i\omega(h_b\theta_2 + r_i(\theta_1 + \theta_2) \cos \alpha_i) \quad (4.16)$$

and

$$\dot{y}_i \approx i\omega\left(\frac{y_L + y_R}{2} - r_i(\theta_1 + \theta_2) \sin \alpha_i\right). \quad (4.17)$$

Next, we will evaluate $(\dot{x}_i, \dot{y}_i) \cdot \mathbf{n}_i$. Ignoring any second-order terms that may arise, we have the following expressions, in which we have separated the x and y terms for clarity:

$$\dot{x}_i n_i^x \approx i\omega(h_b\theta_2 \sin(\alpha_i + \beta_i) + r_i(\theta_1 + \theta_2) \cos \alpha_i \sin(\alpha_i + \beta_i)) \quad (4.18)$$

and

$$\dot{y}_i n_i^y \approx i\omega\left(\frac{y_L + y_R}{2} \cos(\alpha_i + \beta_i) - r_i(\theta_1 + \theta_2) \sin \alpha_i \cos(\alpha_i + \beta_i)\right). \quad (4.19)$$

Therefore, adding these together, and using compound angle formulae to condense the expression, we get

$$(\dot{x}_i, \dot{y}_i) \cdot \mathbf{n}_i \approx i\omega\left(h_b\theta_2 \sin(\alpha_i + \beta_i) + r_i(\theta_1 + \theta_2) \sin \beta_i + \frac{y_L + y_R}{2} \cos(\alpha_i + \beta_i)\right). \quad (4.20)$$

As an aside, if we were to set $\alpha_i = 0$, $\beta_i = \pi/2$, $r_i = a_b$ and $h_b = 0$ this should return the original bridge design as described in Woodhouse (2005). Indeed, this gives

$$(\dot{x}_i, \dot{y}_i) \cdot \mathbf{n}_i \approx i\omega a_b (\theta_1 + \theta_2). \quad (4.21)$$

Finally, Y_i can be written in its full form as

$$Y_i \approx \frac{i\omega\left(h_b\theta_2 \sin(\alpha_i + \beta_i) + r_i(\theta_1 + \theta_2) \sin \beta_i + \frac{y_L + y_R}{2} \cos(\alpha_i + \beta_i)\right)}{F_i}. \quad (4.22)$$

There are four unknowns in this equation: y_L , y_R , θ_1 and θ_2 .

4.2.3 The displacement of the bridge feet

The velocity, v , at the left and right bridge feet can be written in terms of the forces at the two bridge feet, F_L and F_R , as well as the plate admittance, Y_{IJ} . Recall that the plate admittance can

be calculated via the formula

$$Y_{IJ} = \frac{v_I}{F_J} = i\omega \sum_{n=1}^N \frac{\tilde{\mathbf{u}}_{\mathbf{i}}^{(n)}(x_I, y_I) \tilde{\mathbf{u}}_{\mathbf{i}}^{(n)}(x_J, y_J)}{\omega_n^2 + 2i\omega\omega_n\zeta_n - \omega^2}, \quad (4.23)$$

where I and J represent points on the plate. Therefore, the velocity (and by extension the displacement y) at each of the bridge feet can be expressed as

$$v_L = i\omega y_L = Y_{LL}F_L + Y_{LR}F_R \quad (4.24)$$

and

$$v_R = i\omega y_R = Y_{RL}F_L + Y_{RR}F_R. \quad (4.25)$$

The angle θ_2 , which describes the rigid body rotation of the base, can be written in terms of the displacement of the two bridge feet as

$$\theta_2 \approx \frac{y_L - y_R}{d_b}. \quad (4.26)$$

However, given we have equations for y_L and y_R written in terms of the plate admittance, the expression for θ_2 can be rewritten as

$$\theta_2 \approx \frac{1}{i\omega} \frac{(Y_{LL}F_L + Y_{LR}F_R - Y_{RL}F_L - Y_{RR}F_R)}{d_b} \quad (4.27)$$

$$\approx \frac{Y_{LL} - Y_{RL}}{i\omega d_b} F_L + \frac{Y_{LR} - Y_{RR}}{i\omega d_b} F_R \approx A_1 F_L + A_2 F_R, \quad (4.28)$$

where for clarity we have used A_1 and A_2 to denote the terms which multiply with F_L and F_R .

4.2.4 Balancing moments and forces

It has been shown that the displacement of the bridge feet, y_L and y_R , can be written in terms of F_L and F_R . Furthermore, we know that θ_2 can be written in terms of F_L and F_R . Therefore, in order to calculate the bridge input admittance, as defined in Equation 4.22, we still require expressions for three unknowns: F_L , F_R and θ_1 . To find expressions for these, we will calculate governing equations for the base and top half of the bridge by the following procedures:

- balancing moments;
- balancing horizontal forces; and
- balancing vertical forces.

These steps will provide us with simultaneous equations in terms of F_L , F_R and θ_1 , the values required to calculate Y_i .

The bridge base

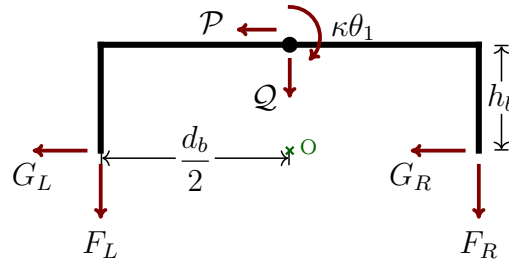


Figure 4.5: A diagram showing the forces present at the location of the spring and at the two bridge feet.

A detailed diagram of the bridge base, illustrating the forces present at the location of the spring and at the two bridge feet, is shown in Figure 4.5. Balancing vertical forces gives

$$F_L + F_R + Q = 0. \quad (4.29)$$

Similarly, balancing horizontal forces gives

$$G_L + G_R + P = 0. \quad (4.30)$$

The base rotates as a rigid body about the origin, O. Taking moments at O, in the context of a clockwise rotation, gives the following expression:

$$-\frac{d_b}{2}F_L + \frac{d_b}{2}F_R + \kappa_b\theta_1 - Ph_b = 0. \quad (4.31)$$

Equations 4.29, 4.30 and 4.31 are our three governing equations for the bridge base.

The upper half of the bridge

We will now apply the same procedure to the upper half of the bridge. Figure 4.6(a) shows a diagram of the forces acting on the upper half of the bridge. Figure 4.6(b) illustrates how the string driving force, F_i , can be defined in terms of horizontal and vertical components. While the bridge base is massless, the upper half of the bridge consists of the bridge mass, m_b . Its location

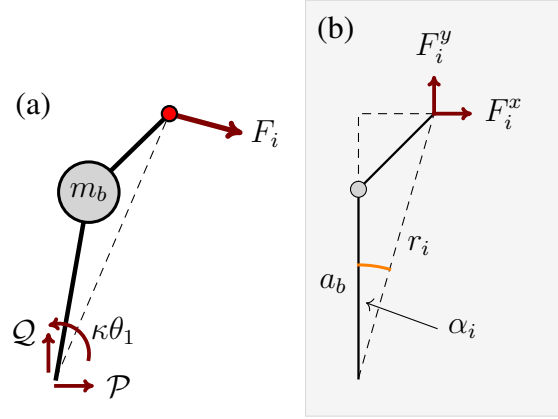


Figure 4.6: (a) A diagram showing the forces acting on the upper half of the bridge. (b) The string driving force, F_i , defined in terms of its horizontal and vertical components.

is given by the coordinate (x_m, y_m) . Balancing vertical forces gives

$$Q + F_i^y = m_b \ddot{y}_m . \quad (4.32)$$

Taking the definition of F_i^y from Equation 4.2 to first-order gives

$$F_i^y \approx F_i \cos(\alpha_i + \beta_i) . \quad (4.33)$$

The coordinate y_m is given by

$$y_m = \frac{y_L + y_R}{2} + h_b + a_b . \quad (4.34)$$

Calculating \ddot{y}_m gives

$$\ddot{y}_m = -\omega^2 \left(\frac{y_L + y_R}{2} \right) . \quad (4.35)$$

Therefore, we can express Equation 4.32 as

$$Q + F_i \cos(\alpha_i + \beta_i) \approx -m_b \omega^2 \left(\frac{y_L + y_R}{2} \right) . \quad (4.36)$$

Balancing horizontal forces gives

$$P + F_i^x = m_b \ddot{x}_m . \quad (4.37)$$

Taking the definition of F_i^x from Equation 4.1 to first-order gives

$$F_i^x \approx F_i \sin(\alpha_i + \beta_i). \quad (4.38)$$

The coordinate x_m is given by

$$x_m \approx h_b \theta_2 + a_b(\theta_1 + \theta_2) \approx (h_b + a_b)\theta_2 + a_b \theta_1. \quad (4.39)$$

Calculating \ddot{x}_m gives

$$\ddot{x}_m \approx -\omega^2(h_b + a_b)\theta_2 - \omega^2 a_b \theta_1. \quad (4.40)$$

Therefore, we can express Equation 4.37 as

$$\mathcal{P} + F_i \sin(\alpha_i + \beta_i) \approx -m_b \omega^2 \left((h_b + a_b)\theta_2 + a_b \theta_1 \right). \quad (4.41)$$

Taking moments at m_b , in an anti-clockwise direction, we have

$$\mathcal{P} a_b + \kappa_b \theta_1 - F_i^x (r_i \cos \alpha_i - a_b) + F_i^y r_i \sin \alpha_i \approx 0. \quad (4.42)$$

Writing F_i^x and F_i^y as first-order expressions in terms of F_i we have

$$\mathcal{P} a_b + \kappa_b \theta_1 - F_i (r_i \cos \alpha_i - a_b) \sin(\alpha_i + \beta_i) + F_i r_i \sin \alpha_i \cos(\alpha_i + \beta_i) \approx 0. \quad (4.43)$$

Equations 4.36, 4.41 and 4.43 are our three governing equations for the upper half of the bridge.

4.2.5 Solving the simultaneous equations

We can use Equation 4.29 to eliminate Q from Equation 4.36. This gives

$$F_i \cos(\alpha_i + \beta_i) \approx F_L + F_R - m_b \omega^2 \left(\frac{y_L + y_R}{2} \right). \quad (4.44)$$

We can further simplify by re-writing y_L and y_R in terms of F_L and F_R :

$$\frac{y_L + y_R}{2} = \frac{1}{2i\omega} (Y_{LL} F_L + Y_{LR} F_L + Y_{RR} F_R + Y_{RL} F_R) \quad (4.45)$$

$$= A_3 F_L + A_4 F_R, \quad (4.46)$$

where

$$A_3 = \frac{Y_{LL} + Y_{LR}}{2i\omega} \quad (4.47)$$

and

$$A_4 = \frac{Y_{RR} + Y_{RL}}{2i\omega}. \quad (4.48)$$

This means that Equation 4.44 can be written as

$$F_i \cos(\alpha_i + \beta_i) \approx (1 - m_b \omega^2 A_3) F_L + (1 - m_b \omega^2 A_4) F_R. \quad (4.49)$$

Re-writing θ_2 in terms of F_L and F_R (see Equation 4.28), we can re-define Equation 4.41 as

$$\mathcal{P} + F_i \sin(\alpha_i + \beta_i) \approx -m_b \omega^2 \left((h_b + a_b)(A_1 F_L + A_2 F_R) + a_b \theta_1 \right). \quad (4.50)$$

This gives us four simultaneous equations (Equations 4.31, 4.43, 4.49 and 4.50) in terms of four unknowns (F_L , F_R , θ_1 and \mathcal{P}). We can write these equations in matrix form:

$$\begin{bmatrix} -\frac{d_b}{2} & +\frac{d_b}{2} & \kappa_b & -h_b \\ -m_b \omega^2 (h_b + a_b) A_1 & -m_b \omega^2 (h_b + a_b) A_2 & -m_b \omega^2 a_b & -1 \\ 0 & 0 & \kappa_b & a_b \\ 1 - m_b \omega^2 A_3 & 1 - m_b \omega^2 A_4 & 0 & 0 \end{bmatrix} \begin{bmatrix} F_L \\ F_R \\ \theta_1 \\ \mathcal{P} \end{bmatrix} \approx \begin{bmatrix} 0 \\ F_i \sin(\alpha_i + \beta_i) \\ F_i (r_i \sin \beta_i - a_b \sin(\alpha_i + \beta_i)) \\ F_i \cos(\alpha_i + \beta_i) \end{bmatrix}. \quad (4.51)$$

This set of linear simultaneous equations is straightforward to solve using MATLAB. This will provide solutions to F_L , F_R and θ_1 which will enable Y_i to be calculated.

4.2.6 How the angles are calculated

The variables which define the location of each string notch (α_i , β_i and r_i) have all been defined in terms of the axis of rotation, i.e. the location of the torsional spring. This was convenient for

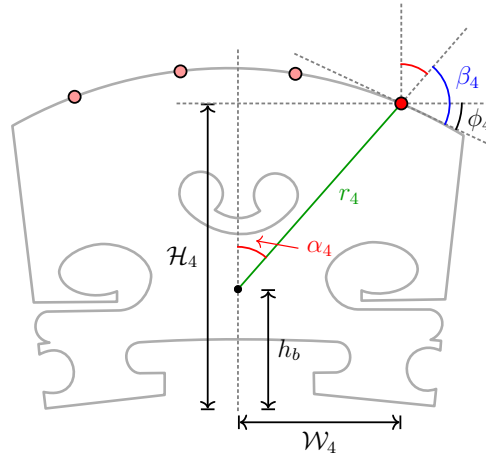


Figure 4.7: A diagram showing how the parameters \mathcal{H}_i , \mathcal{W}_i and ϕ_i are assigned. From these parameters, the values of α_i , β_i and r_i can be calculated. The E string, which is labelled as the fourth string, is shown here as an example.

the purpose of deriving the equations of motion of our system, however, there will be instances where we want to change the position of the axis of rotation and keep the positions of the string notches fixed, in which case we will have to recalculate the values of α_i , β_i and r_i .

To tackle this problem, Figure 4.7 shows how the location of each string notch can be defined in terms of its height measured from the base, \mathcal{H}_i , its distance from the centre, \mathcal{W}_i , and the tangential angle it makes with the curve of the bridge, ϕ_i . From these values, which will remain fixed, we can calculate values of α_i , β_i and r_i using

$$\alpha_i = \arctan \frac{\mathcal{W}_i}{\mathcal{H}_i - h_b}, \quad (4.52)$$

$$\beta_i = \frac{\pi}{2} - \alpha_i + \phi_i \quad (4.53)$$

and

$$r_i = \frac{\mathcal{W}_i}{\sin \alpha_i}. \quad (4.54)$$

It is important to note that violin bridges are not symmetric. That is to say, the profile of the top of the left hand side (i.e. where the G and D string notches are located) is not a mirror reflection of the right hand side. Table 4.1 lists the values of \mathcal{H}_i , \mathcal{W}_i and ϕ_i that we have used for each string.

4.2.7 Calculating the stiffness of the torsional spring

As discussed earlier, the design of our bridge model incorporates a mass and torsional spring in order to model the lowest bridge resonance. This resonance can be obtained when the bridge feet

Table 4.1: The parameters which define the fixed location of each string notch, as illustrated in Figure 4.7.

String, i	\mathcal{H}_i (cm)	\mathcal{W}_i (cm)	ϕ_i ($^\circ$)
1. G	3.2	-1.8	-20
2. D	3.5	-0.6	-5
3. A	3.5	0.6	13
4. E	3.0	1.8	33

are held rigidly and the top half of the bridge exhibits side-to-side rocking motion. The waist of the bridge can be described as acting like a torsional spring and the top half can be represented as a mass on a rigid arm. According to our model, if the bridge is rigidly clamped at the feet, then the resonance frequency of the top half is given by

$$\Omega_b = \frac{1}{a_b} \sqrt{\frac{\kappa_b}{m_b}}. \quad (4.55)$$

Following Woodhouse (2005), we will choose to set Ω_b to be equal to 3 kHz. The mass of the top half of the bridge will be estimated as 0.5 g, and the length of the mass arm, a_b , will be determined in relation to the height of the bridge base height, h_b , and the location of the mass, m_b . Relative to the origin, O, the location of the mass will be kept fixed. This height will be called H_m and will be set at 20 mm. Therefore

$$a_b = H_m - h_b. \quad (4.56)$$

From this we can rewrite Equation 4.55 as

$$\Omega_b = \frac{1}{H_m - h_b} \sqrt{\frac{\kappa_b}{m_b}}. \quad (4.57)$$

The waist stiffness, κ_b , can therefore be calculated using

$$\kappa_b = m_b(H_m - h_b)^2 \Omega_b^2. \quad (4.58)$$

4.2.8 Verifying the model

The bridge model we have introduced here directly builds upon the bridge model developed by Woodhouse (2005). Therefore, a simple verification can be performed using the following values,

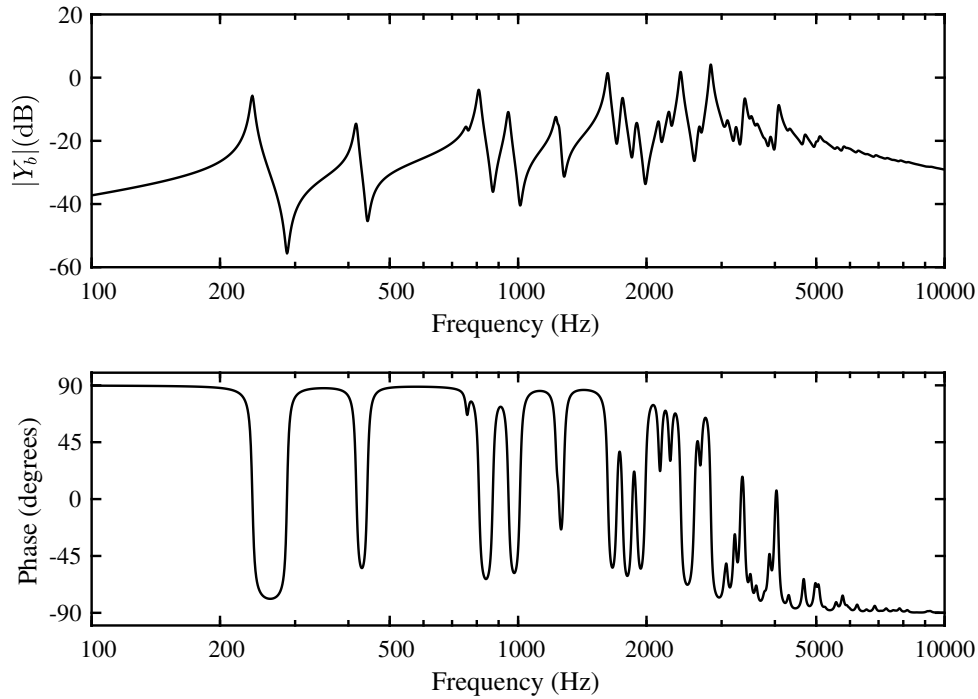


Figure 4.8: The magnitude and phase of the input admittance calculated directly at the mass, Y_b . This plot is based on the model presented here, and shows perfect agreement with Figure 7 by Woodhouse (2005).

which return the model to its form as defined in Woodhouse (2005). These values are

$$\alpha_i = 0, \quad (4.59)$$

$$\beta_i = \frac{\pi}{2}, \quad (4.60)$$

$$r_i = a_b \quad (4.61)$$

and

$$h_b = 0. \quad (4.62)$$

This represents the bridge model without a base height and with the driving force applied horizontally at the mass. To demonstrate agreement with Woodhouse (2005), we will recalculate the result plotted in Woodhouse's Figure 7. This is a plot of the bridge input admittance when the bridge is coupled only to the spruce front plate. Our result is shown in Figure 4.8. Reassuringly, there is perfect agreement. This plot also allows us to see some of the characteristic features of the bridge hill. There is an overall rise in the amplitude of response which peaks around 3 kHz. Beyond this frequency range, there is a steady amplitude decline, and, in conjunction, the phase plot shows a downward trend towards -90° .

4.3 Exploring the influence of the bridge base height

One of the new additions to our bridge model, not present in Woodhouse (2005), is the parameter h_b which describes the height of the rigid bridge base. In this section, we will explore how this new parameter influences the dynamics of the bridge. First, we will calculate the bridge input admittance using different values of h_b and compare any differences. Following this, we will conduct extensive parameter studies to investigate how variations in the base height influence the bridge hill. These studies build upon the parameter studies undertaken in Section 4 of Woodhouse (2005).

All subsequent simulations involving our bridge model will place the two bridge feet at a location near the centre of the front plate, the coordinates of which are given by

$$(x_L, y_L) = \left(a_1 - \frac{a_1}{2.1}, b_1 - \frac{b_1}{2.4} \right) \quad (4.63)$$

and

$$(x_R, y_R) = \left(a_1 - \frac{a_1}{2.1}, \frac{b_1}{2.4} \right). \quad (4.64)$$

The soundpost will be placed near the right hand bridge foot, in a location which corresponds to where it is typically placed in a violin. This choice of soundpost location was also informed by subsequent studies in Chapter 6. Its coordinates are given by

$$(x_S, y_S) = \left(a_1 - \frac{a_1}{1.9}, \frac{b_1}{2.5} \right). \quad (4.65)$$

An illustration of these locations is shown in Figure 4.9. This configuration results in a bridge base length of $d_b = 34$ mm.

4.3.1 The effect of including a bridge base height

In the following simulation, we will explore the effect of including a bridge base height in the model. We will therefore undertake a simple comparative study. This will involve calculating the bridge input admittance for the model first without a bridge base height (i.e. $h_b = 0$) and then for bridge heights of 5 and 10 mm. In all cases, recall that the total height of the bridge remains constant. Figure 4.10 shows the input admittance Y_1 as well as a diagram of the three different bridge models used. For the sake of simplicity, we have considered only the G string input admittance, Y_1 , in this first instance. The parameters of the model follow those laid out in

²The stiffness of the soundpost coupling springs were set to $k = 10^6$ N/m and $\kappa = 10^4$ Nm/rad.

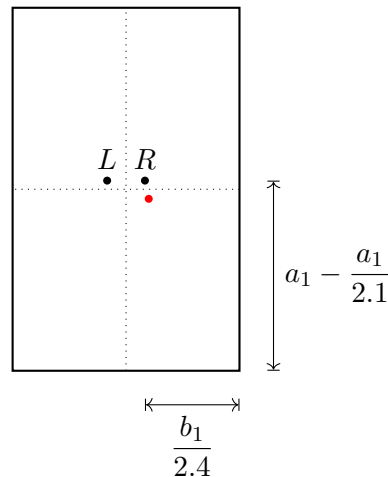


Figure 4.9: A diagram of the front plate showing the location of the left (L) and right (R) bridge feet. The location of the soundpost is shown by a red circle below the right bridge foot.

Section 2 and the model includes a soundpost.² The first main observation is that there is a clear bridge hill feature seen in all three plots. There is a prominent peak in response around 3 kHz which is followed by a decline in amplitude. All three plots closely resemble each other, although, as an overall trend, the amplitude of the resonances increases as the height of the bridge base increases.

One notable addition to these plots, in comparison to Figure 4.8, is that we see a resonance below 200 Hz. As will be discussed in detail in a later section, the appearance of this resonance is a result of there being a vertical component of force at the driving point, a feature which is not found in Woodhouse (2005).

4.3.2 Calculating the response ‘skeleton’

We will now proceed to conduct some further parameter studies where we will vary the bridge bass height, h_b . This study will be conducted in the style of Woodhouse (2005). We will therefore employ a technique based on “Skudrzyk’s mean-value method” (see Skudrzyk, 1980) to look at the underlying bridge hill without individual modes appearing in the frequency response and distracting our attention. The key concept behind the mean-value method is that for any input admittance, the height of an isolated resonance peak is proportional to $\frac{1}{\zeta_n}$, while the depth of an anti-resonance dip is proportional to ζ_n . Furthermore, if this input admittance is plotted on a logarithmic scale, then the resonance peaks extend above the mean value as much as the anti-resonances extend below it. As the damping is increased, the height of the peaks decrease proportionally to the dips, which, on the other hand, are increasing. Ultimately, the peaks and dips will merge to follow the same mean response curve.

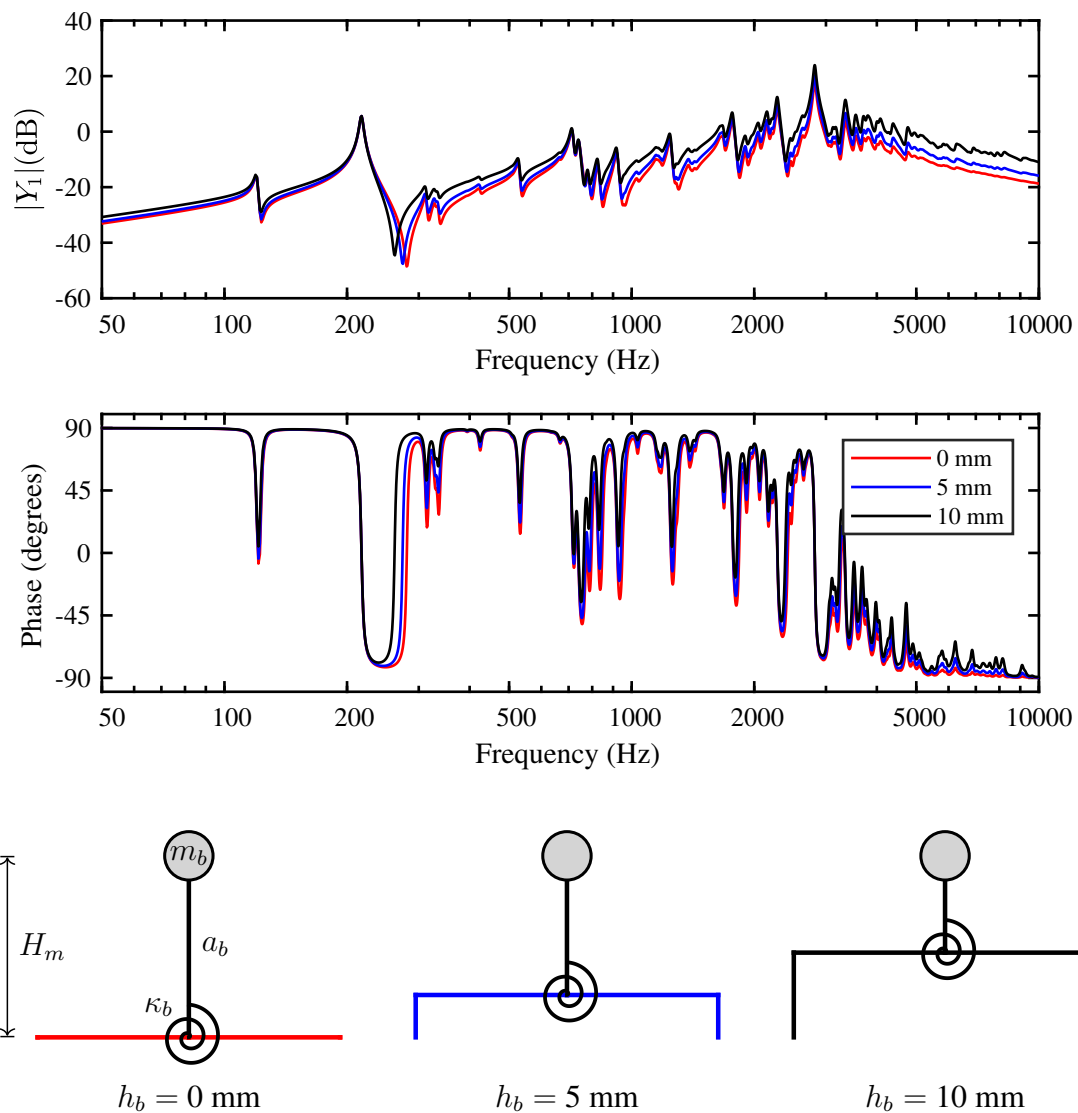


Figure 4.10: The magnitude and phase of the input admittance at the G string for three different base heights: 0, 5 and 10 mm. Three diagrams beneath illustrate these different models. Note that the height of the mass, H_m , remains fixed as h_b is varied. The length of the mass arm, a_b , is adjusted accordingly.

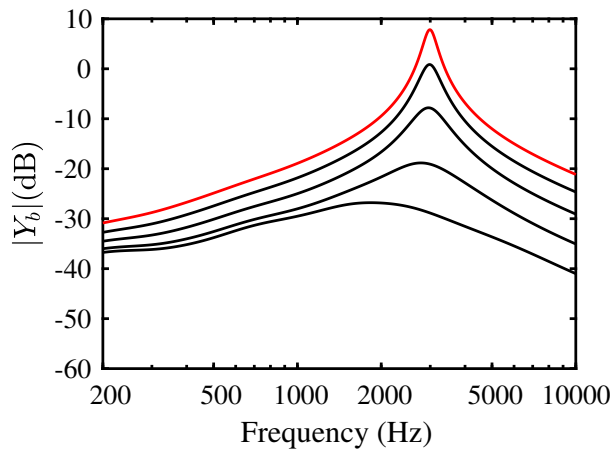


Figure 4.11: A reproduction of Figure 13 from Woodhouse (2005) showing skeleton curves for the bridge input admittance Y_b . In these plots, the bridge frequency, Ω_b , is kept fixed while the mass, m_b , and stiffness, κ_b , are varied. The plots show a mass of $m_b = 0.2, 0.3, 0.5, 1.0$ and 2.0 g, the first value being indicated by a red line and the others following in an obvious sequence.

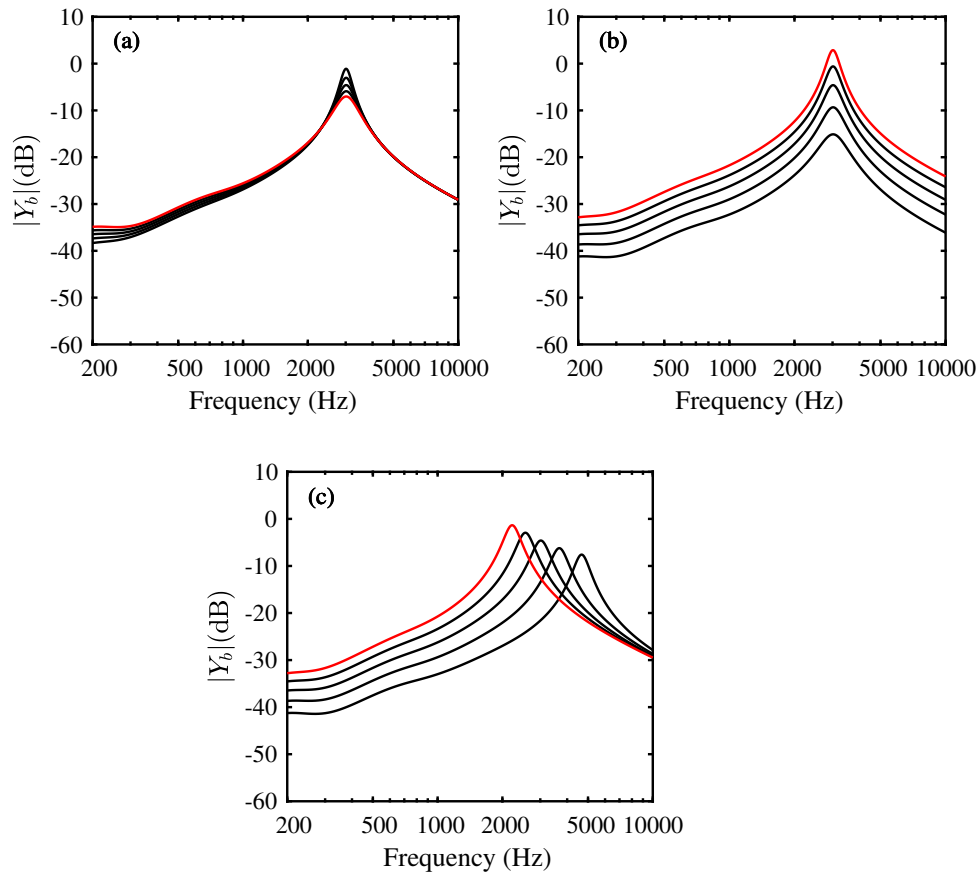
Woodhouse (2005) uses the solution for a point-driven infinite plate to calculate the response skeleton of his bridge model. However, a similar result can equally be obtained using our simplified body model, by just increasing the value of the damping term, ζ_n . To verify good agreement between the two methods, Figure 13 from Woodhouse (2005) is reproduced using our model set to the same parameter values as Woodhouse (2005), but with the modal damping Q -factor set to 2. This result is shown in Figure 4.11.

4.3.3 Varying the bridge base height

In the following study, five values of h_b have been tested: 0, 2.5, 5.0, 7.5 and 10 mm. The location of the mass, H_m , which is measured from the origin, will remain fixed at 20 mm. From Equation 4.57, we see that there remain three independent variables: Ω_b , κ_b and m_b . We will conduct three studies in which we will in turn vary each of these remaining variables in conjunction with h_b . We will not consider the string notches in these simulations, but instead calculate the skeleton curves using Y_b , the bridge input admittance driving horizontally at the mass.

The results are shown in Figure 4.12. We will analyse each sub-plot in turn:

- (a) The stiffness of the waist area, modelled by the torsional spring with stiffness κ_b , is the parameter being varied in this plot, in conjunction with the bridge base height. As h_b increases, keeping m_b and Ω_b fixed, the value of κ_b decreases. This has the effect of increasing the magnitude of the bridge hill resonance.



Variable	Unit	(a)	(b)	(c)
κ_b	Nm/rad	Vary	40	40
m_b	g	0.5	Vary	0.5
Ω_b	Hz	3000	3000	Vary

Figure 4.12: ‘Skeleton’ curves of the input admittance Y_b , showing how the ‘bridge hill’ varies. In each subplot, h_b is varied from 0 mm (plotted in red) to 2.5, 5.0, 7.5 and 10 mm: the order of the plots following in an obvious sequence. In (a), κ_b , the stiffness of the waist area, is varied while keeping m_b and Ω_b fixed. In (b), m_b , the bridge mass, is varied while keeping κ_b and Ω_b fixed. In (c), Ω_b , the bridge frequency, is varied while keeping κ_b and m_b fixed.

- (b) The mass of the bridge, m_b , is the parameter being varied in this plot, in conjunction with the bridge base height. As h_b increases, keeping κ_b and Ω_b fixed, the value of m_b increases. This has the effect of decreasing the magnitude of the Y_b .
- (c) The bridge frequency, Ω_b , is the parameter being varied in this plot, in conjunction with the bridge base height. As h_b increases, keeping κ_b and m_b fixed, the value of Ω_b increases. As expected, we therefore see the bridge hill resonance increasing in frequency. The magnitude of the resonance also falls as h_b and Ω_b increases.

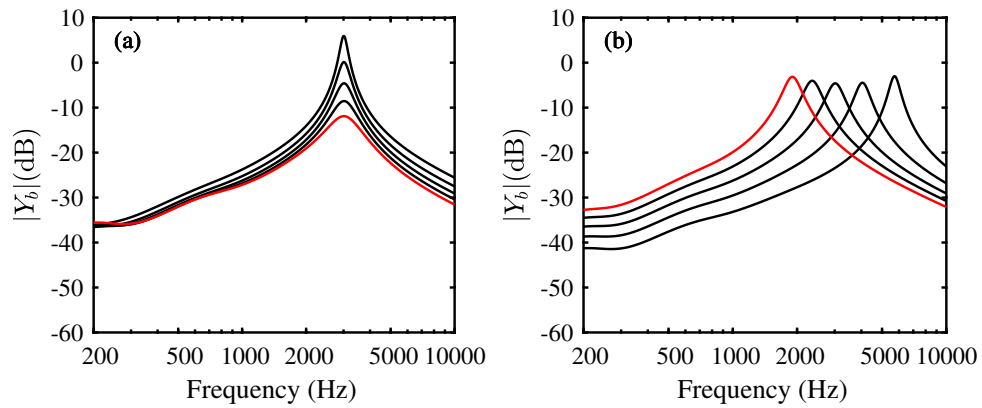
4.3.4 Varying the bridge base height and bridge mass together

To complete this set of studies, we will also proceed to vary the bridge base height and the bridge mass together. The reason for doing this is that if the bridge base height is raised, then this corresponds with a reduction in the size of the top half of the bridge. This acts to lower the mass of the top half. The following values of the bridge mass were chosen: 0.75, 0.6, 0.5, 0.4 and 0.25 g. These correspond with values of h_b in order from 0 to 10 mm. Therefore, the larger the bridge base height, the lower the mass. This leaves two remaining independent variables in Equation 4.57. We will therefore conduct two studies: one where we keep Ω_b fixed and allow κ_b to vary, and one where we keep κ_b fixed and allow Ω_b to vary.

The results are shown in Figure 4.13. Taking each sub-plot in turn:

- (a) The stiffness of the waist area, modelled by the torsional spring with stiffness κ_b , is the parameter being varied in this plot, in conjunction with the bridge base height and bridge mass. As h_b increases and m_b decreases, keeping Ω_b fixed, the value of κ_b decreases. This has the effect of increasing the magnitude of the bridge hill resonance. This change is more pronounced than in Figure 4.12(a).
- (b) The bridge frequency, Ω_b , is the parameter being varied in this plot, in conjunction with the bridge base height and bridge mass. As h_b and m_b increases, keeping κ_b fixed, the value of Ω_b increases. As expected, we see the bridge hill resonance increasing in frequency. However, unlike Figure 4.12(c), the magnitude of the resonance does not fall.

In summary, in this chapter we have developed and derived an enhanced bridge model, building upon the work by Woodhouse (2005). We have validated the model and conducted an extensive parameter study focusing on how variations to the bridge base height influence the ‘bridge hill’ for a single string. These studies complement the work presented by Woodhouse (2005) and extend it by introducing the new bridge base height. In the next chapter, we will build



Variable	Unit	(a)	(b)
κ_b	Nm/rad	Vary	40
m_b	g	Vary	Vary
Ω_b	Hz	3000	Vary

Figure 4.13: ‘Skeleton’ curves of the input admittance Y_b , showing how the ‘bridge hill’ varies. In each subplot, h_b and m_b are varied in conjunction with each other: h_b from 0 mm (plotted in red) to 2.5, 5.0, 7.5 and 10 mm and m_b from 0.75 g to 0.6, 0.5, 0.4 and 0.25 g. The order of the plots follows in an obvious sequence. In (a), κ_b , the stiffness of the waist area, is varied while keeping Ω_b fixed. In (b), Ω_b , the bridge frequency, is varied while keeping κ_b fixed.

upon these results by considering the input admittance at all four strings and studying questions relating to the ‘balance of the strings’.

5

Exploring the behaviour of the enhanced bridge model

In the previous chapter, we developed an enhanced bridge model. The model was tested to verify its validity and preliminary studies were conducted exploring the influence of the bridge base height on the input admittance of the bridge. In this chapter, we will further develop and add detail to our investigation of the vibrational behaviour of the enhanced bridge model.

5.1 Calculating the bridge input admittance without a soundpost

In this section, the bridge input admittance, Y_i , will be calculated at all four string notches. We will do this calculation without a soundpost coupling the two plates. This will allow us to identify what differences are caused when a soundpost is introduced. To help develop an understanding of the dynamics of the bridge, we will also test different angles of the string driving force.

5.1.1 The regular bridge model set-up

In this first stage of our investigation, we will test our regular set-up of the bridge model as defined in Table 4.1. The soundpost has been removed from the model by setting the stiffness of the soundpost coupling springs to zero. This decouples the soundpost from the plates. Figure 5.1 shows the results of calculating the bridge input admittance, Y_i , at each of the four string notches. Both the magnitude and the phase of Y_i are plotted.

Above 200 Hz, the magnitude of Y_i is nearly identical for all four strings. The only significant difference occurs at the first resonance, at around 100 Hz. To fully understand the reason for this,

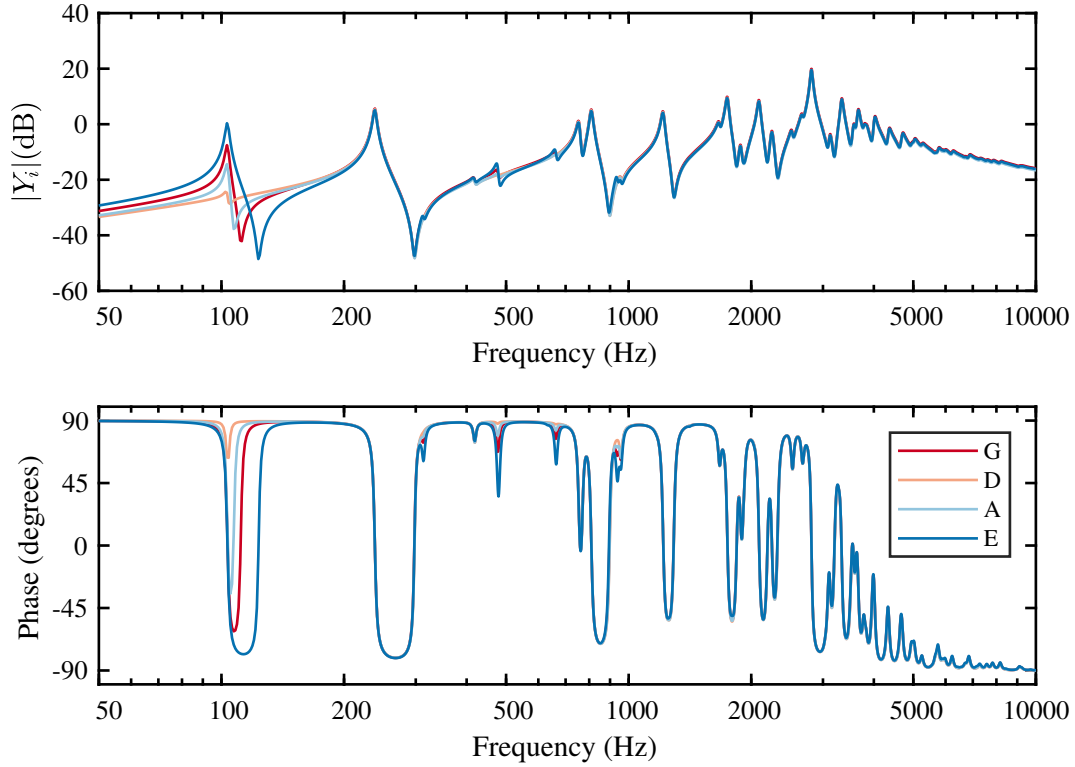


Figure 5.1: The input admittance, Y_i , calculated at the four string notches. This calculation is for the model without a soundpost. The angles of the driving force follow those presented in Table 4.1.

we need to turn our attention to the ‘mode shape’, or, strictly, the operating displacement shape (ODS) associated with this resonance. The steps required to calculate an ODS will be briefly laid out.

Recall from Section 4.2.3 that the displacement at the left and right bridge feet can be calculated using a sum of the two bridge feet forces, F_L and F_R , multiplied by the appropriate combination of admittance, Y_{IJ} . This principle can be extended to points across the entire surface of the plates. For a given frequency ω , the displacement at a particular coordinate (x_C, y_C) on the plates can be calculated using

$$X(x_C, y_C, \omega) = \frac{1}{i\omega} (F_L(\omega)Y_{LC}(\omega) + F_R(\omega)Y_{RC}(\omega)). \quad (5.1)$$

A set of results, which correspond to the input driving force being applied at the G string, is shown in Figure 5.2. The frequencies shown correspond to resonance frequencies from $|Y_1|$ which were selected using a peak finding algorithm. As expected, there is no displacement in the back plate, which is decoupled from the front plate due to the absence of the soundpost.

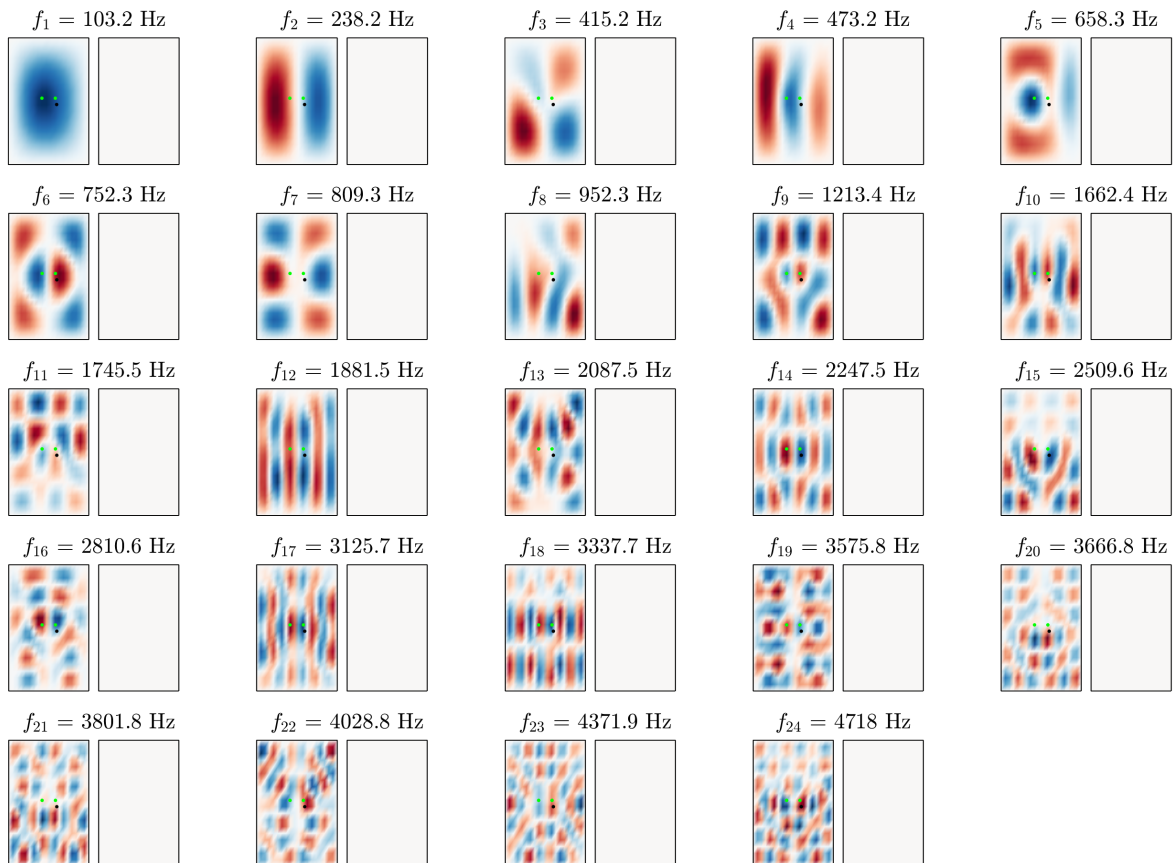


Figure 5.2: Calculating the plate ODS when an input driving force is applied at the G string. Each subplot shows a particular frequency which was chosen as a result of a peak finding algorithm applied to Y_1 , the input admittance of the G string. This model does not include a soundpost. The two filled green circles indicate the position of the bridge feet on the front plate. The filled black circle acts as a guide showing the position of the soundpost were it to be included.

Looking at the first resonance, $f_1 = 103.2$ Hz, in Figure 5.2, we see that this ODS roughly corresponds to a (1,1) mode, see Figure 2.7. This ODS relies on vertical motion applied to the plate from the two bridge feet moving in phase with each other. Therefore, this resonance is directly associated with angle of the driving force, β_i . In particular, if there is no vertical component of the driving force, then the resonance is simply not excited. This is an example of a resonance that the bridge model introduced in Woodhouse (2005) doesn't excite, because the input force there is applied horizontally without any vertical component.

Referring back to Figure 5.1, the magnitude of Y_i at 103.2 Hz is largest for the E string and smallest for the D string. It is not immediately obvious why the four strings are ordered in this way. However, if we look at the magnitude of the angle ϕ_i we see that the larger this angle, i.e. the larger the vertical component of force, the larger the amplitude of this resonance peak.

A useful way to visualise the differences between driving at each of the four string notches is to look at a cross-section through the violin body at the location of the bridge. Figure 5.3 shows plots of this type, for the resonance at 103.2 Hz (from Figure 5.1). The difference between the strings can be clearly seen. The magnitude of ODS is significantly larger for strings 1 and 4, the G and E strings respectively. Additionally, we observe a slight asymmetry in the ODS, when comparing the amplitude on the left and right hand sides of the plate. There is a bulge in the amplitude of the ODS underneath the string that is active. This is likely to be attributed to the greater vertical component of force on that particular side of the bridge.

Figure 5.4 shows the second resonance at 238.2 Hz, (from Figure 5.1). Although in Figure 5.1 the magnitude of the resonance is very similar for the four strings, when looking at the ODS in Figure 5.4 there are some subtle differences. The red crosses in Figure 5.4 highlight the points where a zero crossing occurs. If we look at the location of this red cross in each of the four subplots, 1–4, we see that the position is slightly different in each. To see this most clearly, compare the location of the red cross in the G string plot (Figure 5.4(1)) with the E string plot (Figure 5.4(4)). As with Figure 5.3, despite the bridge being positioned symmetrically on the front plate, these results show that differences in the location and angle of the driving force influence the symmetry of the plate ODS.

5.1.2 A vertical driving force

In this next stage, we will consider a purely vertical driving force at each of the four string notches. The input admittance for this set-up is shown in Figure 5.5. On first glance, it would appear that only results for the A and E strings are shown in this plot. However, the plots for the D and G strings in fact lie underneath the A and E strings respectively. This is due to the symmetry of the

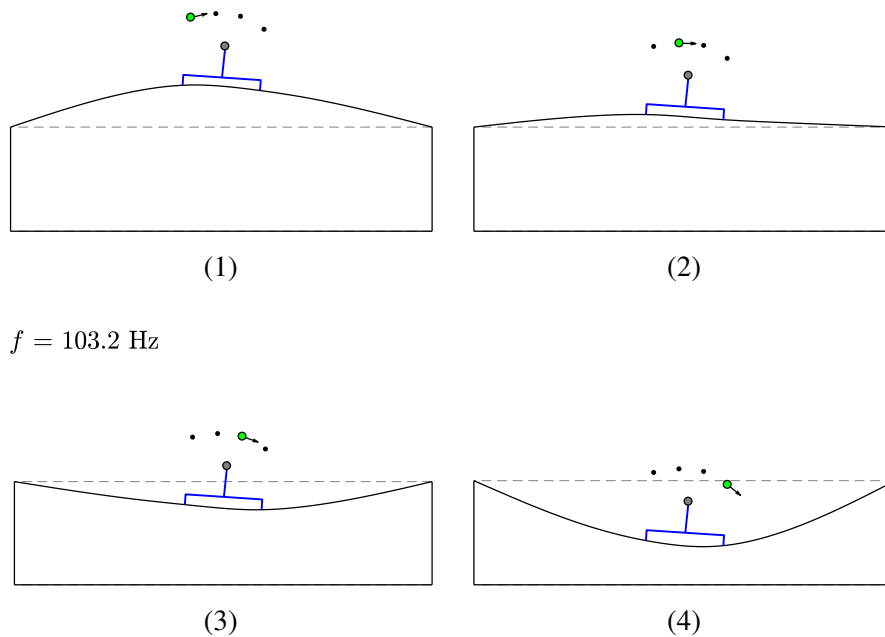


Figure 5.3: Plots showing a cross-section through the box at the position of the bridge. Each subplot corresponds to driving at one of the four strings, the active string is highlighted by a green circle. The outline of the bridge is plotted in blue. The direction of the driving force is shown by an arrow. These particular ODS are associated with the resonance at 103.2 Hz from Figure 5.1. Although the phase of the ODS is dependent on whether the component of vertical force is positive or negative, this is not important to the interpretation of the results.

bridge, now that we are considering a purely vertical driving force. For many resonances, the magnitude of the admittance is larger for the G and E strings, compared to the D and E. We can attribute this to the greater moment of force present when driving at these ‘outermost’ strings. Note, however, that the first resonance has a very similar magnitude for all four strings: this is because this resonance is characterised by the two bridge feet moving in phase with each other, as discussed in detail in the previous section. If the vertical component of the string driving force is the same for all four strings, then the magnitude of this resonance will be similar. To further visualise this result, see the cross-section plot for this first resonance (from Figure 5.5) shown in Figure 5.6. The magnitude of the ODS for all four strings is very similar. However, there is still a very subtle asymmetry to the ODS, depending on which side of the bridge is being driven.

Figure 5.7 shows the ODS of second resonance from Figure 5.5. Here we observe that driving at the outermost strings, G and E, results in similar vibrational behaviour. The only difference is that the shapes are mirrored.

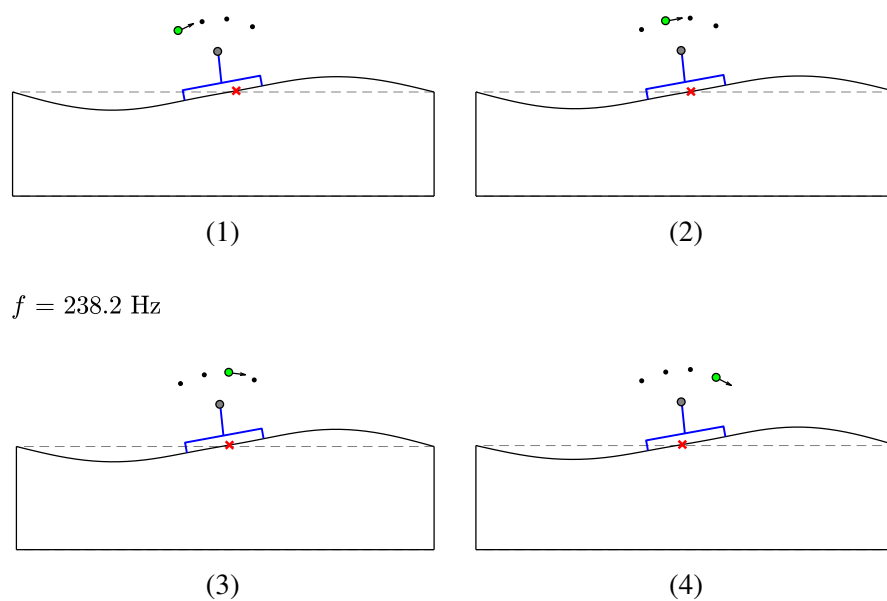


Figure 5.4: Plots showing a cross-section through the box at the position of the bridge. Each subplot corresponds to driving at one of the four strings, the active string is highlighted by a green circle. The outline of the bridge is plotted in blue. The direction of the driving force is shown by an arrow. The red crosses highlight the points where the plate ODS passes through zero. These particular ODS are associated with the resonance at 238.2 Hz from Figure 5.1. Although the phase of each diagram is similar in this instance, the phase is not important to the interpretation of the results.

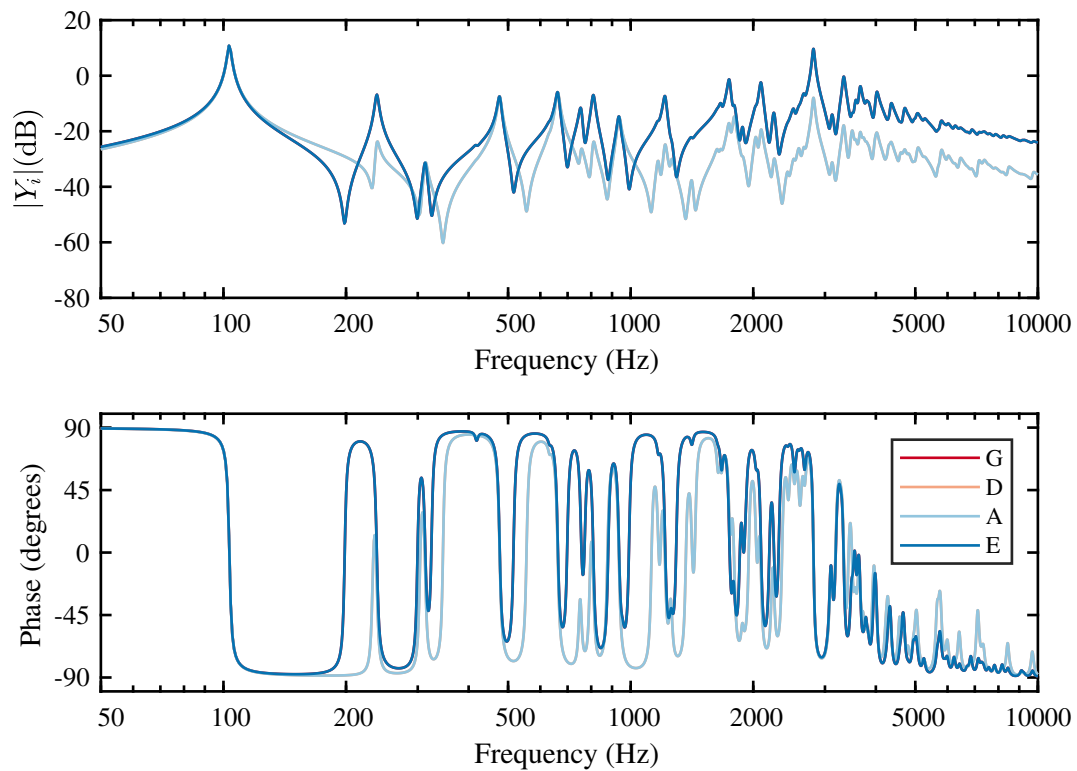


Figure 5.5: The input admittance, Y_i , calculated at the four string notches. This calculation is for the model without a soundpost and with a vertical driving force at the string notch.

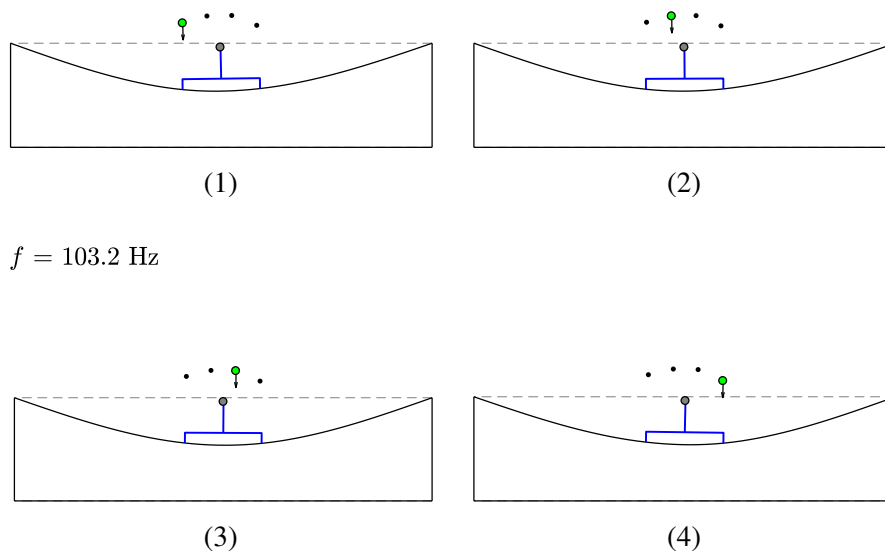


Figure 5.6: Plots showing a cross-section through the box at the position of the bridge. Each subplot corresponds to driving at one of the four strings, the active string is highlighted by a green circle. The outline of the bridge is plotted in blue. The direction of the driving force is shown by an arrow. These particular ODS are associated with the resonance at 103.2 Hz from Figure 5.5.

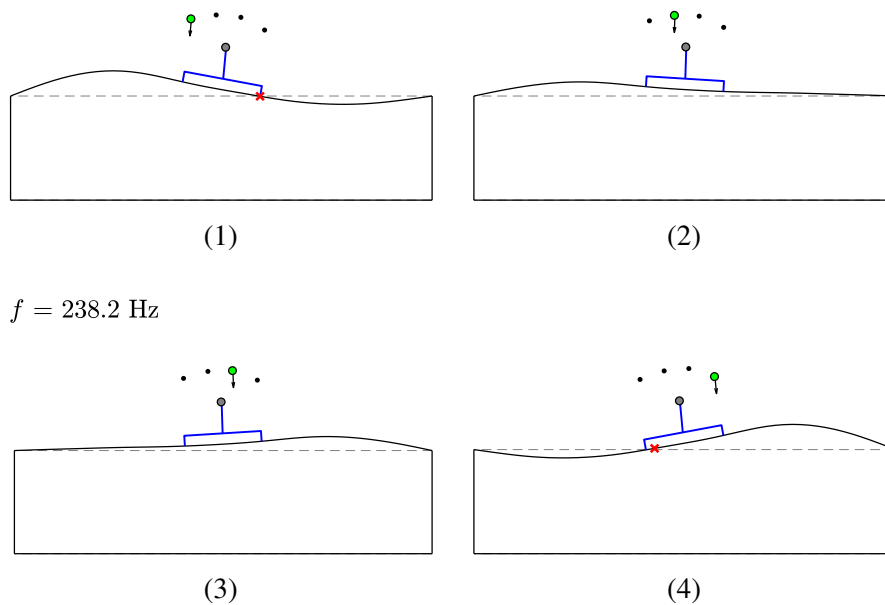


Figure 5.7: Plots showing a cross-section through the box at the position of the bridge. Each subplot corresponds to driving at one of the four strings, the active string is highlighted by a green circle. The outline of the bridge is plotted in blue. The direction of the driving force is shown by an arrow. The red crosses highlight the points where the plate ODS passes through zero. These particular ODS are associated with the resonance at 238.2 Hz from Figure 5.5.

5.1.3 A horizontal driving force

In this next stage, we will look at the case of a purely horizontal driving force. The input admittance for this set-up is shown in Figure 5.8. A very similar frequency response is seen for all four strings. The most notable feature of this graph is the absence of the resonance at around 100 Hz. This is because there is no vertical component of driving force and as a result the ODS in this frequency range is not excited.

The first resonance in this set-up occurs at 238.2 Hz. A cross-section plot is shown in Figure 5.9. We observe that the ODS associated with each string is largely identical for all four strings.

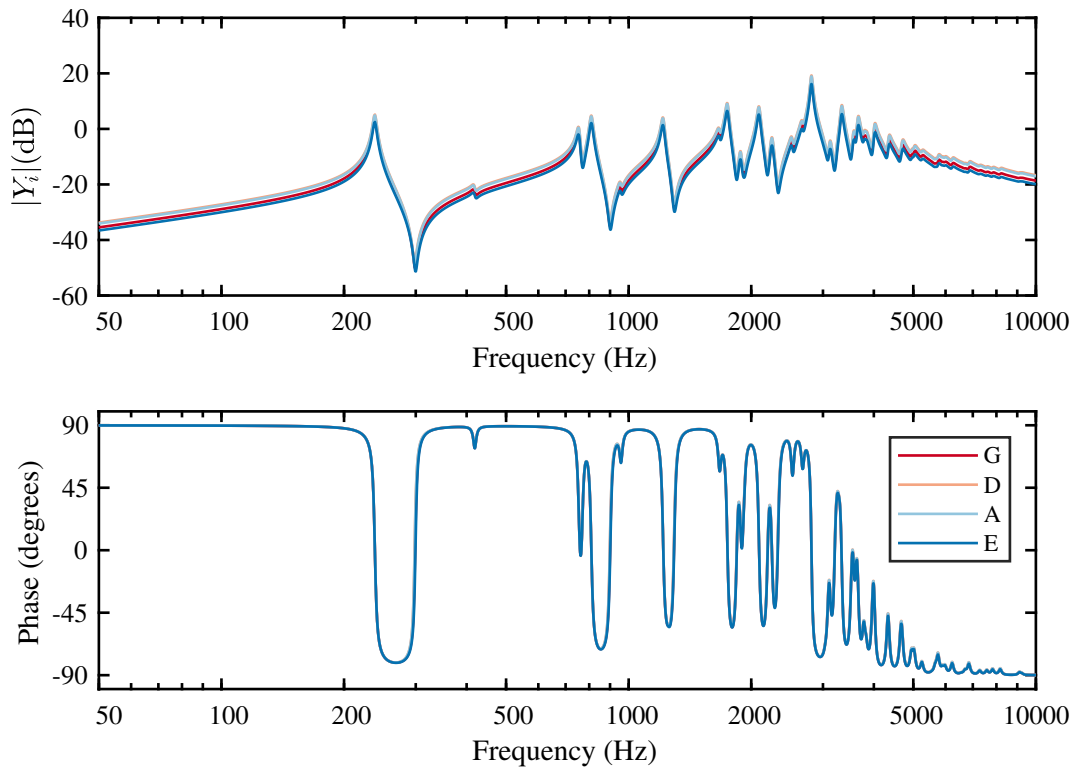


Figure 5.8: The input admittance, Y_i , calculated at the four string notches. This calculation is for the model without a soundpost and with a horizontal driving force at the string notch.

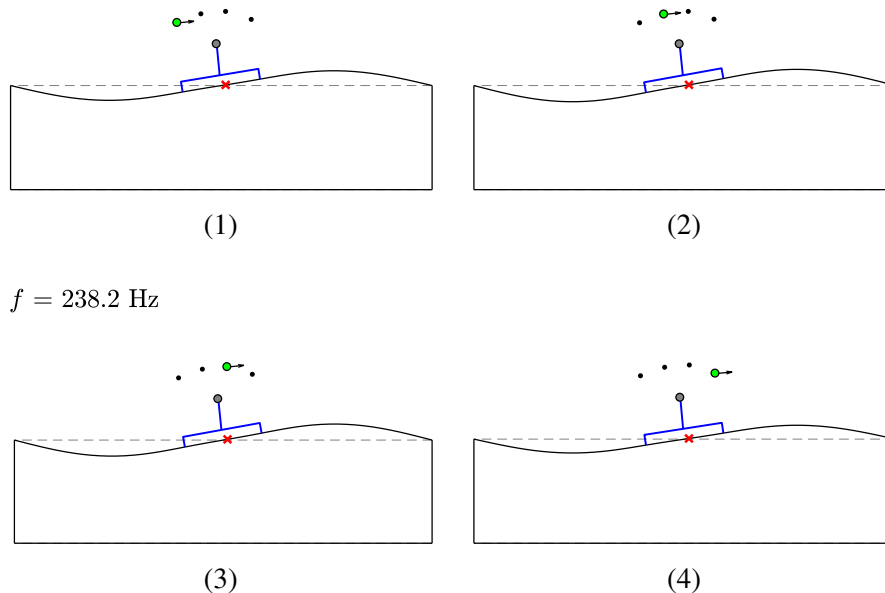


Figure 5.9: Plots showing a cross-section through the box at the position of the bridge. Each subplot corresponds to driving at one of the four strings, the active string is highlighted by a green circle. The outline of the bridge is plotted in blue. The direction of the driving force is shown by an arrow. These particular ODS are associated with the resonance at 238.2 Hz from Figure 5.8.

5.2 Calculating the bridge input admittance with a soundpost

In this section, we will introduce a soundpost into the model. The soundpost has been placed at the same location as identified in Section 4.3, slightly behind the right bridge foot as it would be normally placed in a real violin. We will first consider the regular angles of the bridge driving force, as defined in Table 4.1. Following this, we will investigate some special cases.

5.2.1 The regular model set-up

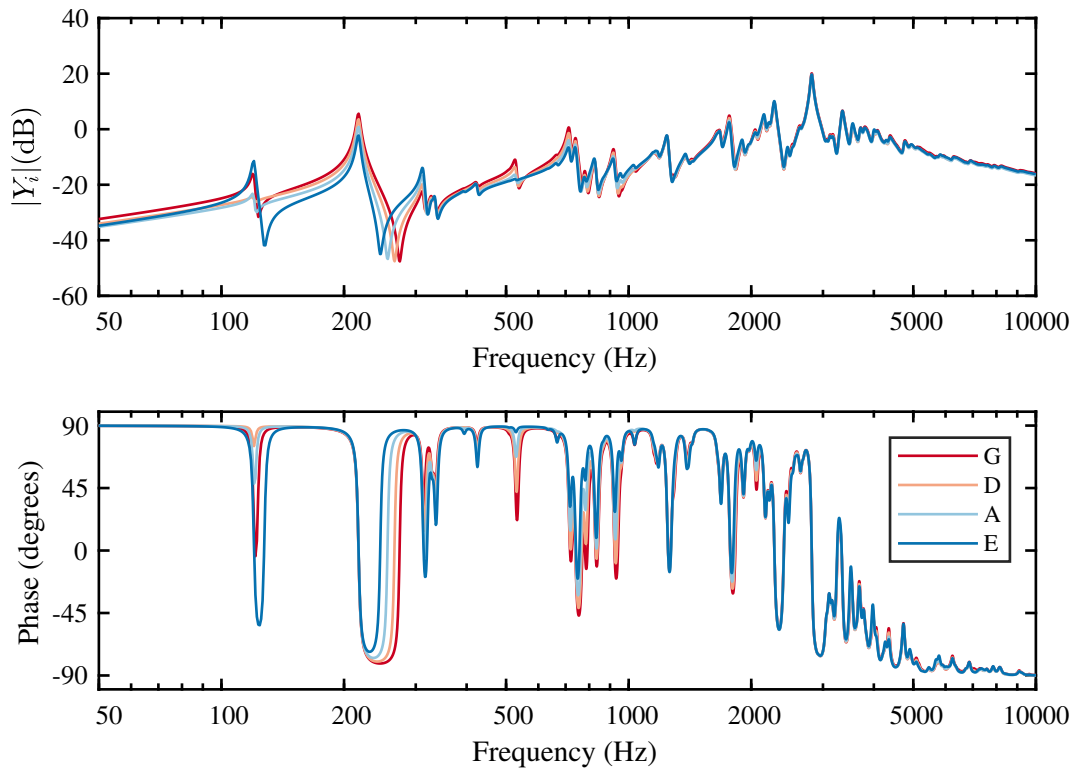


Figure 5.10: The input admittance, Y_i , measured at the four string notches. This calculation is for the model with a soundpost.

Figure 5.10 shows calculations of Y_i when a soundpost is included in the model. The angles of the string driving force follow those defined in Table 4.1. The first resonance, at 119.2 Hz, is similar to the first resonance seen in Figure 5.1 (Figure 5.1 being the direct equivalent of this calculation without a soundpost). As before, we can calculate an ODS for all the main resonances seen in Figure 5.10. These are displayed in the Figure 5.11. At the subplot labelled

$f_1 = 119.2$ Hz, the pattern displayed is similar to the equivalent resonance seen in Figure 5.2 (for the model without a soundpost). The difference is as a result of the fact that the back plate is now coupled to the front plate.

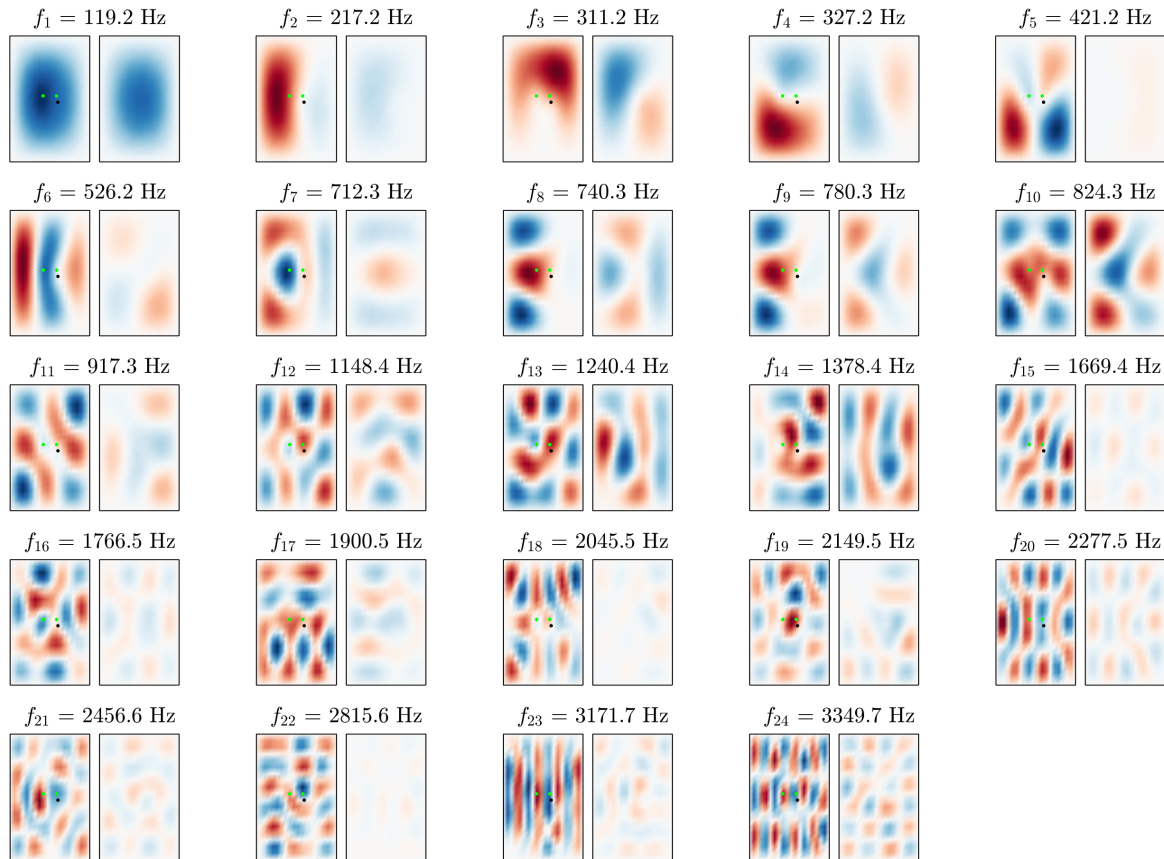


Figure 5.11: Calculating the plate ODS when an input driving force is applied at the G string. Each subplot shows a particular frequency which was chosen as a result of a peak finding algorithm applied to Y_1 , the input admittance of the G string. This model does include a soundpost, which is marked by a filled black circle. The two filled green circles indicate the position of the bridge feet on the front plate.

Figure 5.12 shows a cross-sectional view of the body for this resonance at 119.2 Hz. Comparing these subplots to Figure 5.3, we see similar features. There is a slight asymmetry in the ODS depending on which side of the bridge the input driving force is applied. The main point of difference is that the back plate is now coupled to the front plate, as a result of to the introduction of the soundpost.

The next resonance we will investigate is the second resonance seen in Figure 5.10, which occurs at 217.2 Hz. Upon close inspection of the magnitude of Y_i at this frequency, the four strings are ordered G, D, A, E, from highest amplitude to lowest amplitude. This order also corresponds to the strings as positioned from left to right. To understand why the magnitude

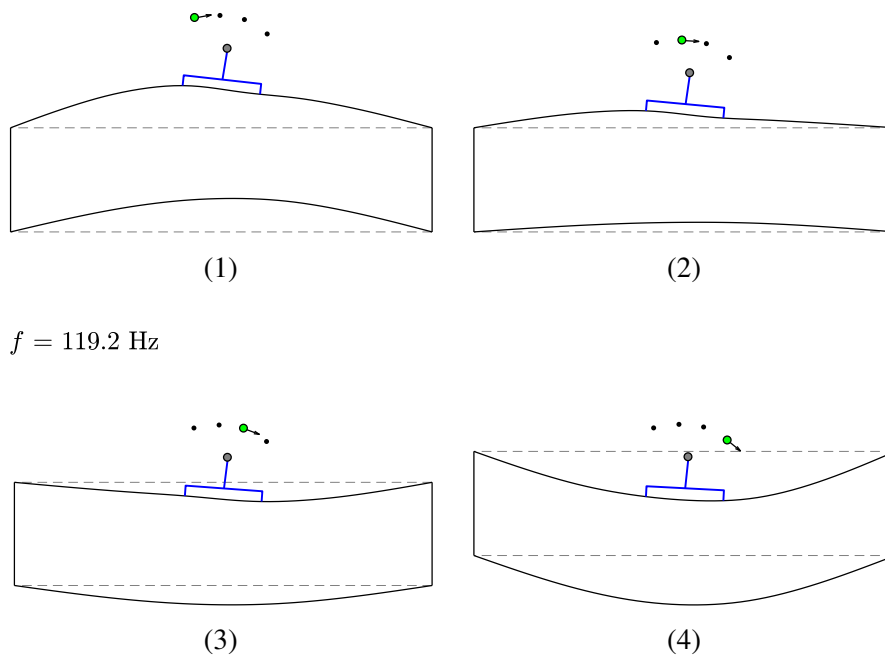


Figure 5.12: Plots showing a cross-section through the box at the position of the bridge. Each subplot corresponds to driving at one of the four strings, the active string is highlighted by a green circle. The outline of the bridge is plotted in blue. The direction of the driving force is shown by an arrow. These particular ODS are associated with the resonance at 119.2 Hz from Figure 5.10.

of the admittance differs between the four strings in this order, we can look at the plate ODS generated for each of the strings. Figure 5.13 shows a cross-section view of the body for each of the four strings at this frequency of 217.2 Hz. Here we can clearly see that the size of the ODS on the plates is largest for the G string and smallest for the E string. The red crosses indicate that the nodal point in each of the four cases occurs around the location of the right hand bridge foot. The soundpost is of course located very close to the right bridge foot, so it is unsurprising that for this particular resonance the nodal point occurs here. What is particularly interesting is visualising the differences in the amplitude of the plate ODS for each string. The further away the driving point is from the right hand bridge foot, the larger the amplitude of the plate ODS and, indeed, the larger the magnitude of Y_i . While the precise dynamics of the bridge are difficult to fully explain, if we consider the moment of force acting about this nodal point, then this is largest when the driving force is located at the string furthest away from this nodal point. This is direct evidence of the soundpost influencing the ‘balance of the strings’, and highlights the merits of our enhanced bridge model in investigating such questions.

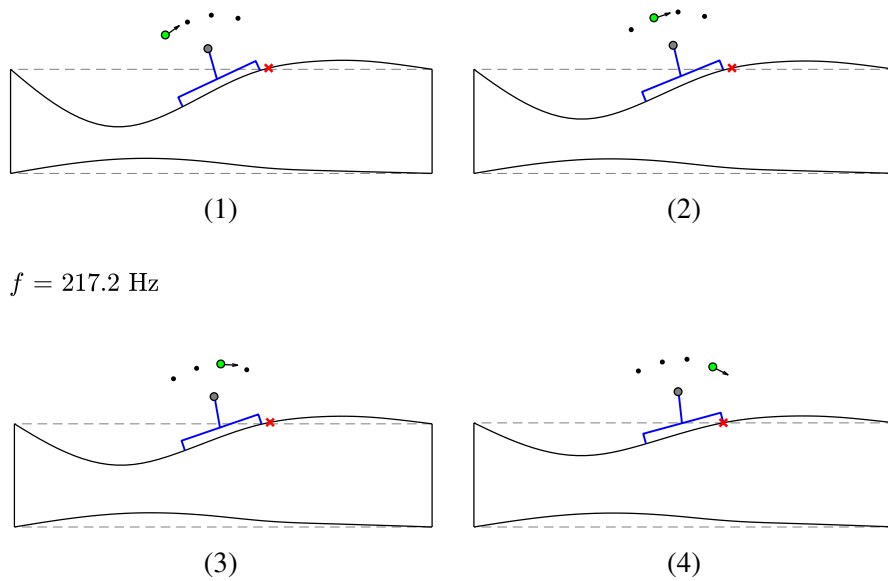


Figure 5.13: Plots showing a cross-section through the box at the position of the bridge. Each subplot corresponds to driving at one of the four strings, the active string is highlighted by a green circle. The outline of the bridge is plotted in blue. The direction of the driving force is shown by an arrow. These particular ODS are associated with the resonance at 217.2 Hz from Figure 5.10.

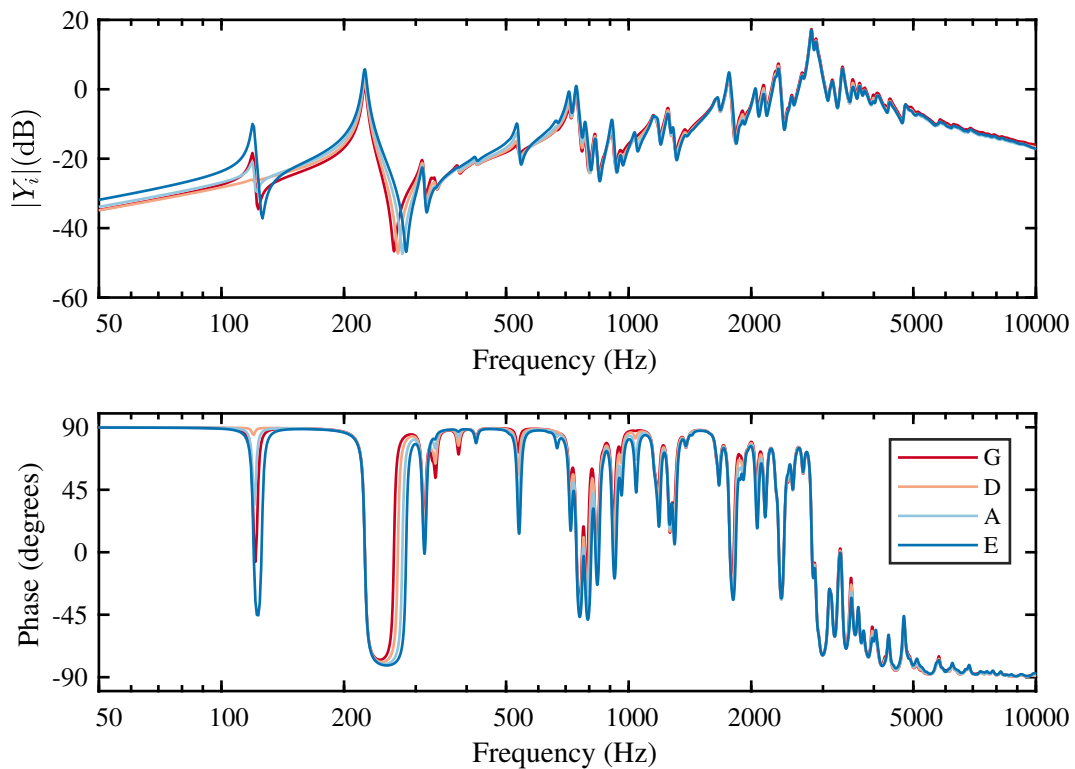


Figure 5.14: The input admittance, Y_i , measured at the four string notches. This calculation is for the model with a soundpost placed directly below the left bridge foot.

5.2.2 Placing the soundpost directly underneath the left bridge foot

To complement the results presented in the previous section, we will now demonstrate results for a soundpost placed directly underneath the left bridge foot. This switches the side of the plate on which the soundpost is located from the right hand side to the left hand side. The input admittance calculated for this arrangement is shown in Figure 5.14.

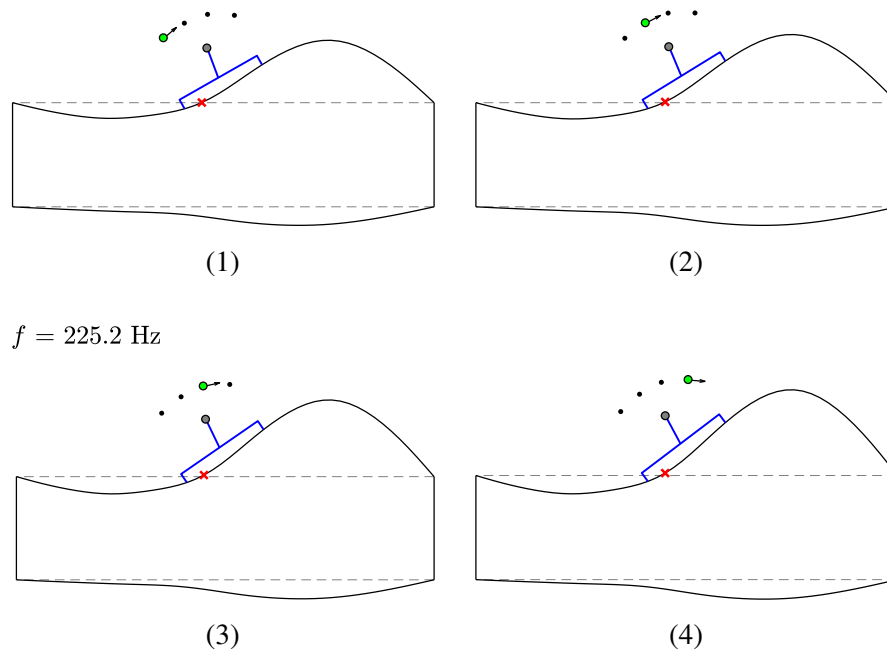
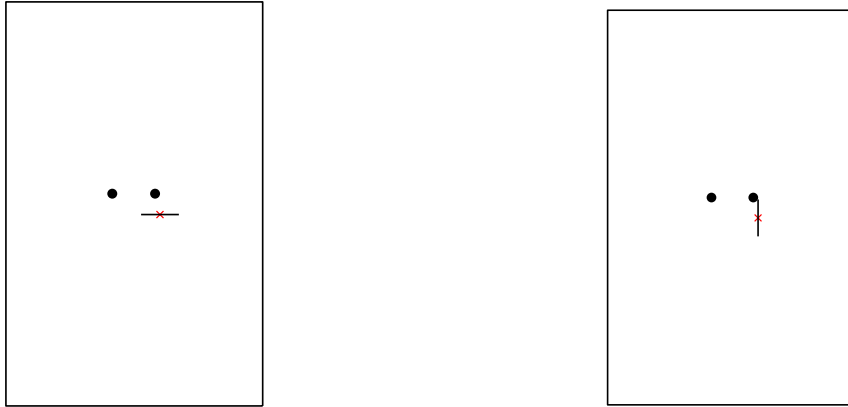


Figure 5.15: Plots showing a cross-section through the box at the position of the bridge. Each subplot corresponds to driving at one of the four strings, the active string is highlighted by a green circle. The outline of the bridge is plotted in blue. The direction of the driving force is shown by an arrow. These particular ODS are associated with the resonance at 225.2 Hz from Figure 5.14.

The most significant feature of this graph is that the order of the magnitude of many resonances is now reversed. Whereas in our earlier results the magnitudes of the resonances were ordered from G to E, these resonances are now ordered from E to G. For example, if we focus on the resonance peak at 225.2 Hz and plot the associated cross-section of the plate ODS (see Figure 5.15), we observe this effect clearly. The amplitude of the plate ODS is largest for the E string and smallest for the G string. This reflects the fact that position of the soundpost has been changed to the left hand side of the plate. The nodal point, marked with a red cross, is now located close to the left hand bridge foot.

5.3 The influence of soundpost position on the bridge input admittance



(a) East–West variation in soundpost position. (b) North–South variation in soundpost position.

Figure 5.16: A face down view of the front plate of our model. The two bridge feet are shown by the black circles. The red cross shows the ‘base’ location of the soundpost. The black line extending out from this shows ± 15 mm.

The position of the soundpost is one of the key aspects of soundpost set-up that makers focus upon. It is of particular interest here, because makers often assert that the ‘balance of the strings’ is directly influenced by the position of the soundpost. In this section, we will vary the position of the soundpost while comparing the input admittance calculated at each of the four strings. The position will be varied in two directions: length-wise and width-wise. In violin making circles, these directions are often referred to as North–South and East–West. These terms will also be used here. Figure 5.16 shows diagrams illustrating how we have varied the position of the soundpost in these two directions, N–S and E–W.

One way to think about the ‘balance of the strings’ is to look at the relative difference between the magnitude of the input admittance calculated at the four strings. For our investigation, we will use the G string as the marker to which we will compare the other strings. Therefore, we will ‘normalise’ the input admittance of the three other strings to the G string input admittance. This can be written as

$$\bar{Y}_i = \frac{|Y_i|}{|Y_1|}. \quad (5.2)$$

Naturally, when we calculate \bar{Y}_1 , this returns a value of one. Therefore, for the G string we will plot Y_1 , without any normalisation factor applied.

5.3.1 East–West variation in soundpost position

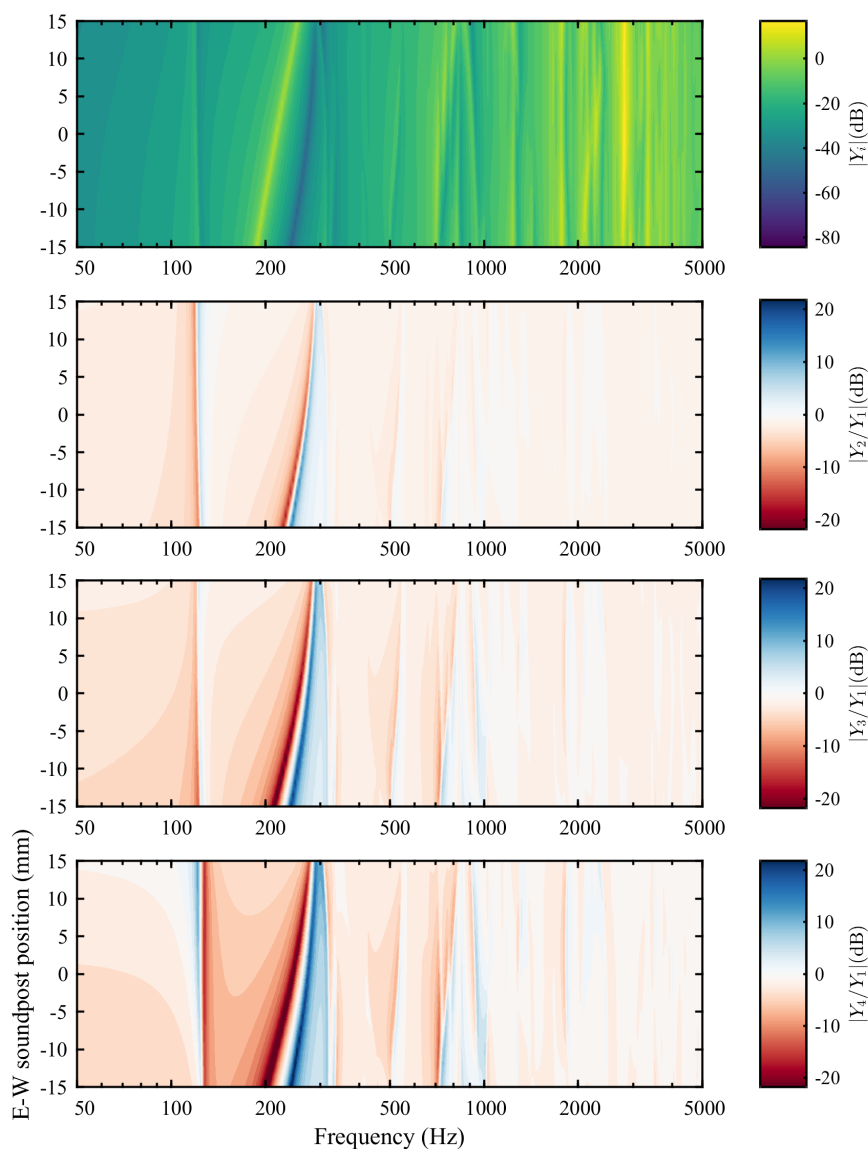


Figure 5.17: *Top:* The input admittance calculated at string number 1, the G string, plotted as the position of the soundpost is varied along the y -axis of the front plate. The position is adjusted ± 15 mm from the base position. See Figure 5.16(a) for a diagram of how the position is adjusted. *Below:* Three graphs showing the input admittance measured at the three remaining strings 2–4, where in each case the input admittance has been divided by the input admittance of string number 1.

Figure 5.17 shows the results of varying the soundpost east and west from its base position. A negative displacement corresponds to moving the soundpost east, while a positive displacement corresponds to moving the soundpost west (as viewed in Figure 5.16). The admittance of strings 2–4 (D, A and E) has been divided by Y_1 , as per Equation 5.2. The first observation we can make is that as the position of the soundpost changes, there are some resonance frequencies which also change. The most noticeable is resonance which varies at around 200–300 Hz.

Areas coloured dark red and dark blue indicate large differences between the input admittance of the string in question compared to the input admittance of the G string. Areas that are displayed in white, indicate no difference between the input admittance of the two strings. Therefore, we are looking to observe whether there are changes in the intensity of the colours as the soundpost position is varied. In Figure 5.17, the plots are dominated by the resonance located between 200–300 Hz. This resonance is associated with the plate ODS shown in Figure 5.11 marked $f_2 = 217.2$ Hz. As the position of the soundpost moves from -15 mm (east) to $+15$ mm (west), the frequency of this resonance increases due to the changing mode shape. However, what is particularly interesting that magnitude of the normalised admittance (for strings 2–4) becomes smaller as the soundpost moves from east to west. This phenomenon can be attributed to the soundpost becoming more central on the plate. A centrally placed soundpost results in a symmetric violin body and neutralises any differences between the four driving points on the bridge.

As further evidence of this effect, we plot a zoomed-in view of Figure 5.17 for the range of 300–5000 Hz. This is shown in Figure 5.18. Between the range of 700–1000 Hz, we see that as the soundpost moves from east to west, the strings become more ‘balanced’. For strings 2–4 at $+15$ mm, the magnitude of the normalised admittance is smaller than at -15 mm.

5.3.2 North–South variation in soundpost position

Figure 5.19 shows the results of varying the soundpost south and north from its base position. A negative displacement corresponds to moving the soundpost south, while a positive displacement corresponds to moving the soundpost north (as viewed in Figure 5.16). The results do not reveal any clear trends. Moving the position of the soundpost, as expected, influences the resonance frequencies, but effects on the balance of the strings are subtle and hard to distinguish from the data.

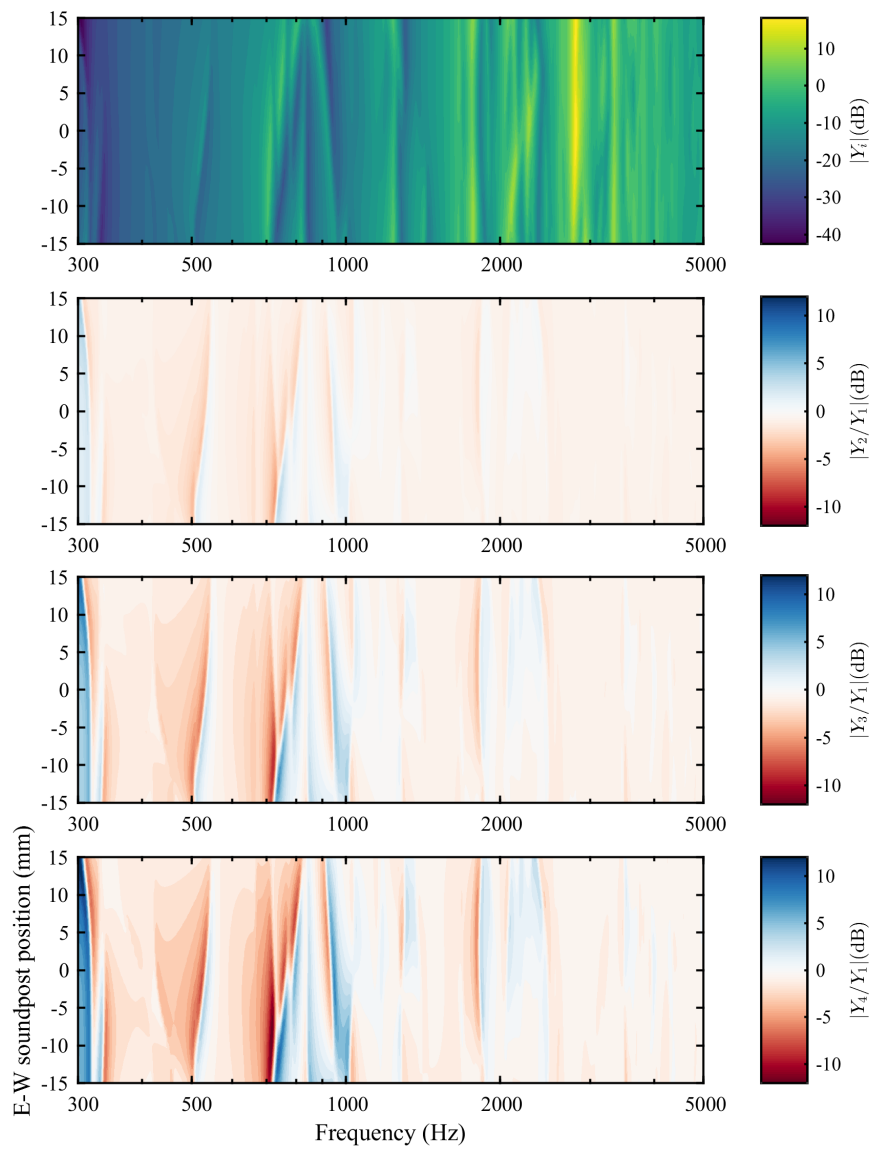


Figure 5.18: The same data as shown in Figure 5.17, but for the frequency range of 300–5000 Hz.

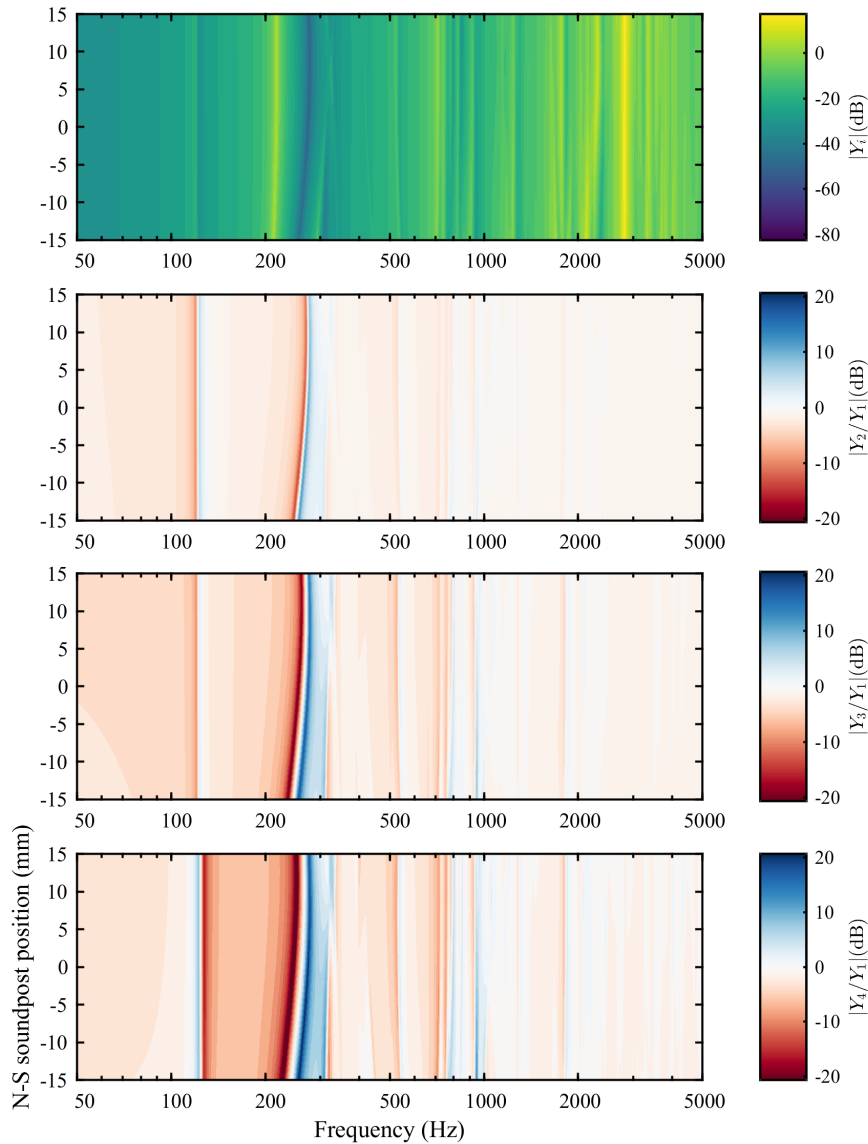


Figure 5.19: *Top:* The input admittance calculated at string number 1, the G string, plotted as the position of the soundpost is varied along the x -axis of the front plate. The position is adjusted ± 15 mm from the base position. See Figure 5.16(b) for a diagram of how the position is adjusted. *Below:* Three graphs showing the input admittance measured at the three remaining strings 2–4, where in each case the input admittance has been divided by the input admittance of string number 1.

5.4 The influence of the soundpost coupling strength on the bridge input admittance

In this section, we will investigate the effect of soundpost coupling strength on the bridge input admittance. In our model, coupling between the soundpost and the plates is governed by axial and bending springs. Therefore, we will now conduct an investigation in which we vary the stiffness of these springs. This type of study will be similar to those presented in Chapter 3. As we have done in the previous section, we wish to investigate questions regarding the balance of the strings. Therefore, we will ‘normalise’ the input admittance of the D, A and E strings to the input admittance of the G string (see Equation 5.2).

First, we will vary the axial spring stiffness, k , while keeping the bending spring stiffness constant at $\kappa = 10^4$ Nm/rad. The results are shown in Figure 5.20. Focusing on Figure 5.20(a), which shows the input admittance of the G string, we see that as the axial stiffness increases, the frequency of many resonances also increase. This bears close resemblance to results demonstrated in Chapter 3, where we were calculating the admittance on the surface of the plates. Because we have altered the soundpost position, the resonance frequencies are not directly comparable to those produced in Chapter 3. We can, however, note similar key features, including the fact that the resonances increase in frequency within a similar range of axial stiffness.

When we compare the three remaining strings to the G string, shown in Figures 5.20(b)–5.20(d), we see that on the whole the differences between the strings are not dependent on axial spring stiffness. This is to say, as the axial spring stiffness increases, the magnitude of Y_2/Y_1 , Y_3/Y_1 and Y_4/Y_1 does not change significantly. The large differences in Y_4/Y_1 , apparent at around 200 Hz, are not relevant as they occur well below the frequency of the E string.

Varying the bending spring stiffness returns a similar pattern of results: see Figure 5.21. We see small changes to the resonance frequencies, in line with results from Section 3.4, however, the magnitude of the normalised admittance for strings 2–4 does not vary significantly as a function of bending spring stiffness.

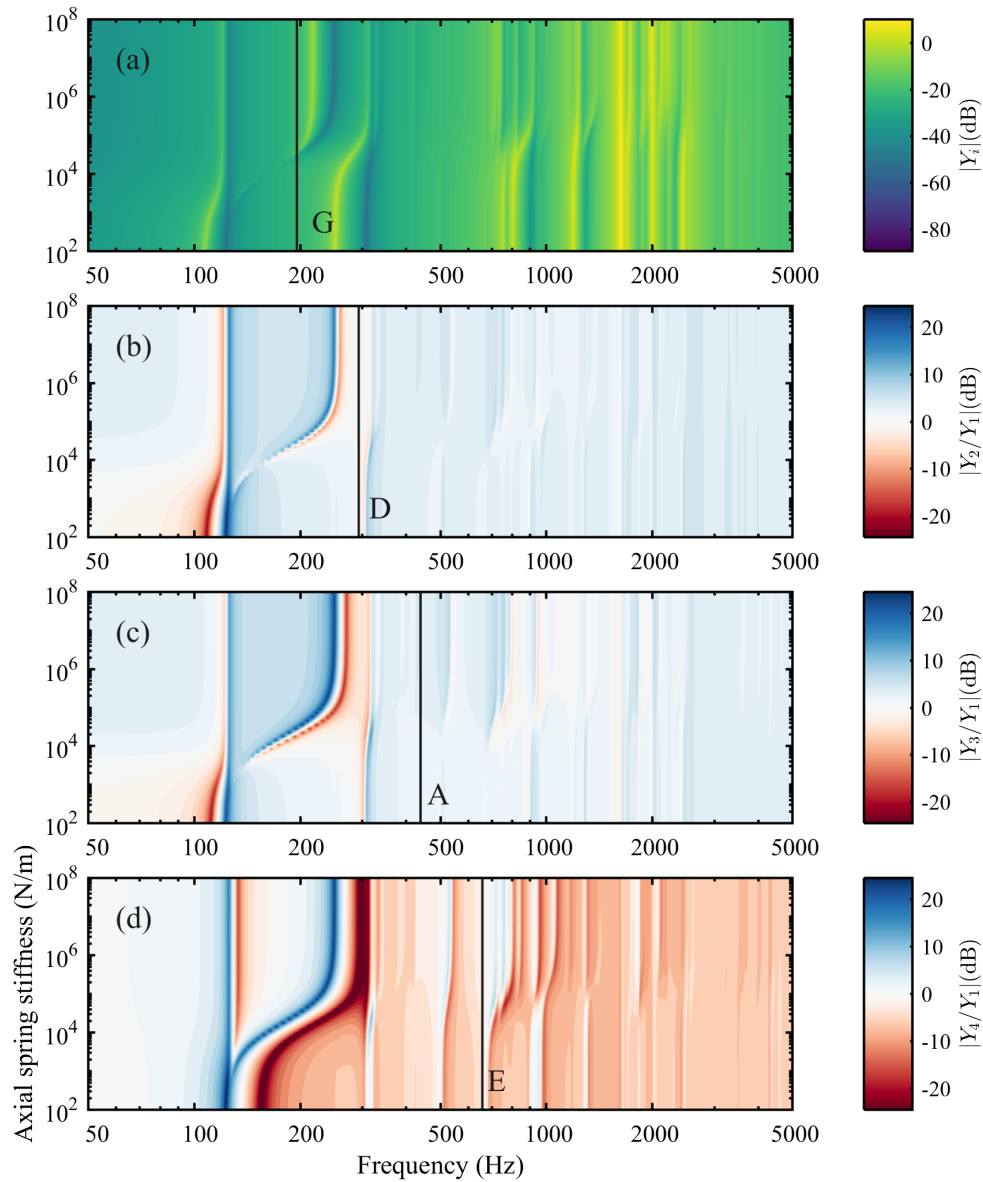


Figure 5.20: (a) The input admittance at the G string plotted as a function of axial spring stiffness. The black vertical line labelled ‘G’ marks the frequency of the open violin G string. (b)–(d) Three graphs showing the input admittance calculated at the three remaining strings (D, A and E) but in each case the input admittance has been divided by the input admittance of the G string. These are also plotted as a function of axial spring stiffness. Similarly labelled vertical black lines indicate the open string frequencies.

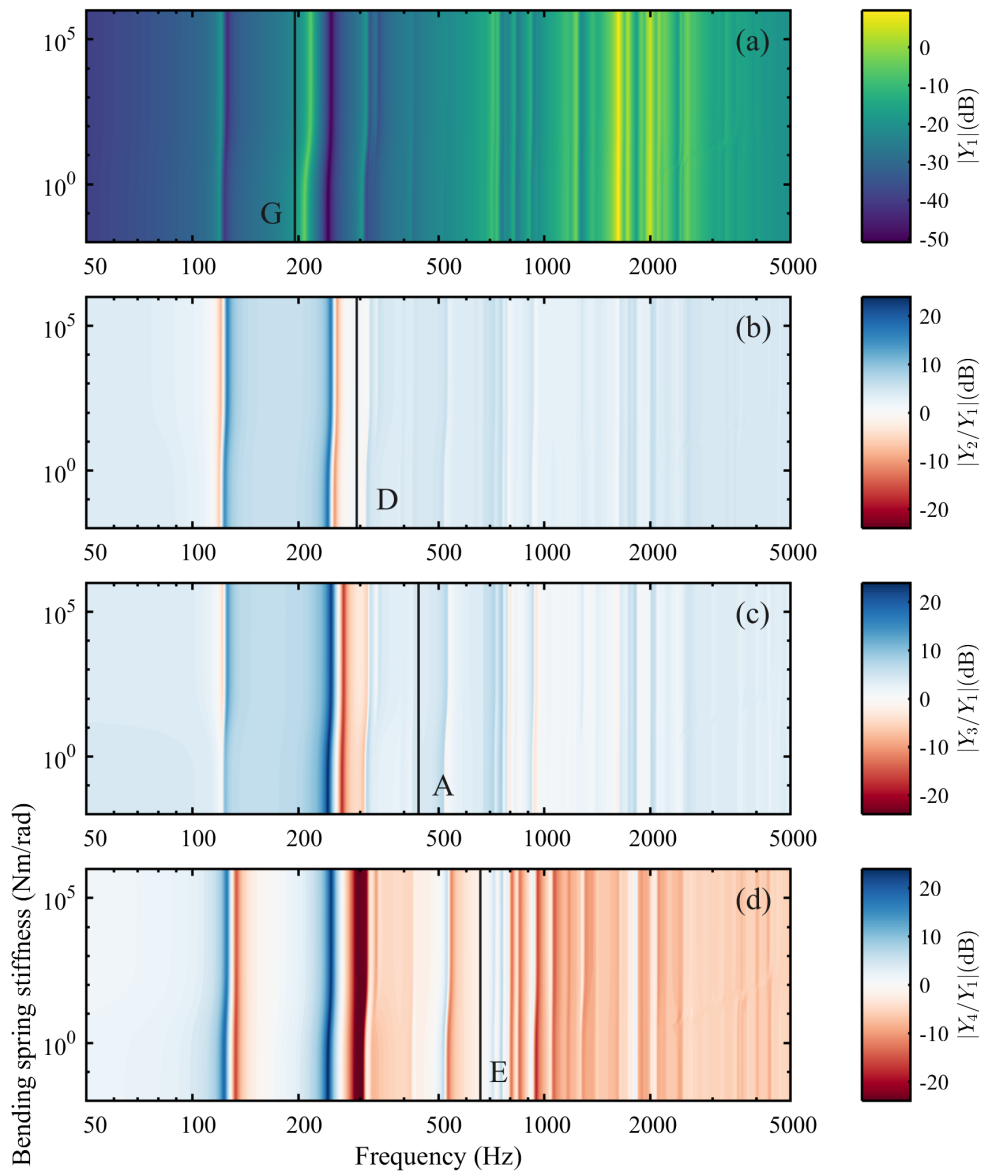


Figure 5.21: (a) The input admittance at the G string plotted as a function of bending spring stiffness. The black vertical line labelled ‘G’ marks the frequency of the open violin G string. (b)–(d) Three graphs showing the input admittance calculated at the three remaining strings (D, A and E) but in each case the input admittance has been divided by the input admittance of the G string. These are also plotted as a function of bending spring stiffness. Similarly labelled vertical black lines indicate the open string frequencies.

6

The influence of the soundpost on radiated sound pressure

In this chapter, we will look at how to estimate radiated sound pressure from our simplified violin body and soundpost model. Up until now, we have been focused on understanding the vibration of the model in purely mechanical terms, rather than considering how the model might ‘sound’ as a result of pressure waves caused by its vibration. Considering radiated sound pressure in this context is important because, ultimately, the violin is an instrument designed for the purpose of music-making.

It has long been recognised that the vibrations of the wooden body of the violin are at the heart of the instrument’s sound. But what do we mean when we talk about the ‘sound’ of an instrument? This is itself a complex scientific and artistic question. One of the main ways of describing the sound of a musical instrument is by referring to concepts of tone and loudness. An instrument’s characteristic ‘tone’ is produced by the combination of different modal frequencies and their relative amplitudes. This sense of ‘tone’ is near-impossible to quantify and has given rise to a vast range of subjective descriptors such as ‘warmth’, ‘brilliance’ and ‘colour’, a field beyond the scope of this thesis. The ‘loudness’ of the instrument is, however, something that can be quantified, at least in a crude sense, if we consider the amplitude of the sound wave only.

The loudness of the instrument is in fact a quality which players and listeners value considerably. In particular, it is widely held that one of the main roles of the soundpost is to increase the sound radiation of the instrument at low frequencies: in other words, to improve its bass response. As previously discussed in more detail in our literature review, it is conjectured that this is because the asymmetric placement of the soundpost in turn produces asymmetric mode shapes, which involve greater net volume change.

Using our simplified violin body and soundpost model, we will now investigate the influence of the soundpost on radiated sound pressure. We will also seek a significantly improved understanding of how the key aspects of soundpost set up, so carefully scrutinised by violin makers — primarily tightness/fit, and position — impact on radiated sound pressure. In the simulations and tests that follow, we vary the position of the soundpost within the model and as well as the tightness/fit, which is modelled by the axial and bending springs connecting the soundpost to the plates.

Over the course of the thesis so far, we have explored different excitation methods; first, excitation via a single point harmonic force, and second, as a result of the introduction of our a simplified bridge model, excitation via the two bridge feet. Both methods will be investigated separately in this chapter.

6.1 Estimating radiated sound pressure from the model

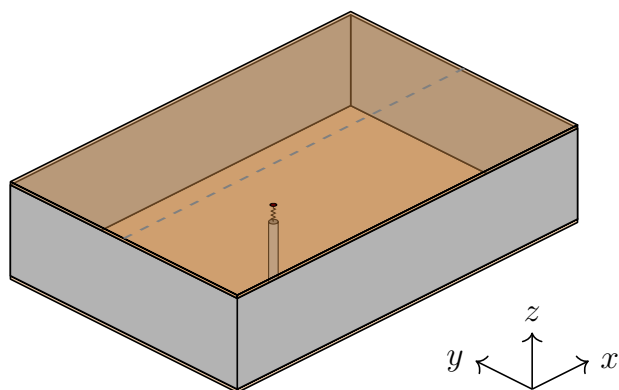


Figure 6.1: A diagram of our simplified violin body and soundpost model with solid sides joining the edges of the front and back plates. This creates a closed box which is analogous to the closed cavity of a violin body.

To estimate the radiated sound pressure from our simplified violin model, we will imagine that our model is a closed violin body. To do this, we will assume that the front and back plates are joined at the edges by rigid sides, like the ribs of a real violin. This creates a closed box which is analogous to the closed cavity of a violin body, see Figure 6.1. Calculating the volume of this cavity is the first step in estimating the amount of radiated sound produced.

Our method for estimating radiated sound pressure involves describing the violin body as a point source radiator or monopole. This requires us to approximate that the source (i.e. the violin body) is small in comparison to the wavelength of the sound waves. Using the monopole

approximation, we can formulate an expression to describe the sound pressure emitted from our model due to net volume change within the box.

6.1.1 Calculating the net volume change of the body

The term ‘net volume change’ refers to the overall change of volume as both plates move. For example, if both plates were to vibrate identically, then despite volume being displaced by each of the plates, there is no net change in the volume of the box overall.

To calculate the net volume change for a given vibration mode of the model, we must first calculate the volume displaced by each of the plates. The volume, $V_i^{(n)}$, displaced by a single plate for given mode, n , can be expressed as the mass-normalised displacement of the plate, $\tilde{\mathbf{u}}_i^{(n)}$, integrated over the surface area of the plate such that

$$V_i^{(n)} = \int_0^{a_i} \int_0^{b_i} \tilde{\mathbf{u}}_i^{(n)}(x, y) \, dx \, dy, \quad (6.1)$$

where

$$\tilde{\mathbf{u}}_i^{(n)}(x, y) = \sum_{p=1}^{N_i} \sum_{q=1}^{N_i} \alpha_i^{pq} \sin\left(\frac{p\pi x}{a_i}\right) \sin\left(\frac{q\pi y}{b_i}\right). \quad (6.2)$$

Substituting this expression for $\tilde{\mathbf{u}}_i^{(n)}$ into Equation 6.1 and evaluating the integral, we obtain the following expression for the volume of a single plate:

$$V_i^{(n)} = \sum_{p=1}^{N_i} \sum_{q=1}^{N_i} \alpha_i^{pq} \left(\frac{a_i b_i}{\pi^2 pq}\right) (1 - \cos p\pi)(1 - \cos q\pi). \quad (6.3)$$

The result of this calculation is a single number representing the volume displaced by the plate. Assuming that the two plates have rigid sides between them, the overall net volume change of the box, $\Delta V^{(n)}$, can be calculated by subtracting the volume displaced by each plate from the other:

$$\Delta V^{(n)} = V_1^{(n)} - V_2^{(n)}, \quad (6.4)$$

where $V_1^{(n)}$ and $V_2^{(n)}$ are the volume displaced by plate 1 (front) and plate 2 (back) respectively. The volume occupied by the soundpost itself is very small, and, in any case, it can be assumed to be constant. Therefore, it does not affect the net volume change.

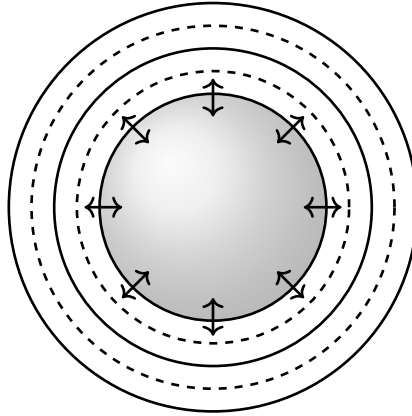


Figure 6.2: A diagram of a pulsating spherical source. The arrows indicate how the sphere is expanding and contracting. The alternating solid and dashed circles surrounding the sphere represent areas of high and low pressure respectively.

6.1.2 The radiated sound pressure from a pulsating sphere

To estimate the sound radiated from the box we will use the approximation of a pulsating spherical source: see Figure 6.2. For wavelengths which are much larger than the dimensions of the object from which they are radiating, this problem can be treated as a monopole source. Cremer (1984) writes that at low frequencies the violin exhibits “point-radiator-like breathing motions of the entire body”. For the purposes of our investigation, we will use 500 Hz as the limit for which this approximation holds. The steps required to derive an expression for the pressure generated by a monopole for a given amount of net volume change, $\Delta V^{(n)}$, will be briefly laid out (see Fahy, 1987, ch. 2, and Cremer, 1984, ch. 13).

At a frequency, ω_n , the pressure, $\mathbf{p}^{(n)}$, as a function of distance, r , from the centre of the monopole is

$$\mathbf{p}^{(n)}(r, t) = i\omega_n \rho_0 \frac{Q}{4\pi r} e^{i(\omega_n t - kr)}, \quad (6.5)$$

where ρ_0 is the density of air and Q is the volume velocity. The volume velocity can be expressed as

$$Q = \frac{dV}{dt}. \quad (6.6)$$

For our model, the volume displaced as a function of time is $\Delta V^{(n)} e^{i\omega_n t}$. Therefore Q can be written as

$$Q = \frac{d}{dt} (\Delta V^{(n)} e^{i\omega_n t}) = i\omega_n \Delta V^{(n)} e^{i\omega_n t}. \quad (6.7)$$

Substituting this into the expression for the pressure gives us

$$\mathbf{p}^{(n)}(r, t) = -\omega_n^2 \rho_0 \frac{\Delta V^{(n)}}{4\pi r} e^{i(\omega_n t - kr)}. \quad (6.8)$$

During this chapter, we will use the following values for ρ_0 and r : the density of air will be given by $\rho_0 = 1.225 \text{ kg/m}^3$ and the distance r from the source will be 1 m.

Now that we have an expression for the pressure generated from a pulsating spherical source, we need to formulate a suitable transfer function to calculate the pressure generated due to a harmonic input force acting on a point \mathbf{r}_d on the structure. If we consider that air surrounding the model can be treated as an extension to the degrees of the freedom of the system, then using the standard response formula (see Equation 2.42), we can calculate

$$Y_P(\mathbf{r}_d, r, \omega) = \sum_{n=1}^N \frac{[\tilde{\mathbf{u}}_1^{(n)}(\mathbf{r}_d)] [\mathbf{p}^{(n)}(r)]}{\omega_n^2 + 2i\omega\omega_n\zeta_n - \omega^2}. \quad (6.9)$$

where \mathbf{r}_d denotes the coordinates of the driving point.

Next, we must decide on a suitable location for \mathbf{r}_d , the driving point. As a first step, we can place the driving point at the location at which one of the bridge feet would be placed. This would serve as a simplified representation of the effect a bridge has on exciting the body. The right-hand bridge foot (also called the bass side bridge foot) is a suitable location to consider first. If we imagine the soundpost is acting like a rigid link, then the motion of the right-hand bridge foot, which is furthest away from the soundpost, is likely to be greater than the left side, which is close to the soundpost. In the simulations that follow, we will use this location as our fixed driving point, before proceeding to simulations incorporating our bridge model, in which a single point harmonic force is replaced by forces driving at the two bridge feet.

We will first undertake a preliminary study that examines how the model radiates sound with and without a soundpost. Following this, a parameter study will be undertaken, in which the position of the soundpost and the stiffnesses of the springs, which couple the soundpost to the plates, will be varied.

6.2 Understanding how the model vibrates with and without a soundpost

In this section, we will investigate the acoustical effect of the absence and presence of a soundpost within the violin body model. It is conjectured that one of the main roles of the soundpost is to

increase sound radiation at low frequencies by creating asymmetric mode shapes with greater net volume change. Having established a method for estimating the radiated sound pressure from our model, we will undertake a simple comparative study, first, examining the model without a soundpost, before adding an asymmetrically placed soundpost to compare any differences. In both cases, we will produce a graph showing the radiated sound pressure as a function of frequency, as well as plots illustrating the plate mode shapes. Using these two sources of information together will allow us to fully understand the influence of the soundpost on radiated sound pressure.

6.2.1 No soundpost

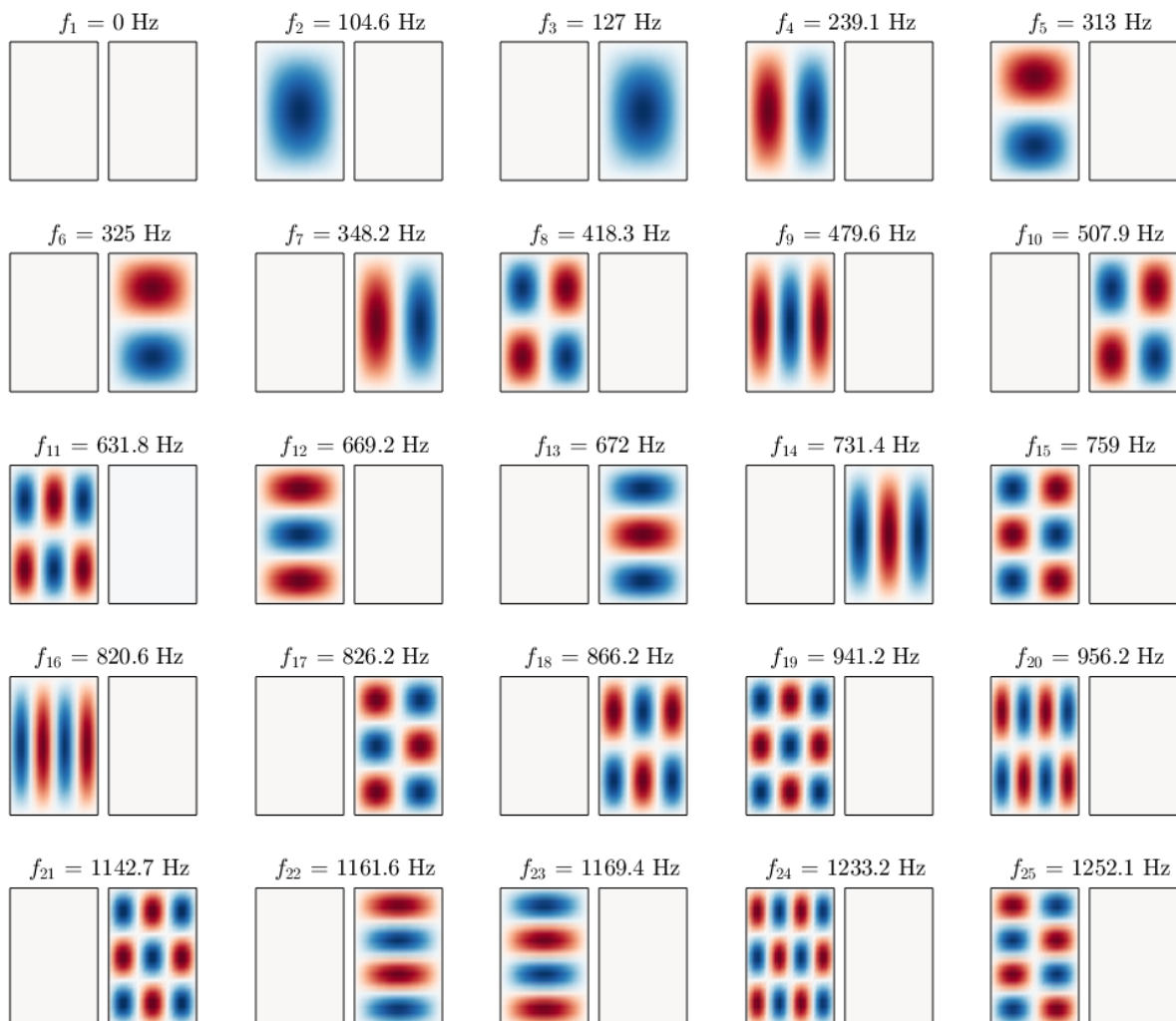


Figure 6.3: The mode shape patterns seen on the plates of the simplified violin body model. The soundpost is completely decoupled from the plates in this instance. Therefore, we observe the standard mode shape patterns for rectangular simply-supported plates. The left hand plate in each pair of plates represents the front plate. The first 25 modes are shown here.

The vibration modes of the model without a soundpost linking the two plates can be straightforwardly understood. The two plates simply vibrate independently of each other and display the standard mode shape patterns for a rectangular simply-supported plate. In the model, this arrangement can be achieved by setting the spring stiffnesses of the axial and torsional springs to zero. This decouples the soundpost from the front and back plates.

A visual representation of the first 25 mode shapes is shown in Figure 6.3. The first mode, $f_1 = 0$ Hz, represents the rigid body mode of the soundpost. The rest of the modes follow as we would expect and as previously described in Section 2.4.1.

We will now calculate the radiated sound pressure, as function of frequency, for this arrangement without a soundpost. As we will discover, not all vibration modes generate radiated sound pressure, but identifying which modes do radiate sound will provide an insight into how certain mode shape patterns are important to sound radiation. In the following simulation, we will apply a point force to the front plate of the model and calculate a transfer function using Equation 6.9. This point force is applied at the approximate location of the bass bridge foot. The back plate will make no contribution to the calculation of this transfer function, as the plates are uncoupled by the absence of the soundpost.

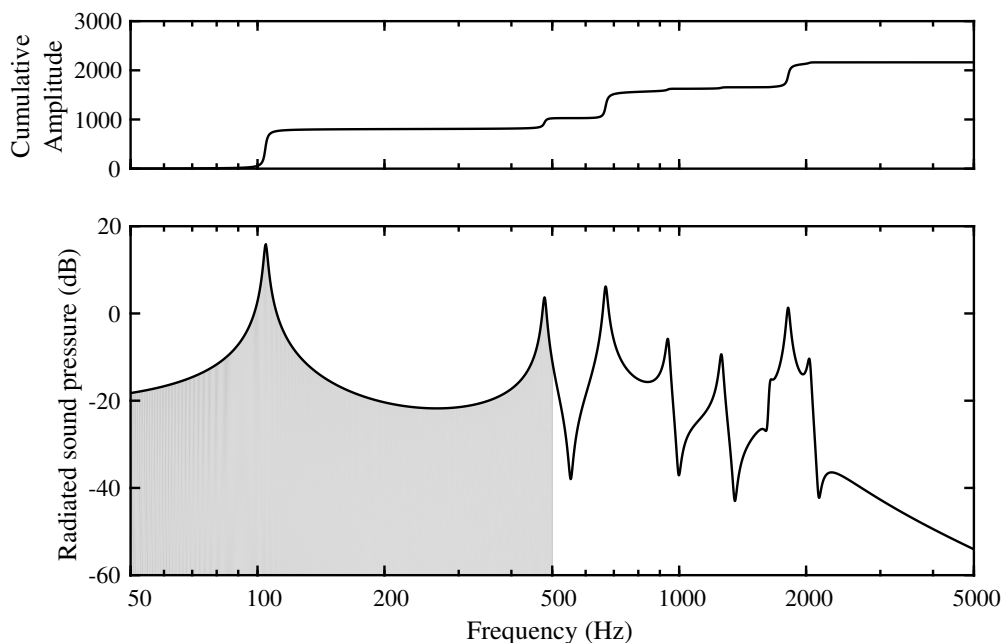


Figure 6.4: The lower graph shows the amplitude of the radiated sound pressure plotted as a function of frequency, using a decibel scale. The upper graph shows a cumulative sum of the amplitude as the frequency increases, shown using a linear scale. The model in question does not have a soundpost. The grey area relates to the ‘total sound pressure radiation’, a metric which will be defined in Section 6.2.3.

The results of this calculation are shown in Figure 6.4. The lower graph shows the amplitude of the radiated sound pressure as a function of frequency, using a decibel scale. Above this graph is a plot showing a cumulative sum of the amplitude as the frequency increases; this is shown using a linear scale. This is important because later in this chapter we will proceed to define a metric called the ‘total radiated sound pressure’, which represents a sum of the radiated sound pressure from 0 Hz to 500 Hz (in the plot this is shown as the grey area beneath the plotted line). Viewing the cumulative sum of the amplitude is useful as it gives us a sense of how much each vibration mode is contributing to the total radiated sound pressure.

Studying the lower plot in Figure 6.4 more closely, we see that below 1000 Hz there are four main resonances. We know that these can only be the result of the vibration of the front plate, and indeed from comparing these frequencies with the mode shapes in Figure 6.3 we find they correspond to $f_2 = 104.6$ Hz, $f_9 = 479.6$ Hz, $f_{12} = 669.2$ Hz and $f_{19} = 941.2$ Hz. Examining the mode shape patterns for these four modes, we can see that they possess one key similarity: they each have an odd number of anti-nodal points. Listed numerically, the modes are classified as (1,1), (1,3), (3,1) and (3,3). The fundamental property of these modes, causing them to radiate sound pressure, is that they generate a net volume change. If we look at a mode such as $f_4 = 239.1$ Hz, this has two equal regions of positive and negative amplitude. As a result, there is no net volume change: the two sides of the mode shape pattern ‘cancel’ each other out. This does not occur with the four modes we have identified in Figure 6.4.

The results of this simulation have confirmed that net volume change is an essential property required for sound radiation. Without a soundpost, many of the mode shape patterns produced are ‘symmetrical’ modes that do not generate a net volume change.

The object of introducing the soundpost into the violin has sometimes been conceived of as a way of breaking the violin’s symmetry. In this next stage of this chapter, we introduce a soundpost and observe how it influences the mode shape patterns, noting which of these modes radiate sound.

6.2.2 With soundpost

The next step is to look at how the model behaves once a soundpost is introduced. A soundpost placed at the location $x = a/\pi$ and $y = b/\pi$ will be used once again, as this serves as a rough estimate of where a soundpost is usually placed in a real instrument. The values of the axial spring stiffness, k , and the bending spring stiffness, κ , were chosen so that the effect of the coupling was apparent. In this case, $k = 10^6$ N/m and $\kappa = 10^4$ Nm/rad were selected.

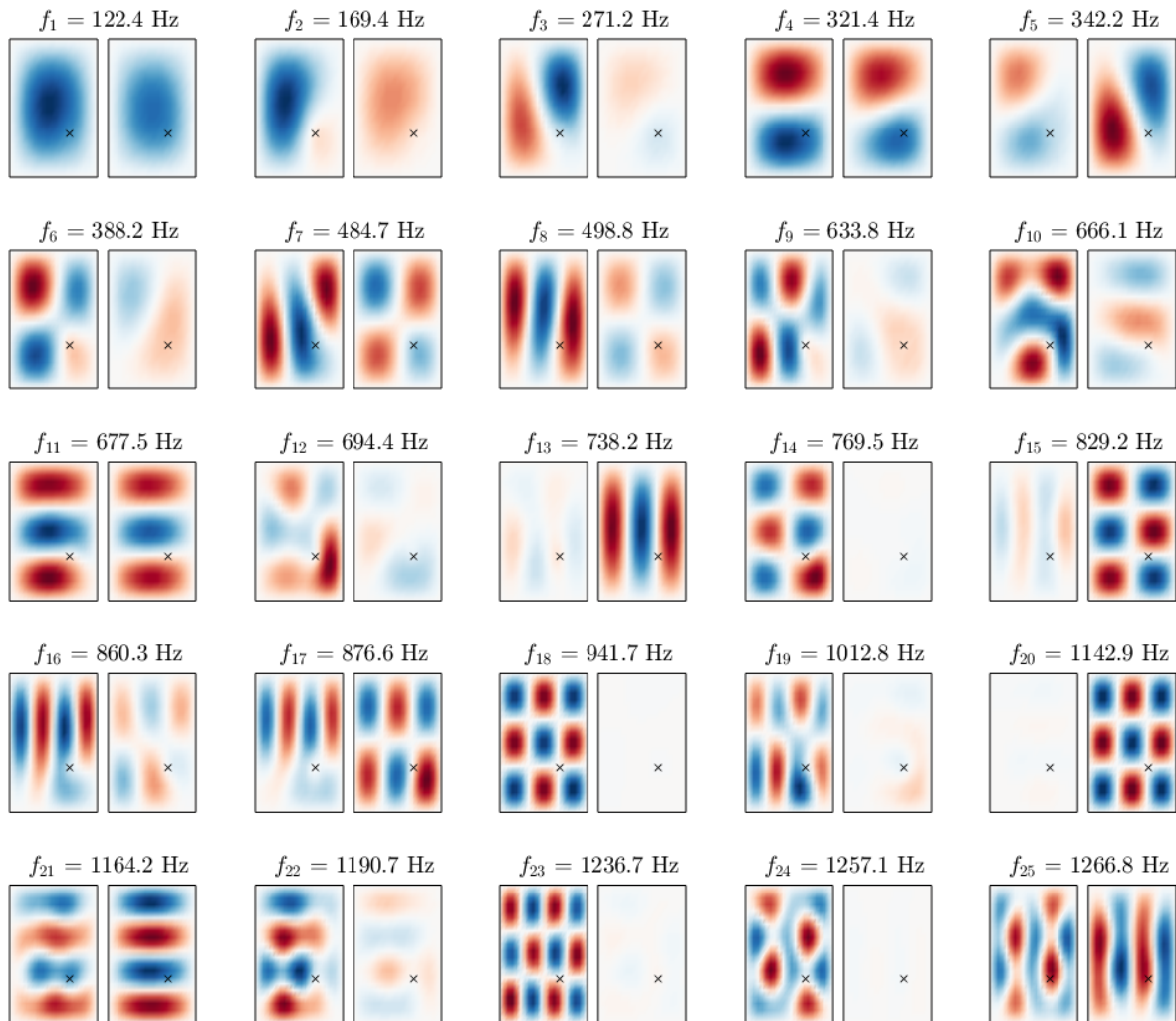


Figure 6.5: The mode shape patterns seen on the plates of the simplified violin body model with a soundpost. The left hand plate in each pair of plates represents the front plate. Only the first 25 modes are shown here. The black cross indicates the location of the soundpost.

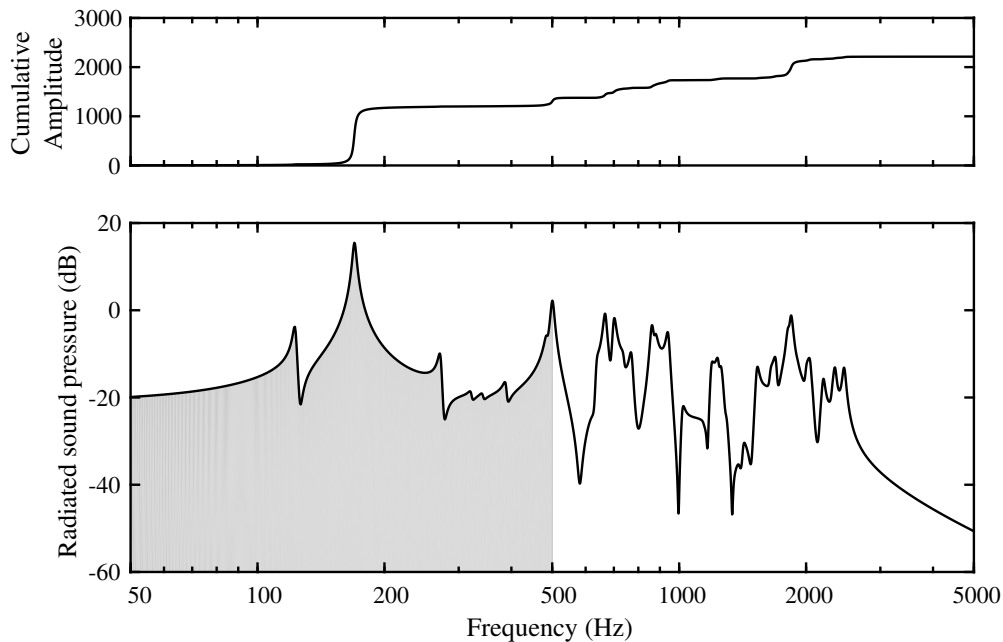


Figure 6.6: The lower graph shows the amplitude of the radiated sound pressure plotted as a function of frequency, on a decibel scale. The upper graph shows a cumulative sum of the amplitude as the frequency increases, shown on a linear scale. The model in question has a soundpost, which is placed at the position shown in Figure 6.5. The grey area relates to the ‘total sound pressure radiation’, a metric which will be defined in Section 6.2.3.

A visual representation of the first 25 modes, shown in Figure 6.5, reveals that the plate modes are now indeed coupled. We are also able to observe two types of mode shape. The first is a mode shape in which the motion of the front and back plates is coupled together, for example $f_1 = 122.4$ Hz, and the second is a mode shape where the location of the soundpost becomes a nodal point, for example $f_2 = 169.4$ Hz. The equivalent plot to Figure 6.4 is shown in Figure 6.6. Notice that many more peaks are now present because nearly all the resonances now have at least some net volume change because of the presence of the soundpost ‘disrupting’ the symmetry of the model.

Up to 500 Hz, the first eight modes can all be seen as peaks in the graph. This shows that all have undergone some net volume change, albeit in many cases a very small one. Indeed from looking at the cumulative amplitude plot, we see that most of these small peaks have a negligible effect on the overall total amplitude. The main contribution comes from the peak at 169.4 Hz, i.e. the mode labelled f_2 in Figure 6.5. Examining this mode shape pattern, this is unsurprising. What we can see here is the front and back plates moving out of phase with each other. This invokes a large net volume change.

This simulation has shown us that the addition of a soundpost certainly has the effect of creating more modes with net volume change resulting in radiated sound pressure. One of the ideas we set out to explore in this chapter was the concept of ‘loudness’. The question which we will now investigate is whether the addition of a soundpost acts to make our simplified violin body model ‘louder’ i.e., whether the radiated sound pressure increases.

6.2.3 A metric for ‘total radiated sound pressure’

At this stage, it is convenient to define a metric for quantifying how much sound pressure is being radiated by the model across a particular frequency range. The total radiated sound pressure, p_{tot} , will be defined as the following:

$$p_{\text{tot}} = \int_0^{\omega_{\text{max}}} |Y_P(\omega)|^2 d\omega. \quad (6.10)$$

This represents the squared area underneath the transfer functions, plotted in Figures 6.4 and 6.6, over the range of 0 Hz to some maximum upper limit, ω_{max} . In this chapter, we will consider the upper limit to be 500 Hz, as we consider the monopole approximation to hold for frequencies below 500 Hz. From the cumulative sum plot in Figure 6.6, we see that the main contributor to radiated sound pressure below 500 Hz is the resonance at 169.4 Hz. The mode shape associated with this resonance, see f_2 in Figure 6.5, can be described as a ‘breathing mode’ of the body, which bears resemblance to the low frequency breathing motions of the violin body as described by Cremer (1984).

Having this metric allows us to assign a single value describing the ‘loudness’ of a particular arrangement of our model. This will be an extremely useful resource as we now undertake a comprehensive parameter study.

6.3 A parameter study using a point excitation force

We will now undertake a parameter study while calculating the total radiated sound pressure from our model. The two obvious variables which lend themselves to being investigated are the position of the soundpost and the stiffness of the soundpost coupling springs. These address the main areas that violin makers focus on when setting up a soundpost, namely position and tightness/fit. In this section, all simulations will involve applying a point excitation force to the model. Later in the chapter, we will include the simplified bridge model and use that to provide the excitation force.

6.3.1 Varying the position

It is straightforward to vary the position of the soundpost within the model. We will do this by setting up a grid of points across the surface area of the plates. Note that for our simulations, we will be using a soundpost that is perfectly ‘upright’ and not slanted. That is to say, the soundpost is coupled with the same x and y coordinate on the front plate and on the back plate. This is consistent with the set-up of a soundpost in a real violin.

For each soundpost location, we can calculate the ‘total radiated sound pressure’ associated with that arrangement. With this data, we can investigate whether there is an ‘optimal’ place to position the soundpost if we are trying to maximise radiated sound pressure.

6.3.2 Varying the axial and bending spring stiffness

In addition to varying the position, we can vary the stiffness of the axial and bending springs which couple the soundpost to the plates. This study will allow us to answer questions including what strength of coupling between the soundpost and the plates produces the most radiated sound from our model.

One school of thought among violin-makers regarding soundpost set-up is that having a more tightly fitting soundpost will lead to a louder instrument. In our model this would correspond to setting the stiffness of the axial and bending springs at a high value. One possibility, however, is that this idea that violins need more tightly fitting soundposts to increase their sound has been distorted by the fact many violins with sound problems have plates which have warped under the pressure of existing tight fitting soundposts. When the plates of a violin warp outwards, because a soundpost is pushing them apart, this causes the tightness of the soundpost to be reduced. The problem is circular: a tight soundpost causes the plates to warp, which in turn causes the coupling between the soundpost and plates to be reduced, which in turn means that a new, longer, soundpost is required to compensate for this, and so the cycle repeats itself.

6.3.3 Testing multiple soundpost locations while keeping the spring stiffness fixed

First, we will consider the simple case of varying the position of the soundpost while keeping the stiffness of the springs which couple the soundpost to the plates constant. The value of k was set to 10^6 N/m and the value of κ was set to 10^4 Nm/rad. Following our studies of the simplified bridge model in Chapters 4 and 5, we will use the location of the right bridge foot as the position of our excitation point. Four hundred different soundpost positions were tested across the plate.

At each position, we will now calculate the radiated sound pressure as a function of frequency and then calculate our metric: the ‘total radiated sound pressure’. Once all soundpost positions have been tested, the values of total radiated sound pressure can be plotted as a surface plot across all the locations on the plate. This will enable us to visualise which soundpost position generates the most radiated sound pressure below 500 Hz, and will give us an indication of where to place the soundpost to maximise the ‘loudness’ of the model.

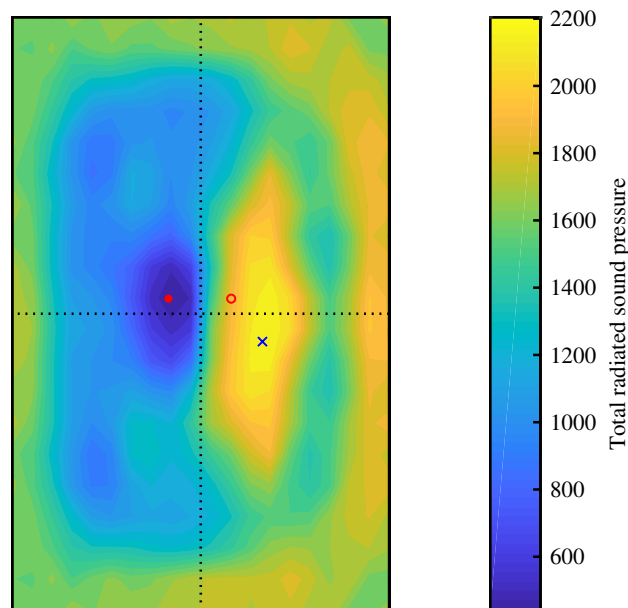


Figure 6.7: A surface plot showing the total radiated sound pressure from the model for different locations of the soundpost. The filled red marker shows the location of the fixed excitation point and the black cross marks the soundpost location which generates the largest total radiated sound pressure. The hollow red circle acts as a guide, showing where the right bridge foot would approximately lie.

The results of this study are shown in Figure 6.7. The filled in red marker shows the location of the excitation point. The hollow red marker acts as a guide, showing the position of where the right bridge foot would lie. The colours on the surface of the plate reflect the total radiated sound pressure from the model if a soundpost is placed at that position. The black cross shows the soundpost position which results in the maximum amount of sound being radiated.

The most significant observation we can make is that the position of the soundpost which leads to the largest amount of total radiated sound pressure lies in a region where we would normally expect a soundpost to be placed. This position is off-centre in relation to the midpoints of both the length and the width, which demonstrates that an asymmetrically placed soundpost

is superior to other arrangements in maximising sound radiation at low frequencies. The low amplitude blue area around the location of the excitation point can be explained, because at this location the plate is being driven directly on top of the soundpost. Therefore, modes which have nodal point at the location of the soundpost — such as f_2 in Figure 6.5 — are not excited. As we have seen in Figure 6.6, this particular mode is a significant contributor to the total radiated sound pressure.

While this is certainly an encouraging result, there are limitations of our model which should be identified here. The location of the excitation point is a decisive factor in determining where the ‘loudest’ soundpost position is located. If the excitation point was placed ‘below’ the midpoint line, which runs across the width, then the ‘loudest’ soundpost position would have occurred ‘above’ our approximated bridge location. Similarly, if the excitation point had been where the hollow red circle is, the ‘loudest’ soundpost position would have occurred on the opposite side of the plate. Therefore, we must acknowledge that our choice of the excitation point being on the ‘bass-bar side’ of the plates has directly influenced this result.

Nevertheless, for this choice of excitation point, it remains reassuring to see this soundpost location emerging as the best position to maximise total radiated sound pressure. In a general sense, it shows that for a centrally located excitation force, the ‘loudest’ soundpost position is at an ‘off-centre’ location. This corresponds to the placement of soundposts in real instruments.

6.3.4 Varying the bending and axial spring stiffness

We will now investigate how varying the axial and bending spring stiffness influences the total radiated sound pressure. We will vary the bending and axial springs independently. For each combination of k and κ , 400 soundpost positions across the plate will be tested and the single highest total radiated sound pressure recorded across all these positions will be recorded. Figure 6.8 shows the result of this simulation. In the main plot, the colour represents the total radiated sound pressure of the ‘loudest’ soundpost location, for that particular combination of spring stiffness. As an additional resource to aid the interpretation of this plot, underneath the main plot are two smaller plots which show the x and y coordinates of the ‘optimal’ soundpost positions that were calculated by the model.

From Figure 6.8, we can draw some important conclusions. We will first look at the region which produced the highest levels of total radiated sound pressure. This is in the upper right hand corner of the main plot. This area corresponds to the axial and bending stiffness both being high. This is reassuring, as it demonstrates that the model does favour the presence of a

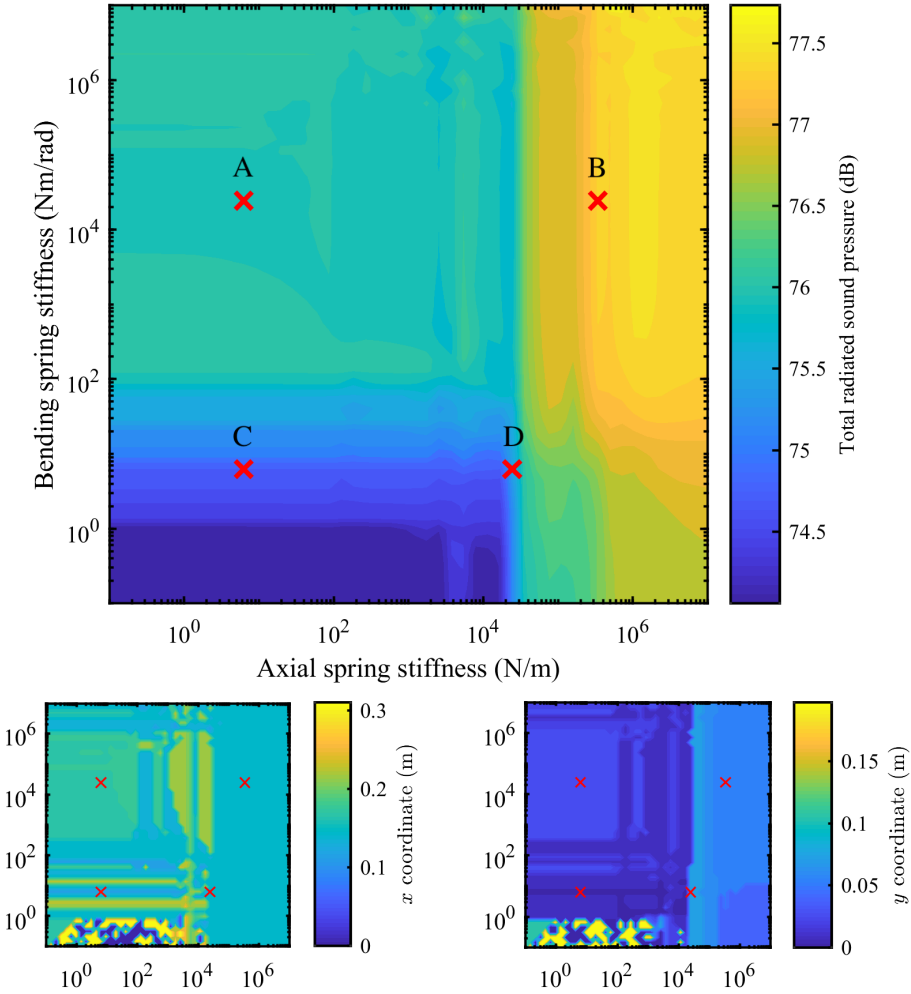


Figure 6.8: In the top plot, multiple soundpost locations were tested for different combinations of the bending spring stiffness and the axial spring stiffness. For each combination, the largest total radiated sound pressure was recorded and this value plotted in the surface plot above. Beneath this, two smaller plots display the x and y coordinates which correspond to the largest value of total radiated sound pressure that was recorded. The red crosses mark the position of plots shown in Figure 6.9.

soundpost. It also shows that a strongly coupled soundpost leads to increased sound radiation at low frequencies.

If we look at the axial stiffness only, we can see that as the axial stiffness increases, the overall trend is for the total radiated sound pressure to increase. Up to $k = 10^4$ N/m, the axial stiffness actually has very little influence on the total radiated sound pressure. It is only after passing $k = 10^4$ N/m that the axial stiffness causes the amplitude to increase. Similarly, for the bending stiffness, we see that it only has an influence between 10^0 – 10^2 Nm/rad. Beyond this, increasing the bending stiffness does not strongly influence the total radiated sound pressure.

These transition zones correspond with our findings from Chapter 3. These are the ranges in which the axial and bending stiffness directly affects the dynamics of the plates. Therefore, what we see here is the effect of the soundpost transitioning from uncoupled to coupled. The resulting changes in the mode shapes is what is influencing the total radiated sound pressure.

6.3.5 The ‘ideal’ soundpost position for different stiffnesses

We will now investigate Figure 6.8 more closely, by looking at four axial and bending stiffness combinations individually. These four values are represented by the red crosses on Figure 6.8. These roughly correspond with four general regions of the plot: low and high bending stiffness, and low and high axial stiffness. For each of these combinations, we will plot data from all the soundpost positions that were tested. This will give us an insight into where the ‘ideal’ soundpost position is located, if we are trying to maximise radiated sound pressure.

Figure 6.9 shows the soundpost position data for these four combinations of axial and bending stiffness. The order of the four plots corresponds to the order of the red crosses shown in Figure 6.8. All plots share the same colour scale which is plotted linearly as opposed to on a decibel scale.

We will start by looking at the two plots on the left hand side, which both correspond with low levels of axial stiffness. We see that no one location stands out as being a significantly more advantageous location for the soundpost than any other. This result is not unexpected, because in this arrangement the soundpost is very weakly coupled to the plates. In other words, it does not make much difference where you place the soundpost as its effect is negligible in any case.

If we look at the top right plot, which corresponds to both high axial and high bending stiffness, we see that when the soundpost is placed directly underneath the driving point there is an area of low total radiated sound pressure. This was previously seen in Figure 6.7 and can be explained by the fact that when the plate is being driven directly on top of the soundpost, modes

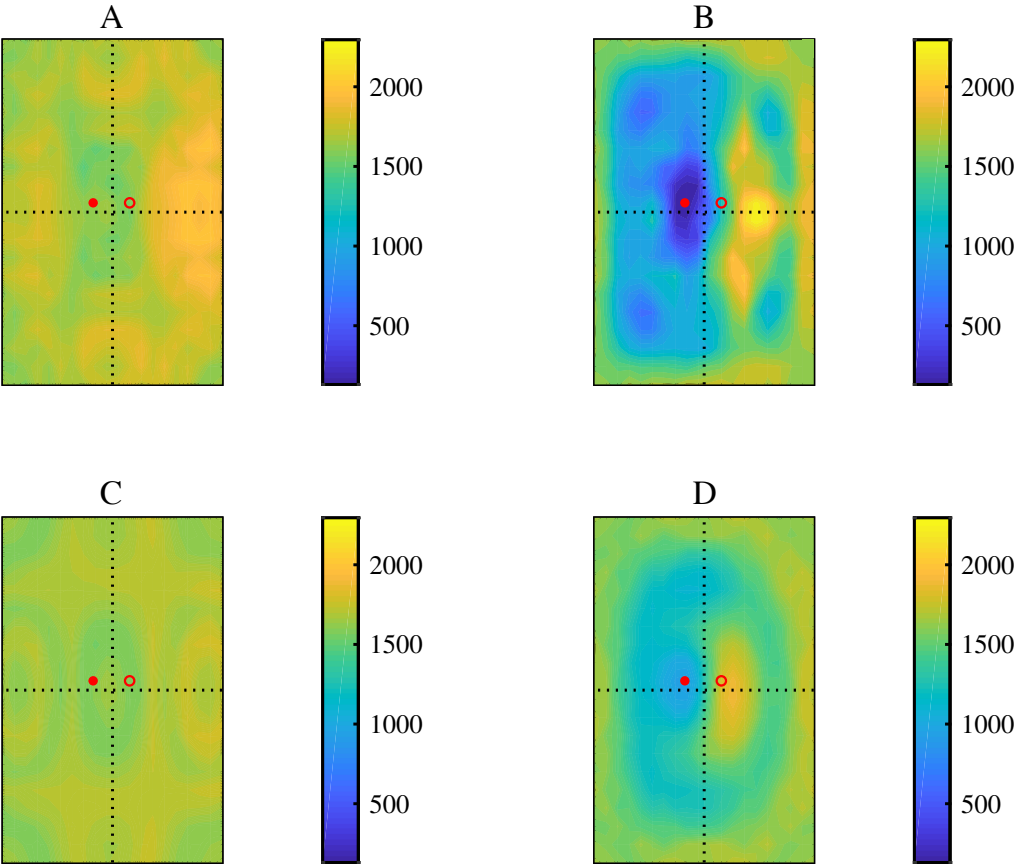


Figure 6.9: Four plots showing the total radiated sound pressure measured at locations across the plate. Each plot represents a fixed value of k and κ and these are indicated on Figure 6.8 by the four red crosses. The order of the plots follows the order of the crosses. The total radiated sound pressure is plotted on a linear scale.

which have nodal point at the location of the soundpost — such as f_2 in Figure 6.5 — are not excited.

6.4 Excitation of the plate using the bridge model

In this next section, we will investigate the radiated sound pressure when our bridge model is combined with our model of the violin body and soundpost. The significant difference, compared to single point excitation, is that now we are applying excitation forces to the front plate at two locations. To calculate the radiated sound pressure in response to the two excitation forces acting on the front plate, we can simply extend the method used in Section 6.1.2. We can calculate the following transfer functions for points at the two bridge feet:

$$Y_{LP} = \sum_{n=1}^N \frac{[\tilde{\mathbf{u}}_1^{(n)}(x_L, y_L)][\mathbf{p}^{(n)}(r)]}{\omega_n^2 + 2i\omega\omega_n\zeta_n - \omega^2}, \quad (6.11)$$

$$Y_{RP} = \sum_{n=1}^N \frac{[\tilde{\mathbf{u}}_1^{(n)}(x_R, y_R)][\mathbf{p}^{(n)}(r)]}{\omega_n^2 + 2i\omega\omega_n\zeta_n - \omega^2}, \quad (6.12)$$

where (x_L, y_L) and (x_R, y_R) are the coordinates of the left and right bridge feet respectively. Using these two transfer functions, we can calculate the radiated sound pressure in response to the forces, F_L and F_R , applied by the bridge feet:

$$Y_{BP} = Y_{LP}F_L + Y_{RP}F_R. \quad (6.13)$$

6.4.1 Varying the stiffness and the position of the soundpost

Following the work presented in Section 6.3, we will now replicate the same studies for the bridge model. First, we do a large scale study and test multiple combinations of k and κ for 400 soundpost positions all over the plate. For each combination of k and κ , we will record which soundpost position produces the highest total radiated sound pressure and record this value.

The results are plotted in Figure 6.10, this plot being equivalent to Figure 6.8 which is for a single point excitation force. We will use the G string as the location of the excitation force on the bridge. The results are similar to our findings in the previous section where a single point force excitation method was used. We see that just above $k = 10^4$ N/m there is a transition where as the axial stiffness gets higher the total radiated sound pressure increases. There is also a transition as the bending stiffness goes from $\kappa = 10^0$ – 10^2 Nm/rad, at low axial stiffness. At a high bending spring stiffness ($\kappa = 10^8$ Nm/rad), there is a very faint band of high radiated sound

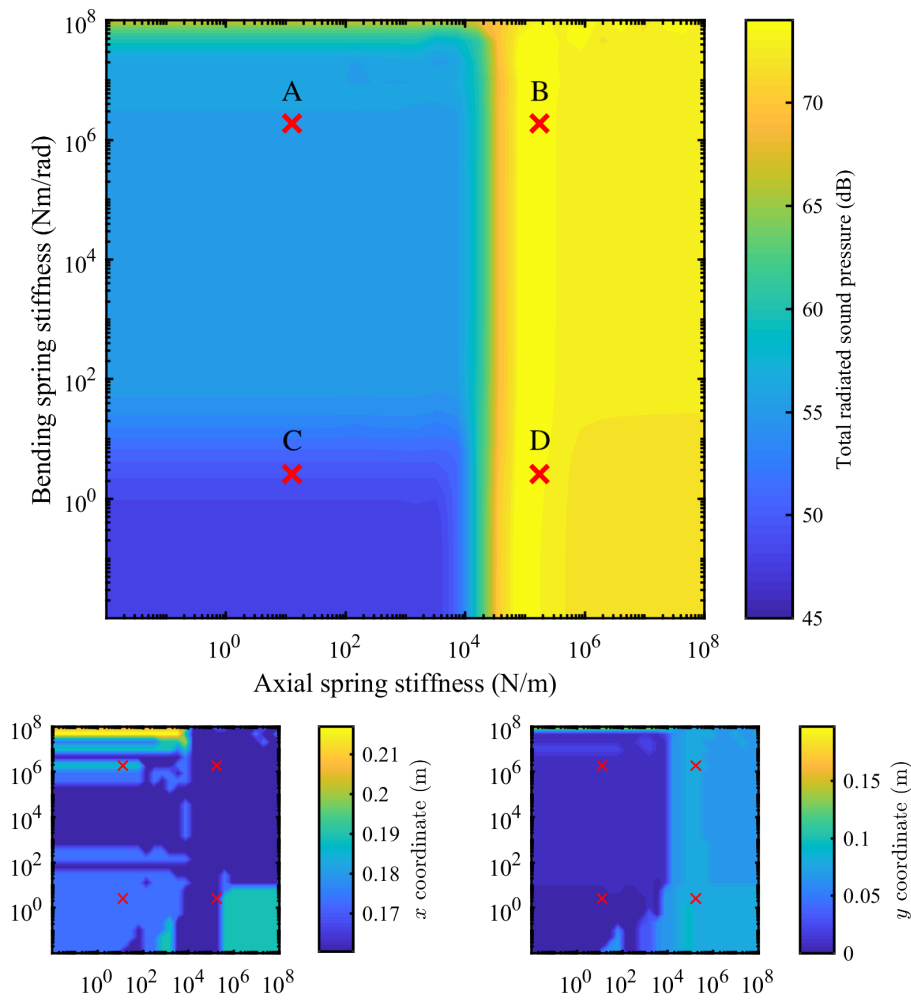


Figure 6.10: In the top plot, multiple soundpost locations were tested for different combinations of the bending spring stiffness and the axial spring stiffness. For each combination, the largest total radiated sound pressure was recorded and this value plotted in the surface plot above. Beneath this, two smaller plots display the x and y coordinates which correspond to the largest value of total radiated sound pressure that was recorded. This figure corresponds with a driving force being applied at the G string notch.

pressure present at the edge of the plot. However, on further investigation this has been shown to be a numerical artefact. Of particular interest to us is a subtle band of high total radiated sound pressure around an axial stiffness of 10^5 N/m. If we plot a ‘slice’ through Figure 6.10 at a fixed bending stiffness of 10^4 Nm/rad, then we can clearly observe that there exists a peak in the total radiated sound pressure at around 10^5 N/m: see Figure 6.11. As the axial spring stiffness increases beyond this, the total radiated sound pressure falls by approximately 1 dB. This suggests that there exists an optimum soundpost coupling strength. A possible explanation for the decrease in total radiated sound pressure at high axial spring stiffness is that the plates become more clamped, inhibiting the motion of the plate ODS.

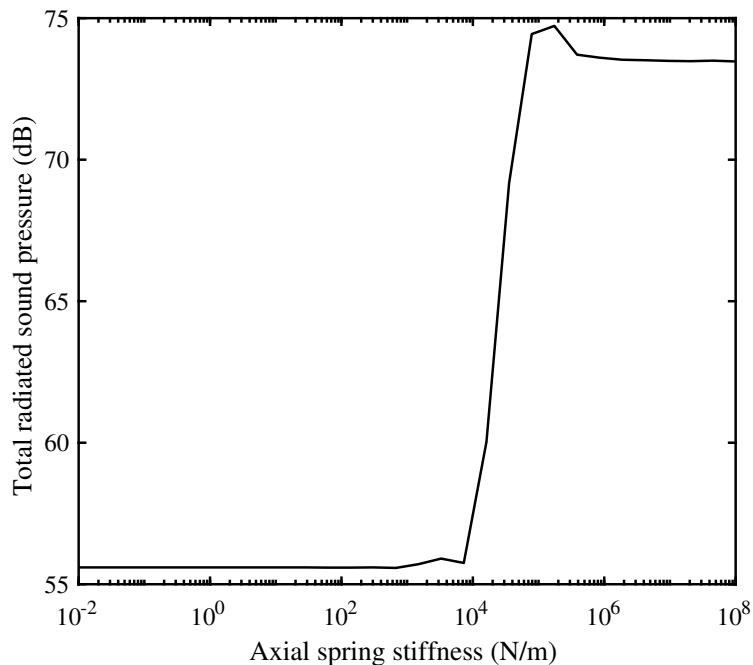


Figure 6.11: A ‘slice’ taken from Figure 6.10 for bending spring stiffness equal to 10^4 Nm/rad.

As we did previously in Figure 6.9, we will examine four individual combinations of axial and bending stiffness for our results with the bridge model. These combinations are marked with red crosses in Figure 6.10 and correspond to areas of low and high axial stiffness and low and high bending stiffness. The total radiated sound pressure associated with all the soundpost positions that were tested for these stiffnesses is shown in Figure 6.12, where the order of the plots follows the order of the red crosses.

Examining the two plots on the left hand side, which correspond to low axial stiffness, we see that the total radiated sound pressure is low across all locations on the plate. At this level of axial

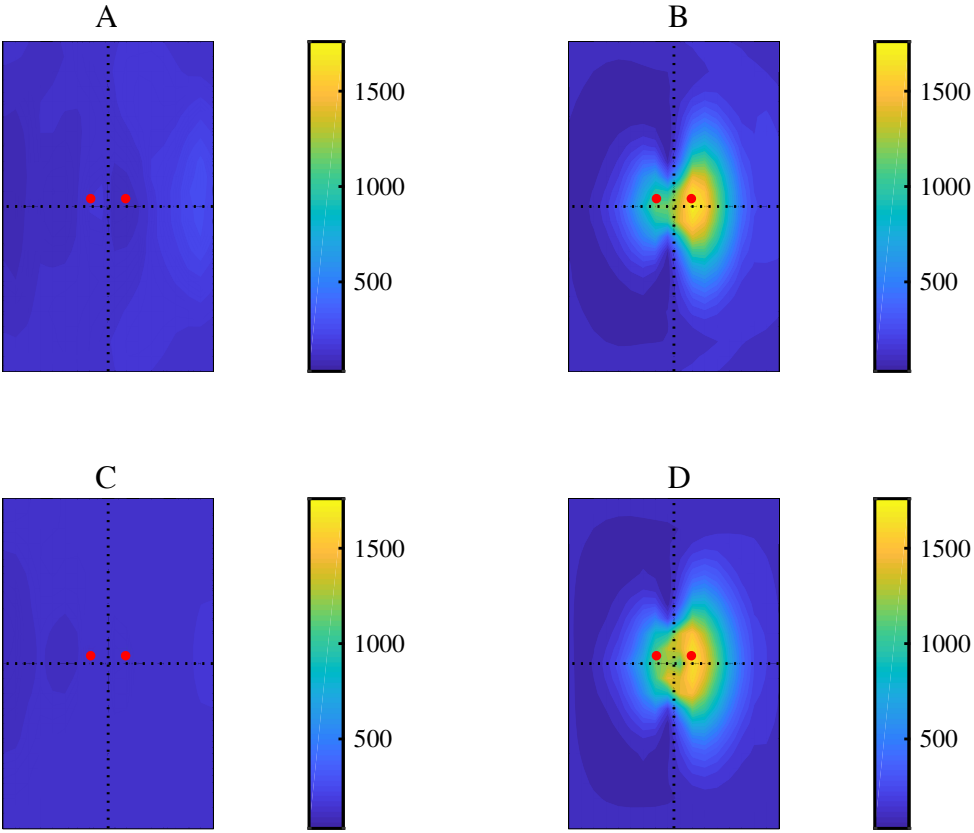


Figure 6.12: Four plots showing the total radiated sound pressure measured at locations across the plate. Each plot represents a fixed value of k and κ , indicated on Figure 6.10 by the four red crosses. The order of the plots follows the order of the crosses.

stiffness, the soundpost is effectively decoupled from the plates, so it is understandable that all soundpost positions return the same result.

Looking at the two plots on the right hand side, which correspond to high axial stiffness, we see that the soundpost position that maximises total radiated sound pressure occurs in an area near the right hand bridge foot. This is very similar to the position at which a soundpost would be placed in a real violin.

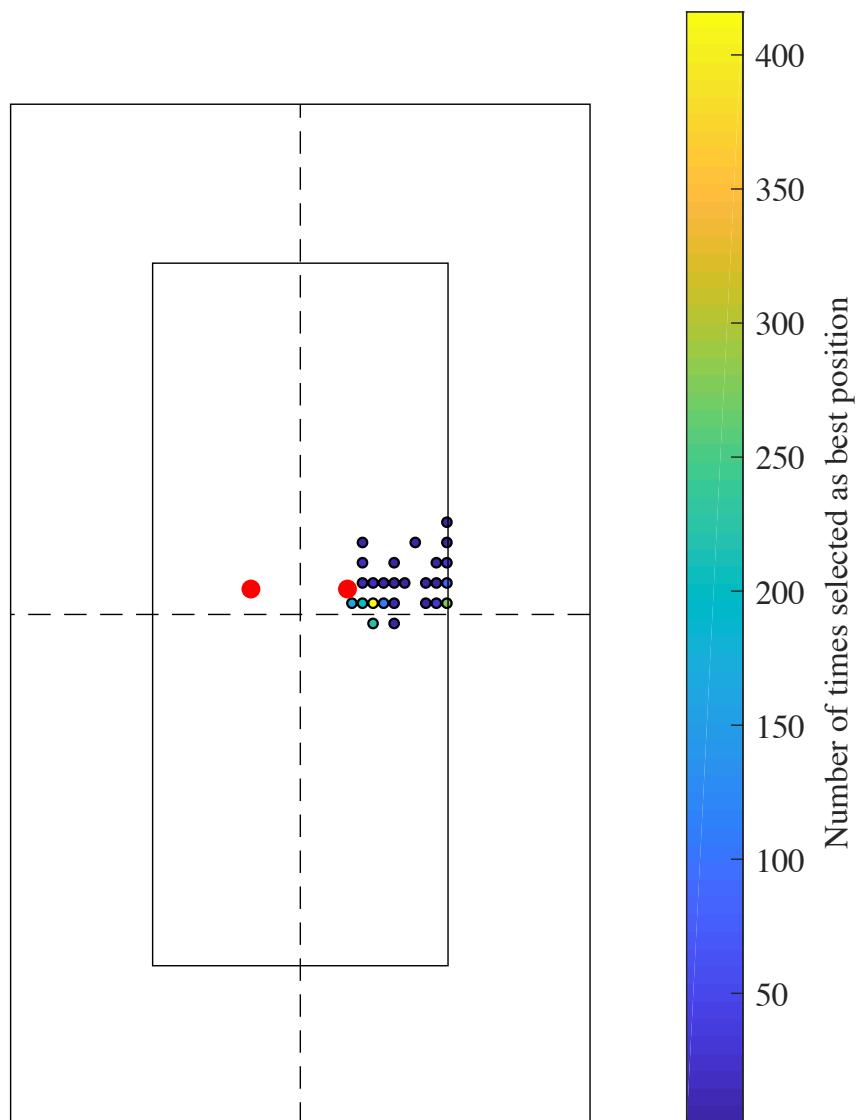


Figure 6.13: A plot showing all the soundpost positions that recorded the largest value of total radiated sound pressure, for combinations of k and κ as used in Figure 6.10. However, in this calculation a smaller area of points were examined, as illustrated by the inner rectangle. The colour of each of the circles indicates how many times that location was chosen. The two red circles represent the location of the two bridge feet.

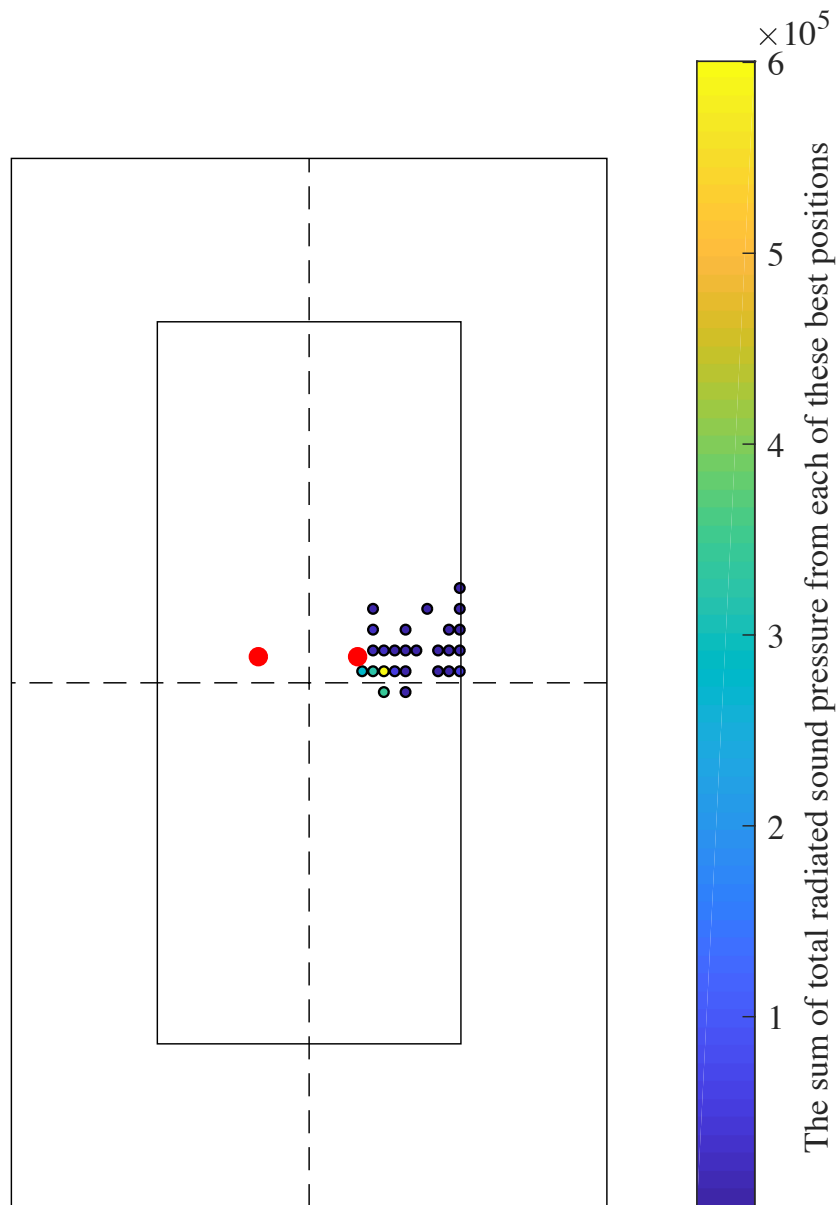


Figure 6.14: A plot showing all the soundpost positions that recorded the largest value of total radiated sound pressure, for combinations of k and κ as used in Figure 6.10. However, in this calculation a smaller area of points were examined, as illustrated by the inner rectangle. The colour of the data points represent the sum of the total radiated sound pressure added up for every instance where it was a ‘maximum’ location.

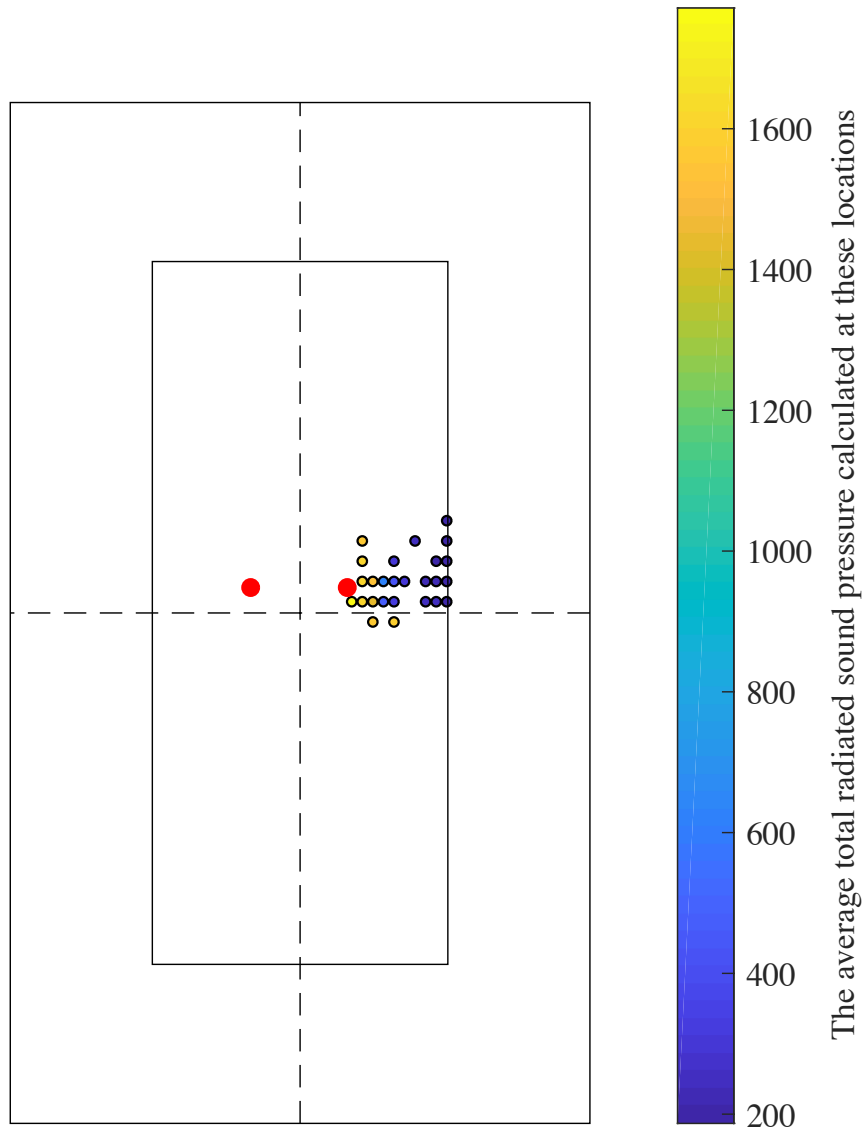


Figure 6.15: A plot showing all the soundpost positions that recorded the largest value of total radiated sound pressure, for combinations of k and κ as used in Figure 6.10. However, in this calculation a smaller area of points were examined, as illustrated by the inner rectangle. The sum of the total radiated sound pressure as shown in Figure 6.14 has been divided by the number of times the location was chosen. This gives an average total radiated sound pressure measured at each of these locations.

Using the data obtained from the calculations required to generate Figure 6.10, there are a number of different analyses we can perform. For each combination of axial and bending spring stiffness, we obtain a soundpost location that maximises total radiated sound pressure. In Figures 6.13–6.15, we present a number of ways to interpret this data. Points on the plate that were selected as being the ‘ideal’ soundpost location are shown using filled circles. In three separate plots, the filled circles are coloured to indicate: the number of times the position was selected as the ‘ideal’ soundpost location, the sum of the total radiated sound pressure obtained each time the position was selected, and the average total radiated sound pressure obtained at all the selected locations.

Figure 6.13 shows the number of times each point was selected as the soundpost position which maximised total radiated sound pressure. Here we see a collection of points that are coloured dark blue, indicating they were selected very few times. The most noticeable data point is the single data point coloured yellow, located to the right of the right hand bridge foot. This point was the position selected the most times by far during the calculation. The location of this point in relation to the two bridge feet shows significant agreement with the arrangement of a soundpost in a real violin. However, we must concede that the location of the two bridge feet bears an influence on this result. Due to the symmetry of our model, if the two bridge feet were located below the midpoint line (i.e. towards the lower bouts), then the results obtained would be exactly mirrored. Therefore, the ideal soundpost location would be located ‘above’ the position of the bridge feet. Nevertheless, these results demonstrate that having a soundpost located near the bridge feet — and crucially slightly off-centre — is an ideal location to maximise radiated sound pressure.

In Figure 6.14 we observe a similar pattern of results to Figure 6.13. The same one soundpost location stands out, when a sum of the total radiated sound pressure recorded each time is made. Figure 6.15 shows the same data in Figure 6.14 except that it has been divided by results in Figure 6.13 to give an average value of the total radiated sound pressure at each of the selected soundpost locations. Here we see that there is a band of soundpost locations which equally produce a high level of total radiated sound pressure. This confirms what we predicted in theory, that the symmetry of our model means there is no strong argument for placing the soundpost either above or below the bridge feet. Both arrangements are equally valid in our model.

6.4.2 The differences between the four strings

So far, we have studied the effect of the bridge model on radiated sound pressure using only the G string notch as the location of our input excitation force. We will now investigate all four

strings. In particular, we will be examining whether there are differences in the radiated sound pressure when driving at each of the four string notches. We will be addressing questions such as how does driving at the different string notches influence the ‘optimal’ soundpost location? And, for a given soundpost location, how does the total radiated sound pressure differ between the four strings?

6.4.3 Small changes to the position

We will first make small adjustments to the position of the soundpost while calculating the total radiated sound pressure. This study acts as an extension to work presented in Section 5.3, because it involves moving the soundpost E–W and N–S from its base location as shown in Figure 5.16. The difference here is that we will use radiated sound pressure as our metric for evaluating the ‘balance of the strings’.

Moving the soundpost E–W

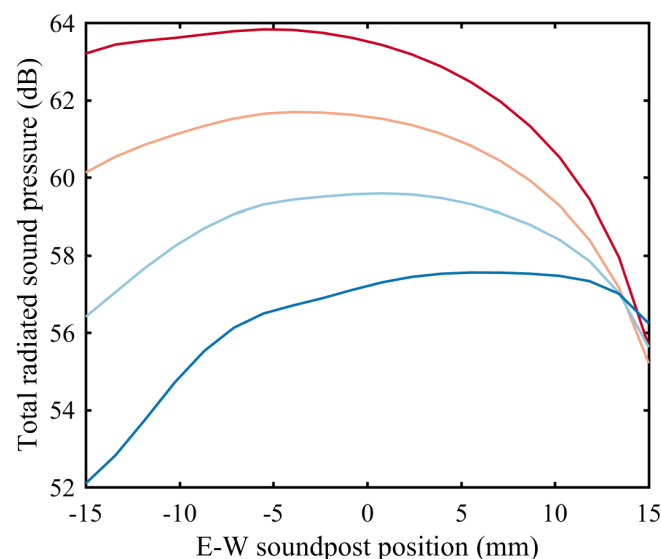


Figure 6.16: The total radiated sound pressure when driving at each of the four strings as a function of East–West soundpost position. A diagram illustrating the position of the soundpost in this plot can be seen in Figure 5.16. The G string is shown in red, the D string in orange, the A string in light blue and the E string in dark blue.

Figure 6.16 shows the radiated sound pressure calculated for an input driving force at each of the four string notches, as the soundpost is varied in position from east to west (according to Figure 5.16). There is a very clear trend in this graph, which is that as the soundpost moves west, i.e. towards the centre of the plate, the total radiated sound pressure approaches the same

value for all four strings. This is a significant result as it shows agreement with our findings in Section 5.3.1. As the soundpost moves west towards the centre of the plate, the strings become more ‘balanced’. We observed this effect when looking at the ‘normalised’ input admittance of the four strings and we are observing this same effect now when calculating the total radiated sound pressure.

Moving the soundpost N–S

Figure 6.17 shows the radiated sound pressure calculated for an input driving force at each of the four string notches, as the soundpost is varied in position from south to north (according to Figure 5.16). We observe that there is a slight increase in the total radiated sound pressure, for all strings, as the soundpost is moved north (i.e. closer to the right hand bridge foot). This includes a subtle peak in the value of total radiated sound pressure around +9 mm. However, in comparison to Figure 6.16, the effect of North–South soundpost position the balance of the strings is far less prominent.

The order of the strings — the G string having the largest value of total radiated sound pressure while the E string has the smallest — shows agreement with Figure 5.13. The amplitude of the plate ODS shown in Figure 5.13 is largest for the G string and smallest for the E string. This influences the net volume change of the box which in turn influences the total radiated sound pressure.

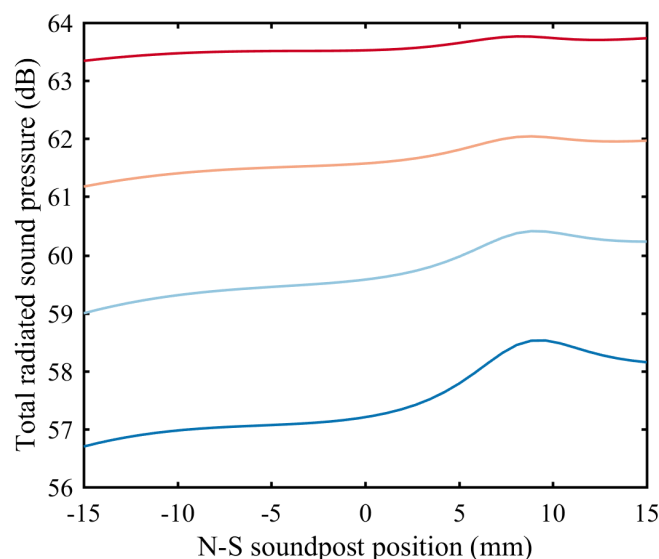


Figure 6.17: The total radiated sound pressure when driving at each of the four strings as a function of North–South soundpost position. A diagram illustrating the position of the soundpost in this plot can be seen in Figure 5.16. The G string is shown in red, the D string in orange, the A string in light blue and the E string in dark blue.

6.4.4 The optimal soundpost location for the four different strings

In Section 6.4.1, we investigated the optimal soundpost location when the driving force is applied at the G string notch (the optimal soundpost location being the location that maximises the total radiated sound pressure). We will now extend this study to cover all four strings. The results are shown for an axial and bending spring stiffness of $k = 10^6$ N/m and $\kappa = 10^4$ Nm/rad. As before, we calculate the total radiated sound pressure at multiple soundpost locations and plot the results as a surface plot over the outline of the front plate.

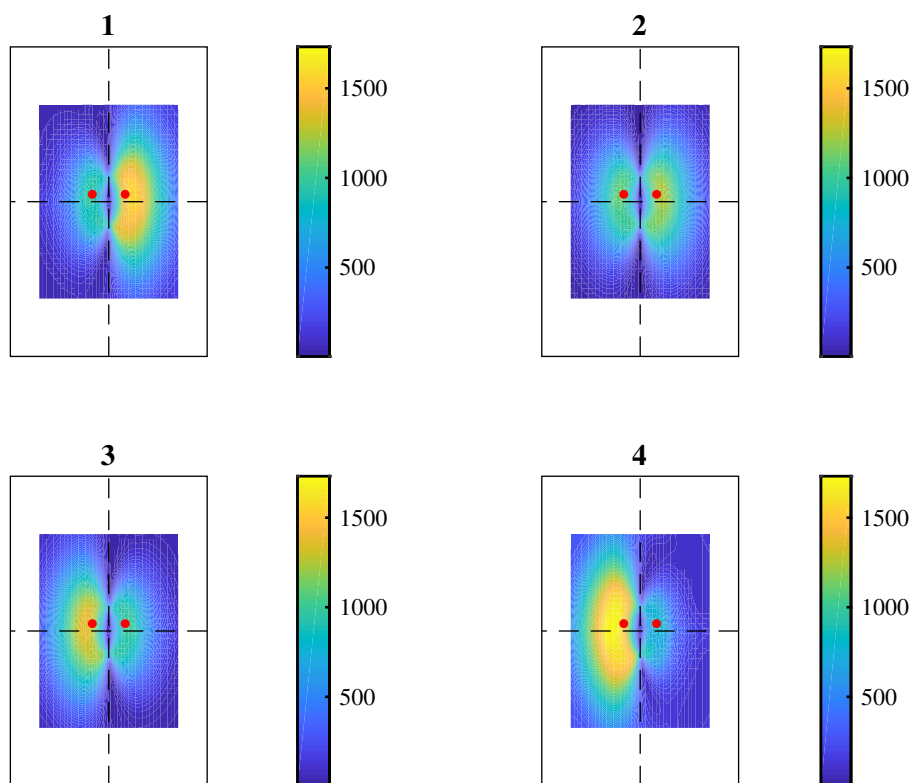


Figure 6.18: Four plots showing the total radiated sound pressure at different soundpost positions when applying the input driving force at the four different strings. The colours represent the total radiated sound pressure using a linear scale. The number above the plot corresponds to string in question. Note that the soundpost positions that were tested lie in a concentrated area around the bridge feet (shown by filled red circles). Hence, the outline of the plate lies beyond the coloured area.

The results for all four strings are shown in Figure 6.18, where the total radiated sound pressure has been plotted here using linear scale. Starting with the G string (1), we see results line in with those already shown Figure 6.12: there is a preference for the soundpost to be located

on the right hand side of the plate, near the right bridge foot. However, we see this trend is reversed when looking at the E string (4). Here, locating the soundpost on the left hand side of the plate is preferable in terms of increasing radiated sound pressure.

These results are reassuring, as they show agreement with our findings in Section 5.2. Here, we observed that a soundpost placed near the right hand bridge foot resulted in resonances at G string being larger in amplitude, while a soundpost placed near the left hand bridge foot resulted in resonances at E string being larger in amplitude.

This is simply a consequence of the symmetry of our simplified violin body model. In a real violin, the bass bar, which is glued underneath the front plate (see Figure 1.2) running underneath the left hand bridge foot, breaks this symmetry.

7

Experimental work

The main focus of this thesis has been to establish and test an enhanced working theoretical model of the violin body, soundpost, and bridge. There are many possibilities for developing experimental methods to supplement this theoretical work. However, substantial experimental challenges make such work a significant undertaking. In this chapter, we outline the experimental work that we have developed as an introduction to the way in which future physical modelling might complement the theoretical work done in this thesis. Following the style of our theoretical modelling approach, we have constructed a simplified physical model of the violin body consisting of two flat rectangular plywood plates, enabling us to investigate its vibrations, including the effect of introducing a soundpost. In this chapter, we are able to make observations about the bending resonances of the soundpost by attaching an accelerometer directly to the soundpost, and to investigate the tightness of the soundpost through the use of a specially designed adjustable soundpost. Finally, we will conclude with some measurements taken on a real violin.

7.1 An overview of the equipment and experimental techniques used

The experimental work undertaken in this chapter falls under the topic of “modal analysis”. We will be investigating the vibration of physical structures in the frequency domain. To do so, we will provide a known excitation force to the structure and measure the resulting motion of the structure, with the ultimate goal of calculating a transfer function: the ratio of the output to the input. Most often, we will be calculating an admittance, i.e. the velocity per unit force:

$$H(\omega) = \frac{V(\omega)}{F(\omega)}. \quad (7.1)$$

As we are interested in studying the vibration of the violin over a frequency range spanning 50–10,000 Hz, we require a method of excitation that can excite all frequencies in this range. An ‘impulse response’ is perfectly suited to this problem (see Maia and Silva, 1997, ch. 3). A miniature instrumented impulse hammer by PCB (Model 086E80) has been used, along with a suitable charge amplifier.

To measure the velocity of the structure in response to the impulse excitation force, we require a sensor. We have chosen to use accelerometers to measure the vibration of the structure. For the frequency range we are interested in, 50–10,000 Hz, a small lightweight accelerometer is required. A miniature piezoelectric single axis accelerometer by PCB (Model 352C22) has been used, along with a suitable charge amplifier.

A number of the experiments which follow involve the use of two accelerometers in order to measure the vibration at two points on the structure. For the purposes of our investigation, absolute calibration of the accelerometers is not required. However, relative calibration of the two accelerometers was carefully considered so that data obtained from each could be compared. For all experiments, the data was logged using a PC running in-house data logging software in MATLAB. All data presented is shown as an average of five repeated measurements, to reduce the effect of measurement noise. Additionally, the coherence of the signal acts as a metric for determining the linearity and general quality of the measurement at a given frequency (see McConnell, 1995).

7.2 A simplified physical model of a violin body

Our aim has been to construct a simplified physical model of a violin body, similar to the theoretical model introduced in Chapter 2. A model was built using two flat rectangular plywood plates (for a diagram of the model see Figure 7.3). The two plates are joined to each other at the four corners using wooden blocks. This design was chosen to facilitate easy access to the space between the plates. Ultimately, our main goal has been to wedge a soundpost in between the plates and study the dynamics of the structure while making adjustments to the soundpost. Having open space on the sides allows these adjustments to be made easily. It is therefore important to acknowledge that because the boundary conditions of our physical model are different to those which apply in our theoretical model, our work here does not enable us to precisely match the dynamics of the two models. The physical model is well enough adapted to allow us to make some observations about general features in the data only.

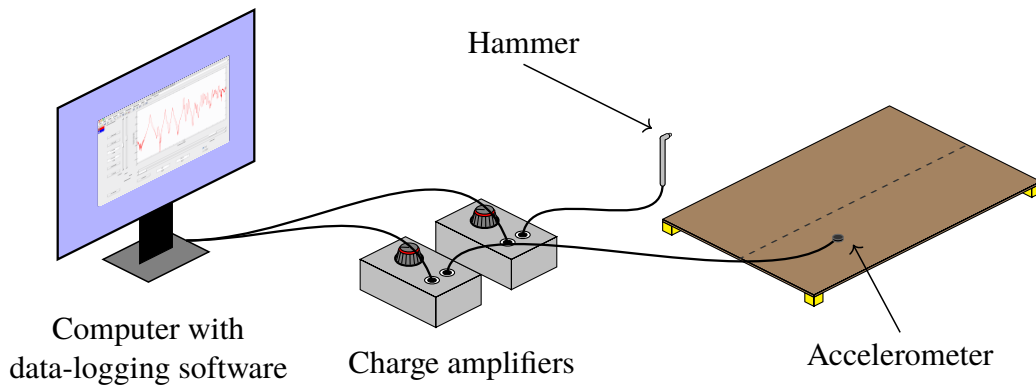


Figure 7.1: A schematic diagram of the experimental set-up used to measure the admittance of the separate plates. The plate is raised off the ground using pieces of foam placed at the edges.

7.2.1 The separate plates

Before describing our experiments on the complete model, we will first look at the properties and vibrational behaviour of the individual plates. Before the model was glued together, modal analysis was conducted on the two plates separately. The experimental set-up is shown in Figure 7.1. An accelerometer is positioned on the surface of the plates at our chosen measurement point. This is attached using a small amount of sticky wax. The measurement location was chosen so that significant nodal points on the plates were avoided. Therefore, the location corresponds to the length and width divided by π , an arrangement that has been previously used in the theoretical work. The plates are suspended on small pieces of foam placed under the corners, allowing for the plate to vibrate with a minimal amount of damping.

Figure 7.2 shows the driving point admittance of each of the plates. The results demonstrate that the plates are very similar, with only some small differences in modal frequencies. These results have enabled us to calculate values for the elastic constants D_1 – D_4 , using the methods described by McIntyre and Woodhouse (1988). A table of the plate properties is shown in Table 7.1.

7.2.2 The complete physical model

We will now examine the vibration of the complete physical model. A schematic diagram of the experimental set-up is shown in Figure 7.3. An additional second accelerometer was placed on the back plate of the model, at the same position as on the front plate, i.e. directly at the point at which the soundpost meets the plate. A hammer impulse was applied to the front plate at a location on the left hand side of the plate, marked in Figure 7.3 by a red cross, replicating the

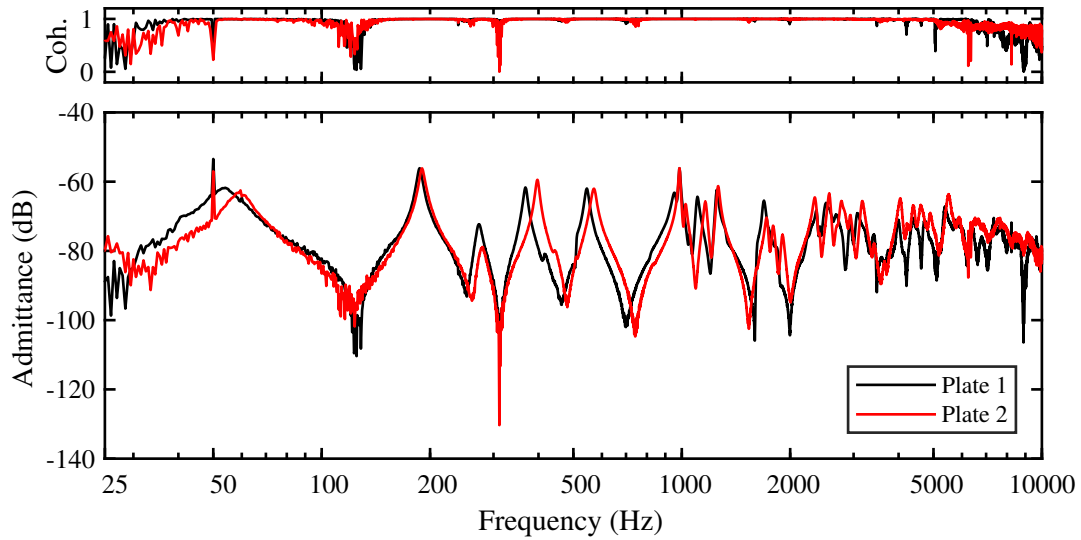


Figure 7.2: The driving point admittance measured on the front and back plates when separated. Figure 7.1 shows a schematic diagram of the experimental set-up.

Table 7.1: Properties of the plywood plates from our experimental model.

Property	Plate 1			Plate 2		
	Symbol	Value	Unit	Symbol	Value	Unit
Length	a_1	299	mm	a_2	299	mm
Width	b_1	225	mm	b_2	225	mm
Thickness	h_1	5.5	mm	h_2	5.5	mm
Density	ρ_1	503	kg m ⁻³	ρ_2	503	kg m ⁻³
Elastic Constants	$D_1^{(1)}$	1419	MPa	$D_1^{(2)}$	1651	MPa
	$D_2^{(1)}$	94	MPa	$D_2^{(2)}$	97	MPa
	$D_3^{(1)}$	118	MPa	$D_3^{(2)}$	122	MPa
	$D_4^{(1)}$	171	MPa	$D_4^{(2)}$	169	MPa

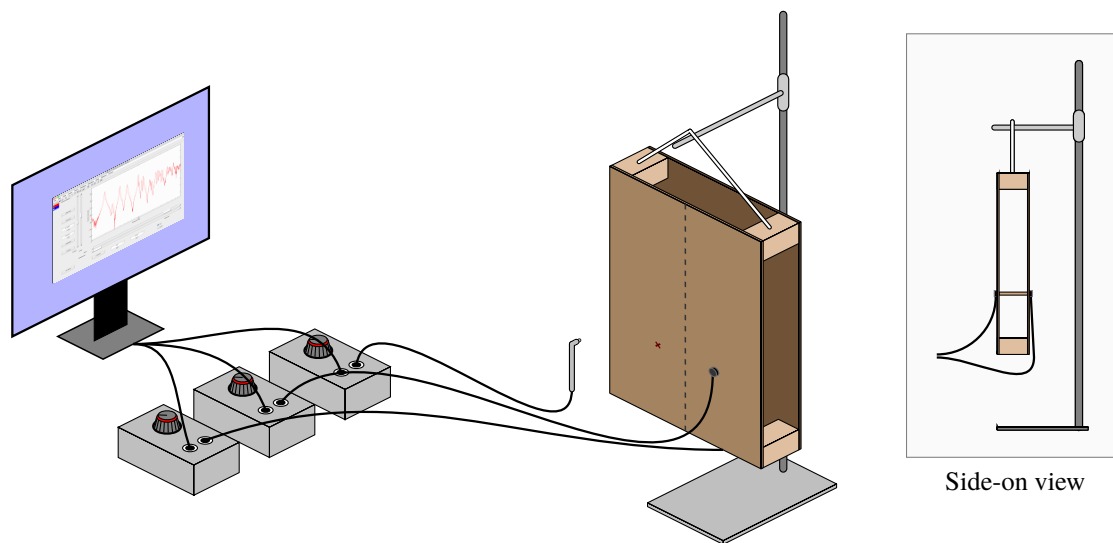


Figure 7.3: A schematic diagram of the experimental set-up used in Sections 7.2.3 and 7.2.4. Our simplified physical model of the violin body is shown hanging from a retort stand. The side-on view illustrates how a soundpost may be positioned between the two plates.

set-up used in the calculations that were performed in Section 3.2. The model was suspended from a retort stand using string attached to the top corner blocks.

7.2.3 Without a soundpost

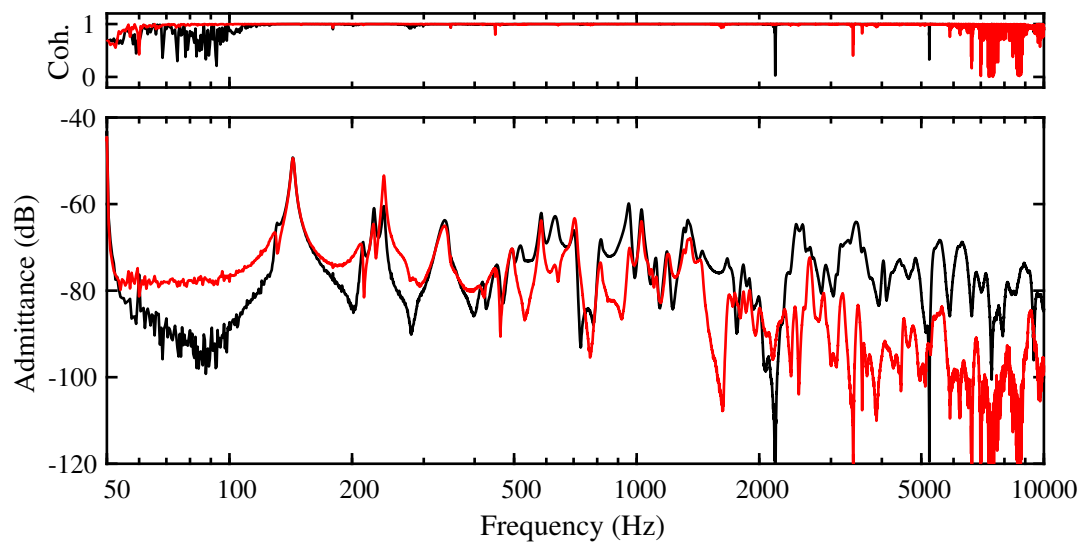


Figure 7.4: The admittance measured on the front plate (black line) and the back plate (red line) for the physical model without a soundpost. A diagram of the experimental set-up is shown in Figure 7.3.

Figure 7.4 shows the admittance measured on the two plates when the model does not have a soundpost. It is important to note that a key point of difference from the theoretical model arises here, as in the physical model the back plate is coupled to the front plate despite there being no soundpost. Whereas the theoretical model would show no response in the back plate for this arrangement without a soundpost, the physical model does. The reason we see resonances in the back plate is because of the coupling at the edges of the plates, via the blocks.

Comparing the two sets of data in Figure 7.4, we see that there are a number of resonances which are detected on both the front and back plates. For some of the lowest resonances, the amplitude of the resonance peaks are also similar in size. These resonances involve the vibration of the entire structure, rather than being isolated to the separate plates. However, at frequencies above 2000 Hz, we see that, in general, the amplitudes of the resonances measured on the back plate are significantly lower than those on the front plate. This reflects the fact that the excitation force has been applied to the front plate of the model, causing resonances associated with it to be excited more strongly.

7.2.4 With a soundpost

Table 7.2: Properties of the soundpost used in our experimental model.

Property	Soundpost		
	Symbol	Value	Unit
Radius	r	2.75	mm
Density	ρ	517	kg m ⁻³
Young's Modulus	E	4.4	GPa

We will next investigate the inclusion of a soundpost in the model. The soundpost used in this experiment has been fabricated out of spruce dowel. The material properties are listed in Table 7.2. The Young's modulus was calculated using the theoretical formula for the bending resonances of a free-free beam, informed by a measurement on a length of dowel supported on foam pads. The length of the soundpost in this experiment was 49.5 mm, which represented a tight fit between the plates. The soundpost was positioned at a fraction of π along the length and width of the plates, i.e. wedged between the plates at the same position as the two accelerometers.

Figure 7.5 shows the admittance measured on the two plates when a soundpost is included in the model. In comparison to the model when it does not include a soundpost, the addition of the soundpost has resulted in a different set of resonance frequencies, as we would expect.

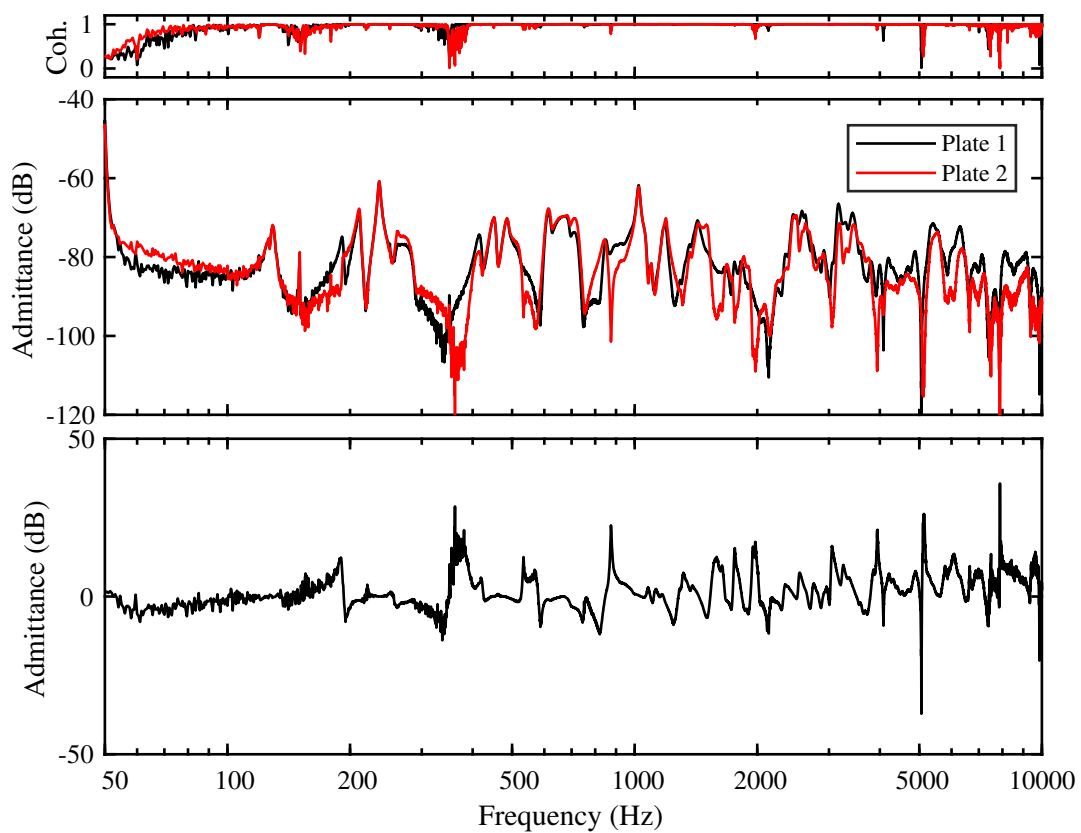


Figure 7.5: *Top:* The admittance measured on the front plate (black line) and the back plate (red line) for the physical model with a soundpost. *Below:* The difference between the two responses, i.e. the response for plate 1 minus the response for plate 2. A diagram of the experimental set-up is shown in Figure 7.3.

The most significant point of difference between Figure 7.5 and Figure 7.4 is that at frequencies above 2000 Hz, the amplitude of the resonance peaks in the back plate are much higher. This is because the soundpost is now coupling the front and back plates together. Specifically, we are measuring at the points on the front and back plate where the soundpost is located. Therefore, if we assume the soundpost acts as a rigid link, we would expect the admittance measured at these two points to be equal. The fact that they are very similar demonstrates that the soundpost is strongly coupled to the plates.

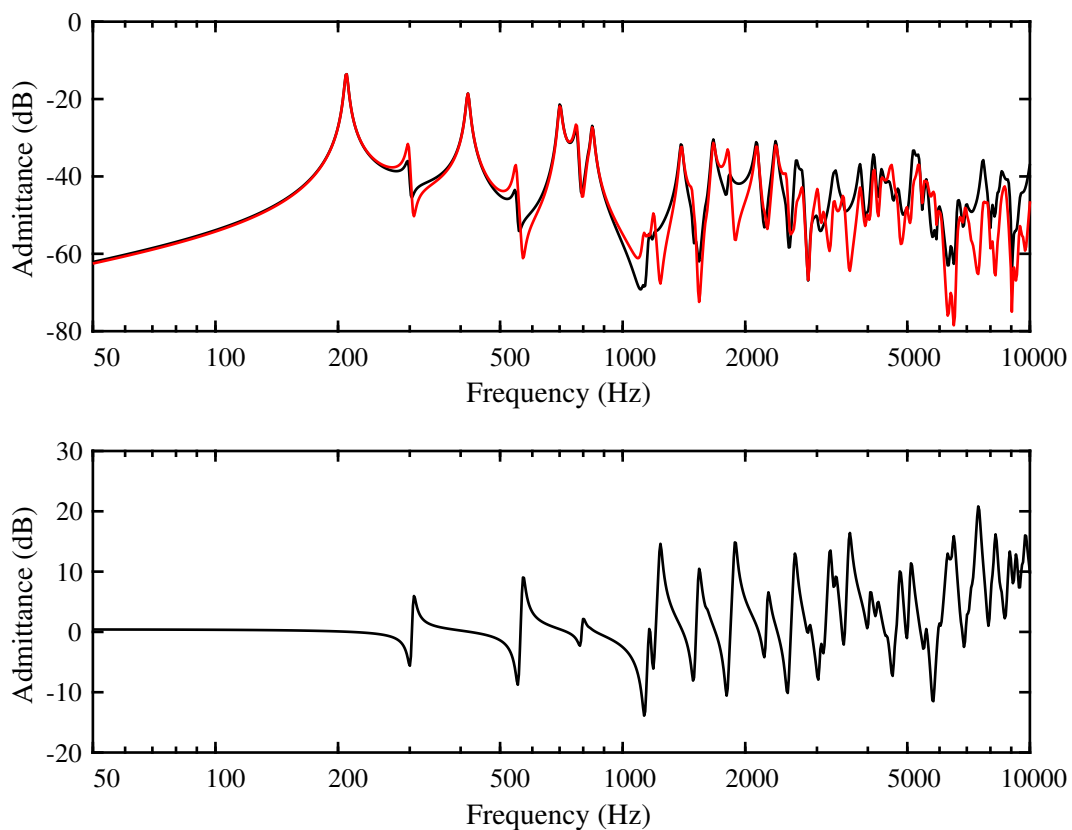


Figure 7.6: A equivalent plot to Figure 7.5 calculated using our theoretical model. *Top:* The admittance calculated on the front plate (black line) and the back plate (red line) for the theoretical model with a soundpost. *Below:* The difference between the two responses, i.e. the response for plate 1 minus the response for plate 2.

In order to make a comparison with the theoretical model, we have calculated the equivalent theoretical set-up of this experiment. This uses the properties of the plates and soundpost as defined in Tables 7.1 and 7.2. The axial and bending spring stiffness is set to $k = 10^6$ N/m and $\kappa = 10^4$ Nm/rad. The results are shown in Figure 7.6. While acknowledging that no precise comparison of the resonance frequencies can be made, we can observe that there is general

agreement between the two results. At frequencies below 2000 Hz, the plates are strongly coupled together, while above 2000 Hz the response on the front plate is slightly larger than on the back plate. The similarity between the experimental and theoretical results demonstrates that using high levels of axial and bending stiffness in the theoretical model is appropriate.

7.3 Examining the vibration of the soundpost

In this section we will examine the vibration of the soundpost by attaching an accelerometer directly to the soundpost. In doing so, we will be predominantly measuring the bending motion of the soundpost. Therefore, this experimental work emulates theoretical work that was presented in Chapter 3, in particular, the theoretical calculations of the soundpost bending resonances in Section 3.3.

As in the theoretical calculations of Section 3.3, the measurement location, i.e. the location of the accelerometer, was chosen so that significant nodal points were avoided. Therefore, a location of L/π was chosen. A hammer impulse was applied to the soundpost at the same position of L/π along the length, but rotated 180° around from the position of the accelerometer. From this, an admittance measurement was taken.

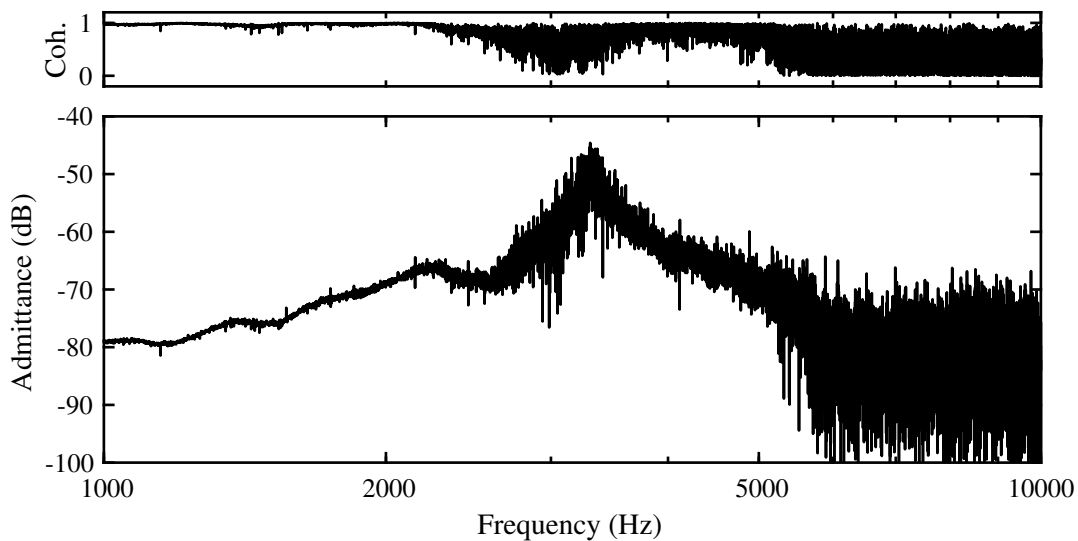


Figure 7.7: The admittance measured on the side of soundpost when an impulse is applied to the side of the soundpost.

The results of this measurement are shown in Figure 7.7. Despite the noticeable presence of noise, this data shows a prominent peak in the response at just above 3000 Hz. This bears strong resemblance to the first bending resonance of the soundpost as predicted theoretically: see Figure 3.11, which shows the bending resonances of the soundpost as a function of bending spring stiffness. Notice that the first bending resonance of the soundpost falls within a range of 2000–5000 Hz, depending on its boundary conditions, as determined by the stiffness of the bending springs. Therefore, this experimental measurement can be used to estimate which

bending spring stiffness would produce an equivalent response in the theoretical model of the soundpost. Estimating the first bending resonance (measured experimentally) to be around 3200 Hz, this would correspond to a bending spring stiffness of around 4 Nm/rad.

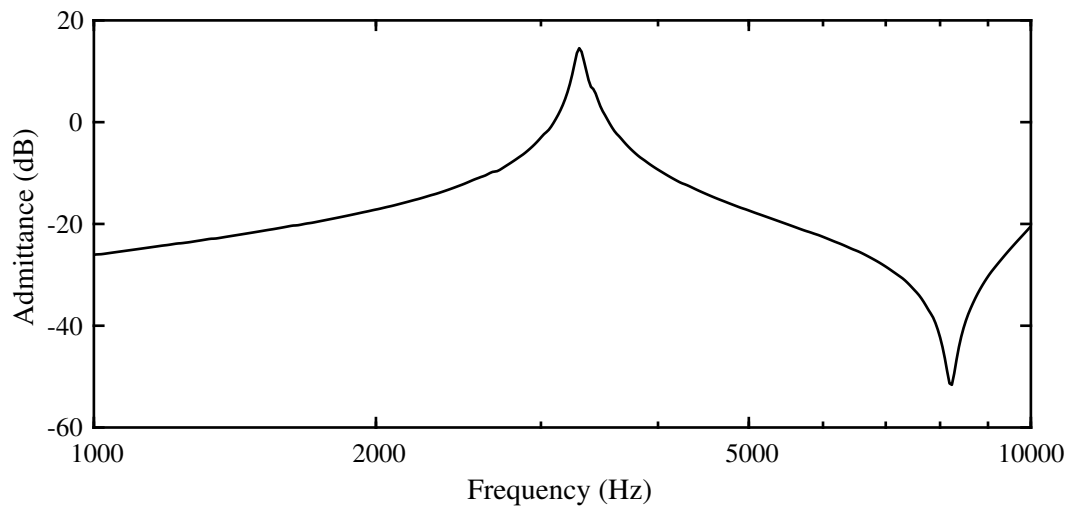


Figure 7.8: The driving point admittance of the soundpost calculated using our theoretical model using a bending spring stiffness of 4 Nm/rad. This value of bending spring stiffness was chosen so that frequency of the first bending resonance matches the experimental result.

Figure 7.8 shows the driving point response of the soundpost calculated using the theoretical model, using a bending spring stiffness of 4 Nm/rad. The similarity with Figure 7.7 is clear.

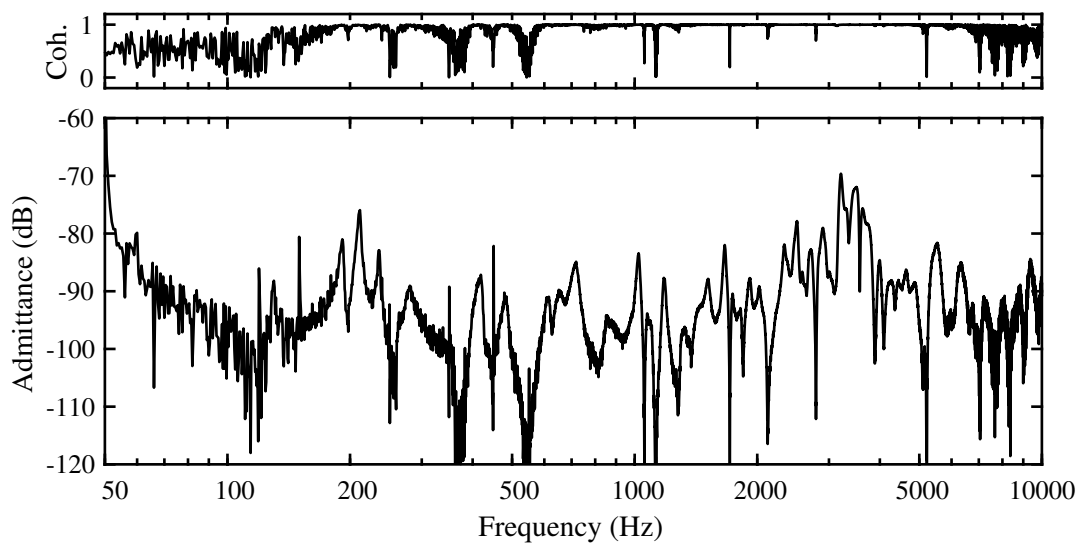


Figure 7.9: The admittance measured on the side of soundpost when an impulse is applied to the front plate. The location of the impulse is the same as that in Section 7.2.2.

Another experiment we can perform is to measure the velocity on the soundpost as before, but repositioning the driving point to a location on the plates. The driving point location on the front plate used in Section 7.2.2 will be used once again in this experiment. The resulting admittance measurement is shown in Figure 7.9. This plot reveals that resonances attributed to the plates can be detected on the soundpost. This can be verified by comparing the peaks in Figure 7.9 to those in Figure 7.5. The main difference is that the amplitudes of the resonances are in general much lower. This reflects the fact that the displacement of the soundpost in comparison to the plates is smaller.

The most striking feature of Figure 7.9 is that the resonance with the largest amplitude occurs at around 3000 Hz. On close inspection, there appears to be a broad peak in the admittance spanning a number of resonances in this region. This feature is most certainly associated with the presence of the soundpost bending resonance, as seen in Figure 7.7.

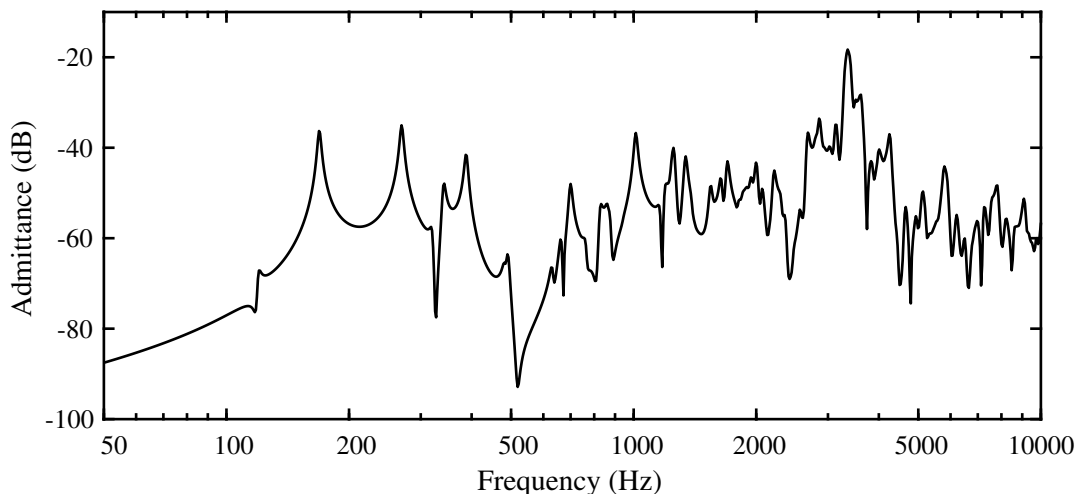


Figure 7.10: An equivalent theoretical calculation of the experimental result presented in Figure 7.9. As in Figure 7.8, a bending spring stiffness of 4 Nm/rad was chosen so that first bending resonance of the soundpost matches the experimental result. The axial springs have been set to 10^6 N/m.

An equivalent theoretical calculation of the experimental result shown in Figure 7.9 can be obtained. This result is shown in Figure 7.10. The most significant feature of this plot is that there is a peak in the response around 3000 Hz. While the differences in the plate boundary conditions in the theoretical and experimental models prevents any exact correspondence of their resonance frequencies, it is significant and encouraging for the validity of our theoretical model that similar trends can be observed in their respective results.

7.4 Experiments using an adjustable soundpost

In a real violin, the maker controls the ‘tightness’ of the soundpost by making adjustments to its length. In the theoretical work carried out earlier in this thesis, the length of the soundpost was a variable that remained constant, and instead, to simulate varying the tightness of the soundpost, adjustments were made to the stiffness of axial springs which connect the soundpost to the plates. In our experimental model, however, we can adjust the length of the soundpost and directly influence the tightness of the soundpost between the two plates. In this section we will therefore address the following question: how does the length of the soundpost affect the dynamics of our physical model?

The most obvious experimental method is to take a wooden soundpost and make systematic adjustments to its length, taking a measurement after each adjustment. Such small adjustments to the length of the soundpost can be made using a sharp knife. This is how a maker would adjust the length of the soundpost and also how they would shape the ends of the soundpost to ensure the desired fit between the soundpost and the plates. This method for adjusting the length of the soundpost was tried and tested in the laboratory, but was found to have a number of limitations. Firstly, it was difficult to accurately reduce the length of the soundpost by a fixed amount when performing successive cuts with a knife. Ideally, our experiment would consist of taking a ‘long’ soundpost, measuring the vibration of model using this soundpost, and then repeating this experiment but each time reducing the length by a small amount (e.g. 0.5 mm). A second difficulty with this ‘length adjustment by hand method’ is that it is difficult to ensure that the knife cuts maintain a perfectly flat surface at the ends of the soundpost. Ideally, the contact between the ends of the soundpost and plates would be the same for all tests.

Because of the experimental limitations associated with adjusting the length of the soundpost by hand, an alternative adjustable soundpost design was sought. Figure 7.11 shows a picture of the adjustable soundpost design that was devised for this experiment. It uses a screw mechanism so that adjustments can be made to its overall length. The principal advantage of this design is that we can accurately adjust the length of the soundpost by turning the screw a given amount. Additionally, the ends of this soundpost remain unchanged, ensuring that the nature of the contact area between the soundpost and plates is kept constant.

Although the dimensions and material properties of this plastic soundpost do not perfectly match that of a wooden soundpost, they are sufficiently similar so that the dynamics of the two designs are very much comparable. This is enough to allow us to draw conclusions from any general trends that emerge from the data.



Figure 7.11: The adjustable soundpost design that we developed. It is made from PVC and consists of two parts: a 1BA screw head and a tapped body (seen in black) of length 3.2 cm. The radius of the screw head, measured at the top is 3.5 mm, while the radius of the body is 4.0 mm.

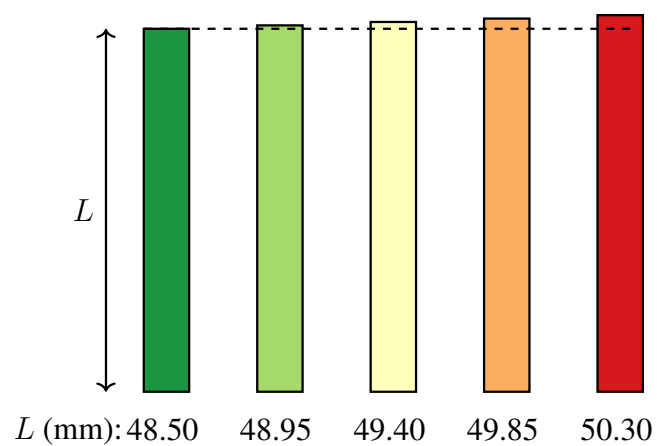


Figure 7.12: A diagram showing the lengths of the adjustable soundpost used in our experiment

Figure 7.12 shows a schematic diagram of the different soundpost lengths used in this experiment. The shortest length, 48.50 mm, represents the length at which the soundpost is only barely held in place by the compressional forces acting on it from the two plates. Any shorter than this and the soundpost would fall out. The subsequent increments in length are all of length 0.45 mm. For the size of screw thread used (1BA), this represents a half rotation. The maximum length, 50.30 mm, was the longest length that could be practicably wedged between the plates.

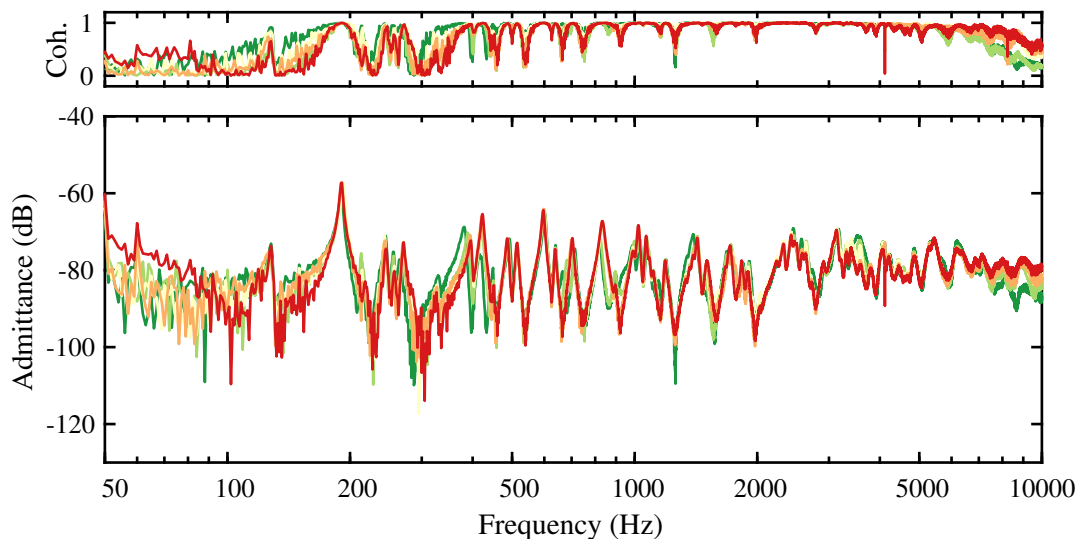


Figure 7.13: The admittance measured on the front plate on top of the position of the soundpost. Each plot shows a soundpost of different length, where green is the shortest and red is the longest: see Figure 7.12.

For each of the five soundpost lengths in Figure 7.12, a driving point admittance measurement was made on the front plate directly above the position of the soundpost. The position of the soundpost is consistent with our previous experiments: at a factor of π along the length and width of the plates. The results are shown in Figure 7.13, with zoomed-in plots of a selection of resonances shown in Figure 7.14

It is at this point that we encounter a significant experimental challenge to the outlines of a physical model of this kind. If we assume that that increasing the length of the soundpost results in the plates becoming stiffer, then this should correspond with a raising of the resonance frequencies. A number of resonances do exhibit this behaviour: for example, Figures 7.14(b) and 7.14(d). However, not all do. Figure 7.14(c) shows an example of a resonance where the frequency lowers as the length of the soundpost is increased. The likely explanation for these differing trends is that there are geometric inconsistencies within the model. An informal experiment using a dial indicator revealed that the plates were not in fact perfectly flat. This makes it very

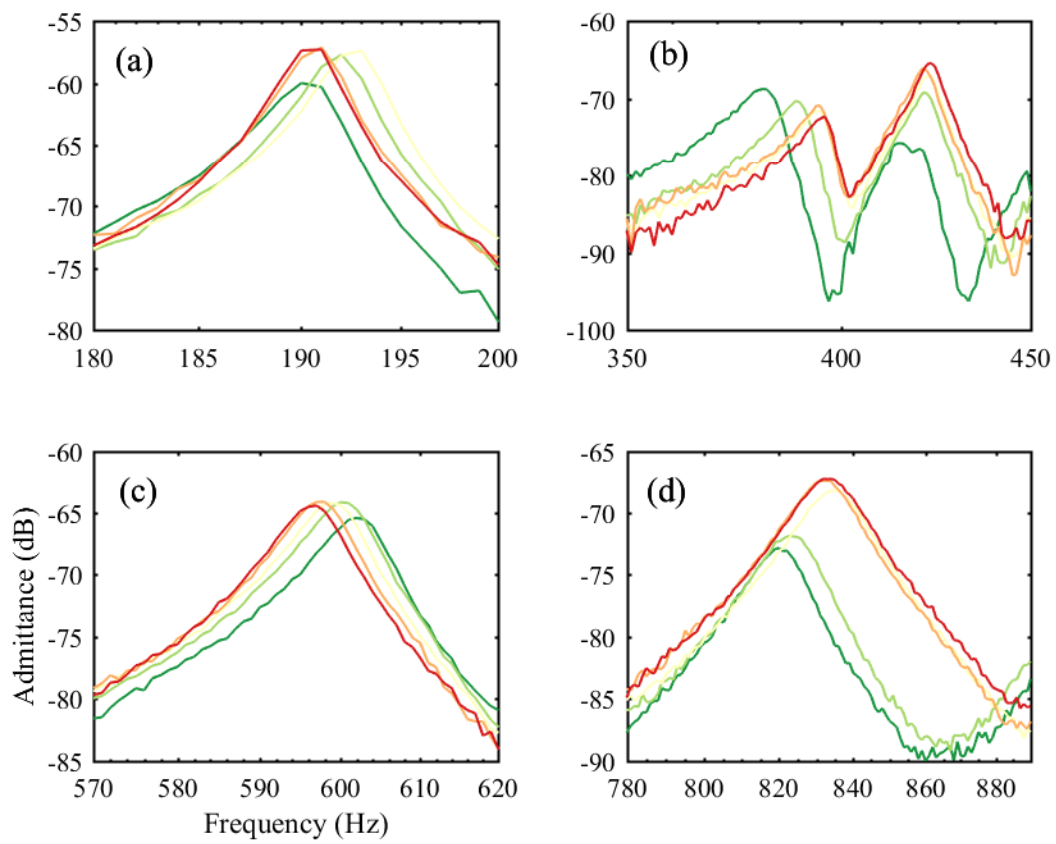


Figure 7.14: A zoomed-in view of a selection of resonances from Figure 7.13.

difficult to accurately account for the effects we are observing: the change in the length of the soundpost is changing the geometry of the plates in such a way that different resonances respond differently to those changes. The challenge is significant, and exceeds the kind of adjustments that could be made to a physical flat plate approximation of the kind outlined in this chapter. Indeed, it suggests that full experimental work incorporating an adjustable soundpost will require a solution beyond the flat plate modelling approach.

Despite its limitations in this context, our outline of an approach to a physical model of an adjustable soundpost allows some promising observations to be made. With a wooden soundpost it was particularly challenging to try and conduct an experiment investigating the effects of variations in soundpost length. However, by introducing a relatively simple adjustable soundpost design, the experimental process was greatly simplified and we were able to record measurements with confidence, knowing that the soundpost length was being adjusted systematically. The fact that the results demonstrate small sequential changes in the resonance frequencies is testament to success the adjustable soundpost design.

It is clear that we must acknowledge that more testing is required to fully understand the influence of soundpost length on particular resonances of a simplified flat plate violin model. However, the important conclusion we can draw from this experiment is that changes to the length of soundpost, in the order of fractions of millimetres, have a measurable influence on the dynamics of the plates. This lends credit to the theory that the soundpost can be used as a resource for sound adjustment because it has the capacity to alter the resonant frequencies of the violin body. The possibilities for developing these observations in further experimental detail are substantial.

7.5 Experiments on a real violin

Here, we will briefly present some experimental results obtained from measurements taken on a real violin, as a short supplement to the physical modelling discussed above. The violin used in these experiments is a modern German instrument of good quality (~£3,000).

Using an equivalent method to that adopted in Section 7.2.4, we have placed two accelerometers on the body of the instrument at the positions on the front and back plate where the soundpost makes contact with the body. The violin was fixed in place using a custom rig, with a clamp fixed to the chinrest and a strap holding it in place at the neck. The strings were damped using a piece of card pressed against them. A hammer impulse was applied to the top left hand side of the bridge, near the position of the G string.

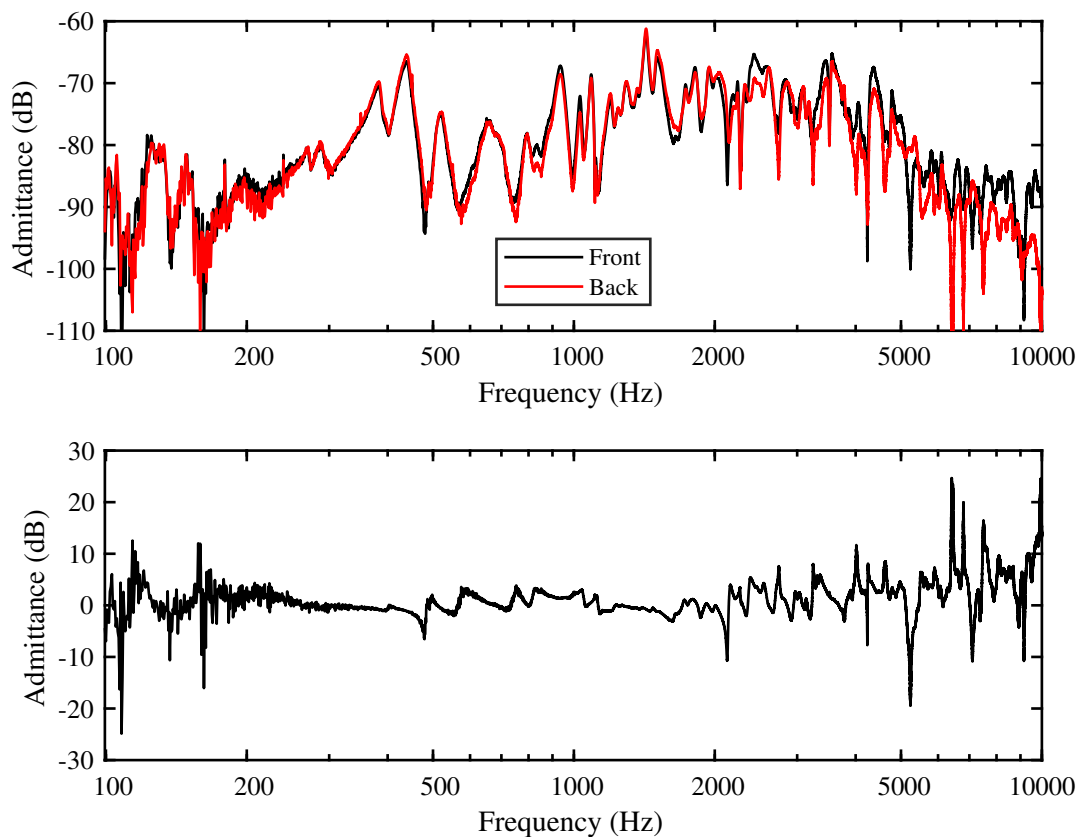


Figure 7.15: *Top:* The admittance measured on the front and back plates at the position of the soundpost, for a hammer impulse applied at the top left hand side of the bridge. *Below:* The difference between the two responses: i.e. the response for the front plate minus the response for the back plate.

The results are shown in Figure 7.15. Examining the response measured at the two plates at frequencies below 2000 Hz, we see the resonance peaks are well matched. This indicates the plates are strongly coupled in this frequency range. Above 2000 Hz, we see that there are some noticeable differences in the magnitude of the resonance peaks when comparing the two responses. This shows similarity with the behaviour observed in Figures 7.5 and 7.6.

Above 6000 Hz, the magnitude of the admittance measured on the front plate is at times significantly higher than that measured on the back plate. This suggests that the soundpost is not acting like a rigid link, which would clamp the two plates together, and that the plates are moving independently of each other. However, we must acknowledge there are limits to how accurately we can measure body resonances in this frequency range. Body resonances measured above 5000 Hz are highly sensitive to the position of the accelerometer. Additionally, although careful measurements were made to ensure that the accelerometers were placed on top of the points where the soundpost made contact with the plates, it is difficult to fully ensure the precision of this measurement.

These measurements show a general agreement with those produced by our physical model, and, though beyond the scope of this thesis, tests on a large number of instruments could provide further verification. Taken alongside the conclusions we have presented in the previous section, these results suggest that further experimental modelling of adjustable soundposts is merited, and that their incorporation in real violins — despite the practical challenges — has real potential.

8

Conclusion

The focus of this thesis been the soundpost, a small and deceptively simple component of the violin, all but invisible to most listeners and many musicians. Despite the proficiency of violin makers over the centuries, its precise mechanical role has been relatively poorly understood until, in more recent years, a growing body of modern acoustical research has begun to significantly advance our understanding. This thesis has drawn on that rich foundation of research in seeking to substantially improve our ability to conceptualise and test the role of the soundpost within a working theoretical model. In this concluding chapter, we will briefly review our main findings and explore the potential for future work in the field.

8.1 An overview of our findings

In Chapter 1, the literature review, we contextualised the soundpost within violin acoustical research more broadly and undertook a comprehensive review of research on the soundpost, both theoretical and experimental. Establishing this basis for our work has played an important role in shaping the research questions that we have gone on to examine. The modern literature has proposed that the main role of the soundpost is to boost sound radiation at low frequencies by creating body resonances with net volume change. Valuable research by Schelleng (1971), which includes the development of a simple theoretical model, has demonstrated the effect of the soundpost on the lowest body resonances. The use of large scale parameter studies employed by Gough (2015b,a) has also provided a significant methodological model for our research. Reviewing the perspectives of violin makers on the soundpost has provided valuable contextual information, enabling us to refine the three main components of soundpost set-up addressed in this thesis: tightness, fit and position.

The primary aim of this thesis has been to develop an enhanced theoretical model incorporating the soundpost. In Chapter 2, we developed and refined the theoretical research developed by Woodhouse (2005) to design and mathematically implement a simplified model of the violin body and soundpost. Following a careful review of potential model parameters, we chose to model the plates of the violin as two flat rectangular plates with simply-supported sides, and the soundpost as both a bending beam and an axial rod. To model the components of tightness and fit, axial and bending springs have been used to couple the soundpost to the plates. Substantially simplifying the violin body in this way — whilst modelling the soundpost faithfully — has provided an effective basis for producing and interpreting our results. At the conclusion of Chapter 2, a range of tests were run in order to verify the validity of the proposed theoretical model.

In Chapter 3, we investigated the vibrational behaviour of the soundpost and springs within the theoretical model and conducted extensive parameter studies, focusing primarily on the coupling between the soundpost and the plates. Our results provided us with a significantly improved understanding of the mechanics of the soundpost as it operates within our simplified model. In this chapter we systematically investigate all aspects of the vibrational behaviour of the soundpost, examining in particular the effect of the axial and bending spring stiffness on the dynamics of the soundpost and the dynamics of the plates. Consistent with our initial predictions, these results demonstrate that increasing the stiffness of the axial and bending springs — or, the tightness and fit of the soundpost — leads to an increase in the resonance frequencies of the model. Further parameter studies examining the effect of variations in the size and material properties of the soundpost also reveal behaviour consistent with theory, and demonstrate agreement with the significant results presented by Gough (2015b,a).

The research presented in Chapters 2 and 3 considers the excitation of our simplified violin model via a single point harmonic force only, without accounting for the fact that a bridge on a real violin has two points of contact with the front plate. As the mechanics of the bridge are fundamental to the way in which the plates of a violin vibrate, the introduction of a bridge model, developed in Chapter 4, has been a key component of our research. Proposing further developments to the research presented by Woodhouse (2005), we have proposed an enhanced bridge model that provides the ability to locate the driving point at each of the four string notches. This is a significant enhancement that has allowed us to address questions regarding the ‘balance of the strings’. Although questions of sound quality are beyond the scope of this thesis, in this chapter we seek to develop an understanding of the physical interaction between the soundpost and bridge by deriving an equation for the bridge input admittance and performing extensive parameter studies, complementing the research of Woodhouse (2005). In this chapter,

our introduction of an adjustable bridge base height is extensively investigated, and the utilisation of skeleton curves allows us to assess the impact of the bridge base height on the ‘bridge hill’.

In Chapter 5, we utilise the bridge model developed and verified in Chapter 4 to explore the differences in the input admittance calculated at all four strings, with and without a soundpost. Our results indicate that the location of the driving force, or string notch, and the angle of the driving force, has a significant influence on the dynamics of the plate. By calculating the operating displacement shapes (ODS) of the plate we are able to visualise the impact of the location of the driving force on the vibration of the plates. Our results reveal that for key resonances, the input admittance calculated at the G string is largest when the soundpost is located near the right hand bridge foot. In this chapter, we closely investigate the impact of the location of soundpost on the balance of the strings by normalising the input admittance of the D, A and E strings with the G string input admittance and observing the relative differences between the responses. We conclude that moving the soundpost ‘west’ towards the centre of the plate results in the strings becoming more ‘balanced’.

In Chapter 6, we address the question of radiated sound pressure, focusing particularly on the role of the soundpost in boosting low frequency sound radiation. We use the approximation of the monopole sound source to estimate the sound radiation from our model at frequencies up to 500 Hz, with particularly illuminating results. We conduct extensive parameter studies involving variations to the stiffness of the axial and bending springs and the location of the soundpost to find the ‘optimal’ location for the soundpost at which radiated sound pressure is maximised. Our findings, using a single point harmonic force, reveal acoustical behaviour consistent with that observed in real violins. We conclude, first, that the soundpost provides an overall benefit by boosting sound radiation at low frequencies, and second, that a soundpost placed near the centre of the plate — but slightly off-centre — is the ideal arrangement for generating mode shapes which maximise the net volume change of the body.

Calculating the total radiated sound pressure using our bridge model returns similar results. However, we find that as a result of the symmetry of our model, the soundpost location that maximises radiated sound pressure depends on whether the excitation force occurs on the left or right hand side of the bridge. Though consistent with our expectations, this result emphasises that further theoretical investigations would benefit from the addition of a bass bar to introduce the asymmetry found in a real violin body.

Finally, in Chapter 7, we depart from our theoretical model to develop the outlines of experimental approaches that could supplement our theoretical results. We develop a physical model of the violin body and soundpost that reflects the flat plate approximation utilised in our

theoretical work. Attaching an accelerometer to the soundpost produces results that allow us to make observations about the bending resonances of the soundpost, and we also investigate the results of varying the length or tightness of the soundpost using a specially designed adjustable soundpost. Experimental challenges lead to our conclusion that future physical experimentation on the soundpost must go beyond the capabilities of a flat plate approximation.

8.2 Directions for future work

In this evolving area of acoustical violin research, there still many questions to address, and as this thesis has demonstrated, the potential for productive further research is substantial.

The theoretical research presented in this thesis has been underpinned by our simplified violin body model, consisting of two rectangular flat plates. The natural progression for any future theoretical research would be to build upon this model by making the plates more ‘violin-like’. Features such as the curvature and profile of the plates, and the introduction of *f*-holes and a bass bar, would all be worthwhile additions to the model. The introduction of the island area would be particularly worthwhile as recent finite-element modelling by Gough (2018) has demonstrated that localised island area modes are strongly perturbed by the presence of an offset soundpost and bass bar.

In the field of violin acoustics, small margins matter. The soundpost truly exemplifies this: the smallest change to its position, size and fit within the instrument can influence the dynamics of the body to the extent that a player can perceive a difference. This makes experimental research on the soundpost a significant challenge and opportunity.

Our research incorporating an adjustable soundpost is very much a first attempt to experimentally measure the effects of soundpost length on the dynamics of the violin body. It is highly encouraging that our adjustable soundpost has been able to function effectively, with incremental changes to its length being both easy to control and repeatable. However, the compressional forces acting on it from the plates mean that it is not possible to adjust the length of the soundpost while keeping it fixed within the model. As a result, the soundpost must be removed from the model for any readjustment to occur. Although the open sides of our model have ensured that this has not been a major practical challenge, adjustments do require careful alignment to ensure that the soundpost is re-positioned in the same place. What is easily overcome in the experimental context, however, makes the design potentially impractical to implement in a real violin, where the requirement to continually remove and replace the soundpost through the tight space of the *f*-holes, and to ensure consistency in the soundpost’s positioning, is more problematic. A

potential solution would be to develop an adjustable soundpost that can be adjusted in its length without rotation occurring at its ends, for example by using a screw mechanism similar to those used in the chin rest of a violin.

Another area with significant potential is the development of enhanced experimental work to complement theoretical investigations into radiated sound pressure. Methods for obtaining such measurements have already been outlined by researchers such as Gough (2013) and Curtin (2009). However, such experiments would again rely on careful adjustment of the soundpost within the instrument body and would significantly benefit from the introduction of an adjustable soundpost that could remain fixed within the instrument while adjustments are made.

These areas of future work represent exciting possibilities. Although violin makers already make very high quality instruments, such developments could enhance their ability to make more accurate and theoretically informed decisions about design and sound adjustment. And, while the violin of the classical period will remain unchanged in its great influence on our culture, rapid advancements in 3D printing and associated technologies suggest intriguing possibilities for the future design of ‘violin-like’ instruments and for theoretical modelling that allows the acoustics of the instrument to be ‘designed from the computer’.

In a 2010 lecture, Professor Jim Woodhouse suggested that the field of violin acoustics can be envisaged as a jigsaw puzzle:

When you make a jigsaw puzzle, what do you do? You build the edge bits first. Not because they show you the picture, but because they’re easier. And they kind of put a frame round things. And then you start trying to piece bits in, islands that you’re not quite sure where they go, and you gradually piece pieces in. Each individual bit doesn’t show you much more of the picture, but it’s cumulative and eventually things emerge. That’s how science works. You have to start with the easy things which are not necessarily the most important. Each individual bit may not seem all that much but you have to keep putting them in and gradually a picture builds up (Woodhouse, 2010).

This thesis has sought to contribute to this shared and cumulative puzzle of ongoing scientific research. Despite the violin’s long life, many more pieces must be filled in before we can arrive at a complete working knowledge of its acoustical secrets.

Bibliography

- Antonio Stradivari, Cremona, 1721, the ‘Lady Blunt’, 2018. URL
<https://tarisio.com/cozio-archive/property/?ID=24222>.
- J. Beament. *The Violin Explained: Components, Mechanism and Sound*. Clarendon Press, Oxford, 1997.
- G. Bissinger. Some mechanical and acoustical consequences of the violin soundpost. *Journal of the Acoustical Society of America*, 97:3154–64, 1995.
- G. Bissinger. Mode-ling the sound of the violin: The VR model and the role of the soundpost. *Catgut Acoustical Society Journal*, 3(5 (Series II)), May 1998.
- G. Bissinger and D. Oliver. 3D laser vibrometry on legendary old Italian violins. *Sound and Vibration*, 2010.
- F. P. Bowden and D. Tabor. *The friction and lubrication of solids*. Clarendon Press, Oxford, 1950.
- L. Cremer. *The Physics of the Violin*. The MIT Press, 1984.
- J. Curtin. Measuring violin sound radiation using an impact hammer. *Journal of the Violin Society of America*, XXII(1):186–209, 2009.
- J. Curtin. Bridge & Soundpost Veneers, 2018. URL
<https://josephcurtinstudios.com/instruments/bridge-and-post-veneers>.
- J. Dilworth. How well did Shakespeare know the violin? *Lutherie by ‘the Strad’*, April 2014.
- J. Dilworth. 7 tips on adjustments to get best out of your instrument, 2017. URL
<https://www.thestrads.com/7-tips-on-adjustments-to-get-the-best-out-of-your-instrument/7018.article>.

- H. Dünwald. Deduction of objective quality parameters on old and new violins. *Catgut Acoustical Society Journal*, (1 (Series II)):1–5, 1991.
- F. Fahy. *Sound and Structural Vibration: Radiation, Transmission and Response*, chapter 2.2 - The Volume Source, pages 56–57. Academic Press, 1987.
- J. J. Fang and O. Rodgers. Violin soundpost elastic vibration. *Catgut Acoustical Society Journal*, 2(1 (Series II)), May 1992.
- A. Filmer. The Basics of Sound Post Setting, 2009. URL <https://andrewfilmer.wordpress.com/bangkok-string-postings/the-basics-of-sound-post-setting/>.
- C. Fritz, I. Cross, B. C. J. Moore, and J. Woodhouse. Perceptual thresholds for detecting modifications applied to the acoustical properties of a violin. *Journal of the Acoustical Society of America*, 122:3640–3650, 2007.
- C. Fritz, J. Curtin, J. Poitevineau, P. Morrel-Samuels, and F. Tao. Preferences among old and new violins. *Proceedings of the National Academy of Sciences*, (109):760–763, 2012.
- C. Fritz, J. Curtin, J. Poitevineau, H. Borsarello, I. Wollman, F. Tao, and T. Ghasarossian. Soloist evaluations of six Old Italian and six new violins. *Proceedings of the National Academy of Sciences*, 111(20):7224–7229, 2014.
- C. Gough. The violin: Chaldni patterns, plates, shells and sounds. *European Physical Journal - Special Topics*, (145):77–101, 2007.
- C. Gough. Acoustic characterization of violin family signature modes by internal cavity measurements. *Proceedings of the Stockholm Music Acoustics Conference*, pages 75–81, 2013.
- C. Gough. Violin plate modes. *Journal of the Acoustical Society of America*, 137(1):139–153, 2015a.
- C. Gough. A violin shell model: Vibrational modes and acoustics. *Journal of the Acoustical Society of America*, 137(3):1210–1225, 2015b.
- C. Gough. The violin bridge-island input filter. *Journal of the Acoustical Society of America*, 143(1):1–12, January 2018.
- K. Guettler. *The bowed string: on the development of Helmholtz motion and on the creation of anomalous low frequencies*. PhD thesis, Royal Institute of Technology, Stockholm, 2002.

- E. Heron-Allen. *Violin-making: as it was and is*, chapter 8, pages 149–152. Ward, Lock & Co. Ltd., 2 edition, 1885.
- C. H. Hodges and J. Woodhouse. Theories of noise and vibration transmission in complex structures. *Reports on Progress in Physics*, pages 107–170, 1986.
- W. Huggins. On the function of the sound-post and on the proportional thickness of the strings of the violin. *Proceedings of the Royal Society of London*, 35:241–248, 1883.
- C. Hutchins. A note on the function of the soundpost. *Catgut Acoustical Society Newsletter*, (21): 27–28, 1974.
- C. Hutchins. A history of violin research. *Journal of the Acoustical Society of America*, 73(5): 1421–1440, 1983.
- E. V. Jansson. Admittance measurements of 25 high quality violins. *Acta Acustica united with Acustica*, 83:337–341, 1997.
- E. V. Jansson. Violin frequency response — bridge mobility and bridge feet distance. *Applied Acoustics*, 65:1197–1205, 2004.
- E. V. Jansson and B. K. Niewczyk. Admittance measurements of violins with high arching. *Acta Acustica united with Acustica*, 83:571–574, 1997.
- E. V. Jansson and B. K. Niewczyk. On the acoustics of the violin: bridge or body hill. *Catgut Acoustical Society Journal*, (3 (Series II)):23–27, 1999.
- E. V. Jansson, N.-E. Molin, and H. Sundin. Resonances of a violin body studied by hologram interferometry and acoustical methods. *Physica Scripta*, 2(6):243–256, 1970.
- K. L. Johnson. *Contact Mechanics*. Cambridge University Press, Cambridge, 1985.
- M. Katz. *The violin: A research and information guide* (Routledge Music Bibliographies). Routledge; Taylor & Francis Group, 2006.
- W. Kolneder and R. G. Pauly. *The Amadeus book of the violin: Construction, history, and music*, page 93. Amadeus Press; Portland, Oregon, 1998.
- N. M. M. Maia and J. M. M. Silva. *Theoretical and Experimental Modal Analysis*. Research Studies Press Ltd., 1997.

- J. Marchese. *The violin maker: Finding a centuries-old tradition in a Brooklyn workshop*, page 10. HarperCollins; New York, 2007.
- K. G. McConnell. *Vibration testing*. Wiley, New York, 1995.
- M. E. McIntyre and J. Woodhouse. On measuring the elastic and damping constants of orthotropic sheet materials. *Acta Metall.*, 26(6):1397–1416, 1988.
- J. E. McLennan. The Effect of the Soundpost on Violin Sound, 2005. URL https://newt.phys.unsw.edu.au/music/people/mclennan_soundpost.html.
- A. Pace. What's in a name? the philology of the violin soundpost. *Catgut Acoustical Society Journal*, 1(1 (Series II)), May 1988.
- S. S. Rao. *Vibration of Continuous Systems*. John Wiley & Sons, Inc., 2007.
- J. W. S. Rayleigh. *The Theory of Sound*. Macmillan and Co. Ltd., 2 edition, 1894.
- W. Reinicke. *Die Übertragungseigenschaften des Streichinstrumentenstegs*. PhD thesis, Technical University of Berlin, 1973.
- O. Rodgers. Effect of sound post adjustment. *Catgut Acoustical Society Journal*, 3(3 (Series II)), May 1997.
- H. O. Saldner, N.-E. Molin, and E. V. Jansson. Vibration modes of the violin forced via the bridge and action of the soundpost. *Journal of the Acoustical Society of America*, 100: 1168–1177, 1996.
- F. Savart. Mémoire sur la construction des instruments à cordes et à archets. *Tech. Rep. Paris, Deterville*, 1819.
- J. C. Schelleng. The action of the soundpost. *Catgut Acoustical Society Newsletter*, (16):11–15, Nov 1971.
- D. Schoenbaum. *The violin: A social history of the world's most versatile instrument*, page 85. W. W. Norton & Co., 2013.
- E. Skudrzyk. *Simple and Complex Vibratory Systems*. The Pennsylvania State University Press, 1968.
- E. Skudrzyk. The mean-value method of predicting the dynamic response of complex vibrators. *Journal of the Acoustical Society of America*, 67:1105–1135, 1980.

- W. H. Stone. *Elementary Lessons on Sound*, chapter 1, page 25. Macmillan and Co. Ltd., 1879.
- E. Szechenyi. Modal densities and radiation efficiencies of unstiffened cylinders using statistical methods. *Journal of Sound and Vibration*, 19(1):65–81, 1971.
- B. H. Tongue. *Principles of Vibration*. Oxford University Press, 2 edition, 2002.
- J. Woodhouse. On the Playability of Violins. Part I: Reflection Functions. *Acustica*, 78:125–136, 1993a.
- J. Woodhouse. On the Playability of Violins. Part II: Minimum Bow Force and Transients. *Acustica*, 78:137–153, 1993b.
- J. Woodhouse. 3C6 lecture notes - Cambridge University Engineering Department, 1995.
- J. Woodhouse. Body vibration of the violin — what can a maker expect to control? *Catgut Acoustical Society Journal*, 4(5):43–49, May 2002.
- J. Woodhouse. On the “bridge hill” of the violin. *Acta Acustica united with Acustica*, 91: 155–165, 2005.
- J. Woodhouse. Reverse engineering the violin. CIRMMT Distinguished Lectures in the Science and Technology of Music, March 2010.
- J. Woodhouse. The acoustics of the violin: a review. *Reports on Progress in Physics*, 77, 2014.
- J. Woodhouse and P. M. Galluzzo. The bowed string as we know it today. *Acta Acustica*, 90: 579–589, 2004.
- J. Woodhouse, C. Beament, and R. Aitchison. Personal communication.
- A. Zhang. *Playability of bowed string instruments*. PhD thesis, The University of Cambridge, 2015.
- A. Zhang and J. Woodhouse. The influence of different driving conditions on the frequency response of bowed-string instruments. *Proceedings of the Stockholm Music Acoustics Conference*, pages 147–152, 2013.